CESI LINEACT — Arts et Métiers Sciences et Technologies

ÉCOLE DOCTORALE SCIENCES ET MÉTIERS DE L'INGÉNIEUR

CESI LINEACT - Campus d'Aix-en-Provence

THÈSE

Présentée par **Mohamed Amine TAZI**
Soutenue le **14 Avril 2026**

Pour obtenir le **Doctorat** *délivré par*

L'École Nationale Supérieure d'Arts et Métiers
Spécialité : **Mécanique-matériaux**

Flexural Strengthening of Steel Structures with Externally Adhesively Bonded Carbon and Flax Composite Patches: Mechanical Performance and Water Ageing Effects

Thèse dirigée par :
Silvio DE BARROS, Directeur de recherche - CESI

et co-encadrée par :
Mouad JEBLI, Enseignant – Chercheur - CESI

		Jury
M. Laurent CHAMPANEY	Professeur – École Nationale Supérieure d'Arts et Métiers	Président
Mme Mariana Doina BANEA	Professeure – Université d'Aveiro	Rapporteure
Mme Émilie LEPRETRE	Ingénieure-Chercheuse – Université Gustave Eiffel	Rapporteure
M. Pascal CASARI	Professeur – Nantes Université	Examinateur
Mme Sofia Teixeira de FREITAS	Professeure – Université Technologique de Lisbonne	Examinateur
M. Romain GRANGEAT	Enseignant-Chercheur – CESI Saint-Nazaire	Examinateur
M. Silvio DE BARROS	Directeur de recherche – CESI Saint-Nazaire	Dir. de thèse
M. Mouad JEBLI	Enseignant-Chercheur – CESI Aix-en-Provence	Co-encadrant

THÈSE

“Theory without experiment is empty; experiment without theory is blind.”

Stephen P. Timoshenko.

Widely regarded as “The Father of Applied Mechanics”.

Remerciements

Ces trois années de doctorat m'ont profondément façonné, tant sur le plan personnel que professionnel et scientifique, et je suis reconnaissant pour toutes les rencontres formidables que j'ai faites durant cette période.

Je souhaite débuter ce texte de remerciement en remerciant profondément les rapporteuses de mon travail de thèse, Mme Émilie Leprêtre et Mme Mariana Doina Banea, pour l'honneur qu'elles me font en acceptant d'évaluer ce travail et pour le temps qu'elles y consacreront.

Je souhaite exprimer ma profonde gratitude à mon équipe d'encadrement, M. Silvio de Barros et M. Mouad Jebli, pour leur confiance, leur disponibilité, et les différents échanges constructifs que nous avons pu avoir tout au long de ces années. Je les remercie pour les différentes opportunités et collaborations internationales dans lesquelles ils m'ont impliqué.

Je souhaite remercier l'équipe de recherche CESI Lineact de la région Sud-Est, en particulier M. David Garcia, directeur de recherche régional, pour le support financier de mon projet de thèse, et pour nous avoir soutenu dans le développement d'un espace expérimental pour la fabrication de matériaux composites au sein du Campus CESI d'Aix-en-Provence. Par la même occasion, je remercie l'ensemble du personnel CESI Aix-en-Provence, pour tous les moments agréables du quotidien.

Je remercie les membres de mon comité de suivi individuel, M. Walid Deboucha et M. William Bettini, pour le sérieux de leur suivi, la pertinence de leurs remarques et leurs critiques constructives tout au long de l'avancement de cette thèse.

Je tiens à très profondément remercier M. Pascal Casari de m'avoir accueilli au cours de mes différents séjours au sein du laboratoire GeM de l'IUT de Saint-Nazaire. Ses conseils techniques, sa disponibilité, son bon sens et sa belle morale m'ont beaucoup marqué. Je tiens par la même occasion à remercier mes amis et doctorants du laboratoire GeM (Maryam, Benjamin, Calixte, Félix, Inès, Ali, Mohammad, Gayelle, Mahmoud, Abdeslam, Mathéus, Cassandre, …), pour les échanges scientifiques stimulants, leur soutien et la convivialité partagée à leurs côtés.

Ma plus profonde gratitude va vers Mme Sofia Teixeira de Freitas. Je la remercie de m'avoir pris sous son aile, et de m'avoir accueilli au sein des campus des instituts TU Delft et IST Lisboa. Sa gentillesse, sa disponibilité, son ouverture me marqueront à tout jamais. Par la même occasion, je tiens à la remercier de m'avoir introduit au sein de son groupe de travail « Interact », dans lequel j'ai rencontré des gens formidables, je pense à Rosemere, Ran, Zhiyuan, Michele, Mik, Charline, Marcello, Andrea, Marcio, …

Je n'oublie pas l'équipe de CESI Saint-Nazaire (Maëlig la directrice de CESI Saint-Nazaire, Karim le directeur de recherche régional, Romain, Hector, Lilian, Youssef, Imane, Ahmed, Chadi, Corentin, Pauline, Mathieu …) qui m'ont accueilli pour les quatre derniers mois de ma thèse et avec qui j'ai partagé de précieux moments de travail, de soutien mutuel et de bonne humeur.

À mes amis proches (Saad, Lyazid, Yahya, Taha, Ghita, Randa, Salma, Sarah, Houssam, Achraf, Nicoleta, Mohand, Amedeo, Carlotta …), à mes cousins (Nizar, Jad, Morad, Layla,

Rachid, Selim, Nina, Hiba, Fatima-Zahra, Hassna, Sofia, Miriam, Saïd, …), à mes oncles et tantes (Ahmed, Rachida, Khadija, Tita, Latifa, …). Je vous remercie pour tous les moments partagés au cours de cette période de thèse, pour la force intérieure que vous me procurez. Ma personne a été forgée autour de ces personnes. Je tiens à sincèrement m'excuser pour les périodes de silence radio que je vous ai fait subir.

À ma copine et âme sœur, Samantha, que j'aime et chéris. Je tiens à te remercier pour ton soutien, pour ta bonté, pour ton amour et ta bienveillance. Je suis très fier des personnes que nous sommes et devenons, et je suis très heureux de partager ma vie à tes côtés depuis plus de sept ans maintenant. Je tiens également à remercier sa petite famille (Jean-Baptiste, Rosanna, Iris et Thomas) pour leur soutien, leur disponibilité, leur accueil, leur écoute, et leurs bons conseils.

C'est avec énormément d'émotions que je finis ce paragraphe de remerciements, et je ne saurais le clôturer autrement qu'en remerciant les personnes les plus chères et précieuses à mon cœur, ma mère Touria, mon père Azzeddine, mon petit frère Ilyas et ma grande sœur Yasmine.

Maman, si j'ai fait une thèse c'est en grande partie grâce à toi, tu m'as inculqué les valeurs de curiosité, tu m'as appris à aller solliciter les gens, à m'intéresser à ce qu'ils font. Tu m'as appris à écouter ce qu'ils ont à me dire. Tu m'as appris à toujours être bienveillant et à savoir correctement m'intégrer socialement.

Papa, tu as toujours été un modèle d'endurance, de travail acharné. Tu m'as inculqué les valeurs du travail, de labeur, et de la rage de réussite.

Yasmine et Ilyas, vous avez toujours été mes meilleurs amis, mes confidents, ma plus grande source de soutien, mon bras gauche et droit. Je ne peux rêver d'une meilleure fratrie, et j'espère que notre amour subsistera jusqu'à notre vieil âge.

À ma petite famille, rien de tout ce que j'accomplis et espère accomplir ne serait possible sans vous. Je vous aime.

Résumé

Cette thèse porte sur le renforcement en flexion de structures en acier par collage externe de patchs en polymère renforcé de fibres (PRF). Elle compare l'influence de différents adhésifs structuraux ainsi que celle de renforts PRF carbone/époxy, lin/époxy et hybrides carbone-lin/époxy, puis analyse l'effet d'un vieillissement par immersion sur la performance de ces renforcements. Le renforcement par patch composite collé constitue une alternative attractive « à froid » au soudage ou au boulonnage, permettant de limiter les contraintes résiduelles, de réduire la masse ajoutée et de s'adapter à des géométries variées. Le travail se situe dans le cadre du renforcement de pièces acier saines, c'est-à dire l'amélioration de leur rigidité et de leur capacité par rapport à l'état initial, où la compréhension du transfert de charge acier–adhésif–composite est déterminante, l'adhésif concentrant fréquemment les contraintes interfaciales critiques. La première phase de la thèse a consisté à évaluer l'adhérence interfaciale d'assemblages collés acier/PRF lin au moyen du test de pelage standard dit « floating roller peel test ». Ce test a permis de comparer les efforts de pelage, d'identifier les modes de rupture et de sélectionner des adhésifs adaptés au collage de substrats acier et PRF. Bien que ce test soit principalement employé pour la résistance au pelage et l'analyse des surfaces de rupture, il peut aussi être exploité dans une approche de mécanique de la rupture ; une contribution de modélisation par éléments finis a ainsi été développée afin d'identifier des grandeurs énergétiques pertinentes, tel que l'énergie de libération, associées à la propagation de la rupture dans l'adhésif, à partir des résultats expérimentaux. La deuxième phase a porté sur des essais de flexion quasi-statique de plaques d'acier renforcées par patchs PRF collés, en mobilisant des adhésifs de comportement contrasté, allant d'un époxy rigide à des solutions plus ductiles (acrylate et polymère modifié silane). Cette partie met en évidence l'intérêt de stratégies de conception visant à réduire les concentrations de contraintes interfaciales, par le choix de l'adhésif et par l'optimisation de l'architecture des patchs hybrides, afin de retarder l'amorçage et le développement du décollement. La troisième phase a été consacrée à la caractérisation du comportement hygro-mécanique des patchs PRF, par essais gravimétriques en immersion, mesure du gonflement hygroscopique et essais de flexion avant/après vieillissement. Les résultats confirment une sensibilité très faible du composite carbone aux effets de l'eau en flexion, alors que le composite lin présente une dégradation marquée de la rigidité et une évolution vers une réponse plus ductile après vieillissement, avec une baisse du module en flexion de l'ordre de 6,3 % pour le carbone contre 53,6 % pour le lin, dans les conditions étudiées. Enfin, une stratégie de modélisation éléments finis des comportements hygro-mécaniques est proposée, en s'appuyant sur l'analogie entre conduction thermique et diffusion de l'eau, ainsi que sur une formulation de type « wetness fraction » permettant de traiter la discontinuité de teneur en eau aux interfaces. L'ensemble apporte des éléments de compréhension et des leviers de conception pour des renforcements acier composite collés plus performants et plus robustes vis-à-vis de l'eau.

Abstract

This PhD thesis investigates the flexural strengthening of steel structures using externally adhesively bonded fiber-reinforced polymer (FRP) patches. It compares the influence of different structural adhesives as well as that of carbon/epoxy, flax/epoxy, and hybrid carbon-flax/epoxy FRP reinforcements, and then analyses the effect of immersion ageing on the performance of these strengthening solutions. Strengthening with bonded composite patches is an attractive "cold" alternative to welding or bolting, as it helps limit residual stresses, reduces added weight, and can be adapted to a wide range of geometries. The work focuses on strengthening sound steel components, meaning improving their stiffness and load-carrying capacity compared with the initial state, where understanding load transfer across the steel–adhesive–composite assembly is critical, since the adhesive layer frequently concentrates critical interfacial stresses. The first phase of the thesis consisted in assessing the interfacial adhesion of bonded steel/flax-FRP assemblies using the standard peel test known as the "floating roller peel test". This test made it possible to compare peel loads, identify failure modes, and select adhesives suitable for bonding steel and FRP substrates. Although this test is primarily used to evaluate peel resistance and analyze fracture surfaces, it can also be exploited within a fracture mechanics framework; a finite element modelling contribution was therefore developed to identify relevant energetic quantities, such as the energy release rate, associated with crack propagation within the adhesive, based on the experimental results. The second phase focused on quasi-static bending tests on steel plates strengthened with bonded FRP patches, using adhesives with contrasting mechanical behavior, ranging from a stiff epoxy to more ductile solutions (acrylate and silane-modified polymer). This part highlights the value of design strategies aimed at reducing interfacial stress concentrations, through adhesive selection and optimization of hybrid patch layup, in order to delay the initiation and growth of debonding. The third phase was devoted to characterizing the hygro-mechanical behavior of FRP patches through immersion gravimetric tests, hygroscopic swelling measurements, and bending tests before and after ageing. The results confirm the very low sensitivity of the carbon composite to water effects in bending, whereas the flax composite exhibits a marked stiffness degradation and an evolution towards a more ductile response after ageing, with a flexural modulus reduction of about 6.3% for carbon versus 53.6% for flax under the investigated conditions. Finally, a finite element modelling strategy for hygro-mechanical behavior is proposed, based on the analogy between heat conduction and water diffusion, together with a "wetness fraction" formulation that enables the discontinuity of water content at interfaces to be addressed. Overall, this work provides mechanistic insight and design levers for more efficient and more water-robust adhesively bonded steel–composite strengthening solutions.

General Content

Remerciements 3
Résumé 5
Abstract 6
General Content 7
List of Figures 9
List of Tables 13
Table of Abbreviations 15
A. General Introduction 19
B. Literature Review 29
Résumé du chapitre en Français 31
B.1. Presence and importance of metallic structures in the industry 35
B.2. Damage mechanisms of steel structures 37
B.3. Externally adhesively bonded FRP method 40
B.4. Assessment for repair 47
B.5. Installation process 50
B.6. FRP-steel bond behavior 51
B.7. Flexural strengthening performance of FRP-Steel bonded joints 59
B.8. Environmental durability of FRP-Steel bonded joints 61
B.9. Compilation of existing technical guidelines for the design and construction of externally bonded FRP systems for strengthening metallic structures 67
B.10. Successful case studies 69
B.11. Modeling and strength prediction of bonded assemblies 80
B.12. Natural fiber composites: focus on Flax FRPs 88
B.13. Durability of FFRP in humid environments 91
C. Interfacial Adhesion Evaluation of a Steel-FFRP Joint with Different Adhesive Types Using the Floating Roller Peel Test 95
Résumé du chapitre en Français 96
C.1. Introduction 98
C.2. Materials and specimen manufacturing 100
C.3. Experimental methods 105
C.4. Experimental results and discussion 107
C.5. Finite element modeling 117
C.6. Conclusion 119

D. Influence of Adhesive Type and Layup of Hybrid Flax/Carbon Composite Patches on the Flexural Performance of Steel Plates 123
Résumé du chapitre en Français 125
D.1. Introduction 127
D.2. Materials 129
D.3. Specimen manufacturing 132
D.4. Experimental methods 137
D.5. Experimental results and discussion 139
D.6. Finite element modeling 144
D.7. Conclusion 155
E. Hygro-Mechanical Behavior of Hybrid Flax/Carbon Composites and Their Modeling Through the Thermal/Diffusion Analogy in FEM Framework 159
Résumé du chapitre en Français 160
E.1. Introduction 163
E.2. Materials and specimen manufacturing 166
E.3. Experimental methods 167
E.4. Experimental results and discussions 173
E.5. Numerical modeling 180
E.6. Conclusion 196
Appendix A 199
Appendix B 200
Appendix C 202
Appendix D 204
References 207

List of Figures

Figure B-1. Simplified representation of the anodic and cathodic reactions occurring on the surface of the metal. Adapted from (Esfandiari et al. 2020) 38
Figure B-2. Development of metallic structures and FRP strengthening techniques. Adapted from (Stratford et al. 2004) 41
Figure B-3. Repair system including corroded structure, adhesive layer (epoxy) and FRP laminate as reinforcement. Adapted from (ABS 2022)..... 42
Figure B-4. Geometric parameters of taper: ltp is the taper length and $tend$ is the thickness at the end of the taper. Inspired and enhanced from (Bouchikhi et al. 2013) 43
Figure B-5. Outline of damage assessment and decision-making process for choice of repair method. Inspired and enhanced from (DNV 2015; ABS 2022))..... 49
Figure B-6. Schematic representation of typical failure modes in FRP-steel bonded joints. Adapted from (Zhao and Zhang 2007)..... 58
Figure B-7. Representation of strengthening performance and conditions of calculation of live load. Inspired from (D. Schnerch et al. 2007). 59
Figure B-8. Typical tensile stress-strain behavior of rigid epoxy adhesives as a function of temperature. Adapted and enhanced from (Ke et al. 2020)) 63
Figure B-9. Tickford Bridge, Newport Pagnell, Buckinghamshire, UK (Courtesy of FaberMaunsell Structural Plastics, Beckenham, Kent, UK). Adapted from (Hollaway and Cadei 2002) 69
Figure B-10. Strengthened Hythe bridge, Oxfordshire, UK (Courtesy of Mouchel Consulting, West Byfleet, UK). Adapted from (Hollaway and Cadei 2002) 70
Figure B-11. Cross section of Hythe bridge. Adapted from (Hollaway and Cadei 2002) 71
Figure B-12. Hythe bridge: prestressed composite plated cast iron beam view. Adapted from (Hollaway and Cadei 2002)..... 71
Figure B-13. Installation of CFRP plate at Slattocks Canal Bridge (Courtesy of Mouchel Consulting, West Byfleet, UK). Adapted from (Hollaway and Cadei 2002)..... 72
Figure B-14. Upgrading of a principal curved beam, Nottingham, UK (Courtesy of Taylor Woodrow, Southall, UK and ACG, Derbyshire, UK). Adapted from (Hollaway and Cadei 2002)..... 73
Figure B-15. Upgraded King Street Railway Bridge. Stain gauges bonded to the composite plates and to the cast iron girder (Courtesy of Tone Gee and Partners, Cobham, Surrey, UK). Adapted from (Hollaway and Cadei 2002) 76
Figure B-16. Christina Creek Bridge (I-704) cross section. Adapted from (Miller et al. 2001) 77
Figure B-17. a) Full width CFRP plate sections and b) CFRP plates clamped to girder G5. Adapted from (Miller et al. 2001) 78
Figure B-18. Ultra-high modulus carbon fiber composite bonded to the flange of a universal beam (Courtesy of DML, Devonport, Devon, UK). Adapted from (Hollaway and Cadei 2002) 79
Figure B-19. Comparison of different traction-separation laws. Adapted from (Ramalho et al. 2020)..... 83
Figure B-20. Representation of loading modes for bonded joints 86
Figure B-21. Classification of natural fibers (enhanced and adapted from (Baley 2020; Célino et al. 2014)). 89

Figure B-22. Effect of water on fiber–matrix interface: (a) Formation of micro-cracks due to fiber swelling; (b) water molecules diffuse in the bulk matrix and flow along the fiber-matrix interface (c) water soluble substance leaching; and (d) debonding of fiber-matrix interface. Adapted from (Azwa et al. 2013). 92
Figure C-1. Surface roughness analysis results, a) 3D representation, b) Total profile, c) Roughness profile 102
Figure C-2. Assembly set-up and adhesive thickness control 103
Figure C-3. Microscope image of the zone of crack initiation 104
Figure C-4. Scheme of peel sample dimensions. 104
Figure C-5. a) Scheme of Floating roller peel test (Teixeira de Freitas et al. 2017), b) Experimental set-up for floating roller peel tests 106
Figure C-6. Example of cohesive failure areas (highlighted) for BioPU Specimen 1. (CF: Cohesive failure, and AF: Adhesive failure) 107
Figure C-7. Load-displacement curves for Epoxy Specimens (AxsonSika® ADEKIT A155/H9955), and b) corresponding fracture surface of composite rigid adherend for specimen 1 109
Figure C-8. a) Peel angle-displacement curves for Epoxy Specimens (AxsonSika® ADEKIT A155/H9955), and specimen 1 pictures, b) Zone of early debonding – Image captured at 16 mm of displacement, c) Drop in peel angle – Image captured at 22 mm of displacement, d) Steady peel force – Image captured at 91 mm of displacement 110
Figure C-9. a) Load-displacement curves for SMP specimens (Sikaflex®-554), and corresponding fracture surfaces for specimen 1, b) Steel interface and c) FFRP interface ... 112
Figure C-10. Peel angle-displacement curves for SMP specimens (Sikaflex®-554), and specimen 1 pictures, b) Image captured at 76 mm of displacement, c) Image captured at 174 mm of displacement 113
Figure C-11. Load-displacement curves for BioPU specimens (Castor-oil derived Polyurethane Kehl®), and fracture surfaces for specimen 1, b) Steel interface and c) FFRP interface and corresponding measured adhesive thickness in the mapped area 115
Figure C-12. a) Peel angle-displacement curves for BioPU specimens (Castor-oil derived Polyurethane Kehl®), and specimen 1 pictures, b) Beginning of loading – Image captured at 11 mm of displacement, c) Zone with no adhesive thickness and brutal debonding occurrence – Image captured at 52 mm of displacement, d) Zone with greater adhesive thickness – Image captured at 178 mm of displacement 117
Figure C-13. Representation of the numerical model of floating roller peel test 118
Figure C-14. Comparison of experimental load-displacement results of specimen 3 bonded with SMP adhesive, with FEM numerical results for $Gc = 25; 30; 35\ N.mm-1$ 119
Figure D-1. Engineering stress-strain curves of tensile tests on steel specimens 129
Figure D-2. Engineering stress-strain curves of tensile tests on FRP specimens 130
Figure D-3. Specimen geometry and dimensions. 132
Figure D-4. Steel substrate before (on top) and after (the white below) surface preparation 133
Figure D-5. a) Bonding area control using a 3D-printed part, b) Target triangular bead shape of adhesive joint, c) housing of the composite patch in the bonding area and d) 3D-printed U-shaped bracket 135
Figure D-6. Three point bending test set-up and imposed loading-unloading cycles 138
Figure D-7. Area of interest (AOI) and data extraction line, at the outer surface of the composite patch via DIC monitoring 138

Figure D-8. Load-deflection curves under three-point bending, regrouped by a) adhesive A, b) adhesive B and c) adhesive C 141
Figure D-9. a) Microscope images of composite failure mode a) side view, b) bottom view with F5 composite configuration and c) with C5 configuration 143
Figure D-10. a) Image of patch debonding failure a) side view and b) thin cohesive failure 143
Figure D-11. Graphical representation of mechanical property gains 144
Figure D-12. Visual representation of the CAE model 145
Figure D-13. Modeling of material behavior of steel 146
Figure D-14. Comparison of experimental and FE load-deflection curves for specimens bonded with composite patch configuration F3C2 148
Figure D-15. Comparison of DIC and FEM out-of-plane displacement W and first principal in-plane strain $\epsilon 11$ along data extraction line 149
Figure D-16. a) Peel b) shear stresses, and c) damage initiation criterion along the cohesive elements (Adhesive A) at 4% of final imposed displacement 151
Figure D-17. Visualization of data extraction path and ply numbering 153
Figure D-18. Longitudinal stresses S11 at 5% of final imposed displacement a) adhesive B b) Adhesive C 154
Figure D-19. Longitudinal stresses S11 at 50% of final imposed displacement a) adhesive B b) Adhesive C 154
Figure E-1. Experimental setup used for hygroscopic swelling measurements: the laser displacement sensor scans the specimen surface along a line while a stainless steel reference ensures calibration stability. 171
Figure E-2 Experimental setup used for three-point bending tests showing the 3R Labo testing machine, specimen, digital camera and 60 mm support span with 5 mm radius supports and loading nose. 172
Figure E-3. Evolution of water content as a function of the square root of immersion time for two composite configurations. The flax composite (F_{10}) exhibits the highest water uptake, while the carbon composite (C_{10}) shows minimal absorption. 173
Figure E-4. Evolution of water content as a function of the square root of immersion time for two composite configurations. The hybrid composite with two configurations: F6C4 and C2F6C2. 176
Figure E-5. Evolution of hygroscopic strain components (εxx, εyy and εzz) as a function of water content for flax (F10) and carbon (C10) composites. Experimental data are shown for fiver specimens per material, and solid lines represent the linear regression. 177
Figure E-6. Stress–strain curves obtained from three-point bending tests for the C10 and F10 composites, comparing unaged (3 specimens) and aged (5 specimens) conditions. 178
Figure E-7. Flexural modulus (ISO 178) of the C10 and F10 composites before and after ageing, with percentage values indicating the relative decrease in modulus due to hygrothermal exposure. 179
Figure E-8. Representation of a) discontinuity of water content ($CA$and CB) at the interface between two materials (A and B) having two respective water content saturations $CsatA$ and $CsatB$. b) continuity of wetness fraction (w) at the interface of two materials (A and B) with respective water contents at saturation $CsatA$ and $CsatB$ (adapted from (Ee Hua Wong et al. 1998)). 181
Figure E-9. Procedure for hygro-mechanical analysis using thermal-diffusion analogy for mono-materials. 183

Figure E-10. Procedure for hygro-mechanical analysis using thermal-diffusion analogy for multi-materials. 184
Figure E-11. Surfaces where water diffusion boundary condition is imposed (highlighted in red) for configuration C2F6C2. 187
Figure E-12. Visual observation of geometric change for hybrid laminates a) F6C4 and b) C2F6C2. 191
Figure E-13. Comparison of FEM vs Experimental gravimetric results. 192
Figure E-14. Evolution of hygroscopic strain components (εxx, εyy and εzz) as a function of water content for hybrid composite C2F6C2. Experimental data are shown as markers for five specimens per material, and dashed lines represent the numerical predictions. 193
Figure E-15. Numerical model representation of three point bending test for configuration C2F6C2. 194
Figure E-16. Comparison of experimental three point bending test results with FEM predictions of elastic behavior before and after ageing for the four composite specimen configurations. 195

List of Tables

Table B-1. Ratio of metallic bridges in France for each manager 36
Table B-2. Adhesive fracture mechanics test methods (adopted and enhanced from (Budzik et al. 2022; DNV 2015))..... 52
Table B-3. Review of strength analysis test methods of FRP-Steel flanged structures bonded joints 53
Table B-4. Review of experimental studies on adhesively bonded FRP strengthened steel structures under flexion loads. 60
Table B-5. Typical values of thermal expansion coefficients for different relevant substrates63
Table B-6. Existing technical guidelines for the design and construction of externally bonded FRP systems for strengthening metallic structures 67
Table B-7. Tensile mechanical properties of plant-based fibers vs. synthetic fibers (Shelly et al. 2025; Baley 2020; Célino et al. 2014) 89
Table C-1. Adhesive materials properties and type of bonding technique 101
Table C-2. Parameters for surface roughness analysis based on ISO 4287:1997 Standard... 102
Table C-3. Average surface roughness parameters (Ra – Arithmetic Mean Deviation of the roughness profile, Rt – Total Height of roughness profile) 102
Table C-4. Total specimen thickness, width and adhesive thickness..... 104
Table C-5. Average peel loads and failure mechanisms 107
Table D-1. Mechanical properties of ASTM A36 Steel (mean ± standard deviation)..... 129
Table D-2. Mechanical properties of carbon/epoxy and flax/epoxy composites (mean ± standard deviation) 130
Table D-3. Mechanical properties of Sika® adhesives (based on datasheets (Sika®Sikaflex-554 2023; Sika®Sikafast-555-l05 2023; Sika®Sikapower-1200 2023))..... 131
Table D-4. Manufactured composite patch layup configurations 133
Table D-5. Microscope parameter setting for on-line roughness analysis in accordance with ISO 21920-2:2021 134
Table D-6. Roughness analysis results..... 134
Table D-7. Nomenclature of the test specimens and adhesives thicknesses 136
Table D-8. Mechanical property gains for bonded assemblies 142
Table D-9. Element types for each part of the assembly 145
Table D-10. Numerical mechanical properties of carbon/epoxy and flax/epoxy laminates .. 146
Table D-11. Numerical mechanical properties of adhesives (based on datasheets) 147
Table E-1. Manufactured composite layup configurations. 166
Table E-2. Identified diffusion parameters and geometric characteristics of the reference (C10, F10) with 3D Fick model and hybrid (F6C4, C2F6C2) composites with mixing-law model. 175
Table E-3. Hygroscopic expansion coefficients identified for the reference C10 and F10 configurations. 177
Table E-4. Coefficient of reduction in modulus induced by hygrothermal ageing identified for the reference C10 and F10 composites. 180
Table E-5. Methodology of FEA parameters input for thermal-diffusion analogy in mono-material case. 182
Table E-6. Methodology of FEA parameters input for thermal-diffusion analogy in multi-material case. 183

Table E-7. Input numerical material parameters. 187
Table E-8. Visual representation of nodal temperature field output at the first, fifth and last increment of the hygro-mechanical analysis for the four composite configurations. 190

Table of Abbreviations

Abbreviation	Definition
ADCB	Asymmetric Double Cantilever Beam
AF	Adhesive failure
AOI	Area of interest (in DIC post-processing)
ASTM	ASTM International (standards organization)
BioPU	Bio-based polyurethane
BK	Benzeggagh–Kenane (mixed-mode fracture criterion)
C10	Carbon/epoxy laminate configuration with 10 carbon plies
C2F6C2	Hybrid laminate configuration with 2 carbon plies + 6 flax plies + 2 carbon plies
C5	Carbon/epoxy patch configuration with 5 carbon plies
CAE	Computer-aided engineering
CF	Cohesive failure
CFRP	Carbon fiber reinforced polymer
COST	European Cooperation in Science and Technology
CTE	Coefficient of thermal expansion
CZM	Cohesive zone modeling
DCB	Double Cantilever Beam
DIC	Digital image correlation
DLS	Double lap shear (test)
DMA	Dynamic mechanical analysis
ELS	End Loaded Split (beam)
ENF	End Notched Flexure
FE	Finite element
FEA	Finite element analysis

Abbreviation	Definition
FEM	Finite element method / finite element modelling
FFM	Finite fracture mechanics
FDM	Finite Differences Method
FFRP	Flax fiber reinforced polymer
F10	Flax/epoxy laminate configuration with 10 flax plies
F3C2	Hybrid patch configuration with 3 flax plies + 2 carbon plies (flax plies adjacent to the adhesive in this manuscript)
F5	Flax/epoxy patch configuration with 5 flax plies
F6C4	Hybrid laminate configuration with 6 flax plies + 4 carbon plies
FRP	Fiber reinforced polymer
FRPT	Floating roller peel test
GFRP	Glass fiber reinforced polymer
GPS	Geometrical Product Specifications (surface texture standards framework)
HM	High modulus
LCA	Life cycle assessment
LM	Low modulus
LTM	Low-temperature moulding
MDI	4,4′-methylenediphenyl diisocyanate
MMB	Mixed mode bending
MPC	Multi-point constraint
NM	Normal modulus
PU	Polyurethane
SCB	Split Cantilever Beam
SERR	Strain energy release rate
SIF	Stress intensity factor
SLJ	Single lap joint

Abbreviation	Definition
SMP	Silane modified polymer
TAST	Thick adherend shear test
TDCB	Tapered Double Cantilever Beam
T_g	Glass transition temperature
UD	Unidirectional
UHM	Ultra-high modulus
XFEM	eXtended finite element method

A.General Introduction

French version:

Les structures métalliques telles que les ponts en acier, les structures navales, les composants offshore et les charpentes industrielles occupent une place centrale dans les infrastructures modernes. Elles sont exposées à des mécanismes de dégradation à long terme, tels que la perte de section induite par la corrosion et la fissuration par fatigue. Lorsqu'un dommage est détecté, les stratégies de réparation et de renforcement doivent restaurer la capacité portante sans introduire de nouvelles vulnérabilités, tout en restant réalisables sous les contraintes du terrain et compatibles avec l'inspection et les pratiques de conception recommandées (Hollaway and Cadei 2002; DNV 2015; ABS 2022). Dans ce contexte, les renforts composites en polymère renforcé de fibres (PRF) collés en surface se sont imposés comme une alternative attractive « à froid » aux réparations en acier soudées ou boulonnées. Ces composites sont légers, peuvent être installés avec une interruption de service limitée, et évitent tout apport thermique (par soudage par exemple) qui peut s'avérer impraticable ou préjudiciable dans certains secteurs industriels tels que l'offshore et le transport pétrolier (Stratford and Cadei 2006). Cependant, malgré des démonstrations convaincantes et des études de cas réussies, l'adoption plus large du renforcement par PRF collés pour les structures métalliques reste freinée par le fait que le joint de colle constitue fréquemment le maillon critique. Sous chargement de service (en particulier dans les scénarios dominés par la flexion, typiques des éléments de type plaque et des semelles de poutres), la couche d'adhésif doit simultanément transférer la charge de manière efficace afin de mobiliser la rigidité du patch composite, et tolérer de sévères concentrations locales de contraintes, incluant des composantes de pelage/clivage susceptibles de déclencher un décollement prématuré aux extrémités du patch et au droit des défauts (Smith and Teng 2001; Deng et al. 2004; Stratford and Cadei 2006). Par conséquent, améliorer la fiabilité du renforcement acier–PRF exige une vision couplée de la qualité de l'adhésion, du comportement mécanique de l'adhésif, de l'architecture du composite et de la sensibilité environnementale.

La présente thèse s'inscrit dans cette motivation d'ingénierie : contribuer à la mise en œuvre de patchs composites collés pour le renforcement de structures métalliques telles que les ponts en acier, avec un accent particulier sur le comportement du collage acier–PRF. La thèse explore un espace de conception dans lequel des matériaux biosourcés et respectueux de

l'environnement (tels que les fibres de lin) peuvent être intégrés à des concepts de renforcement sans sacrifier la performance structurale, et où les outils de modélisation peuvent soutenir l'interprétation et le transfert vers la pratique de l'ingénieur. Les stratifiés en polymère renforcé de fibres de lin (FFRP) présentent un intérêt particulier car les fibres de lin sont renouvelables et peuvent offrir des caractéristiques rigidité/poids attractives dans certaines architectures (comparables aux fibres de verre), tout en présentant des bénéfices potentiels en termes d'empreinte environnementale et de chaînes d'approvisionnement locales européennes et françaises (Baley 2020). Dans le même temps, les composites à base de lin présentent une affinité à l'humidité supérieure à celle des stratifiés à base de carbone, en raison de la nature hydrophile des fibres végétales, ce qui rend la durabilité et l'évolution hygro-mécanique des considérations incontournables pour des concepts de renforcement collé destinés à un service en milieu humide. Cette thèse aborde donc non seulement la question « quel niveau de renforcement peut être atteint », mais aussi « qu'est-ce qui le limite », « comment le choix de l'adhésif déplace le mécanisme limitant », et « comment l'exposition environnementale peut modifier la base matérielle sur laquelle le renforcement est construit ». Conformément aux objectifs de la thèse, quatre chapitres (B à E) ont été développés, et leurs contenus sont décrits de manière synthétique dans le texte ci-après.

Le chapitre B établit le socle bibliographique nécessaire pour cadrer les choix expérimentaux et interpréter les résultats observés et générés dans les chapitres C, D et E. Il rappelle d'abord la prévalence des structures métalliques et résume les mécanismes d'endommagement dominants qui motivent la réparation, à savoir la corrosion et la fatigue. Il passe ensuite en revue la méthode des PRF collés en surface, incluant les principes de conception géométrique, les règles de sélection des matériaux pour les patchs PRF et les adhésifs, les étapes d'évaluation de l'aptitude à la réparation, et les processus d'installation, où la préparation de surface et les conditions de cuisson sont reconnues comme des contributeurs décisifs à la qualité de collage obtenue. Le chapitre synthétise également l'état de l'art sur le comportement du collage PRF–acier, incluant les méthodes d'essai courantes et les modes de rupture rapportés dans les systèmes en acier renforcés, et passe en revue les performances de renforcement en flexion rapportées dans la littérature ainsi que les préoccupations de durabilité environnementale. Enfin, la revue de littérature s'élargit vers la présentation des stratégies de modélisation analytiques et numériques existantes pour les assemblages collés, puis introduit les composites à fibres naturelles avec un accent sur les PRF de lin, en établissant pourquoi les renforts à base de lin sont mécaniquement viables mais sensibles à l'environnement, et pourquoi leur

intégration dans le renforcement collé de l'acier soulève des questions spécifiques qui ne sont pas entièrement couvertes par une littérature majoritairement orientée carbone/époxy.

Le chapitre C constitue le premier chapitre de travaux et est délibérément positionné comme une étape de sélection de l'adhésion pour le collage acier–FFRP. Le décollement prématuré étant largement rapporté comme une limitation gouvernante des renforts collés en surface, et la performance du collage étant très sensible à la préparation de surface, à la chimie de l'adhésif et aux conditions de mise en œuvre, la thèse évalue d'abord la qualité de l'adhésion interfaciale dans une configuration contrôlée, à dominante de pelage, avant de procéder aux comparaisons de renforcement structural. L'essai de pelage au rouleau flottant (Floating Roller Peel Test) est employé conformément à la norme ASTM D3167, car un chargement de type pelage impose un champ de contraintes localisé à dominante d'ouverture en pointe de fissure, et se révèle donc particulièrement sensible à l'intégrité interfaciale et à la sélection du chemin de rupture. Le chapitre C exploite les résultats de charge de pelage, l'évolution de l'angle de pelage et les observations des faciès de rupture pour classer les types d'adhésifs étudiés et déterminer si la rupture est majoritairement adhésive (contrôlée par l'interface) ou cohésive (contrôlée par le volume), clarifiant ainsi le « maillon faible » du système acier/adhésif/FFRP. En outre, les essais de pelage étant des essais de propagation de fissure dans lesquels les charges mesurées intègrent à la fois la dissipation de rupture et les contributions de flexion du bras pelé, une approche de modélisation par éléments finis est introduite pour soutenir l'interprétation énergétique, en l'absence de voie d'extraction analytique directe pour la configuration du rouleau flottant. Le résultat du chapitre C n'est donc pas seulement un classement de la qualité d'adhésion sous un mode de chargement représentatif des conditions propices au décollement, mais aussi un ensemble d'hypothèses relatives aux interfaces qui sont reportées dans l'étude de renforcement menée au chapitre D.

Le chapitre D passe ensuite du criblage d'adhérence à la performance structurale, en évaluant le renforcement en flexion de plaques d'acier par patchs composites collés en surface. L'analogie structurale motivante est la semelle tendue des poutres en I, où la flexion induit des contraintes de traction qui peuvent être atténuées par un renfort collé en surface, à condition que le transfert de charge soit effectif et que le décollement soit maîtrisé. Le chapitre est explicitement construit pour clarifier comment les comportements mécaniques de différents adhésifs et l'empilement du patch (stratifiés carbone/époxy, lin/époxy et hybrides lin/carbone) gouvernent l'efficacité du renforcement, sa répétabilité et les mécanismes de ruine. Il aborde en

particulier le compromis intrinsèque qui sous-tend les renforts collés acier–PRF : les adhésifs rigides peuvent maximiser le transfert de déformation et les gains de renforcement, mais peuvent élever les contraintes interfaciales de pelage/clivage et déclencher un décollement prématuré, tandis que des adhésifs plus souples peuvent atténuer les concentrations de contraintes mais réduire l'efficacité du renforcement en limitant le transfert de charge. Pour compléter les réponses expérimentales en flexion trois points et les mesures de déformation par corrélation d'images numériques (DIC), la modélisation par éléments finis est utilisée pour interpréter les tendances observées en termes de développement des contraintes interfaciales de pelage et de cisaillement et de distributions de contraintes dans l'épaisseur du patch composite, fournissant ainsi des explications au niveau des contraintes pour les transitions entre décollement contrôlé par l'interface, rupture du composite et absence de rupture dans la plage de flèche imposée. Dans le récit de la thèse, le chapitre D établit donc, expérimentalement et avec appui numérique, des critères de sélection de l'adhésif et de la séquence d'empilement du patch composite qui favorisent la réduction des contraintes interfaciales tout en maximisant la performance mécanique (capacité portante et rigidité).

Le chapitre E aborde enfin une question fondamentale qui devient incontournable dès lors que des stratifiés à base de lin et hybrides sont envisagés pour le renforcement collé : comment l'exposition à l'humidité modifie le comportement du patch composite qui est implicitement supposé lors de l'interprétation de l'efficacité du renforcement et des scénarios de ruine. Le chapitre évalue le comportement hygro-mécanique des stratifiés lin/époxy, carbone/époxy et hybrides lin/carbone, en mettant l'accent sur les mêmes configurations hybrides que celles utilisées au chapitre D, de sorte que les constats à l'échelle du matériau puissent être reconnectés au comportement à l'échelle structurale. Un programme expérimental combinant suivi gravimétrique de l'absorption, identification des paramètres de diffusion, mesures de gonflement hygroscopique et essais de flexion avant et après vieillissement fournit des preuves quantitatives des cinétiques d'humidité, des déformations hygroscopiques induites et de l'évolution de la rigidité et de la résistance. Le transport d'humidité est discuté à l'aide de cadres de type Fick, couramment appliqués aux matrices polymères et aux PRF sur les plages d'exposition pertinentes, tandis qu'une attention particulière est portée aux implications de l'hybridation, où des tendances de gonflement discordantes peuvent générer des contraintes internes et une courbure induite par l'humidité. Pour soutenir la modélisation prédictive des stratifiés multi-matériaux, le chapitre E développe et implémente également un cadre éléments finis fondé sur l'analogie thermique–diffusion, en étendant les concepts de fraction d'humidité

(« wetness fraction ») qui assurent la continuité du champ moteur aux interfaces entre matériaux et permettent un calcul stable des champs spatiaux d'humidité dans les hybrides. L'approche de modélisation validée est positionnée comme une passerelle vers de futures analyses de durabilité des assemblages collés, car elle fournit une voie pratique pour intégrer les champs d'humidité et les propriétés dépendantes de l'humidité dans les simulations.

Dans l'ensemble, la thèse a été construite pour progresser selon une approche cohérente et graduelle, afin de contribuer à l'amélioration de la conception et de l'évaluation des systèmes de renforcement collés acier–FFRP : en établissant d'abord la qualité de l'adhésion sous chargement à dominante de pelage (chapitre C), puis en quantifiant l'influence du comportement mécanique de différents adhésifs et des séquences d'empilement des patchs composites sur le renforcement en flexion résultant et les modes de ruine observés dans les joints collés PRF–acier (chapitre D), et enfin en caractérisant l'évolution du comportement du patch composite sous l'effet de l'humidité, accompagnée d'un cadre de modélisation capable de représenter le comportement hygro-mécanique des multi-matériaux (chapitre E). Ces travaux contribuent à consolider les éléments de preuve nécessaires pour raisonner à la fois sur la performance et sur la fiabilité des renforts collés pour les structures métalliques.

English version:

Metallic structures such as steel bridges, ship structures, offshore components, and industrial frames occupy a central position in modern infrastructure, but they are also intrinsically exposed to long-term degradation mechanisms, most prominently corrosion-driven section loss and fatigue cracking. When damage is detected, repair and strengthening strategies must restore structural capacity without introducing new vulnerabilities, while remaining feasible under field constraints and compatible with inspection and recommended design practices (Hollaway and Cadei 2002; DNV 2015; ABS 2022). In this context, externally adhesively bonded fiber-reinforced polymer (FRP) reinforcements have emerged as an attractive "cold work" alternative to welded or bolted steel repairs: they are lightweight, can be installed with limited interruption of service, and avoid thermal input (through welding for example) that may be impractical or detrimental in some industrial fields such as the offshore and oil transport sectors (Stratford and Cadei 2006). However, despite convincing demonstrations and successful case studies, the wider adoption of adhesively bonded FRP strengthening for metallic structures remains constrained by the fact that the bondline is frequently the critical link. Under service loading (particularly bending-dominated scenarios typical of plate elements and beam flanges) the adhesive layer must simultaneously transfer load efficiently to mobilize the stiffness of the composite patch and tolerate severe local stress concentrations, including peel/cleavage components that can trigger premature debonding at patch terminations and defects (Smith and Teng 2001; Deng et al. 2004; Stratford and Cadei 2006). As a result, improving the reliability of steel–FRP strengthening requires a coupled view of adhesion quality, adhesive mechanical behavior, composite architecture, and environmental sensitivity.

The present thesis is positioned within this engineering driver: contributing to the implementation of adhesively bonded composite patches for the strengthening of metallic structures such as steel bridges, with a specific focus on steel–FRP bond behavior. The thesis explores a design space where bio-based and environmentally friendly materials (such as flax fibers) can be integrated into reinforcement concepts without sacrificing structural performance and where modelling tools can support interpretation and transfer to engineering practice. Flax fiber reinforced polymer (FFRP) laminates are of particular interest because flax fibers are renewable and can provide attractive stiffness-to-weight characteristics in certain architectures (comparable to glass fibers), while also offering potential benefits in terms of environmental footprint and local European/French supply chains (Baley 2020). At the same time, flax-based

composites exhibit higher affinity to moisture than carbon-based laminates due to the hydrophilic nature of plant fibers, making durability and hygro-mechanical evolution unavoidable considerations for bonded strengthening concepts intended for humid service. This thesis therefore addresses not only “how much strengthening can be achieved” but also “what limits it”, “how adhesive choice shifts the limiting mechanism”, and “how environmental exposure can modify the material basis on which strengthening is built”. In accordance with the objectives of the thesis, four chapters (B to E) have been developed, and their contents are described synthetically in the text above.

Chapter B provides the literature foundation required to frame the experimental choices and interpret the observed and generated results in chapters C, D and E. It first recalls the prevalence of metallic structures and summarizes the dominant damage mechanisms that motivate repair, namely corrosion and fatigue. It then reviews the externally adhesively bonded FRP method, including geometric design principles, material selection guidelines for FRP patches and adhesives, assessment steps for repair suitability, and installation processes where surface preparation and curing conditions are recognized as decisive contributors to achieved bond quality. The chapter further synthesizes the state-of-the-art on FRP–steel bond behavior, including common test methods and the failure modes reported in strengthened steel systems, and it reviews flexural strengthening performance reported in the literature as well as environmental durability concerns. Finally, the literature review expands toward presenting existing analytical and numerical modelling strategies for bonded assemblies, then introduces natural fiber composites with a focus on flax FRPs, establishing why flax-based reinforcements are mechanically feasible yet environmentally sensitive, and why their integration into bonded steel strengthening raises specific questions not fully covered by the predominantly carbon/epoxy-oriented literature.

Chapter C constitutes the first work chapter and is deliberately positioned as an adhesion selection step for steel–FFRP bonding. Because premature debonding is widely reported as a governing limitation for externally bonded reinforcements and because bond performance is highly sensitive to surface preparation, adhesive chemistry, and processing conditions, the thesis first evaluates interfacial adhesion quality in a controlled, peel-dominated configuration before performing structural strengthening comparisons. The Floating Roller Peel Test is employed following ASTM D3167, because peel-type loading imposes a localized opening-dominated stress field at the crack tip and is therefore particularly sensitive to interfacial

integrity and fracture-path selection. Chapter C exploits peel load results, peel angle evolution, and fracture surface observations to rank the investigated adhesive types and identify whether failure is predominantly adhesive (interface-controlled) or cohesive (bulk-controlled), thereby clarifying the "weak link" in the steel/adhesive/FFRP system. In addition, because peel tests are crack propagation tests in which measured loads embed both fracture dissipation and peel-arm bending contributions, a finite element modelling approach is introduced to support energetic interpretation in the absence of a direct analytical extraction route for the floating roller configuration. The outcome of Chapter C is thus not only a ranking of adhesion quality under a representative debonding-prone loading mode, but also a set of interface-related assumptions that are carried forward into the strengthening study performed in chapter D.

Chapter D then moves from adhesion screening to structural performance by evaluating the flexural strengthening of steel plates by externally bonded composite patches. The motivating structural analogy is the tensile flange of I-section beams, where bending induces tensile stresses that can be mitigated by an externally bonded reinforcement, provided that load transfer is effective and debonding is controlled. The chapter is explicitly constructed to clarify how different adhesives' mechanical behaviors and patch layup (carbon/epoxy, flax/epoxy, and hybrid flax/carbon laminates) govern strengthening efficiency, repeatability, and failure mechanisms. In particular, it addresses the intrinsic trade-off that underpins steel–FRP bonded reinforcements: stiff adhesives can maximize strain transfer and strengthening gains but may elevate interfacial peel/cleavage stresses and trigger premature debonding, whereas more compliant adhesives can mitigate stress concentrations but reduce strengthening efficiency by limiting load transfer. To complement experimental three-point bending responses and DIC-based deformation measurements, finite element modelling is used to interpret observed trends in terms of interfacial peel and shear stress development and through-thickness stress distributions in the composite patch, thereby providing stress-level explanations for transitions between interface-controlled debonding, composite rupture, and non-failure within the imposed deflection range. In the thesis narrative, Chapter D therefore establishes experimentally, and numerically backed, criteria for selection of adhesive and composite patch stacking sequence which promote the reduction of interfacial stresses while maximizing mechanical performance (load-bearing capacity and rigidity).

Chapter E finally addresses a fundamental question that becomes unavoidable once flax-based and hybrid laminates are considered for bonded strengthening: how moisture exposure modifies

the composite patch behavior that is implicitly assumed when interpreting strengthening efficiency and failure scenarios. The chapter evaluates the hygro-mechanical behavior of flax/epoxy, carbon/epoxy, and hybrid flax/carbon laminates, with emphasis on the same hybrid configurations used in Chapter D, so that the material-level findings can be connected back to structural-scale behavior. An experimental program combining gravimetric uptake monitoring, diffusion-parameter identification, hygroscopic swelling measurements, and flexural testing before and after ageing provides quantitative evidence of moisture kinetics, induced hygroscopic strains, and stiffness/strength evolution. Moisture transport is discussed using Fick-type frameworks commonly applied to polymeric matrices and FRPs over relevant exposure ranges, while particular attention is paid to the implications of hybridization, where mismatched swelling tendencies can generate internal stresses and moisture-induced curvature. To support predictive modelling for multi-material laminates, Chapter E also develops and implements a finite element framework based on the thermal–diffusion analogy, extending wetness-fraction concepts that ensure continuity of the driving field across material interfaces and enable stable computation of spatial moisture fields in hybrids. The validated modelling approach is positioned as a bridge toward future durability-oriented analyses of bonded assemblies, because it provides a practical route to incorporate moisture fields and moisture-dependent properties into simulations.

Overall, the thesis was built to advance in a coherent, stepwise approach to contribute to the improvement of design and assessment of steel–FFRP bonded strengthening systems. By first establishing adhesion quality under peel-dominated loading (Chapter C), then quantifying the influence of different adhesives' mechanical behavior and composite patch stacking sequences on the resulting flexural strengthening and failure modes observed in FRP-Steel bonded joints (Chapter D), and finally characterizing moisture-driven evolution of the composite patch behavior together with a modelling framework capable of representing hygro-mechanical behavior of multi-materials (Chapter E). The works contribute to building more evidence needed to reason about both performance and reliability of bonded reinforcements for metallic structures.

B. Literature Review

CONTENT

B. Literature Review 29
Résumé du chapitre en Français 31
B.1. Presence and importance of metallic structures in the industry 35
B.2. Damage mechanisms of steel structures 37
B.2.1. Corrosion 37
B.2.2. Fatigue 39
B.3. Externally adhesively bonded FRP method 40
B.3.1. Context 40
B.3.2. Geometric design guidelines 42
B.3.2.i FRP Patch 42
B.3.2.ii Adhesive 43
B.3.3. Material selection guidelines 44
B.3.3.i FRP Patch 44
B.3.3.ii Adhesive 46
B.4. Assessment for repair 47
B.5. Installation process 50
B.6. FRP-steel bond behavior 51
B.6.1. Bond test methods 51
B.6.1.i Fracture analysis 51
B.6.1.ii Strength analysis 51
B.6.2. Failure modes in externally bonded FRP-Steel systems 58
B.7. Flexural strengthening performance of FRP-Steel bonded joints 59
B.8. Environmental durability of FRP-Steel bonded joints 61
B.8.1. Elevated temperatures 61
B.8.2. Moisture absorption 65
B.9. Compilation of existing technical guidelines for the design and construction of externally bonded FRP systems for strengthening metallic structures 67
B.10. Successful case studies 69
B.10.1. Tickford bridge (2000) 69
B.10.2. Hythe bridge (2001) 70

B.10.3. Slattocks Canal Bridge (2001) 71
B.10.4. Plate bonding a curved surface 72
B.10.5. King Street Railway Bridge (2000) 74
B.10.6. Christina Creek Bridge (2000) 76
B.10.7. Blast strengthening of a universal column 79
B.11. Modeling and strength prediction of bonded assemblies 80
B.11.1. Existing methods 80
B.12. Natural fiber composites: focus on Flax FRPs 88
B.12.1. Context 88
B.12.2. Classification of natural fibers 88
B.12.3. Flax fibers 90
B.12.4. Flax composites 91
B.13. Durability of FFRP in humid environments 91

Résumé du chapitre en Français

Ce chapitre établit le socle bibliographique nécessaire pour situer les choix expérimentaux et interpréter les résultats présentés dans les chapitres C, D et E. Il couvre successivement le contexte des structures métalliques et leurs mécanismes d'endommagement, la méthode de renforcement par patchs polymères renforcés de fibres (PRF) collés, le comportement de l'assemblage collé acier–PRF, la durabilité environnementale, les référentiels techniques et retours d'expérience, les stratégies de modélisation des assemblages collés, et enfin les composites à fibres naturelles avec un accent particulier sur les PRF à fibres de lin (FFRP).

La première section (B.1) rappelle la place prépondérante des structures métalliques dans l'industrie et le génie civil. Elle retrace le développement historique des matériaux métalliques de construction — fonte grise, fer puddlé, acier au carbone et fonte ductile — et en présente les propriétés mécaniques de base. L'acier, en raison de son excellent rapport résistance/poids et de sa facilité de fabrication et de mise en œuvre, y est identifié comme le matériau de référence ; le terme « métallique » désigne donc l'acier dans la suite du manuscrit. Les données récentes de l'Observatoire national de la route (2024) montrent que les ponts métalliques représentent une part significative du parc français, notamment à l'échelle des métropoles, et qu'une proportion importante de ces ouvrages présente des défauts nécessitant un entretien spécialisé, voire des travaux de réparation.

La section B.2 traite des mécanismes d'endommagement des structures en acier. Après une distinction étymologique entre réparation (restaurer l'état initial) et renforcement (dépasser la capacité initiale), elle rappelle que des insuffisances peuvent provenir de la conception, de la construction ou de l'évolution des conditions d'usage et des normes. Les statistiques de défaillance en France, aux États-Unis et à l'international identifient la corrosion et la fatigue comme les deux mécanismes de dégradation dominants. La corrosion, de nature essentiellement électrochimique, se décline en corrosion généralisée, par piqûres, en sillons ou de bords ; au-delà de la perte de section, elle crée des concentrations de contraintes qui dégradent la ténacité et accélèrent l'amorçage de fissures. La fatigue, processus progressif et localisé sous chargement cyclique, se développe en trois phases (amorçage, propagation stable, rupture instable) à partir de sites de concentration de contraintes tels que les détails soudés, les trous de rivets ou les piqûres de corrosion ; les études européennes indiquent qu'environ 80 à 90 % des défaillances des structures en acier sont liées à la fatigue et à la rupture.

La section B.3 introduit la méthode de renforcement par PRF collés en surface. Face à une structure déficiente, le renforcement présente souvent un intérêt économique et patrimonial supérieur à la démolition-reconstruction. Par rapport aux solutions traditionnelles soudées ou boulonnées, le collage de patchs PRF évite les contraintes résiduelles thermiques, réduit la masse ajoutée, s'adapte aux géométries courbes (procédé par voie humide) et permet d'orienter les propriétés du matériau. La section détaille ensuite les règles de conception géométrique : les biseaux d'extrémité (tapers) du patch réduisent significativement les pics de contraintes interfaciales (de l'ordre de 30 % en cisaillement et 50 % en pelage selon les analyses élastiques de la littérature) ; la longueur de collage doit dépasser la longueur effective de transfert au-delà de laquelle le gain devient marginal ; l'épaisseur de l'adhésif lisse les concentrations de contraintes au prix d'une moindre efficacité de transfert ; les congés d'adhésif (spew fillets) retardent l'amorçage des fissures en extrémité. Concernant la sélection des matériaux, le patch est choisi avant tout pour sa rigidité axiale (module × épaisseur), le carbone constituant la référence, avec les nuances haut module pour les éléments massifs ; la sensibilité galvanique du couple carbone/acier en milieu humide impose toutefois une isolation électrique ou le recours à des fibres non conductrices. Pour l'adhésif, l'époxy demeure la solution industrielle de référence, mais la littérature montre qu'un adhésif plus souple et tenace peut redistribuer les contraintes interfaciales et retarder le décollement, et que des solutions bi-adhésives (rigide au centre, souple aux extrémités) constituent une voie prometteuse.

La section B.4 décrit le processus décisionnel d'évaluation avant réparation, inspiré des pratiques recommandées (DNV, ABS) : identification du caractère critique de l'élément endommagé, évaluation de la criticité du dommage selon des critères d'acceptation (perte d'épaisseur admissible, longueur de fissure), et choix entre réparation collée et réparation conventionnelle. La méthode reste peu certifiée à l'échelle industrielle et des efforts de recherche (par exemple l'action COST CA18120) visent à établir une feuille de route de certification des structures primaires collées. La section B.5 souligne le rôle décisif du processus d'installation : préparation de surface par abrasion, nettoyage au solvant, découpe et manipulation des tissus, interposition d'un pli de verre isolant entre acier et carbone, application uniforme de l'adhésif, chasse des bulles d'air, formation de congés et respect du cycle de cure — autant d'étapes qui conditionnent directement l'adhérence obtenue et le risque de décollement prématuré.

La section B.6 se concentre sur le comportement du joint collé acier–PRF, identifié comme le maillon faible de l'assemblage. Elle distingue deux familles d'essais : les essais de mécanique

de la rupture (DCB, TDCB, ENF, ELS, SCB, ADCB, MMB), qui caractérisent la propagation de fissure et l'énergie de rupture selon les modes I, II, III et mixtes, et les essais de résistance (traction de plaques renforcées, flexion trois/quatre points, joints à simple et double recouvrement, TAST, essais de pelage en T et au rouleau flottant FRPT), qui évaluent la capacité globale d'un assemblage. Les modes de rupture typiques des systèmes acier–PRF collés y sont recensés : rupture adhésive aux interfaces acier/adhésif ou PRF/adhésif, rupture cohésive de l'adhésif, délaminage du composite, rupture du PRF et plastification de l'acier.

La section B.7 dresse l'état de l'art des performances de renforcement en flexion quasi-statique. Le collage d'un patch PRF améliore la rigidité, la charge à plastification et la charge ultime de l'élément renforcé. Une synthèse actualisée des campagnes expérimentales de la littérature (poutres et profilés renforcés par CFRP de module normal à ultra-haut, avec différents adhésifs) montre des gains de charge ultime très variables, d'environ 7 % à plus de 70 % selon la rigidité relative du renfort, la configuration et le mode de ruine.

La section B.8 examine la durabilité environnementale des joints acier–PRF, en se concentrant sur les deux menaces principales : la température et l'humidité. À l'approche de la température de transition vitreuse des adhésifs structuraux (60–130 °C), module et résistance chutent fortement — la résistance de joints à double recouvrement peut être réduite de moitié à 70 °C — d'où la règle de conception limitant la température de service à Tg − 20 °C ; un effet bénéfique de post-cuisson est toutefois possible sous exposition modérée. Les écarts de coefficients de dilatation thermique entre acier, composites et adhésifs génèrent par ailleurs des contraintes internes sous variations de température. Concernant l'humidité, l'eau absorbée plastifie l'adhésif (baisse de Tg, du module et de la résistance, partiellement réversible pour l'eau libre), dégrade l'adhésion interfaciale acier/adhésif par hydratation de la couche d'oxydes — avec un basculement progressif d'une rupture cohésive vers une rupture interfaciale — et induit un gonflement hygroscopique contrarié qui superpose des contraintes de pelage et de cisaillement aux extrémités de recouvrement, là où l'ingression d'eau est la plus rapide.

La section B.9 compile les référentiels techniques existants pour la conception et la mise en œuvre des systèmes PRF collés sur structures métalliques (ICE 2001, CIRIA C595, CNR-DT 202, propositions de Schnerch et al., règles DNV et ABS, guide AASHTO/NSBA, etc.), en les situant historiquement. La section B.10 présente sept études de cas réussies, principalement au Royaume-Uni et aux États-Unis : ponts de Tickford, de Hythe (première application précontrainte sur fonte), de Slattocks Canal, de King Street et de Christina Creek, renforcement d'une poutre courbe à Nottingham et renforcement anti-souffle d'un poteau. Ces retours

d'expérience démontrent la faisabilité en site des solutions collées, y compris sur fonte ancienne, surfaces courbes et sous contraintes patrimoniales.

La section B.11 passe en revue les méthodes de prédiction de la résistance des assemblages collés : méthodes analytiques, mécanique des milieux continus, mécanique de la rupture, mécanique de l'endommagement, méthode des éléments finis étendus (XFEM), méthodes sans maillage, et surtout la modélisation par zones cohésives (CZM), retenue comme méthode principale de la thèse. Le formalisme des lois de traction–séparation y est développé : réponse élastique, critères d'amorçage de l'endommagement (contrainte nominale maximale, critère quadratique), variable d'endommagement scalaire et évolution pilotée par l'énergie de rupture, avec prise en compte de la mixité de mode via des critères en loi puissance ou de type Benzeggagh–Kenane.

Enfin, les sections B.12 et B.13 introduisent les composites à fibres naturelles. Après une classification des fibres (végétales, animales, minérales), l'attention se porte sur les fibres de lin, dont la rigidité spécifique élevée, la disponibilité sous de multiples architectures et l'ancrage de la filière en Europe — la France, et notamment la Normandie, dominant la production mondiale — en font le renfort végétal de référence. La faisabilité structurelle des composites lin/polymère est aujourd'hui démontrée et industrialisée. Toutefois, l'hydrophilie des fibres végétales confère aux FFRP une sensibilité particulière à l'eau : la diffusion, généralement analysée par gravimétrie dans un cadre fickien, s'accompagne d'un gonflement anisotrope des fibres qui, contrarié par la matrice, engendre des contraintes internes, un affaiblissement de l'interface fibre/matrice et de la microfissuration, même en l'absence de chargement extérieur. Ce constat justifie l'étude hygro-mécanique dédiée menée au chapitre E et fonde la problématique centrale de la thèse : intégrer des renforts biosourcés dans le renforcement collé de structures acier sans en compromettre la performance ni la durabilité.

B.1. Presence and importance of metallic structures in the industry

Throughout history, the development of metallic materials has started with cast iron at the end of the 18th century and wrought iron in the middle of the 19th century. Steel was first produced at the end of the 19th century, and has been continuously developed ever since.

Many metallic structures over the world are likely to be fabricated from one of the following materials: (a) grey cast iron; (b) wrought iron; (c) carbon steel; and (d) ductile cast iron. A detailed discussion of these materials is beyond the scope of this manuscript; however, their basic properties and historical development will be presented below according to (Hollaway and Cadei 2002):

(a) Grey cast iron was widely used in the UK and other parts of the world between 1700 and 1880. It is an iron alloy containing 2.5 – 4% carbon, primarily in the form of graphite flakes. Other elements, present as impurities, significantly influence its material properties. Due to its brittle nature, the behavior of cast iron is challenging to predict accurately, and its properties exhibit large variations. Its typical tensile and compressive strengths range from 120 – 160 MPa and 500 – 650 MPa, respectively. The material exhibits nonlinear behavior in both tension and compression, with a pronounced nonlinearity in tension. Its low elastic limit in tension corresponds to the initial localized yielding at the graphite flakes' tips, which act as stress concentrators.

(b) In the mid-1840s to early 1850s, wrought iron replaced cast iron as the preferred structural material due to its superior performance. However, by the late 19th century, it was eventually replaced by mild steel. The production of wrought iron involved heating cast iron to a high temperature and exposing it to a strong air blast, which eliminated carbon and other impurities. The purified iron was then reheated to a welding temperature and rolled to further reduce slag (mainly a mixture of metal oxides and silicon dioxide) content. Depending on the desired quality, this rolling process could be repeated up to four times. The resulting material was nearly pure iron—softer than steel but more resistant to corrosion. The quality of wrought iron varied depending on its time and place of production, leading to significant differences in its mechanical properties. Apart from variations in strength, potential defects such as laminations, inclusions, and irregularities could influence failure modes. Wrought iron's strength is anisotropic, typically ranging from 310 to 360 MPa in the rolling direction, while in the perpendicular direction, it is approximately two-thirds of that value.

(c) Carbon steel was first commercially produced in Britain around 1860, but it was not widely used for structural applications until 1890. By that time, it had largely replaced wrought iron in construction. The quality of early steels varied significantly compared to modern steels. A common structural steel, such as Grade 43 mild steel, typically has a yield strength of approximately 275 MPa and an elastic modulus of 205 GPa. Yielding begins at a strain of about ~ 0.13%, with plastic deformation continuing until a strain of roughly ~ 16%.

(d) Ductile cast iron has similar properties to carbon steel and is used in structures where the formability or thickness is essential. It is more expensive than standard steel plates and profiles.

Throughout the discussions presented in this manuscript, the term "metallic" material, will always refer to steel unless otherwise stated. Steel structures are indeed the most commonly used structures due to their many advantages including high strength to weight ratio, ease of transportation, manufacturing and industrial application (Tafsirojjaman et al. 2022). For the civil engineering field, structural members such as beams and columns are made of steel, where flexural, fatigue and compressive stresses are induced in these members.

The recent 2024 report of the ONR (Observatoire national de la route), presents the number total number of bridges and ratio of metallic ones managed by different managers, namely the French state, departments and metropoles (IDRRRIM 2024). This information is presented in **Table 0-1**. It can be seen that metallic bridges represent a significant proportion, especially at the metropole scale and % in surfaces. Moreover, the same report evaluates the deterioration state of the metallic bridges at the metropole scale, and indicates that 51.2% of these bridges have defects and require specialized maintenance work, 10.1% have an impaired condition and require repair work, and a relatively small percentage of these structures are critically deteriorated which led to a reduction in load-bearing capacity in short-term.

Table 0-1. Ratio of metallic bridges in France for each manager

Manager	Total number of bridges in sample	% in number of bridges classified as "Metallic and Steel-Concrete"	% in surface of bridges classified as "Metallic and Steel-Concrete"
State	11850	5.5%	-
Departments	72974	5%	11.7%
Metropoles	1786	17.9%	20.9%

B.2. Damage mechanisms of steel structures

Before examining the different mechanisms of damage in metallic structures, it is useful to pause and consider the etymology of the terms **repair** and **strengthening**, which are central to strategies for dealing with structural deficiencies. The word repair derives from the Latin "*reparare*", meaning "to make ready again" or "to restore," reflecting the idea of returning a structure to its original condition. In contrast, strengthening comes from the Old English "*strengþu*" (strength), rooted in the Proto-Germanic "*strangithō*", meaning "power" or "force," and denotes the act of making something stronger than it originally was. Together, these terms frame the two main approaches used to extend the service life of metallic structures.

Steel structures may be found structurally unsatisfactory in service for a variety of reasons. At the design stage, deficiencies such as marginal safety factors, design errors, the use of substandard materials, or poor construction workmanship and management can prevent structures from achieving their intended design strengths. Once in service, several additional factors can reduce structural adequacy. These include stricter safety requirements, changes in usage leading to stress redistribution, modernization or alterations introducing new load conditions, increases in the intensity or magnitude of applied loads, and the upgrading of design standards that render existing structures noncompliant (Hollaway and Cadei 2002). These deficiencies often create the need for strengthening interventions to enhance structural capacity.

In addition to design or usage related inadequacies, steel members are also subject to deterioration. Most recent found failure statistics of metallic bridges in France (Cerema 2017), USA (Lee et al. 2013) and worldwide (Imam and Chryssanthopoulos 2010; Frangopol et al. 2010), indicate that fatigue and corrosion are the significant and most common damage mechanisms. In these cases, repair interventions are issued.

In the subsections below, a brief description of the latter two damage modes reported in the literature is presented.

B.2.1. Corrosion

Corrosion is a natural process that converts a refined metal into a more chemically stable oxide. It is the gradual deterioration of a metal by chemical or electrochemical reaction with their environment. Since most corrosion reactions are electrochemical in nature, this corresponds to the formation of a corrosion cell consisting of an anode, a cathode, and an electrolyte (a conductive aqueous medium). The current flows from the cathode to the anode through the ions present in the electrolyte, and from the anode to the cathode through the electrons moving

within the metal. The anodic reaction provides electrons at the anode (oxidation reaction), which are then consumed at the cathode by a reduction reaction. **Figure 0-1** visually represents the corrosion phenomena.

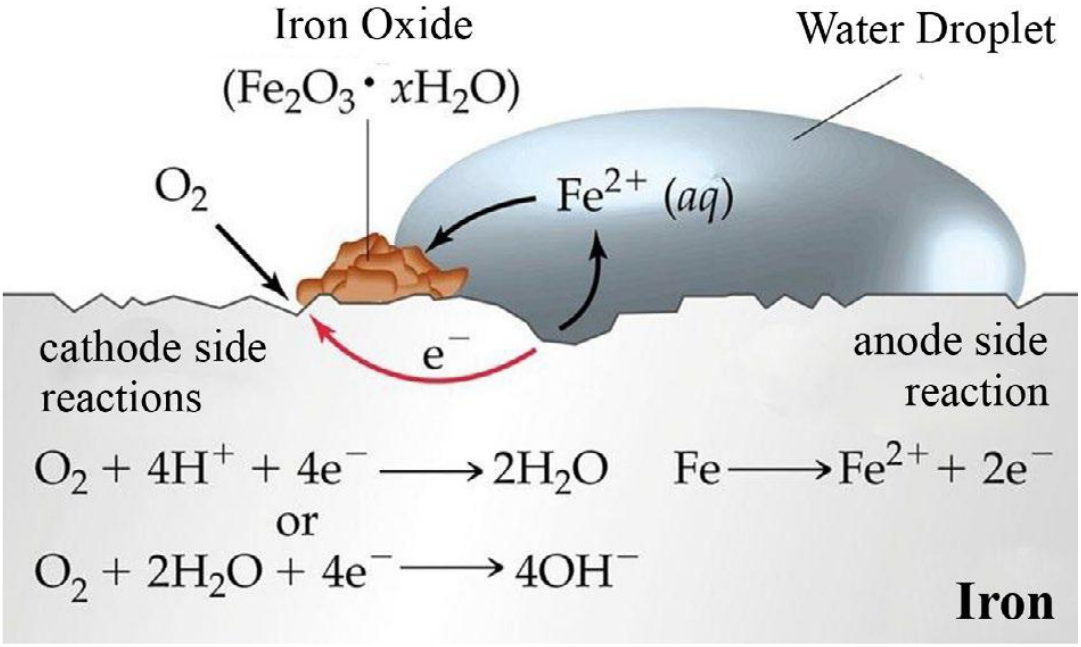

Figure 0-1. Simplified representation of the anodic and cathodic reactions occurring on the surface of the metal. Adapted from (Esfandiari et al. 2020)

According to (ABS 2022) corrosion can be divided into the following categories :

- *General Corrosion*. Uniform corrosion with uniform loss of metal over an entire surface.
- *Pitting Corrosion*. A form of localized corrosion, which is an attack with localized pits on the steel surface. The intensity of the pitting is to be estimated. Typically, pitting repairs include renewal of plates, building up pits by welding, or application of filler compounds such as epoxy or epoxy with glass-flake.
- *Grooving Corrosion*. Another form of localized corrosion, which is localized material loss normally adjacent to welding joints.
- *Edge Corrosion*. Local material wastage at the free edges of plates and stiffeners.

Corrosion damage not only causes the effective cross-section loss of steel structure but also forms uneven rust pits on its surface, the existence of rust pits will give rise to surface stress concentration and reduces its plasticity and fracture toughness, which is bound to accelerate the crack initiation and propagation, and consequently result in the serious deterioration of fatigue performance of steel structure (Li et al. 2022).

B.2.2. Fatigue

Fatigue is a progressive and localized damage process produced by cyclic loading, in which a structural component can fail after a large number of load cycles even when the maximum nominal stress remains below the monotonic yield strength. The defining feature is that the damage accumulates incrementally and is not necessarily accompanied by noticeable macroscopic plastic deformation before final rupture, which makes fatigue particularly insidious for in-service metallic structures subjected to repetitive actions such as traffic-induced bending, vibration, or wave loading (Cerema 2017). From a fracture mechanics standpoint, fatigue failure is commonly described as a sequence involving (i) crack initiation at sites of stress concentration and microstructural discontinuity, followed by (ii) stable crack propagation over many cycles, and finally (iii) unstable fracture when the remaining ligament can no longer sustain the applied load.

In practical steel structures, typical initiation sites include welded details, geometrical discontinuities, notches, rivet or bolt holes, and corrosion pits, all of which elevate local stress ranges and promote early cracking under repeated loading (Emilie Lepretre 2017). This link between service-induced stress cycling, local stress concentration and progressive crack growth explains why fatigue is consistently identified as a dominant deterioration mechanism in metallic infrastructure and why it is treated explicitly in bridge design and assessment standards.

This subsection does not seek to provide a comprehensive review of fatigue phenomena, as fatigue is not a primary focus of the present PhD work; nevertheless, fatigue constitutes a major concern in the service performance of metallic structures, and a brief introduction felt therefore necessary to be included in the manuscript to establish the context. The reader is therefore referred to more specialized literature on the subject, including (E. Lepretre et al. 2018; DNV 2011; EN 1993-1-9 (Eurocode 3) 2005; Schijve 2009; Anderson 2005; Stephens and Fuchs 2001).

Indeed, numerous European studies and technical reports indicate that fatigue is a dominant failure mode for steel bridges and other metallic structures. For instance, European Commission–supported review of fatigue damage in railway bridges notes that roughly 80 - 90% of failures in steel structures are related to fracture and fatigue (European Commission. Directorate General for Research and Innovation. 2014).

B.3. Externally adhesively bonded FRP method

B.3.1. Context

When faced to a deficient steel structure, two options are generally available. Demolition and rebuild, or strengthening/repair. The choice between the two options depends on many factors, such as material and labor costs, time during which the structure is out of commission or functioning only partially, and distribution of other facilities. However, the financial benefits of strengthening, as opposed to demolition, can often be considerable, particularly if a simple, quick strengthening technique is available. In addition, if the structure in question has historical importance, the possibility of demolition may be precluded (Hollaway and Cadei 2002).

The repair of steel structures is historically and conventionally performed by welding and/or bolting of a steel patch to the damaged area. Although effective, the application of these solutions cause an increase in dead weight, inflexibility, exposure to corrosion, and development of residual stresses caused by welding (Samali et al. 2023).

The main advantage of FRP laminates over steel plates in the strengthening of steel structures is its high strength-to-weight ratio, leading to ease and speed of transportation and installation, thus reducing disturbance to services and traffic (Chataigner and Lepretre 2025). Another significant advantage of FRP, which applies only to FRP laminates formed via the wet lay-up process, is the ability of such FRP laminates to follow curved and irregular surfaces of a structure. A third advantage of FRP is that its material properties in different directions can be tailored for a particular application. The combination of adhesive bonding with shape flexibility makes bonded wet lay-up FRP laminates an attractive strengthening method in a number of applications. Needless to say, steel plates can also be adhesively-bonded but bonding is less attractive for steel plates due to their heavy weight and inflexibility in shape. Furthermore, for the same tensile capacity, a steel plate has a much larger bending stiffness than an FRP laminate so a steel plate leads to higher peeling stresses at the interface between the steel plate and the steel substrate (Paboeuf et al. 2025; Teng et al. 2012).

The bonding of FRP laminates is superior to the welding of steel plates in the following situations (Teng et al. 2012):

1. Bonding of FRP laminates for enhanced fatigue resistance has the advantage that the strengthening process does not introduce new residual stresses;

2. In certain applications (e.g. oil storage tanks and chemical plants) where fire risks must be minimized, welding needs to be avoided (or is even forbidden) when strengthening an operational structure; bonding of FRP laminates is then a very attractive alternative;
3. High-strength steels suffer significant local strength reductions in heat-affected zones of welds, so bonded FRP laminates offer an ideal strength compensation method.

The first use of FRP materials for structural strengthening is believed to have taken place in 1991. The initial development of FRP strengthening techniques focused on concrete structures, and the extension of the technique to metallic structures has been a more recent development (Stratford et al. 2004). **Figure 0-2** presents a visual timeline of the development of metallic materials and FRP strengthening techniques.

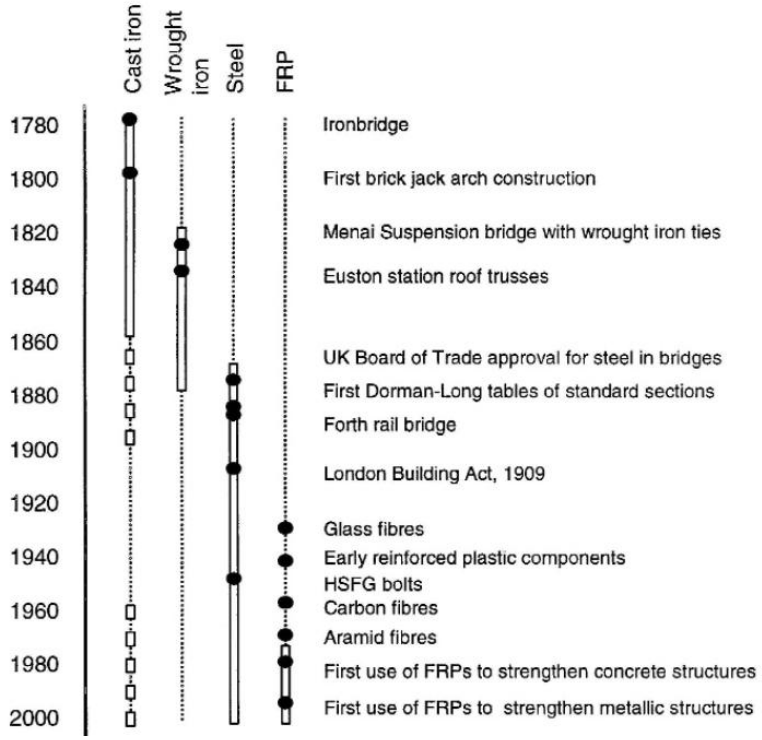

Figure 0-2. Development of metallic structures and FRP strengthening techniques. Adapted from (Stratford et al. 2004)

In general, research efforts on retrofitting civil engineering steel elements by adhesive bonding of FRP materials have examined the following four areas as noted in (AASHTO/NSBA 2024):

a. repair of naturally deteriorated steel girders,
b. repair of a girder or steel plates artificially notched to simulate fatigue cracks,
c. strengthening an intact section to increase the girder stiffness and flexural capacity, and

d. increasing the composite action between the steel girder and concrete deck in bridge application.

The work carried out in this thesis falls under objectives a and c. **Figure 0-3** is a visual representation of the adhesively bonded FRP method.

Moreover, a very important aspect in steel strengthening with FRP bonded patches, is the understanding of load transfer, from the steel substrate, through the adhesive layer, to the composite patch (Hollaway and Cadei 2002). Most of the time the adhesive layer is the component where critical interfacial stresses will develop, and will fail; While the composite patch is significantly below the values of stress which it can endure. Design guidelines regarding the geometric, and material selection constraints for ensuring that the composite patch is put under work, while reducing interfacial stresses in the adhesive to avoid its failure, and also ensuring enough load-bearing capacity to the structure will be discussed in what follows.

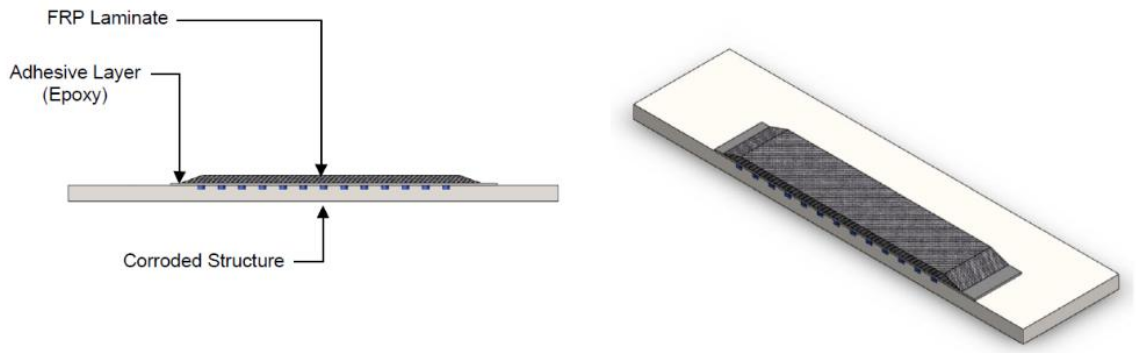

Figure 0-3. Repair system including corroded structure, adhesive layer (epoxy) and FRP laminate as reinforcement. Adapted from (ABS 2022)

B.3.2. Geometric design guidelines

B.3.2.i FRP Patch

One of the most important aspects of geometric design of adhesively bonded FRP patches, are the edge tapers. **Figure 0-4** is a visual representation of a taper and presents its geometric parameters. (Bouchikhi et al. 2013) combined analytical developments with finite element analyses to demonstrate the effectiveness of FRP tapers in substantially reducing FRP/adhesive interfacial stresses and, consequently, in delaying premature debonding. Complementary elastic stress analyses dedicated to steel beams strengthened with adhesively bonded plates were reported by (Stratford and Cadei 2006), and by (Deng et al. 2004), who similarly highlighted the beneficial role of end tapering: their theoretical predictions indicate reductions of peak

interfacial stresses that can be on the order of ~30% in shear and ~50% in normal (peeling) components, which directly supports the objective of suppressing early plate-end debonding.

Thickness of the composite patch also plays a big role as thicker patches tend to produce higher interfacial stresses. A similar problem occurs when working with bonded steel plates as they have higher bending stiffness, which induces higher peeling stresses at the edges (Hollaway and Cadei 2002).

However, while the literature has therefore largely converged on geometric strategies aimed at lowering interfacial stress peaks (through tapering, thickness tailoring, etc.) most studies emphasize the stress reduction aspect without explicitly quantifying the potential penalty in global stiffness contribution or strengthening efficiency associated with these geometric modifications.

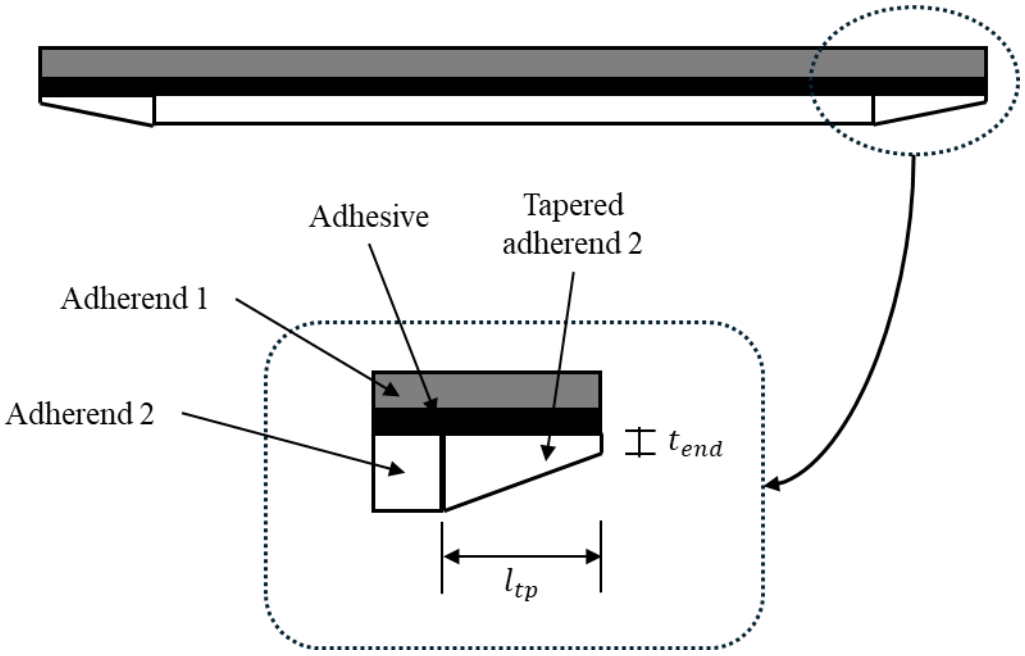

Figure 0-4. Geometric parameters of taper: l_{tp} is the taper length and t_{end} is the thickness at the end of the taper. Inspired and enhanced from (Bouchikhi et al. 2013)

B.3.2.ii Adhesive

The bond length is one of the most important geometric parameters of the adhesive for the design of adhesively bonded FRP strengthening solutions. It directly influences the development and distribution of interfacial stresses; indeed, the strain level experienced by the adhesive (particularly at the overlap ends) drops significantly when a longer bonded length is used, making debonding more likely for short overlaps, whereas sufficiently long bond lengths tend to shift the governing failure mode towards CFRP rupture or steel yielding, depending on the reinforcement stiffness. This behavior is consistent with the elastic stress analyses

developed for plated/bonded strengthening, which show that the adhesive end regions govern the peak shear and peel (normal) stresses, and that these peaks control the onset of premature debonding (Deng et al. 2004; Stratford and Cadei 2006). Numerous experimental and numerical studies further indicate that load transfer between the steel substrate and the FRP laminate occurs over a finite effective bond length, beyond which additional bonded length provides diminishing structural benefit; in other words, once the transfer zone is fully developed, extending the overlap doesn't improve capacity (Y. Yang et al. 2017; Guo et al. 2023; Calabrese et al. 2024).

Besides the bonded length, the adhesive thickness also plays a major role because it changes the local compliance of the bondline and therefore the amplitude of stress concentrations near the overlap ends. In their analytical stress analysis of CFRP-plated steel beams, (Deng et al. 2004) showed that increasing the adhesive thickness decreases the maximum interfacial stresses, which can be understood as a stress-smoothing effect due to higher shear deformability of the adhesive layer; however, this geometric benefit must be balanced against the reduced load-transfer efficiency associated with an overly compliant bondline, especially when the objective is to mobilize the reinforcement at service loads.

A third geometric aspect concerns the end geometry of the adhesive layer, since abrupt adhesive terminations exacerbate the shear/peel peaks that trigger debonding. In bonded-joint mechanics, introducing spew fillets at the overlap ends is a well-established way to reduce end stress/strain concentrations and delay crack initiation (M. Y. Tsai and Morton 1995; Akpinar et al. 2013). In the specific context of plated strengthening of beams, the combined influence of plate-end shaping and adhesive spew geometry has also been explicitly addressed, showing that end-shaping strategies can be used to reduce the severity of the interfacial stress concentrations that govern premature debonding (Deng and Lee 2008).

B.3.3. Material selection guidelines

B.3.3.i FRP Patch

The choice of the FRP patch for externally bonded strengthening of steel members is first a matter of stiffness compatibility. In practice, the composite reinforcement is rarely sized by its tensile strength alone; instead, it is selected so that its axial rigidity (through its elastic modulus and thickness) is sufficient to attract load from the steel at service levels and to reduce steel strains in a measurable way. This is why carbon-fiber laminates have become the reference solution in steel strengthening: for a given thickness, CFRP provides a markedly higher

modulus than glass- or basalt-based systems, which translates into a higher strengthening efficiency per unit added thickness and weight. Experimental campaigns on steel beams strengthened with CFRP plates consistently confirm that the stiffness gain and strain reduction increase with the stiffness of the reinforcement, while the global response remains strongly dependent on how effectively the patch can be engaged along the bonded length (Siwowski and Siwowska 2018).

Within CFRP systems, an additional guideline is to distinguish between “standard” and high-modulus reinforcements. For large steel members, conventional CFRP may remain relatively compliant compared to steel, which limits the achievable stiffness increase unless large composite thicknesses are used. This was one of the drivers behind the development and use of high-modulus CFRP (HM-CFRP) strips for steel bridges and steel structural elements, with the explicit aim of increasing reinforcement efficiency without unpractical laminate build-ups. In this context, (D. Schnerch et al. 2007) proposed design-oriented considerations for externally bonded HM-CFRP on steel structures and emphasized that the reinforcement stiffness level must be selected together with the intended anchorage strategy to avoid premature loss of effectiveness through end-driven damage mechanisms. Even when the focus is strictly on material selection, this point remains essential: selecting a very stiff patch is not automatically “better”, because higher axial rigidity tends to concentrate load transfer near the patch ends and increases the sensitivity of the system to termination detailing and load introduction; therefore, the most relevant patch is the stiffest one that can be reliably mobilized under the expected loading regime for the chosen geometry.

Durability constraints also provide direct material-selection criteria for the patch itself. A distinctive issue for CFRP-to-steel applications is the electrical conductivity of carbon fibers, which can promote galvanic coupling with steel in the presence of an electrolyte. Recent investigation by (M. Yang et al. 2025) confirm that galvanic corrosion is thermodynamically favored in CFRP–steel assemblies exposed to atmospheric moisture films, with localized corrosion prone to develop near electrical contact points, and with the corrosion severity depending on environmental conditions and system resistance. Consequently, when the service environment is humid or saline, the patch material choice must either incorporate a reliable electrical isolation concept or, when appropriate, favor non-conductive alternatives. In this respect, glass- and basalt-fiber composites offer an intrinsic advantage: they are electrically insulating, which reduces concerns regarding galvanic interaction with steel.

Overall, the material selection guideline for the FRP patch can be stated as follows: the reinforcement should be chosen to provide the required axial rigidity (modulus × thickness) for the targeted stiffness or strain reduction, while remaining consistent with the expected load-transfer conditions and the exposure-driven constraints specific to steel/FRP assemblies, notably the galvanic sensitivity of carbon-based reinforcements in wet or saline service.

B.3.3.ii Adhesive

There are wide ranges of adhesives which can be used to bond FRPs to metallic substrates and these include epoxies, polyurethanes (PU), silane modified polymers (SMP), acrylics, cyanoacrylate, but the one that is commonly used and trusted in industrial applications is epoxy. There is a large number of epoxies on the market, but the selected one must be compatible with the curing conditions. Those with the most desirable properties normally require curing at elevated temperatures, but systems are available that cure at ambient temperature; and these are best suited to civil engineering applications (Hollaway and Cadei 2002).

Adhesive selection should not be reduced to maximizing static strength or stiffness. Analytical and numerical studies of plated steel beams consistently show that the governing failure risk is often associated with pronounced shear and peel stress concentrations at the overlap ends, driven by the abrupt discontinuity in axial stiffness between the reinforced and non-reinforced regions; these localized peaks are the main initiators of debonding (Deng et al. 2004). In this context, a relatively compliant and/or tougher adhesive can be advantageous because it redistributes interfacial stresses and delays crack initiation and growth at the critical ends, even if it slightly reduces initial load-transfer efficiency in the central bond region (Heshmati et al. 2015; Deng et al. 2004). Therefore, the appropriate adhesive is best understood as the one that achieves the required service-load load transfer while providing sufficient damage tolerance against end-driven debonding.

Literature supports the idea that an optimal solution can involve spatial tailoring of adhesive properties rather than a single uniform material. Mixed-adhesive (bi-adhesive) joints, using a stiffer adhesive in the central region to maintain load transfer, and a more compliant/tough adhesive near the ends to blunt stress concentrations, have been shown numerically to significantly reduce peak interfacial stresses, especially when combined with plate-end tapering (Bouchikhi et al. 2013). More recent work continues to exploit the same principle in steel/CFRP repair joints by placing an extremely tough adhesive in the critical region, targeting end-dominated damage while maintaining overall joint performance (Mohabeddine et al. 2023).

Although mixed-adhesive implementations are less standardized in field applications than single-adhesive systems, they provide a literature-backed route to reconcile stiffness-driven strengthening objectives with robustness against debonding initiation when geometric constraints limit overlap length or taper severity.

B.4. Assessment for repair

At the industrial scale, externally bonded FRP patches are still not a routine strengthening solution for steel structures, not because the concept lacks technical interest, but because its deployment remains constrained by qualification and long-term reliability considerations. The decision-making process on whether to use the adhesively bonded FRP patch method or another method is summarized in **Figure 0-5** and is detailed in the text above.

As part of a regular inspection on a steel structure, damage can be detected. A damage assessment process is subsequently launched. First, it is determined whether the damaged element is critical or not:

- Critical elements are structural members or areas within the structure that may have higher probability of failure during the life of the structure compared to the surrounding areas, even though they may have been designed in the interest of reducing such probability. Examples of critical elements include: vessel plating, structural bulkheads, piping, tank bulkhead, etc…
- Non-critical elements can be structural or non-structural elements excluded by critical elements and typically not subject to significant loads. The structural integrity of the original structure will not be compromised by their deterioration. The failure of non-critical elements will not generate the risk of progressive collapse of the overall structure. Structural strength evaluation for non-critical elements is not required. Examples of non-critical elements include: Brackets, stiffeners, etc…

If the element is non-critical, it may be repaired using adhesively bonded FRP patch. In most cases, inspections and surveys focus on critical elements. In the case of a damaged critical elements, the criticality of the damage is assessed. As previously stated in **Section B.2**, typical damage modes are fatigue cracks and/or corrosion. Damage assessment is performed based on a checklist or some acceptance criteria depending on the followed recommended practice or technical guideline. Examples of checklist, corrosion section loss limits criterion and fatigue crack length criterion are given respectively in *Appendix C* of (DNV 2015), *Subsection 1-2/7.2* and *1-2/8* of (ABS 2022). For instance, if a loss in thickness of a steel plate or pipe is observed,

but is still above the minimum thickness specified by the acceptance criterion of the followed technical document, the damage is non critical. Cracks on the other hand may often be considered critical as there are no acceptance criteria, or at least it is hard to define one. Consequently, if the damage is assessed to be non-critical, then it can be repaired using an adhesively bonded FRP patch. Else traditional repairs, i.e. welding or bolting of a steel plate, are to be applied, following existing standards, rules and certifications.

It should be concluded that adhesively bonded FRP patch method is not yet very mature, and state-of-the-art data is lacking in order to move forward with its certification. Significant research efforts are made in order to broaden the application cases of adhesively bonded FRP systems on steel structures, such as the recent COST Action CA18120 on “Reliable roadmap for certification of bonded primary structures”.

Finally, it is also important to keep in mind and ensure that the repair does not accelerate damage growth, or create new problems by e.g. attracting new loads or preventing inspection. Moreover, even in cases where the bonded FRP patch method is accepted, one has to take into account the surrounding “system” the element is part of. A corroded pipe – as a critical element enduring non-critical damage – may look quite simple to repair. However, it may supply a crucial function to another component with quite severe consequences to the overall structure if it fails.

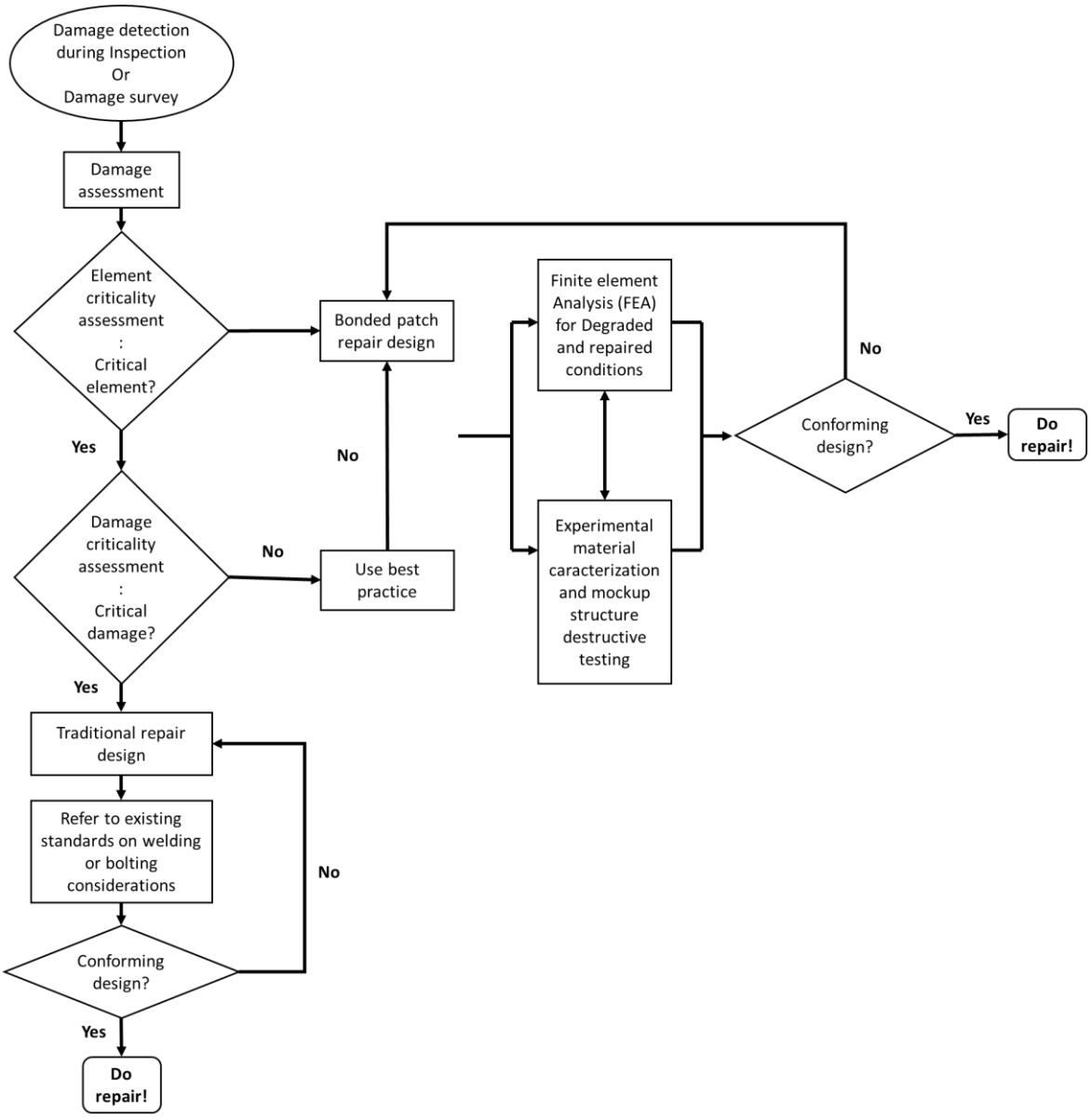

Figure 0-5. Outline of damage assessment and decision-making process for choice of repair method. Inspired and enhanced from (DNV 2015; ABS 2022))

B.5. Installation process

Field installation is a decisive contributor to the performance of adhesively bonded FRP repairs, because the quality of surface preparation (Sourisseau et al. 2022), cleanliness, fiber alignment, and cure conditions directly governs the achievable interfacial adhesion and the likelihood of premature debonding.

In its guidance for steel bridge repairs, the (AASHTO/NSBA 2024) Steel Bridge Collaboration proposes a practical installation sequence for bonded fiber patches, explicitly emphasizing surface roughening and solvent cleaning, careful handling of fabrics, and a controlled lay-up procedure to avoid entrapped air and misalignment. The steps required for installing the repairs are detailed as follows:

1) The surface on which the patches will be installed should be roughened using a grinder, sandblaster or grit-blaster.
2) The roughened surfaces should be thoroughly cleaned with a solvent (acetone, isopropanol, …) to remove particles from grinding or blasting.
3) The required fiber patches should be cut to size and wiped with a cloth dampened with solvent to remove any dust, then left to dry in order for the solvent to evaporate.
4) Glass fiber mats, used as an insulating first layer between the steel adherend and CFRP, should be cut approximately 2.5cm larger in both dimensions than the carbon fibers to provide an adequate insulating layer should there be any slight misalignment during application.
5) Adhesive should be spread on the roughened steel surface in a uniform layer using a spatula.
6) A layer of fibers should then be placed on top of the adhesive and gently pressed into the adhesive and smoothed to remove any air bubbles and align fibers.
7) It is recommended that carbon fibers and basalt fibers be saturated with the resin (the glass fiber fabric layers are not necessarily to be saturated) before they are placed.
8) The fiber patches should be placed such that the unidirectional fibers are aligned perpendicular to the crack plane.
9) After all the layers are applied, spew fillets (i.e. rounded surface of a fillet adhesive) around the patches should be formed by hand from additional adhesive to create a smooth transition between the patch and the steel.
10) The adhesive and FRP patch should be allowed to harden before steel is handled or exposed to live loads per the manufacturer's specified cure time.

B.6. FRP-steel bond behavior

Most of the time, the weakest link – which is prone to fail – in the plate bonding of FRPs to a metallic adherend is the bond line. Therefore, this section will be devoted to the behavior of the bond.

B.6.1. Bond test methods

In this section, two main categories of bond test methods are distinguished, those designed for:

- **Fracture analysis**, based on the evaluation of evolution of adhesive properties due to crack growth, in respect to the adherends it is bonded to.
- **Strength analysis**, which aim to evaluate the overall strength of an assembly or in service structure, by evaluating ultimate failure stresses and strains.

B.6.1.i Fracture analysis

fracture-mechanical approach assumes the presence of cracks (defects) in the material, which in combination with external mechanical loading lead to fracture initiation, growth of a main crack and finally to critical failure of the tested material or structure (Budzik et al. 2022). The objective of this subsection is not to do a thorough introduction to fracture mechanics, but to compile the robust existing test methods referenced in literature and standards for determination of adhesive material properties (cf. **Table 0-2**). More information and references on fracture mechanics can be found in (Budzik et al. 2022) overview on testing mechanical performance of adhesively bonded composite joints in engineering applications.

B.6.1.ii Strength analysis

Strength analysis is usually specific to the type of structures we work on, this type of analysis is usually performed on prototypes of structures. Since the work of this thesis is oriented towards plate steel structures and beams, we shall do a state-of-the-art of the test methods proposed in literature for steel structures with flanges (cf. **Table 0-3**). Moreover, some generally accepted, standardized, and easy to perform tests will also be presented. A more extensive list of FRP-steel test methods is presented in *Zhao's et al.* review (Zhao and Zhang 2007).

Table 0-2. Adhesive fracture mechanics test methods (adopted and enhanced from (Budzik et al. 2022; DNV 2015))

2D Schematic representation	Designation/ Mode of loading	Applicable standard(s)	Other references	Comments
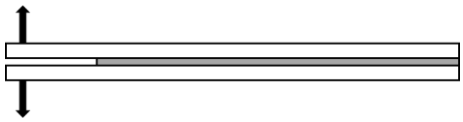	DCB Mode I	ASTM D5528 ISO 25217	(B. Blackman and Kinloch 2001) (Brunner et al. 2001)	-
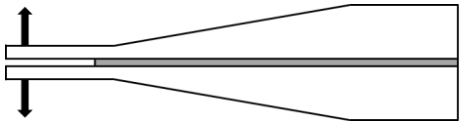	TDCB Mode I	ISO 25217 BS 7991	-	-
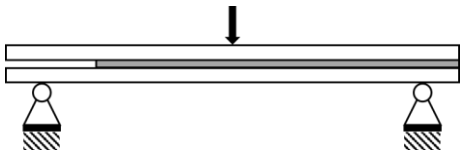	ENF Mode II	ASTM D7905	(Davies et al. 2001) (B. R. K. Blackman et al. 2005)	Unstable fracture commonly encountered
	ELS Mode II			
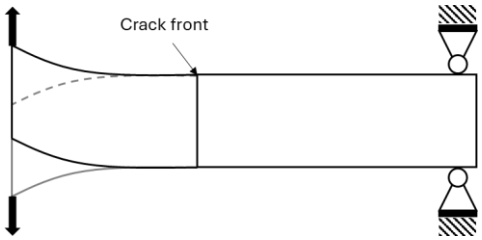	SCB Mode III	-	(Donaldson 1988)	-
	ADCB Fixed ratio Mixed mode I and II	-	(B. R. K. Blackman et al. 2001)	Different substrate thickness, or different material
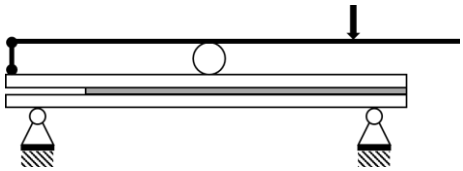	MMB Variable ratio Mixed mode I and II	ASTM D6671	-	-

DCB Double cantilever beam
TDCB Tapered DCB
ENF End notched flexure
ELS End loaded split beam
SCB Split cantilever beam
ADCB Asymmetric DCB
MMB Mixed mode bending

Table 0-3. Review of strength analysis test methods of FRP-Steel flanged structures bonded joints

2D Schematic representation	Designation/Test name	Applicable standards	References	Comment
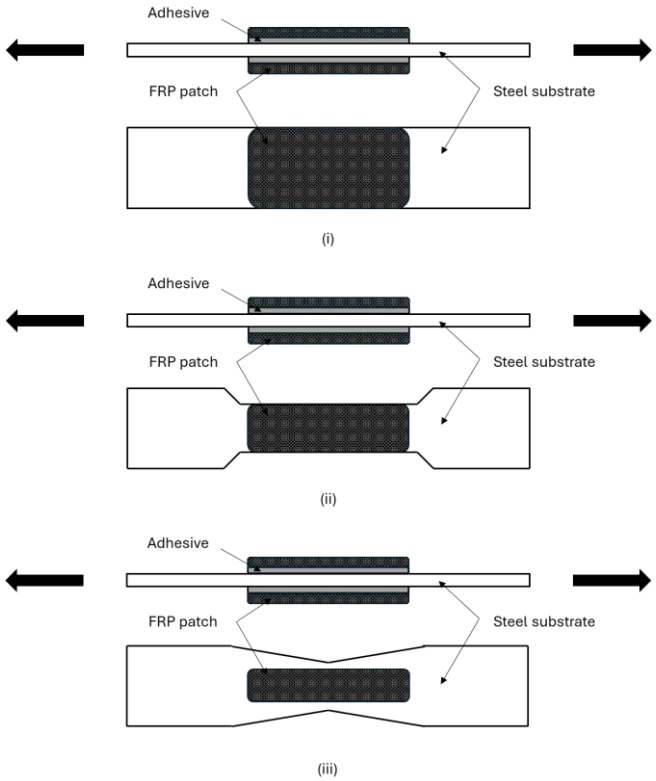	Tensile tests of reinforced plate	-	(Zhao and Zhang 2007)	In this type of testing method, the force is transferred from the steel element to the FRP plates or sheets. A continuous plate with uniform width can be used as shown in (i). However, yielding of steel may occur outside the FRP strengthened area if the specimen has a uniform width. Modified shapes (ii) and (iii) were adopted to avoid steel yielding. This test method is more suitable for studying strengthening rather than the bonding between steel and CFRP, because it is not trivial to monitor crack propagation.

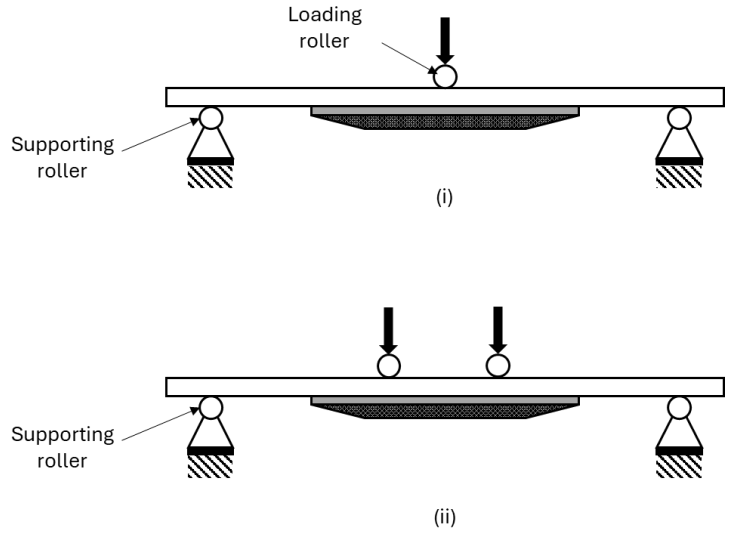	Flexural test of reinforced plate (3 or 4 pbt)	-	(Chataigner et al. 2017; Lye et al. 2021)	-
	Single strap joint	-	(Delzendeh Moghadam et al. 2024)	In the single strap joint configuration, two steel plates are attached by CFRP only on one side.
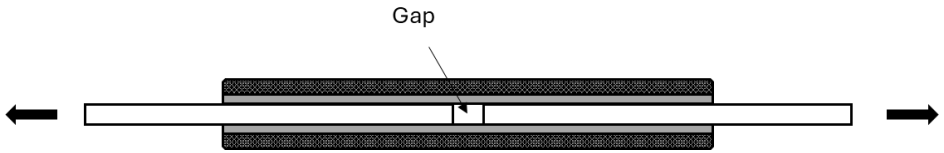	Double strap joint	STP12583S	(Miller et al. 2001; Zhao and Zhang 2007; Chataigner et al. 2017; Delzendeh Moghadam et al. 2024)	Double strap joints are configurations where FRPs are attached to both sides of steel plates. The loading is applied to the steel plates.

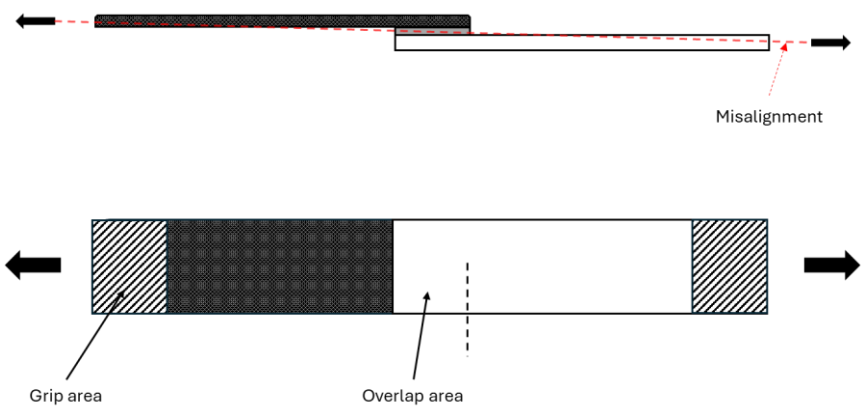	Single lap joint (SLJ)	ASTM D5868 ISO 4587 NF EN 1465	(Budzik et al. 2022)	-
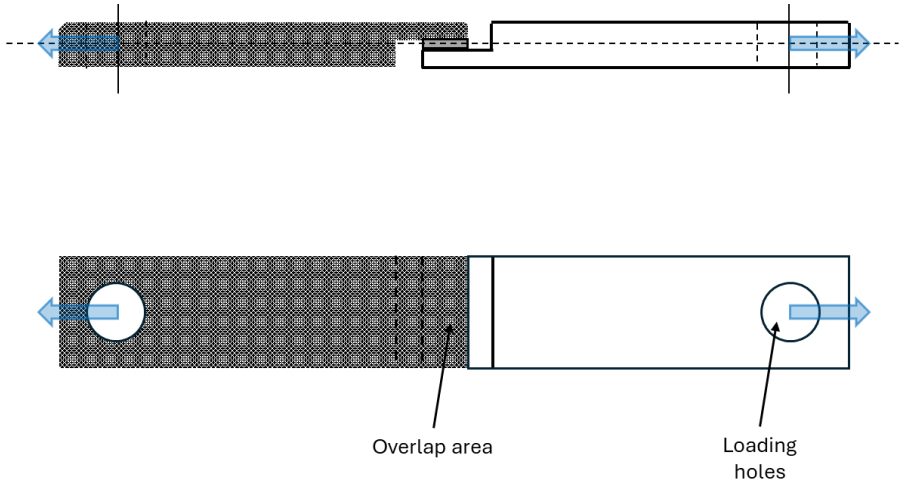	Thick adherend shear test (TAST)	ASTM D5656 ISO 11003-2	(Budzik et al. 2022)	-

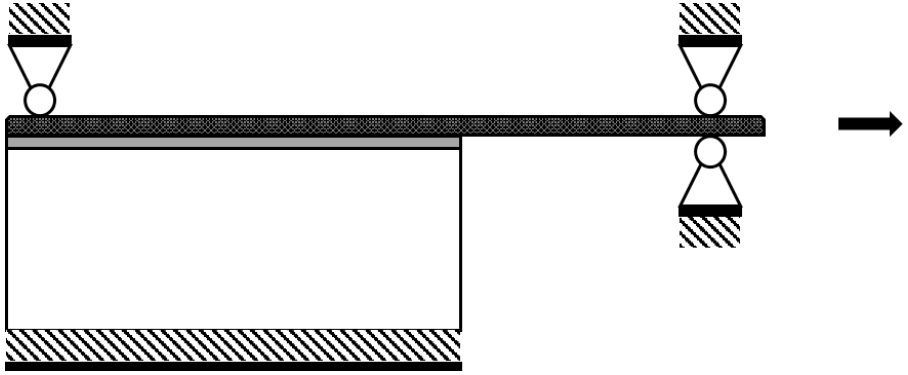	Single lap shear joint	-	(Zhao and Zhang 2007)	-
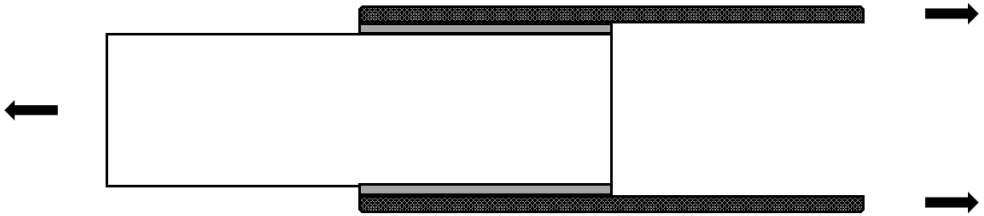	Double lap shear joint	ASTM D3528	(Zhao and Zhang 2007; Chataigner et al. 2017)	-

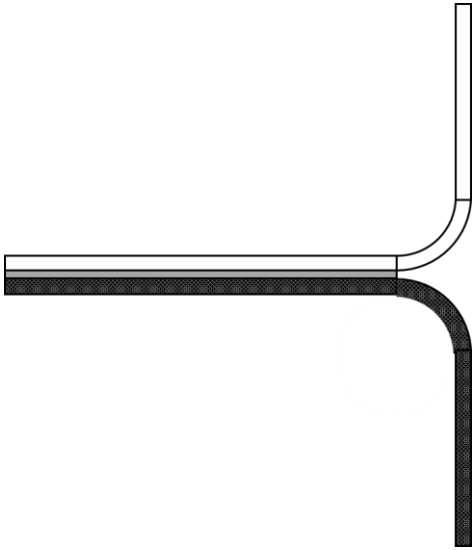	T-peel	ASTM D1876 ISO 11339	(Budzik et al. 2022)	-
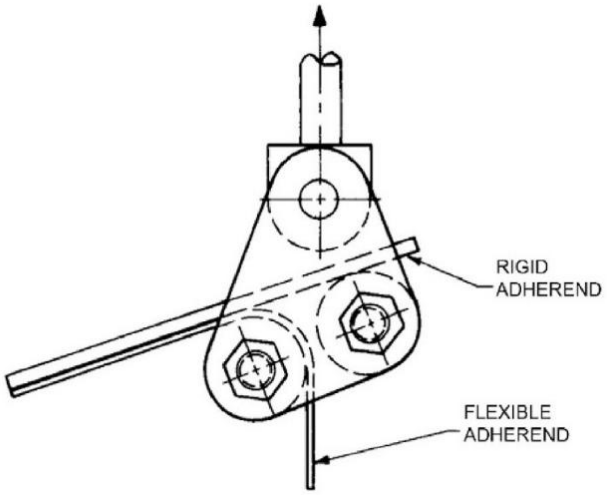	Floating roller peel test (FRPT)	ASTM D3167 ISO 4578	(Teixeira de Freitas et al. 2017)	-

B.6.2. Failure modes in externally bonded FRP-Steel systems

Possible failure modes in a FRP patch bonded steel system subjected to a flexural load include (Zhao and Zhang 2007):

a) Adhesive failure (steel/adhesive interface)
b) Cohesive failure (adhesive bulk layer failure)
c) Adhesive failure (FRP/adhesive interface)
d) FRP delamination (separation of some carbon fibers from the resin matrix)
e) FRP failure
f) Steel yielding.

A schematic view of failure modes is given in **Figure 0-6**.The failure modes presented above are just families of outcomes which can happen at failure. Different very precise reasons can be behind a type of outcome. For instance, debonding, be it cohesive or adhesive, may happen because of blistering, creep, or adhesive property changes due to environmental conditions. An extensive list of failure causes is presented in (ABS 2022).

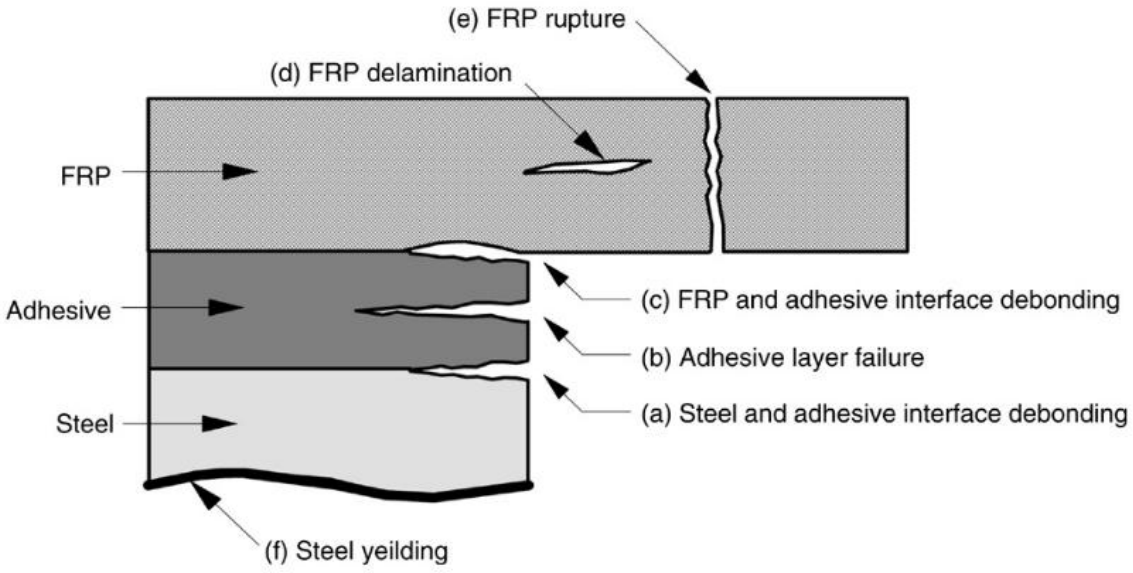

Figure 0-6. Schematic representation of typical failure modes in FRP-steel bonded joints. Adapted from (Zhao and Zhang 2007).

B.7. Flexural strengthening performance of FRP-Steel bonded joints

When strengthening a steel structure under flexion by adhesively bonding an FRP laminate, the quasi-static load-deflection behavior of the structure is enhanced as shown in **Figure 0-7**. The parameters which can be enhanced include, rigidity (slope $m = \frac{dP}{ds}$), yield strength ($\frac{P_{y,S}}{P_{y,US}}$) and ultimate strength ($\frac{P_{u,S}}{P_{u,US}}$). Once failure in the strengthened structure happens (be it debonding or failure of the FRP patch), the structure will at least go back to the steel reference strengthened behavior. (D. Schnerch et al. 2007) also propose similar understanding for steel strengthening of steel bridges with FRP materials.

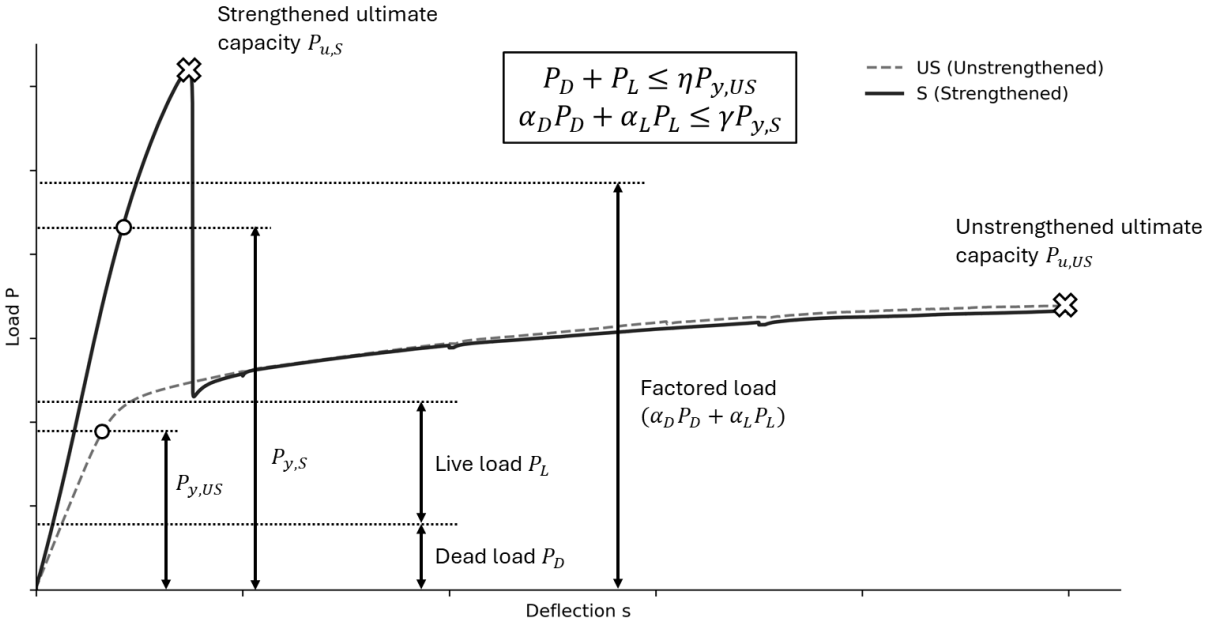

Figure 0-7. Representation of strengthening performance and conditions of calculation of live load. Inspired from (D. Schnerch et al. 2007).

In this section we will provide a literature review of the quasi-static flexural mechanical performance of steel structures strengthened with adhesively bonded FRP materials. It should be noted that this section is exclusively devoted to steel structures subjected to "Quasi-Static Flexural" loads, as they are the main topic of this PhD work.

(Delzendeh Moghadam et al. 2024) presented a review of studies on the flexural behavior of CFRP-strengthened steel beams in their recent literature review. **Table 0-4** presents a thoroughly updated, corrected and enhanced version of what they proposed.

Table 0-4. Review of experimental studies on adhesively bonded FRP strengthened steel structures under flexion loads.

Ref.	Loading condition	Test Setup	Steel cross section	L_{span} (mm)	E_s (GPa)	f_y (MPa)	f_u (MPa)	FRP type	t_p (mm)	E_p (GPa)	f_p (MPa)	Adhesive type	t_a (mm)	E_a (GPa)	f_a (MPa)	τ_a (MPa)	Ultimate load gain (%)
(A. Peiris and Harik 2021; N. A. Peiris 2011)	Quasi-Static	F	** W10 x 22 C7 x 98	2743	200	407 414	510 531	UHM CFRP	1.2	514	1924	Spabond-345	1	3	34.6	-	39
(Zeng et al. 2018)	Quasi-Static	F	H-section	1800	185	210	332	NM CFRP	1.2	167	2398	Sikadur-30	1	11.3	22.3	-	9.8
(Siwowski and Siwowska 2018)	Quasi-Static	F	HEB 280 I-beams	4800	197	390	540	NM CFRP HM CFRP	1.4	160 207	3280 2790	Neopoxe 30	2	>9.9	>30	-	8.5 6.7
(Tabrizi et al. 2015)	Quasi-Static	F	W8 x 13	3350	-	-	-	NM CFRP strand HM CFRP strand	4 layers 4 layers	135 226	2288 2218	Epoxy	-	-	-	-	71 67
(Karam 2015)	Quasi-Static	F	** UC203 x 303 x 46	2000	200	318.75	459	LM CFRP	4 layers	65	737	Sikadur-330	-	4.5	30	-	15.4
(Linghoff et al. 2010)	Quasi-Static	F	HEA180	2000	212	330	-	HM CFRP UHM CFRP	1.4 1.8	200 330	3300 1500	Epoxy	2	7	25	-	28.6 17.6
(David Schnerch and Rizkalla 2008)	Quasi-Static	F	** W310 x 45	6550	-	369-408		HM CFRP UHM CFRP	4 3.2 2.9	229 457	1224 1534	Spabond-345	-	-	-	-	-
(Deng and Lee 2007)	Quasi-Static	T and F	127 x 76UB13	1200	205	-	-	HM CFRP	3	212	-	Sikadur 30	1	8	29.7	-	30.1
(Colombi and Poggi 2006)	Quasi-Static	T	HEA140	2500	-	331	469	HM CFRP	1.4	197	>2800	Sikadur 30 Sikadur-330	1.1 0.8	4.5 3.8	24.8 30	24.8 -	14.4 34.3
(X. Liu 2003)	Quasi-Static	* T	W12 x 14	2743.2	-	-	-	HM CFRP	1.4	>200	>2300	-	-	-	-	-	-
(Al-Saidy 2001)	Quasi-Static	* F	** W8 x 15	3048	200	364.4	496.4	NM CFRP HM CFRP	1.4	152 200	2482 >2482	Epoxy	3.2	-	68.9	-	23.4 33.4

(*) Test set-up: T = Three-point bending; F = Four-point bending
(**) Steel/concrete composite beam

B.8. Environmental durability of FRP-Steel bonded joints

The efficiency of FRP-strengthening technique is highly dependent on the durability of the adhesive bonding between FRP and steel surface. In this section, we will present the state-of-the-art review on bond degradation in FRP-steel joints under different environmental conditions in accordance with literature reviews from (Samali et al. 2023; Heshmati et al. 2015; Gholami et al. 2013). The main environmental threats which will be discussed in this subsection, are related to the effect of elevated temperature and moisture absorption. Other factors – such as low temperature, freeze/thaw cycles, extreme temperatures caused by fire events, chemical attack and Ultra Violet radiation (UV) – are also of great relevance, but have either relatively lower influence than temperature and humidity, or statistically very lower chances of occurrence. Consequently, they will not be discussed in this manuscript, and are out of the scope of the thesis work.

B.8.1. Elevated temperatures

The effect of temperature on the strength of adhesively bonded joints and consequently on design guidelines is quite straightforward. Due to glass transition temperature (T_g) of structural adhesives that ranges between 60°C and 130°C (L. F. M. da Silva et al. 2018), bonding between steel and FRPs is in risk of major strength loss under high temperature exposures. Consequently design guidelines such as (ABS 2022) recommend that design and operating temperature for polymer materials, be lower that $T_g - 20°C$. It must be reminded that all studies presented in this subsection focus on high ambient temperatures and not extreme temperatures caused by major fire events.

Indeed, (Ke et al. 2020) tested the performance of CFRP-Steel joints bonded with four different two-component ambient cured epoxy adhesives including Araldite 2014, Araldite 420, Sikadur 30, and J133 under temperatures between 25°C and up to 70°C. They first characterized the mechanical properties of the adhesives through Dynamic Mechanical Analysis (DMA) and tensile testing, then tested CFRP-Steel double-lap shear joints according to (ASTM D3528 2002). Their finding revealed that all the adhesives experienced modulus and strength loss with the increase of temperature, and **Figure 0-8** shows typical stress-strain behavior for different values of temperature relative to T_g to represent that phenomenon. For the CFRP-Steel double-lap shear joints, they showed that the bond strength is reduced to less than 50% at 70°C compared to the measured performance at room temperature.

Exposure to temperature can also have a positive impact on the adhesive and FRP-Steel bonded joint. It should first be reminded that polymeric material physical properties are significantly dependent on curing temperature and time. For most adhesives, to obtain high T_g values, curing should be performed at relatively high temperature. Moreover, complete curing is a quite long process which keeps evolving through time, and the T_g value keeps slowly increasing in parallel. In some industrial situations, curing is performed under imposed room temperature conditions, which constrains structure designers to use conservative T_g values. A post-curing effect, and thus an improvement of T_g and bond properties compared to the designed values after curing, can happen for first exposures to temperature. Indeed, (Al-Shawaf et al. 2009) conducted a series FRP-steel Double Lap Shear (DLS) tests, formerly subjected to temperatures ranging between 20°C up to 60°C for 45 to 60 min. They studied the response of three different adhesives: Araldite 420 A/B, Mbrace Saturant and Sikadur-30. When the temperature was below their T_g, the increase in temperature caused reduction in capacity of specimens with Araldite adhesive, whereas the strength of specimens with the two other adhesives slightly enhanced. The enhancement in strength of these adhesives was claimed to be attributed to post-curing effect. Nonetheless, at temperatures above the adhesives T_g, the bond capacity substantially dropped in all specimens.

An additional subject to study is the influence of cyclic temperature near T_g, on the bond strength of FRP-Steel joints. This corresponds to real life operating temperatures for structures. (Wang and Xian 2021) have imposed 150, 300 and 500 temperature cycles between -20°C and 40°C to CFRP samples, two epoxy adhesive samples and CFRP-Steel SLJ joints. They have shown that the temperature cycles had little influence on the CFRP tensile properties (in fact they were slightly improved at 500 cycles), and overall a slight reduction of tensile properties of the adhesives and strength of the bonded joint.

Another important aspect of exposing FRP-Steel bonded joints to variable temperature conditions is the development of internal stresses due to differences in coefficients of thermal expansion (CTE) of the bonded materials. As shown in **Table 0-5**, steel typically has a positive CTE (~11×10^{-6}/°C), whereas unidirectional CRFP composites often have much lower, near-zero or even negative thermal expansion in the fiber direction. Adhesives generally exhibit higher CTEs. This mismatch in thermal expansion induces internal stresses when the assembly is subjected to temperature variations, with the adhesive bondline typically experiencing the most critical thermal stresses, which can interact with mechanical stresses and lead to premature

failure of the joint. Some authors have pointed out this issue (Borrie et al. 2021; Wang and Xian 2021), but scarse studies have dove into assessing it.

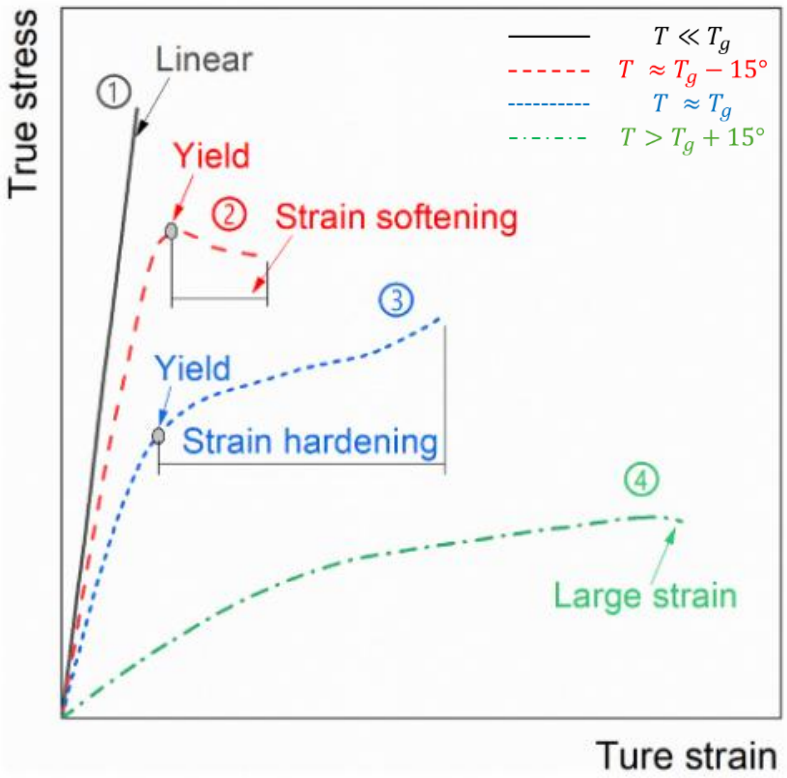

Figure 0-8. Typical tensile stress-strain behavior of rigid epoxy adhesives as a function of temperature. Adapted and enhanced from (Ke et al. 2020))

Table 0-5. Typical values of thermal expansion coefficients for different relevant substrates

Material	**Orientation**	**Direction**	**Thermal expansion coefficient α ($10^{-6} \times °C^{-1}$)**	**References**
Steel A36	-	Isotropic	11 – 13	(ASTM A36 2019; Kumar et al. 2024)
Carbon-epoxy (CFRP)	Unidirectional (UD) laminate	Longitudinal	-0.7 – 0.2	(Mulle et al. 2007; Mesquita et al. 2022)

		Transverse & through thickness	20 – 40	(Chang and Teng 2004; Ran et al. 2014)
	Bidirectional (woven) laminate	In-plane	4 – 12	(Dong et al. 2017; Graciani et al. 2020)
		Through-thickness	25 – 45	
Glass-epoxy (GFRP)	Unidirectional (UD) laminate	Longitudinal	5 – 10	(Al-Azzawi et al. 2024; Shakir Abbood et al. 2021; Goodenough et al. 2023)
		Transverse & through thickness	25 – 40	
	Bidirectional (woven) laminate	In-plane	10 – 15	(Takeda et al. 2015, 2004)
		Through-thickness	25 – 45	
Flax-epoxy (FFRP)	Unidirectional (UD) laminate	Longitudinal	-5 – 5	(Saidane et al. 2021)
		Transverse & through thickness	40 – 80	
	Bidirectional (woven) laminate	In-plane	10 – 25	(Yan et al. 2014; Hansen et al. 2024)
		Through-thickness	50 – 90	
Adhesives	Epoxies	Isotropic	30 – 70	(Shiu and Tsai 2014; Selvan et al. 2026)
	Acrylates		50 – 120	(Sarfaraz et al. 2015; Esposito et al. 2013; Sideridou et al. 2004)
	Polyurethanes		80 – 200	(Čolić et al. 2024; Zain et al. 2016)

B.8.2. Moisture absorption

Moisture ingress into an adhesively bonded steel/FRP joint is generally governed by diffusion through the polymeric constituents (adhesive layer, FRP matrix and interphases), with local preferential transport paths influenced by defects such as voids, imperfect wetting zones and free edges. In structural epoxies commonly used for FRP-to-steel bonding, absorbed water exists in different "states" (often discussed as free and bound water), leading to distinct and sometimes partially reversible effects. Free water tends to plasticize the polymer network, increasing chain mobility and thereby reducing the glass transition temperature, stiffness and strength of the adhesive; these changes can be partly recovered after drying. Bound water, in contrast, is associated with specific interactions with polar groups and may contribute to longer-term, less reversible changes, especially when coupled with elevated temperature and repeated wet/dry cycles (Datla et al. 2011; Mubashar et al. 2009).

At the bulk-adhesive scale, the most consistently reported mechanical consequence of moisture uptake is a marked decrease in elastic modulus and, depending on the formulation, a reduction of yield stress and fracture resistance; these trends have been quantified for adhesives used in civil-engineering FRP/steel assemblies and have been shown to correlate with the absorbed moisture content. In the comprehensive experimental–numerical studies by (Heshmati et al. 2015, 2017) on double-lap FRP/steel joints and corresponding bulk adhesive coupons, immersion and high-humidity ageing led to significant softening of the adhesive (modulus decrease with moisture content), while joint-level stiffness could remain comparatively less sensitive due to the dominant contribution of adherends, until damage initiates.

Beyond bulk softening, moisture promotes damage phenomena that localize critically at interfaces between adhesive and adherends. First, moisture-assisted interfacial degradation is frequently reported as a governing durability driver for polymer–metal bonds. For steel adherends, water can interact with the native oxide/hydroxide layer and weaken interfacial adhesion through hydration and chemical alteration of the interphase (Grangeat 2019), with the practical outcome being a progressive shift in failure mode from cohesive (within the adhesive) toward interfacial (adhesive/steel) as exposure increases in aggressive conditions (Ruoranen 2018). In parallel, if moisture reaches the steel surface in the presence of oxygen and electrolytes, corrosion reactions may occur; the formation of corrosion products and changes in local chemistry/roughness can disrupt the intimate contact required for adhesion and create wedging stresses that accelerate debonding. From the FRP side, moisture affects the composite matrix and the fiber/matrix interphase; water-induced matrix plasticization and interphase

weakening can reduce the effectiveness of stress transfer near the bonded region and can facilitate near-surface damage that couples with bondline cracking (Heshmati et al. 2015). Overall, durability is therefore controlled by the coupled evolution of bulk adhesive properties (stiffness/strength/fracture), interfacial adhesion at steel/adhesive and FRP/adhesive boundaries, and the spatial distribution of moisture (often strongly non-uniform across thickness and along overlap length), which determines where damage initiates and how it propagates (Katsivalis et al. 2020; Katsivalis and Feih 2022).

Moisture uptake also induces hygroscopic swelling of the adhesive. At first order, this phenomenon can be represented by a moisture-expansion strain proportional to local moisture content, generating hygroscopic strains analogous to thermal expansion (i.e., a "hygro-expansion coefficient" playing a role similar to the CTE). When the adhesive layer is constrained by stiff adherends (steel and an FRP laminate with strongly anisotropic in-plane stiffness), swelling cannot develop freely, so it is converted into internal stresses. Two effects are particularly detrimental. The first is the development of through-thickness stress gradients because moisture concentration is higher near exposed surfaces/edges than in the core of the bondline during transient diffusion; these gradients generate peeling (normal) stresses and additional shear stresses even in the absence of external mechanical loading. The second is the mismatch in hygroscopic response between the adhesive and adjacent materials (steel has essentially no hygroscopic strain, whereas the FRP may swell mainly in matrix-dominated directions), which increases constraint and promotes stress concentrations at the overlap ends where classical adhesive-joint mechanics already predicts maxima (Bonilla Mora et al. 2018). These hygroscopic stresses superimpose with service loads and with moisture-driven property degradation, thereby accelerating crack initiation and mixed-mode debonding growth. In practical terms, this coupled mechanism can be interpreted as a progressive reduction and distortion of the effective traction–separation (or bond–slip) response of the joint with exposure time: the adhesive becomes more compliant and weaker, while swelling-induced self-equilibrated stresses bias the bondline toward earlier interfacial damage, particularly near free edges and overlap ends where moisture ingress is fastest and constraint is highest (Heshmati et al. 2017; Bordes et al. 2009).

B.9. Compilation of existing technical guidelines for the design and construction of externally bonded FRP systems for strengthening metallic structures

The transition from laboratory demonstrations to field implementation of externally bonded FRP strengthening systems requires that design and construction decisions be framed within recognized technical guidance. **Table 0-6** therefore compiles the existing technical guidelines applicable to externally bonded FRP systems for metallic structures and positions them historically, then briefly presents their scope and intent with respect to the steel-strengthening context addressed in the present thesis.

Table 0-6. Existing technical guidelines for the design and construction of externally bonded FRP systems for strengthening metallic structures

Design Guideline	Comments
2001 – FRP composites: Life extension and strengthening of metallic structures (ICE) *Moy S.S.J* **United Kingdom**	**Earliest found document on the strengthening of metallic structures with adhesively bonded FRP composites**
2004 – CIRIA C595: Strengthening metallic structures using externally bonded FRPs *Cadei J.M.C, Stratford T.J, Hollaway L.C and Duckett W.G* **United Kingdom**	**Scope extension of ICE guide**
2004 – Advanced polymer composites for structural applications in construction: ACIC 2004; proceedings of the 2. international conference, held at the University of Surrey, Guildford, UK *Hollaway L.C, Chryssanthopoulos M.K and Moy S.S.J* **United Kingdom**	**Relevant conference session on strengthening of steel substrates with adhesively bonded CFRP**
2005 – CNR-DT 202: Guidelines for Design and Construction of Externally Bonded FRP Systems for Strengthening Existing Structures *National Research Council* **Italy**	**This document was regarded as the first step towards the definition of specific design guidelines and followed the UK guidelines and USA academic works (CIRIA 2004, ICE 2001, Schnerch et al. 2006)**
2007 – Construction and Building Materials: Proposed guidelines for FRP strengthening of steel bridges *Schnerch D, Dawood M, Rizkalla S, Sumner E* **USA/Canada**	**Introduction of design guidelines for use of high modulus CFRP for strengthening of steel bridges and structures**

2012 (revised 2015) – DNV-RP-C301: Design, Fabrication, Operation and Qualification of Bonded Repair of Steel Structures *Det Norske Veritas* **Norway (International scope)**	**First comprehensive recommended practice, with international scope, to serve as an accepted industry practice and reference document in contractual matters**
2015 – EASA-CM-S-005: Bonded Repair Size Limits in accordance with CS-23, CS-25, CS-27, CS-29 and AMC 20-29 *European Aviation Safety Agency* **Europe**	**European Certification Memorandum (CM) providing guidance on the determination of bonded repair size limits for composite and metallic critical aerospace structures**
2015 (revised 2018) – ASME PCC-2: Repair of Pressure Equipment and Piping *American Society of Mechanical Engineers* **USA**	**American Standard including a part on repairs of pressure equipment and piping with non-metallic means, such as composite bonding and wraps**
2019 – Formulation of Guidelines for Repair and Strengthening of Structures using Externally Bonded FRP *Japan Society of Civil Engineers* **Japan**	**Published research studies on the strengthening of structures by externally bonded FRP, including steel substrates. Only in Japanese, no English version**
2022 – ABS: Requirements for Bonded and Composite Repairs of Steel Structures and Piping *American Bureau of Shipping* **USA**	**Most comprehensive and recent found technical document.**
2024 – G14.2: Guidelines for Field Repairs and Retrofits of Steel Bridges *American Association of State Highway and Transportation Officials* **USA**	**Includes a very small section on strengthening of bridges with externally bonded materials, and the relevant advantages of this solution**

B.10. Successful case studies

B.10.1. Tickford bridge (2000)

Tickford bridge, shown in **Figure 0-9** is the oldest operational cast iron highway bridge in the world. It was designed by Thomas Wilson and built over the River Ouzel in summer of 1810, and is a Scheduled Ancient Monument. FaberMaunsell, Beckenham, Kent, UK was appointed to suggest the most appropriate strengthening strategy and recommended that the 3 tonne gross weight restriction could be removed, and that the full highway loading could be achieved by strengthening the structure with CFRP. The selected system was a wet lay-up carbon fiber sheet strengthening system. This offered an advantage over other carbon fiber systems, which cannot be readily applied to curved surfaces. In particular, in critical areas, the curing temperature of the composite was elevated to between 50 and 60°C. In addition, a continuous filament polyester drape veil was installed to provide insulation between the carbon fiber and the cast iron to avoid any possibility of galvanic corrosion. In total, 120m² carbon fiber preimpregnated sheet was applied in up to 14 layers and repainted. The maximum thickness of 10 mm demonstrates that this system of strengthening can be achieved with negligible visible affect to the bridge appearance. The work was completed within 10 weeks.

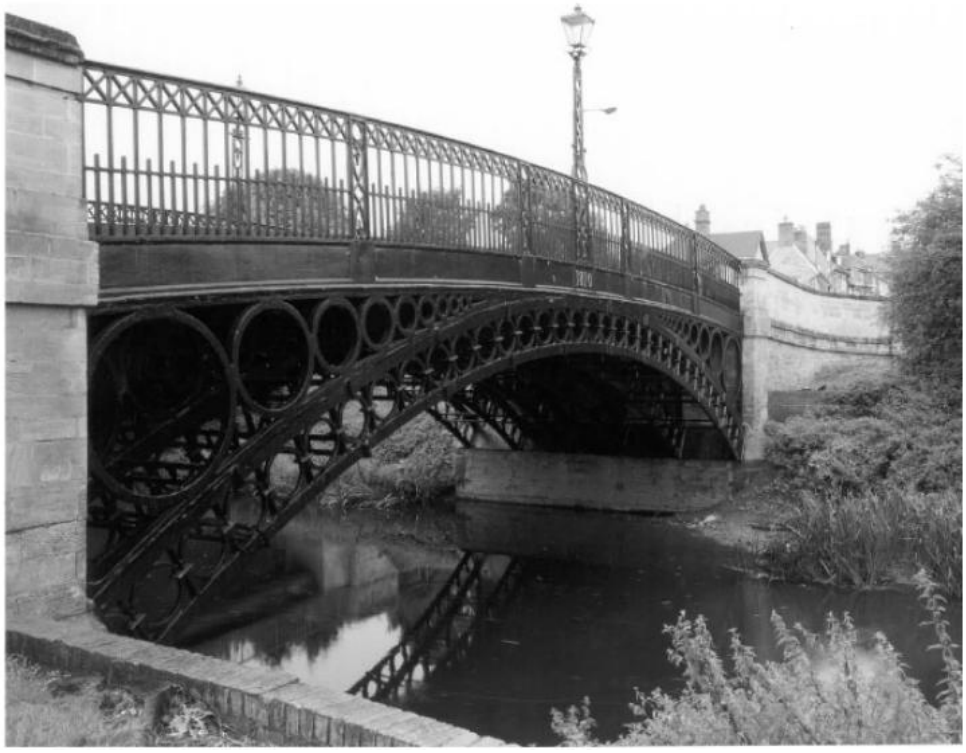

Figure 0-9. Tickford Bridge, Newport Pagnell, Buckinghamshire, UK (Courtesy of FaberMaunsell Structural Plastics, Beckenham, Kent, UK). Adapted from (Hollaway and Cadei 2002)

B.10.2. Hythe bridge (2001)

The first known application of the prestressed FPP technique for flexural upgrading of cast iron bridges was on the Hythe bridge, Oxford, built in 1874 over the River Thames (cf. **Figure 0-10**). It is a two spans bridge with a clear span equal to 7.8 m. It was realized by 8 reversed T cast iron girders and transversal masonry arches that sustain the traffic loading (cf. **Figure 0-11**). The main girders were prestressed by pultruded laminas (two per each edge of the girders) and CFRP sheets (cf. **Figure 0-12**). The compressive stress level was selected in order to remove the tensile stresses in the cast iron girders for a given traffic volume (vehicle weights up to 400kN). The prestressed technique used: anchored as well as movable terminals, jacks and a fixed framework. The fixed terminals were used to guarantee the adhesion of the FRP to the existing structure, taking into account the stress concentration at the edges of the plate. Stresses were transferred to the FRP by the bolts connected to the movable terminals bonded to the FRP. The use of the jacks as well as the moveable terminals gave a correct strengthening alignment of the cast iron struts. These FRP interventions were carried out prior to the adhesive curing.



Figure 0-10. Strengthened Hythe bridge, Oxfordshire, UK (Courtesy of Mouchel Consulting, West Byfleet, UK). Adapted from (Hollaway and Cadei 2002)

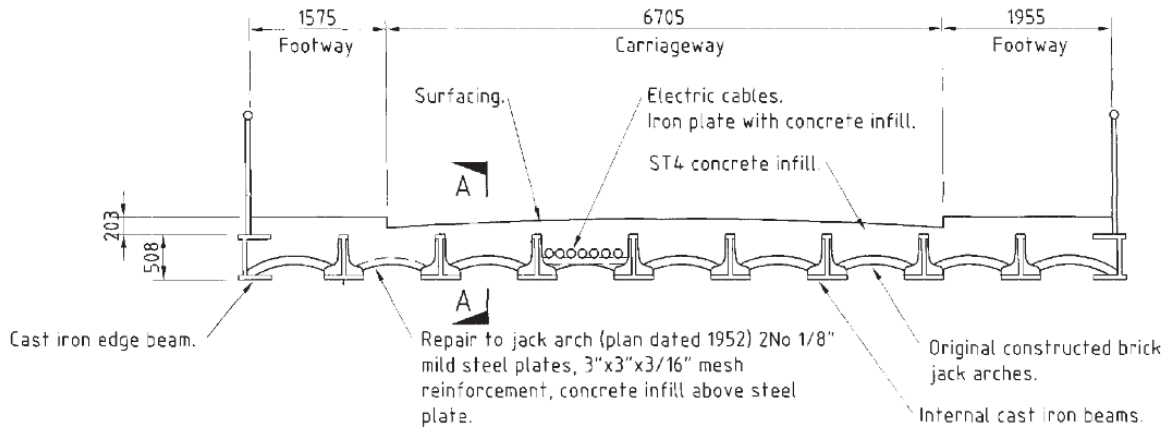

Figure 0-11. Cross section of Hythe bridge. Adapted from (Hollaway and Cadei 2002)

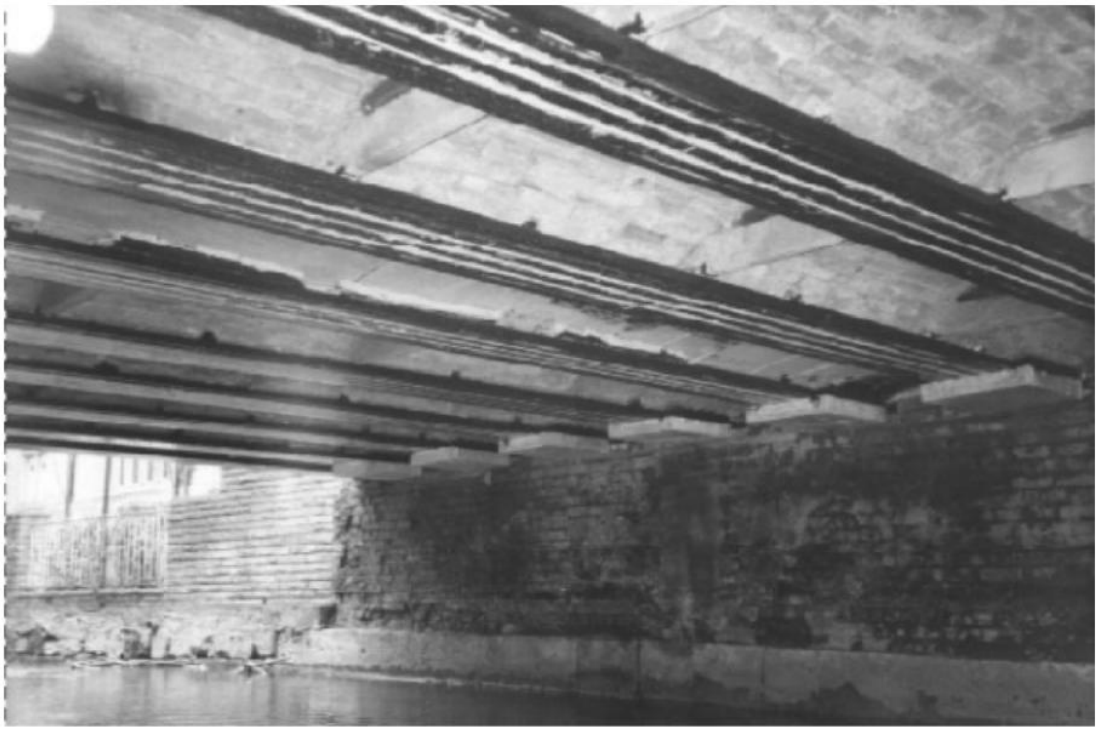

Figure 0-12. Hythe bridge: prestressed composite plated cast iron beam view. Adapted from (Hollaway and Cadei 2002)

B.10.3. Slattocks Canal Bridge (2001)

Slattocks Canal Bridge, a historic steel bridge, was constructed, in 1935, over the Rochdale canal. It is a single span bridge with a span equal to 7.6 m supported by twelve double "T" laminated girders and a reinforced concrete deck. The bridge had been restricted to 17 tonne load since 1996 and this necessitated diversion routes which caused inconvenience to businesses and residences in the immediate vicinity. In 2000 the bridge was upgraded to 40 tonne load by plate bonding an 8 mm thick, 100 mm wide, unstressed CFRP plates to each of

the innermost rolled steel joist (RSJ) beams. The strengthening solution involved an elastoplastic design, whereby the plastic capacity of the steel RSJs was mobilized, but the CFRP plates were working well within their elastic range. The bond stresses in the adhesive were limited to values which ensured that no peak stress effects were encountered. The upgrading maintained the navigable clearance required for the canal and has had minimal impact on the overall appearance of the structure and its surrounds. The bridge upgrading, received a Historic Bridge Awards commendation in the year 2000. **Figure 0-13** Illustrates the in-field installation of the CFRP plates. The consulting engineer for the design of the plate bonding system was Mouchel and the contractor was Balvac. The contract value was £70,000 and the program lasted 8 weeks.



Figure 0-13. Installation of CFRP plate at Slattocks Canal Bridge (Courtesy of Mouchel Consulting, West Byfleet, UK). Adapted from (Hollaway and Cadei 2002)

B.10.4. Plate bonding a curved surface

A principal curved steel beam on the Boots building in Nottingham was strengthened with a low-temperature moulding (LTM) advanced polymer composite material, manufactured by ACG, Derbyshire, UK; Taywood Engineering was the specialist subcontractor for this work. The beam is curved in plan to connect two straight members around the corner of the building. The purpose of the strengthening scheme was to restore the flexural and torsional capacity of

the beam to above its original uncorroded level so that an anticipated increase in floor loading could be accommodated. The thickness of the composite strengthening layer, which comprised unidirectional, 0-90° and ±45° fiber orientation, was 2 mm. The unidirectional fibers were aligned along the direction of the beam's length for flexural strengthening. The 0-90° fiber directions were used to resist shear and torsional loading, created by the curvature of the beam. The preimpregnated composite layers were based upon glass and carbon fibers, with a low-temperature-curing epoxy resin developed by ACG. After surface preparation of the steel adherend, an ambient-cured epoxy adhesive was painted onto the clean, dry steel surfaces to act as a bonding aid. The installation procedure for the composite involved utilization of cold-cure preimpregnated material under vacuum and a cure temperature of 65°C. **Figure 0-14** illustrates the final placement of the carbon fiber preimpregnated layers around the flanges and web of the steel beam.



Figure 0-14. Upgrading of a principal curved beam, Nottingham, UK (Courtesy of Taylor Woodrow, Southall, UK and ACG, Derbyshire, UK). Adapted from (Hollaway and Cadei 2002)

B.10.5. King Street Railway Bridge (2000)

King Street cast iron Railway bridge was constructed in 1870 in Mold, Flintshire on behalf of the Railway Board and in 2000 was strengthened to allow 40 tonne vehicles to use it. Concrete Repairs, Ltd. was the contractor for the upgrading.

The construction of the bridge consists of brick arches spanning between six cast iron girders, supported on brick abutments. The bridge carries the B544 road over the railway, which originally had two tracks. In the 1960s one track was removed and a propping system was installed beneath one half-span. In the 1980s the Borough Coucil acquired the disused railway line to provide access between two car parks and took over responsibility for the bridge. In 1999 an assessment of the bridge capacity indicated that it was suitable only to carry vehicles up to 17 tonne gross weight; this was well short of the 40 tonne target, and consequently, a weight restriction was applied to the bridge whilst a strengthening scheme was designed.

The bridge has a clear span of 8.93 m and consists of six cast iron girders skewed at an angle of approximately 28°. Masonry jack arches, which span 1.99 m, are supported on the bottom flanges of the cast iron girder and have ties, which resist lateral thrust.

There were a number of proposed designs for upgrading the bridge and the one finally selected was to install temporary preloaded struts to support the deck, then removing the existing props and applying strengthening materials before removing the temporary struts. Since some of the permanent load is thereby transferred into the FRP strengthening, the system can be regarded as partially prestressed solution.

Strengthening of cast iron bridges is notoriously difficult. Air voids and other defects found in the material are typical of finished cast iron products used in the 19th century. Consequently, the material can fail in an unpredictable brittle manner at relatively low tensile stresses, in comparison with modern metals. In addition, crack propagation from defects is exacerbated by cyclic loading from vehicle passage. Ultra-high-modulus, unidirectional, carbon fiber and glass fiber laminate reinforcements were used as the strengthening material; this had a mean elastic modulus of elasticity of 360 GPa and a tensile strength of 1.1 GPa. The carbon fibers were selected for their high stiffness, and the glass fibers were used to give the laminates transverse strength and to prevent galvanic action from taking place.

On each of the four internal girders two 170x33 mm laminates were required to be positioned 153 mm apart; this allowed sufficient gap for the heads of the hydraulic jacks to be positioned, thus allowing a preload to be applied to the temporary struts. The plates were tapered at the

ends to a length of 2.5 m to minimize the longitudinal shear stresses and end peel stresses. The edge girders had a different cross-section from that of the internal girders. The thickness of the edge laminates was limited to 10 mm, and they also had a 153-mm space between them. The surface of the cast iron was prepared by grit-blasting to achieve a specific texture and to remove any corrosion and, if necessary, localized repairs were made with a filled epoxy resin.

the thickness of the adhesive layer, applied to both the cast iron substrate and laminate surface, varied between 2 and 10 mm. During the curing cycle clamps were used to apply a small force to the laminate and a weatherproof enclosure surrounded the plate to enable a temperature of at least 5°C to be maintained at all times. To ensure that the designed strains were not exceeded and to monitor the performance of the bridge over a number of years, strain gauges were bonded, at specific points, to the plates and to the cast iron girders (**Figure 0-15**).

The advantages, over other more conventional materials, of using carbon fiber to upgrade this structure are: the durability of the material has been shown to be superior; the loss of headroom under the bridge due to the application of the layer of composite is minimal; and the erection procedure was simpler.



Figure 0-15. Upgraded King Street Railway Bridge. Stain gauges bonded to the composite plates and to the cast iron girder (Courtesy of Tone Gee and Partners, Cobham, Surrey, UK). Adapted from (Hollaway and Cadei 2002)

B.10.6. Christina Creek Bridge (2000)

The Christina Creek Bridge (I-704) in Delaware (USA), carries southbound I-95 traffic over the Christina creek outside Newark, Delaware. It is characterized by a mixed steel – concrete slab-on-girder structure (very widely used superstructure in the US) that has been recently FRP strengthened. (Miller et al. 2001) have given a full description of this upgrading. The strengthening was proposed by the Department of Transport of the University of Delaware (DelDOT), with a purely scientific aim, to gain experience in the technique of CFRP plate bonding onto metallic structure, studying a completely intact structure; the failure of the system would not compromise the integrity of the structure.

The bridge has three simple spans with a total length of 35 m and a skew angle of 13°. The main span acts compositely with the deck slab and is 19 m long. The two approach spans were designed non-compositely and measure 7.5 m in length. **Figure 0-16** shows a cross section of the bridge. The northern approach span consists of four W 24x84 steel girders spaced at 2.4 m centers (G3-G6). Two W 36x150 facia girders at the same spacing were also used (G7 and G8). Two separate road-widening schemes incorporated three W 36x150 girders to each side of the bridge (G1-G2 and G9-G12). Girder G5, over which the northern approach spans, was the one chosen for rehabilitation. This girder was subjected to the highest stress cycles and greatest stress range.

Six CFRP plates, shown in **Figure 0-17**.**a**, consisting of one layer of composite, were installed over the full length of the beam, as shown in **Figure 0-17**.**b**. The strips were beveled to 45° at the reinforcement end in order to reduce stress concentration. Each plate section was 1.5 m in length and had 300-mm staggered joints; this allowed for easier transportation, adhesive application and installation. Both Ciba-Geigy AV8113/HV8113 and Plexus MA/ 555 were used as the structural adhesive, to a thickness of 1.5 mm. In order to prevent galvanic corrosion, a GFRP sheet was placed between the CFRP lamina and the substrate.

The two load tests which were performed on the bridge, one prior to and one after the rehabilitation, indicated that there was good bond and no slip between the two adherends; the addition of the high modulus CFRP plates resulted in an increase of stiffness of 11.6%, and after using equivalent sections to compute a new moment of inertia, calculations indicated a strain decrease in the tensile flange of the steel girder of 10%.

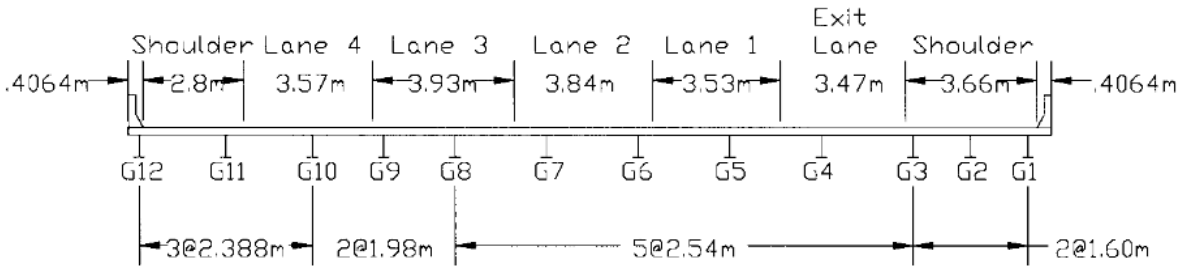

Figure 0-16. Christina Creek Bridge (I-704) cross section. Adapted from (Miller et al. 2001)

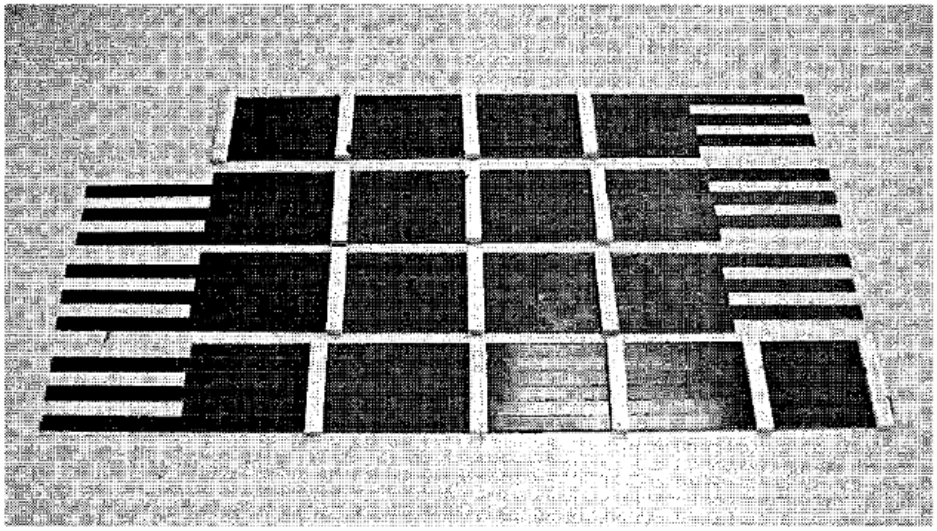

a)

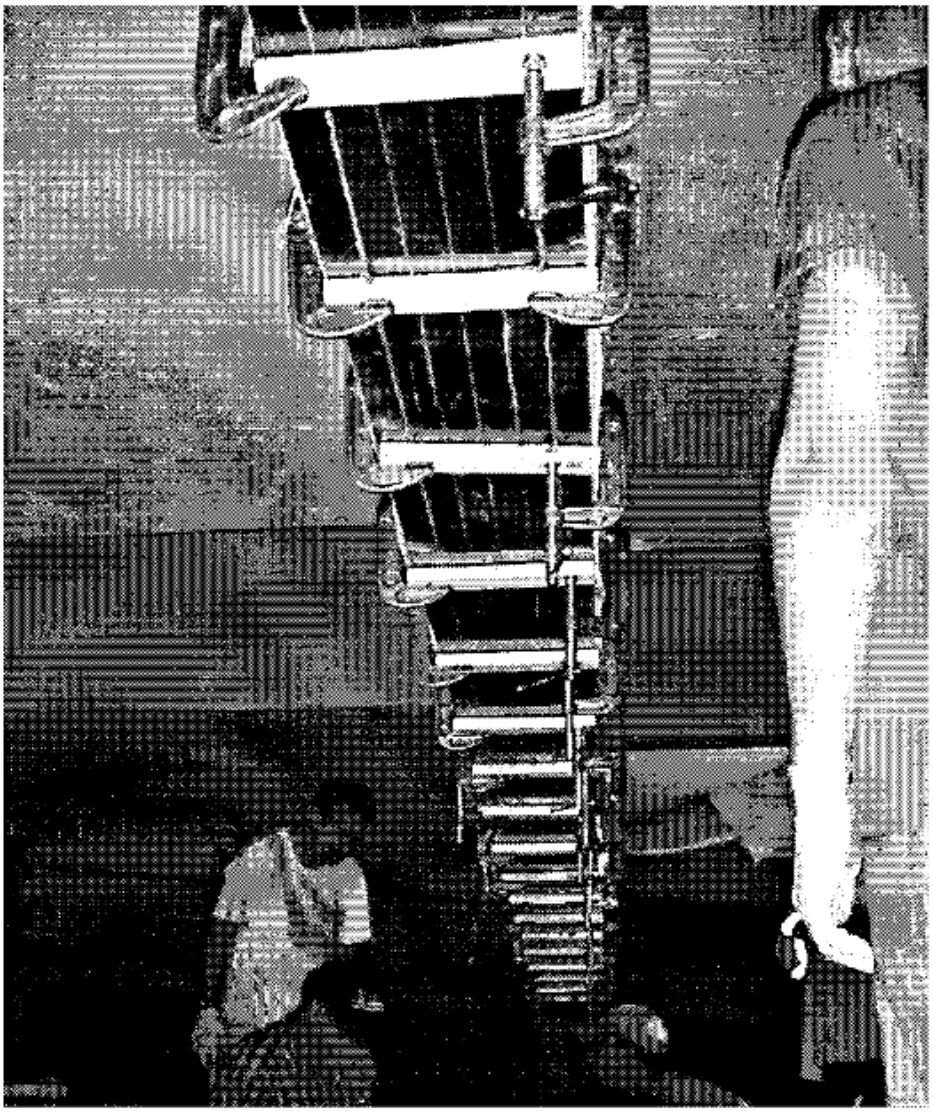

b)

Figure 0-17. a) Full width CFRP plate sections and b) CFRP plates clamped to girder G5. Adapted from (Miller et al. 2001)

B.10.7. Blast strengthening of a universal column

Figure 0-18 shows an ultra-high-modulus carbon fiber composite bonded to the compression flange of a universal column supporting a steel blast wall. This scheme was undertaken by DML, Devonport, Devon. This enabled the upgrading of the blast wall. The photograph shows the strengthened universal column highlighted by chevrons to warn welders not to strike an arc on them.

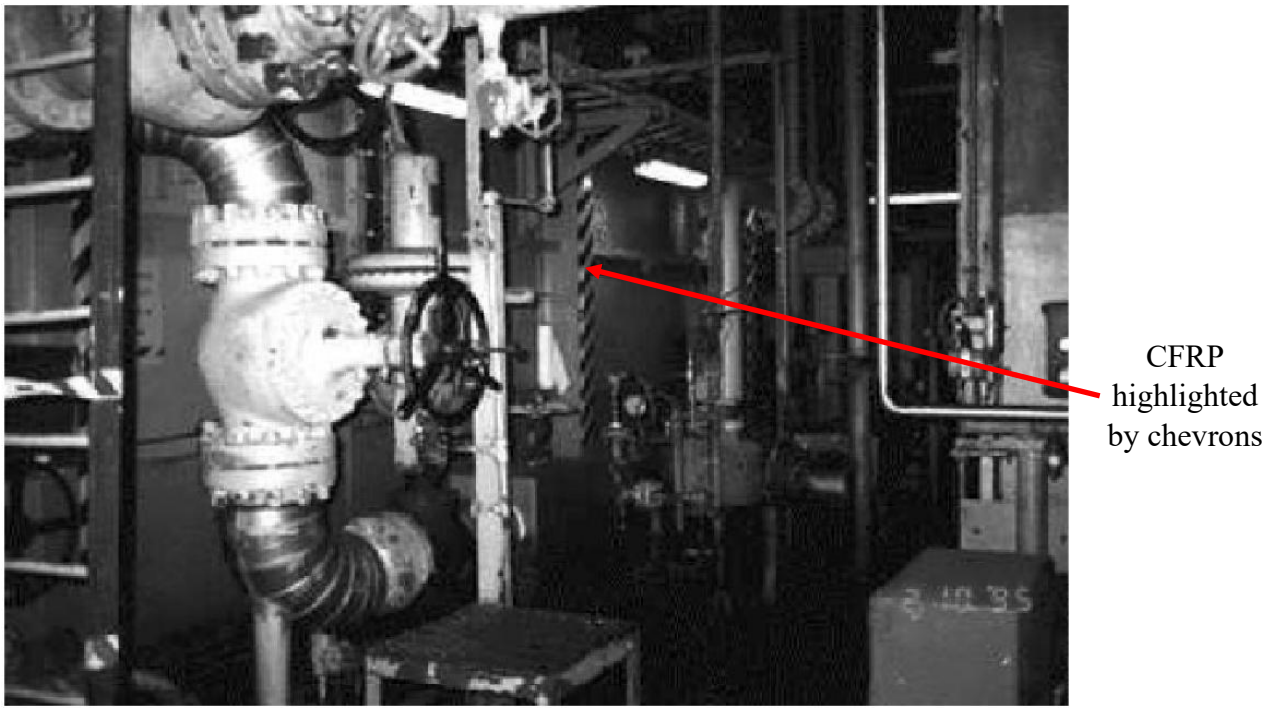

Figure 0-18. Ultra-high modulus carbon fiber composite bonded to the flange of a universal beam (Courtesy of DML, Devonport, Devon, UK). Adapted from (Hollaway and Cadei 2002)

B.11. Modeling and strength prediction of bonded assemblies

The main objective of this section is to present a literature review of the methods and possibilities of stress analysis and static strength prediction of adhesive joints, and to focus on cohesive zone modeling (CZM) as the main numerical method used throughout my PhD work.

B.11.1. Existing methods

(Ramalho et al. 2020) presented a recent literature review regarding this topic. They have reviewed the different methods used to predict the strength of adhesive joints under static loading presented in literature from the last decade. They have concluded that there are 7 main methods to predict strength analysis of adhesive joints under static loading comprising:

- Analytical methods
- Six numerical methods:
    - Continuum mechanics
    - Fracture mechanics
    - Damage mechanics
    - Cohesive zone modeling (CZM)
    - eXtended finite element method (XFEM)
    - Meshless methods

Each method will be briefly presented, we will describe their merits and limitations, except the CZM method where a more comprehensive description will be provided later.

- **Analytical methods**

Analytical methods are the oldest way to predict the strength of a joint. They usually rely on closed-form solutions for stresses or strains, and they must be coupled with a failure criterion to predict the strength. These methods are often associated to fast output results and are mostly easy to program in a software for data analysis using a spreadsheet system, such as Microsoft Excel® or dedicated calculation and matrix manipulation software such as Matlab® or scripting languages such as Python. Analytical methods are often used as a first trial in the design of adhesive joints. However, it should be noted that analytical formulations rely on simplifying assumptions that neglect particular issues of the joints' behavior, such as complex constitutive models of the adhesives or adherends, through thickness stress simplifications and others. As a result, each analytical formulation is generally only able to predict the strength of a specific type of joint due to the differences between each joint type. Therefore, numerical methods have

been the object of intense study in the strength prediction of adhesive joints due to their versatility, and will be presented in what follows.

- **Continuum mechanics**

Continuum mechanics provide the simplest approach by assessing joint failure by stress or strain parameters of the material. Models based on continuum mechanics are easy to apply and generally do not require large computational resources. Compared to analytical methods, unlimited geometries can be modelled, and complex material behaviors can be easily implemented. However, this technique still disregards energetic concepts, which can be vital to obtain accurate strength predictions for adhesive joints. Moreover, the stress/strain singularity near the adherend/adhesive interface can cause a mesh dependency on the predictions without convergence being attained. In brief, continuum mechanics is notoriously a more refined technique than analytical methods, but its use in design should be exercised with caution.

- **Fracture mechanics**

Fracture mechanics approaches enable the use of energetic concepts and criteria to simulate crack growth, which brings accurate modelling for all materials, ranging from brittle to ductile. Traditional fracture mechanics concepts used to determine crack propagation include the Stress Intensity Factor (SIF) and the Strain Energy Release Rate (SERR), which are related. In mixed-mode loading and plane strain conditions, for the simple case of a linear elastic isotropic material with a crack, the relation is expressed by:

$$G = K_I^2 \frac{1-\nu^2}{E} + K_{II}^2 \frac{1-\nu^2}{E} \qquad \textbf{(0-1)}$$

Where K_I and K_{II} are the modes I and II SIF, respectively, and E and ν are the Young's modulus and Poisson's ratio of the material separating.

There are several techniques to determine the SIF of the SERR, including J-integral or Virtual Crack Closure Technique, but these will not be detailed in the following subsection.

An important drawback of the fracture mechanics approach is that it is traditionally limited to problems with an initial crack, such that the imposed criteria can propagate it. Thus, in pristine structures without initial defects, coalescence of cracks is not possible, unless specific algorithms are developed such as the Finite Fracture Mechanics (FFM) introduced by (Leguillon 2002). These limitations are on the origin of a residual use of this technique for strength prediction of adhesive joints.

- **Damage mechanics**

Damage mechanics generally uses a damage internal variable that gradually decreases material stiffness after a given stress/strain is achieved. This technique is able to account for different damage mechanisms, such as cohesive failure of the adhesive and adherend failure, including in composite laminates (in this specific case, the different failure modes occurring in composite materials can be modelled). These methods are also able to determine crack propagation through random paths and can provide accurate strength predictions in adhesive joints with arbitrary geometric and materials conditions. However, parameter calibration and the physical meaning of the damage variables used to depreciate the material properties can be complicated. Due to this limitation and to the uprising of techniques such as CZM, which promote crack growth with energetic principles (i.e., based on physically sound and measurable parameters), damage mechanics is not much widespread for strength prediction in adhesive joints.

- **Cohesive zone modeling (CZM)**

The works from this decade show that CZM is the joint strength prediction method that has been studied more extensively in academia, providing accurate strength predictions for a wide range of joints, due to being based on a mixed formulation, including continuum mechanics principles for damage initiation and fracture mechanics parameters for crack propagation. Currently, this technique is extremely powerful and accurate for adhesive joints with virtually any geometry and material characteristics.

Cohesive zone modeling is based on the definition of a constitutive traction-separation law, which is dependent on three bases:

1- Elastic traction response
2- Damage initiation
3- Damage evolution

A large number of traction-separation laws have been developed in literature to accommodate for the behaviors of different bulk adhesives (rigid to ductile, linear to non-linear, etc.) and interfaces as shown in **Figure 0-19**. For instance, in the case of a triangular traction-separation law, the elastic traction response is linear and is written as:

$$\boldsymbol{t} = \begin{Bmatrix} t_n \\ t_s \\ t_t \end{Bmatrix} = \begin{bmatrix} K_{nn} & K_{sn} & K_{tn} \\ K_{ns} & K_{ss} & K_{ts} \\ K_{nt} & K_{st} & K_{tt} \end{bmatrix} \begin{Bmatrix} \delta_n \\ \delta_s \\ \delta_t \end{Bmatrix} \quad \textbf{(0-2)}$$

Where the traction stress vector $\boldsymbol{t}$, consists of three components (two in two-dimensional problems) t_n, t_s and t_t, which represent the normal and two shear tractions respectively. The corresponding separations are denoted by δ_n, δ_s and δ_t. Finally, K_{ij} correspond to the elastic rigidity components which are dependent on the thickness of the cohesive element.

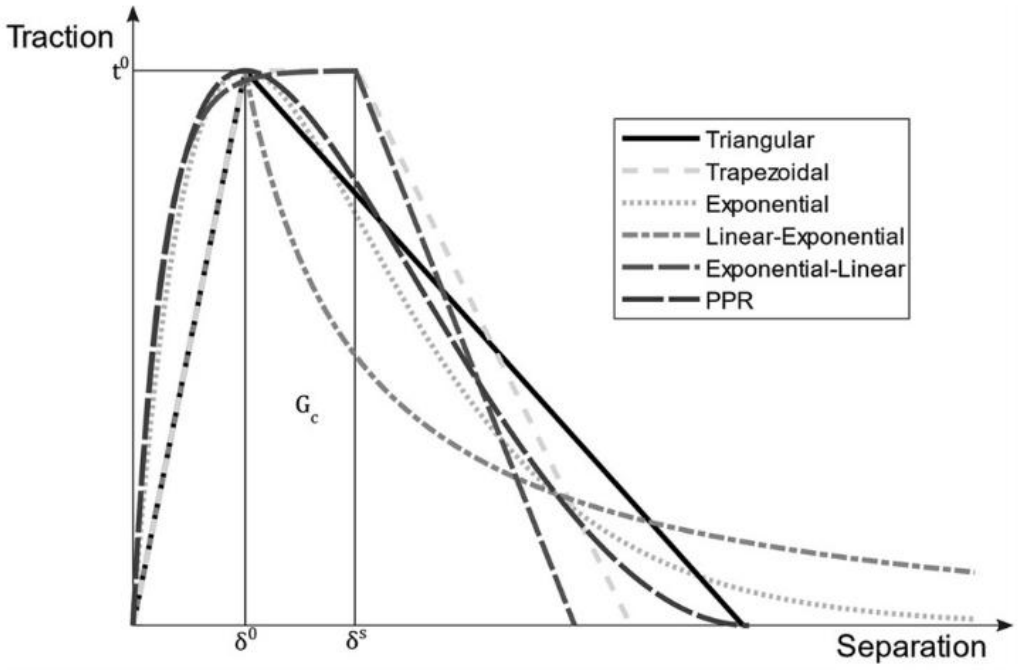

Figure 0-19. Comparison of different traction-separation laws. Adapted from (Ramalho et al. 2020)

Moving on to damage initiation, which refers to the beginning of degradation of a cohesive element, it begins when the stresses (or separations) satisfy a certain criterion. Several damage initiation criteria are available and have been presented in the literature, some of which are:

Maximum Nominal Stress Criterion

$$max\left\{\frac{\langle t_n\rangle}{t_n^0}, \frac{t_s}{t_s^0}, \frac{t_t}{t_t^0}\right\} = 1 \qquad \textbf{(0-3)}$$

Quadratic Nominal Stress Criterion

$$\left\{\frac{\langle t_n\rangle}{t_n^0}\right\}^2 + \left\{\frac{t_s}{t_s^0}\right\}^2 + \left\{\frac{t_t}{t_t^0}\right\}^2 = 1 \qquad \textbf{(0-4)}$$

Where the symbol $\langle\ \rangle$ represents the Macaulay bracket with the usual interpretation.

Finally, damage evolution describes the rate at which stiffness is degraded when the corresponding initiation criterion is active. Conceptually, CZM merges concepts describing the damage evolution in bulk materials (damage mechanics) and energy due to surface separation (fracture mechanics).

Indeed, a scalar damage variable D, represents the overall damage in the cohesive element and captures the combined effects of all the active mechanisms. It initially has a value of 0, and monotonically evolves (i.e. just increases) until reaching 1 (completely degraded element). The stress components of the traction-separation model are affected by the damage according to:

$$t_n = \begin{cases} (1-D)\bar{t_n}, & \text{if } \bar{t_n} \geq 0 \\ \bar{t_n}, & \text{otherwise (no damage to compressive stiffness)} \end{cases}$$
$$t_s = (1-D)\bar{t_s} \qquad \textbf{(0-5)}$$
$$t_t = (1-D)\bar{t_t}$$

Where $\bar{t_n}$, $\bar{t_s}$ and $\bar{t_t}$ are the stress components predicted by the elastic traction-separation behavior for the current strains without damage.

In CZM, to compute the evolution of damage variable D, FE solvers use the input value of fracture energy G_c, which we remind is an energy quantity which can be characterized experimentally. The fracture energy may be prescribed in the model as a single, mode-independent critical value; however, interfacial fracture studies consistently show that the critical energy required for crack advance is often mode-mix dependent. In other words, G_c varies with the relative contributions of opening (Mode I) and shear (Mode II/III) – cf. **Figure 0-20**, who in turn evolve with the crack path. This is why mixed-mode criteria are frequently adopted to represent $G_c(\psi)$, where ψ is the mode-mixity parameter.

Denoting by G_n, G_s and G_t the work done by the tractions and their conjugate relative displacements in the normal, first and second shear direction, respectively and defining $G_T = G_n + G_s + G_t$, the mode mix definitions based on energies are as follow:

$$m_1 = \frac{G_n}{G_T}, \qquad m_2 = \frac{G_s}{G_T}, \quad \text{and} \quad m_3 = \frac{G_t}{G_T} \qquad \textbf{(0-6)}$$

The two most used mixed-mode definitions are:

- Power law form:

Where the dependence of the fracture energy on the mode mix can be defined based on a power law fracture criterion. The power law criterion states that failure under mixed-mode conditions is governed by a power law interaction of the energies required to cause failure in the individual (normal and two shear) modes. It is given by:

$$\left\{\frac{G_n}{G_n^C}\right\}^{\alpha} + \left\{\frac{G_s}{G_s^C}\right\}^{\alpha} + \left\{\frac{G_t}{G_t^C}\right\}^{\alpha} = 1 \qquad \textbf{(0-7)}$$

Where G_n^C, G_s^C and G_t^C refer to the critical fracture energies required to cause failure in the normal, the first and the second shear directions, respectively, and α is the power law parameter. The mixed-mode fracture energy $G_c = G_T$ is calculated when the above condition (**Eq. (0-7)**) is satisfied. In other words:

$$G_c = 1\Big/\left(\left\{\frac{m_1}{G_n^C}\right\}^{\alpha} + \left\{\frac{m_2}{G_s^C}\right\}^{\alpha} + \left\{\frac{m_3}{G_t^C}\right\}^{\alpha}\right)^{\frac{1}{\alpha}} \qquad \textbf{(0-8)}$$

- Benzeggagh-Kenane (BK) form:

The Benzeggagh-Kenane fracture criterion (Benzeggagh and Kenane 1996) is particularly useful when the critical fracture energies during deformation along the first and second shear directions are the same; that is, $G_s^C = G_t^C$. It is given by:

$$G_c = G_n^C + (G_s^C - G_n^C)\left\{\frac{G_S}{G_T}\right\}^{\eta} \qquad \textbf{(0-9)}$$

Where $G_S = G_s + G_t$, $G_T = G_n + G_S$, and η is the BK law parameter (dependent on material).

Finally, when the value of fracture energy is calculated, the corresponding evolution of damage variable D can be performed, and will be imposed to conform to the traction-separation law. For instance, linear and exponential damage evolution are imposed as such:

Linear Damage Evolution

$$D = \frac{2G_c\left(\bar{T}_{eff}^{max} - T_{eff}^0\right)}{\bar{T}_{eff}^{max}\left(2_{G_c} - \frac{\left(T_{eff}^0\right)^2}{K_{eff}}\right)} \qquad \textbf{(0-10)}$$

Where $\bar{T}_{eff}^{max}$ is the maximum (history) value of the undamaged effective traction, T_{eff}^0 is the effective traction at damage initiation and K_{eff} is the effective linear elastic rigidity component.

Exponential Damage Evolution

$$D = \int_{\delta_m^0}^{\delta_m^{max}} \frac{T_{eff}\,d\delta}{G_c - G_0} \qquad \textbf{(0-11)}$$

Where δ_m^0 refers to the effective displacement at the initiation of damage, δ_m^{max} to the maximum value of the effective displacement attained during the loading history, T_{eff} and δ are the effective traction and displacement, respectively, and G_0 is the elastic energy at damage initiation.

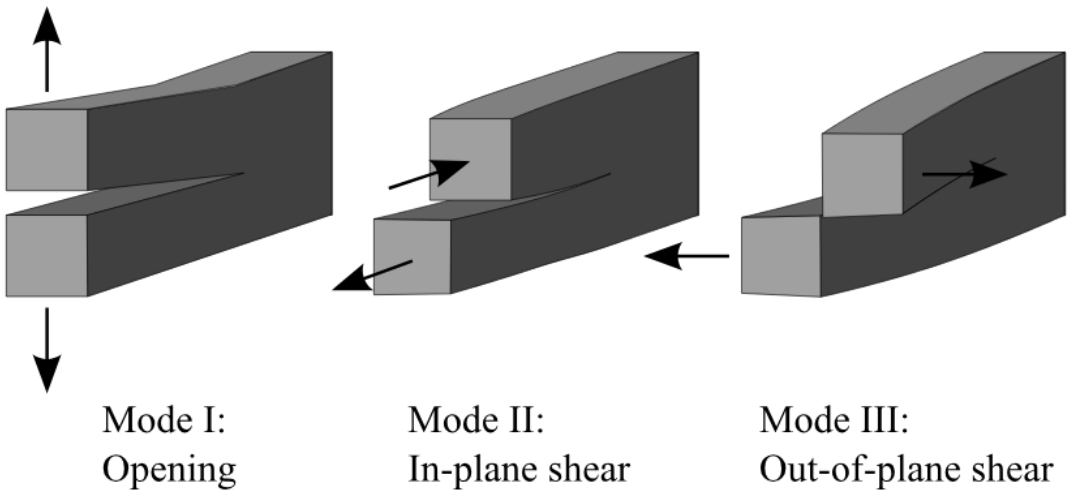

Figure 0-20. Representation of loading modes for bonded joints

One additional advantage of CZM method is its mesh insensitivity, provided that enough integration points undergo softening simultaneously. As a result, this technique is recommended for the best results in adhesive joints' design. Nonetheless, two limitations arise with CZM. The first one is that this method usually requires the measurement of geometrically dependent adhesive properties. The second one is that CZM modelling requires to place the cohesive elements in potential fracture planes to enable crack propagation, i.e., if a failure path is not equated, damage modelling along that path is not included in the models. However, in adhesive joints, typically the potential fracture paths are easy to define beforehand, thus this limitation loses relevance.

- **eXtended finite element method (XFEM)**

The XFEM was only recently used to study adhesive joints, but it shows some promise due to also relying on fracture concepts for crack growth. It excels fracture mechanics techniques by including continuum-based criteria for damage initiation and algorithms to partition solid elements and promote the nucleation and growth of cracks. This method is able to predict crack propagation through random paths, but in adhesive joints this sometimes results in the crack propagating from the adhesive to the adherends due to the criteria used for crack direction estimation, which is not consistent with the real behavior. This occurrence mostly takes place in joints with large deformations and rotations of the adhesive layer (such as SLJ), and prevents total failure to occur. A recent improvement on the XFEM is able to deflect the crack when the stiffness of the material where the crack is present is lower than that of the material to where

the crack is predicted to propagate. However, at this stage, the possibility of crack growth anywhere in the model is not a major advantage for adhesive joints. Thus, together with the pointed limitations, no clear advantage exists nowadays over CZM modelling.

- **Meshless methods**

Meshless methods are advanced numerical techniques which are an alternative to the FEM. The use of these method to study adhesive joints is limited, but they could be adopted more extensively in the future. Since these methods do not require a mesh, it could be advantageous to used them with fracture and damage mechanics criteria, because they do not need to remesh to simulate crack propagation. Currently, they were already used in conjunction with the popular CZM (C. L. Tsai et al. 2014), achieving accurate strength predictions. However, these methods are generally computationally slower than the FEM.

B.12. Natural fiber composites: focus on Flax FRPs

B.12.1. Context

The use of natural fibers as reinforcement for composite materials is justified by:

- adding value to a local resource in less industrialized countries;
- developing materials and technologies that reduce environmental impact;
- using renewable resources.

Throughout this PhD journey, it has been understood that there are multiple misconceptions regarding natural fibers. The use of natural fibers as reinforcement in materials is often associated with an eco-design approach, but this is not straightforward as implied by multiple studies and authors. Indeed, the environmental impacts need to be assessed using life cycle assessment (LCA) tools in order to quantify the benefits. Natural fibers can be associated with poor mechanical performance, but multiple natural fibers have a structural role in nature.

It is also necessary to challenge preconceived ideas on topics such as, for example, the ageing of plant fibers in humid environments, the use of bio-composites in severe service conditions, and the adhesion between plant fibers and polymers. Without denying the complexity of these fields of study, I quote (Baley 2020) who ironically emphasized that "it is possible to wash a garment made of plant fibers several times, to build boat hulls from wood, and to construct glued laminated timber structures".

B.12.2. Classification of natural fibers

Natural fibers can be subdivided into three main categories according to their origin (cf. **Figure 0-21**):

- Plant-based fibers (cellulosic)
- Animal-based fibers (proteins)
- Mineral fibers

In this manuscript only plant-based fibers will be of interest. Indeed, they are the one presenting the most interesting properties overall (Baley 2020), and **Table 0-7** presents the mechanical properties of commonly used plant-based fibers in comparison to synthetic fibers.

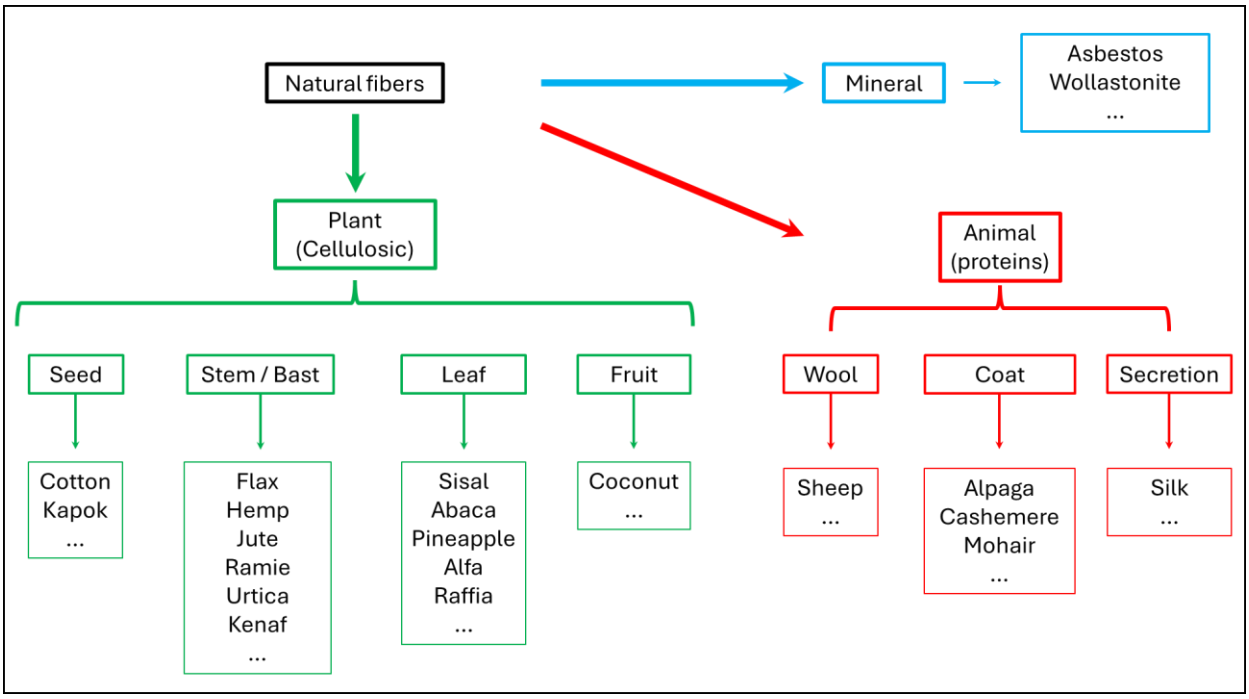

Figure 0-21. Classification of natural fibers (enhanced and adapted from (Baley 2020; Célino et al. 2014)).

Table 0-7. Tensile mechanical properties of plant-based fibers vs. synthetic fibers (Shelly et al. 2025; Baley 2020; Célino et al. 2014)

Fiber	Young's modulus, E (GPa)	Elongation at break, ε_f (%)	Tensile strength, σ_u (MPa)	Density (g.cm^{-3})
Carbon Toray T300	230	1.5	3530	1.7–1.9
Aramid Kevlar® 49	124	2.9	3620	1.44
E-glass	72	1.7–2.1	1200–2000	2.54
Flax	38–75	1.7–3	600–1400	1.50
Abaca	8–20	2–8	400–980	1.35
Alfa / Halfa	18–22	1.4–2.4	229–474	1.40
Bamboo	32–44	3.8–5.8	1200–1610	1.41
Hemp	23.5–90	1–3.5	270–900	1.45
Coir / coconut	4–6	15–40	131–175	1.15

Cotton	5.5–13	3–10	287–800	1.5–1.6
Jute	20–40	1.5–1.8	280–773	1.44
Kenaf	21–80	1.6	284–800	1.40
Nettle (Urtica dioica)	87	2.11	1594	-
Ramie	24.5–65	1.6–3.8	331–1250	1.51
Sisal	9–21	3–7	350–700	1.45

B.12.3. Flax fibers

Among plant-based reinforcements for polymer composites, flax fibers (Linum usitatissimum) are widely regarded as one of the most mature and technically relevant options, largely because their specific stiffness can be high relative to their low density, while being sourced from renewable feedstocks and processed with comparatively low abrasiveness (Yan et al. 2014).

In the context of natural-fiber reinforced polymers (NFRPs), flax is often highlighted as a "benchmark" bast fiber, since it can be supplied in a broad range of architectures—short fibers, nonwovens, yarns, woven fabrics, and unidirectional tapes—thereby enabling property tailoring from quasi-isotropic panels to directional stiffness-dominated laminates (Bourmaud et al. 2018; Yan et al. 2014). This multi-scale and multi-format availability is directly linked to the plant's anatomical structure (bundles of elementary fibers) and to the industrial sequence of retting, scutching, hackling and/or tow preparation, which governs fiber cleanliness, fiber individualization, defect content and ultimately property scatter.

From a mechanical standpoint, flax fibers are primarily cellulosic, and their longitudinal properties derive from the microfibrillar architecture of the secondary cell wall. The resulting anisotropic behavior explains why flax can deliver comparatively high axial stiffness and strength at the fiber level, while remaining more compliant in transverse directions; in composites, this often translates into good stiffness-to-weight ratios when fibers are aligned and well impregnated. In parallel, flax fibers are frequently positioned as a lower-impact alternative to glass fibers for applications where the design is stiffness-driven and where moderate absolute strength is acceptable, especially when the environmental profile of the reinforcement is part of the selection criteria (Bourmaud et al. 2018; Yan et al. 2014).

In addition to these technical motivations, the flax value chain is strongly rooted in Western Europe, and France occupies a central position in global supply. Life cycle inventory work on flax for technical textiles reports that Europe represents a dominant share of world flax production, with the Normandy region responsible for a very large fraction of the European output; this situation is frequently presented as making France a world leader in flax fiber production, supported by favorable agronomic conditions (humid climate and suitable soils) and long-established know-how (Gomez-Campos et al. 2021).

B.12.4. Flax composites

The feasibility of flax fiber reinforced polymers is no longer a speculative topic: a substantial body of literature demonstrates that flax-reinforced thermoset and thermoplastic composites can reach mechanical performances compatible with load-bearing functions, provided that fiber architecture, fiber volume fraction, impregnation quality, and interface engineering are appropriately controlled (Lau et al. 2018).

Several industrial actors now commercialize flax-based reinforcements and demonstrate repeatable manufacturing routes for high-performance parts. A representative example is Bcomp, which markets engineered flax technical fabrics (e.g., ampliTex^{TM}) for lightweight composite structures and reports deployment in demanding applications spanning sports equipment and automotive components (Bcomp, 2025). In parallel, suppliers such as Eco-Technilin/LINEO have industrialized flax semi-products and prepregs with tailored sizing strategies aimed at improving fiber–matrix compatibility. More recently, fully recyclable bio-composite propositions have also emerged, such as Flaxcomp® (DEMGY × Terre de Lin), illustrating that the flax-composite value chain is expanding from reinforcement fabrics toward application-ready material systems (Flaxcomp, 2026; DEMGY, 2026).

B.13. Durability of FFRP in humid environments

Section B.8 has already addressed the general durability issues of FRP systems in humid environments, with emphasis on mechanisms primarily governed by the polymer matrix. In contrast, the purpose of the present **Section B.13** is to focus on the specific consequences of water diffusion within flax fibers embedded in a polymer matrix, and on how fiber hygroscopicity governs the hygro-mechanical response and damage evolution of FFRP laminates.

When water diffuses into a composite laminate, a widely used experimental approach to quantify the uptake kinetics is gravimetric monitoring (Célino et al. 2013), i.e. repeated mass

measurements during conditioning. The resulting mass-gain curves are commonly analyzed to identify diffusion regimes (often approximated as Fickian at the laminate scale) and to extract apparent transport parameters for the considered geometry and exposure conditions.

In FFRPs, water absorption by flax fibers is accompanied by anisotropic fiber swelling. Because this swelling is constrained by the surrounding matrix, it generates internal stresses at the fiber/interphase and ply scales, which can promote interfacial weakening, matrix microcracking, and progressive damage even without external loading as shown in **Figure 0-22** (Neto et al. 2022; Azwa et al. 2013).

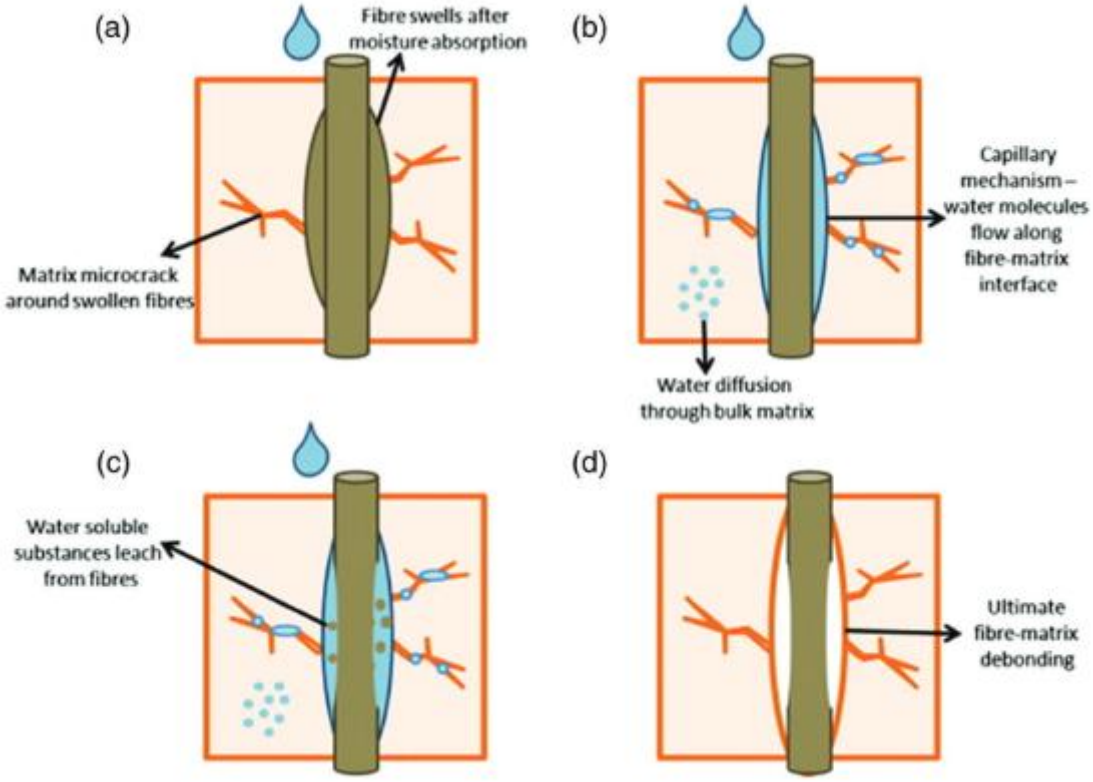

Figure 0-22. Effect of water on fiber–matrix interface: (a) Formation of micro-cracks due to fiber swelling; (b) water molecules diffuse in the bulk matrix and flow along the fiber-matrix interface (c) water soluble substance leaching; and (d) debonding of fiber-matrix interface. Adapted from (Azwa et al. 2013).

C. Interfacial Adhesion Evaluation of a Steel-FFRP Joint with Different Adhesive Types Using the Floating Roller Peel Test

Content

C. Interfacial Adhesion Evaluation of a Steel-FFRP Joint with Different Adhesive Types Using the Floating Roller Peel Test 95
Résumé du chapitre en Français 96
C.1. Introduction 98
C.2. Materials and specimen manufacturing 100
C.2.1. Steel surface treatment 101
C.2.2. FFRP plate manufacturing 103
C.2.3. Adhesive application, substrate fixture and curing time 103
C.2.4. Water jet cutting of the specimens 104
C.3. Experimental methods 105
C.4. Experimental results and discussion 107
C.4.1. Epoxy 108
C.4.2. SMP 111
C.4.3. BioPU 114
C.5. Finite element modeling 117
C.6. Conclusion 119

Résumé du chapitre en Français

Ce chapitre constitue la première contribution expérimentale de la thèse et vise à évaluer la qualité de l'adhérence interfaciale d'un assemblage collé acier–composite lin/époxy (FFRP), afin de sélectionner des systèmes adhésifs adaptés au renforcement de structures métalliques par patchs collés. Cette étape de sélection est un prérequis à la campagne de renforcement en flexion du chapitre D : le décollement prématuré étant le mécanisme limitant le plus fréquemment rapporté pour les renforts PRF collés, il est nécessaire de distinguer les déficiences liées à l'adhésion interfaciale des limitations mécaniques propres à l'adhésif massique et au patch composite. Une partie de ces travaux a été publiée dans l'International Journal of Adhesion and Adhesives (Tazi et al., 2024).

Trois adhésifs ont été étudiés : un époxy bi-composant (AxsonSika® ADEKIT A155/H9955), un polymère modifié silane mono-composant (SMP, Sikaflex®-554) et un polyuréthane biosourcé bi-composant dérivé de l'huile de ricin (BioPU, Kehl®), retenu comme alternative biosourcée potentielle. L'essai de pelage au rouleau flottant (FRPT), mené selon la norme ASTM D3167, a été choisi car son chargement à dominante d'ouverture en pointe de fissure le rend particulièrement sensible à l'intégrité interfaciale, et qu'il est bien adapté aux assemblages de matériaux dissemblables. Trois grandeurs sont exploitées : la charge de pelage par unité de largeur, l'analyse des faciès de rupture (rupture adhésive AF ou cohésive CF, quantifiée par traitement d'images), et — apport original de ce travail — l'évolution de l'angle de pelage au cours de l'essai.

Les éprouvettes associent une tôle d'acier au carbone S235/A36 de 1,76 mm (adhérent souple) et une plaque FFRP de 8,2 mm mise en oeuvre par infusion sous vide (douze plis de sergé de lin 300 g/m², empilement $[\pm 45°]_{12}$, résine SikaBiresin® CR83). L'acier a été sablé (Ra = 2,84 µm) puis dégraissé à l'acétone, avec un nettoyage complémentaire au Sika® Aktivator-205 pour les collages SMP et BioPU. L'épaisseur d'adhésif a été contrôlée par des fils calibrés de 1 mm, un film antiadhérent créant une amorce de fissure de 25 mm, et les éprouvettes ont été découpées au jet d'eau aux dimensions normalisées. Trois éprouvettes par adhésif ont été pelées à 125 mm/min.

Les résultats établissent un classement net. Les éprouvettes SMP présentent le comportement le plus robuste et répétable : charge de pelage moyenne de 35,1 ± 2,9 N/mm avec plateau stable, rupture 100 % cohésive (proche de l'interface FFRP/adhésif, signe d'une adhérence acier/adhésif supérieure) et angle de pelage constant (114,6° ± 0,7°), signature d'un pelage

stable et d'un collage de qualité. Les éprouvettes époxy montrent une forte dispersion (11,8 ± 4,5 N/mm), des instabilités de type stick-slip, des décollements précoces couplés à des chutes simultanées de charge et d'angle de pelage, et une rupture 100 % adhésive à l'interface acier/époxy : l'adhérence acier/époxy est insuffisante dans les conditions de préparation de surface adoptées, cet adhésif étant très exigeant sur l'état de surface. Le BioPU affiche la charge la plus faible (3,2 ± 0,8 N/mm) et une rupture mixte à dominante adhésive (86 % AF), fortement affectée par la difficulté de contrôle de l'épaisseur du joint : la sensibilité de l'isocyanate à l'humidité ambiante (formation de CO_2, défauts piégés, zones sans adhésif) a gouverné localement la charge et l'angle de pelage.

Un modèle éléments finis 2D en déformations planes (Abaqus/Explicit) complète l'analyse : l'acier est élasto-plastique bilinéaire, le FFRP élastique, et l'adhésif est représenté par des éléments cohésifs à loi de traction–séparation. En l'absence de solution analytique d'extraction de l'énergie de rupture pour le FRPT — la charge mesurée intégrant la dissipation plastique de flexion du bras pelé —, une étude paramétrique par comparaison essais/calculs, limitée au cas SMP (seul cas à propagation cohésive stable), identifie une énergie de rupture adhésive comprise entre 25 et 35 N/mm.

En conclusion, le SMP est retenu comme référence fiable pour le chapitre D ; l'époxy testé est remplacé par un système plus compatible avec le collage acier–PRF (SikaPower®-1200) ; le BioPU, pénalisé par son procédé de mise en œuvre, est abandonné au profit d'un adhésif acrylate de ductilité intermédiaire.

C.1. Introduction

The objective of this first work performed during the PhD period is to assess the interfacial adhesion quality of a steel–FFRP bonded joint in order to support the selection of a suitable adhesive system for externally bonded strengthening and repair of metallic structures. In the thesis context, this screening step is not an end in itself: it is a prerequisite to the flexural strengthening campaign developed in Chapter D, where load transfer and the achievable strengthening efficiency depend directly on the integrity of the steel/adhesive/composite interfaces. Indeed, premature debonding remains one of the dominant limiting mechanisms reported for adhesively bonded FRP reinforcements, because the bondline is subjected to a combination of shear and peel stresses that peak near overlap ends and defects, making the performance highly sensitive to surface preparation, adhesive chemistry, and processing conditions (Smith and Teng 2001; Deng et al. 2004; Stratford and Cadei 2006). Consequently, a dedicated adhesion-oriented chapter is needed before diving into flexural strengthening performance, because it enables separating deficiencies driven by interfacial adhesion, from genuine mechanical limitations of the adhesive bulk and the composite patch.

Three adhesives were selected to secondary bond the substrates. A bi-component epoxy from Sika®: Epoxy AxsonSika® ADEKIT A155 / H9955, a single-component Silane Modified Polymer (SMP) also from Sika®: Sikaflex®-554, and a bi-component BioPolyurethane derived from Castor Oil and developed by Kehl®, comprising a polyol and an isocyanate. The latter adhesive was selected as a potential bio-based alternative, and to assess its suitability for steel–FRP bonding in comparison with the synthetic industrial adhesives.

To probe adhesion under a loading state representative of critical debonding conditions in bonded reinforcements, we employed the Floating Roller Peel Test (FRPT), following the (ASTM D3167 2017) standard. Peel-type tests are well known to be particularly sensitive to interfacial integrity because they impose a highly localized opening-dominated stress field at the crack tip. In the specific case of FRPT, manufacturing of the specimens is quite simple, the tests are easy to perform, and it is a suitable test for dissimilar materials (de Freitas and Sinke 2014, 2014; M. M. Arouche et al. 2018; Teixeira De Freitas et al. 2017; Marcio M Arouche et al. 2019). Two main outputs are exploited from FRPT. First, the peel load which is reported as the load per unit width required to propagate separation, derived from the recorded machine load and specimen width in accordance with (ASTM D3167 2017) standard. Second, the fracture surfaces which are examined to identify the dominant failure mechanisms (adhesive failure at an interface versus cohesive failure within the adhesive layer) since the fracture path

is a key indicator of whether the limiting link is the interface (surface preparation/compatibility) or the adhesive bulk (toughness), and it is therefore central to adhesive selection. A third output have been newly introduced, which is the peel angle evolution, as an effort of understanding the influence of peel angle on the resulting peel-loads of the bonded joints.

Beyond adhesion selection objective, the work presented in this chapter also addresses the potential of FRPT as a fracture-based characterization route. Peel tests are, by nature, crack propagation tests, and in principle they can provide access to an adhesive fracture energy. However, analytical modeling of peel tests involves an energy balance in which the measured load reflects not only interfacial dissipation but also significant elastic-plastic bending energy in the peel arm; therefore, objective extraction of an adhesive fracture energy requires plastic corrections for arm bending, which is non-trivial and strongly geometry-dependent (Kinloch et al. 1994; Kawashita et al. 2006). In the particular case of FRPT, the coupling between peel angle evolution, local curvature, plasticity of the steel arm, and adhesive fracture energy change makes analytical treatment especially complex, and the (ASTM D3167 2017) standard does not provide a direct procedure for fracture energy extraction. For this reason, the chapter introduces a finite element (FE) modelling approach intended to bypass the lack of an analytical solution: a 2D plane strain Abaqus/Explicit model is developed, and a parametric study on cohesive fracture energy is used to identify an adequate range of values by comparison between experimental and numerical load-displacement responses.

The chapter is organized as follows. Section C.2 details the materials, surface preparation protocols, and specimen manufacturing steps for the steel–FFRP joints. Section C.3 presents the FRPT experimental setup and methods, namely: the calculation of peel load, the measurement of peel angle evolution, and the fracture surface analysis procedure used to quantify cohesive versus adhesive failure areas. Section C.4 discusses the experimental results for the three adhesive types, discussing repeatability, peel response features, and fracture-path interpretation. Section C.5 presents the FE modelling strategy and its contribution to interpreting the peel response in energetic terms. Finally, Section C.6 synthesizes the key outcomes and translates them into practical constraints for the remainder of the thesis. In particular, the adhesion ranking and the identified limiting mechanisms are used to inform Chapter D, where the selected adhesive systems are evaluated in flexural strengthening of steel plates, and where interface-related assumptions must be consistent with the adhesion evidence established herein.

Part of the work presented in this chapter has been reviewed and published in "International Journal of Adhesion and Adhesives" (Tazi et al. 2024).

C.2. Materials and specimen manufacturing

To evaluate the interface adhesion properties of a bonded joint between carbon steel and Flax Fiber Reinforced Polymer (FFRP), floating roller peel test specimens were manufactured.

A carbon steel plate (S235 / ASTM A36) with a modulus of elasticity of 200 GPa, a Poisson's ratio of 0.3 and a thickness of 1.76 ± 0.47 mm (average ± standard deviation) was selected as a parent/flexible adherend for the bonded joint.

To prepare the composite material, a dry twill woven Flax fiber weighing 300 g/m² was used. The Flax fiber composite was manufactured using the bi-component epoxy SikaBiresin® CR83, and was left to cure for at least one week prior to bonding.

Three adhesive materials were subsequently used to secondary bond the substrates. One bi-component epoxy from Sika®: Epoxy AxsonSika® ADEKIT A155 / H9955. One single-component Silane Modified Polymer (SMP) also from Sika®: Sikaflex®-554. And one bi-component BioPolyurethane derived from Castor Oil and developed by Kehl®, comprising a polyol and an isocyanate. The polyol has yellow color and density of 1.0 g/cm³. The isocyanate is composed by 4,4'- methylenediphenyl diisocyanate (MDI) with a density at 1.24 g/cm³. Obtaining this BioPolyurethane involves reacting the diisocyanate with the supplied castor-oil derived polyol at a ratio of 1:1 wt.%.

Table 0-1 summarizes the adhesive materials used in the study, including their properties, and the associated bonding techniques employed to bond the dissimilar substrates.

Table 0-1. Adhesive materials properties and type of bonding technique

Specimens' nomenclature	Adhesive Material	Type	Tensile Strength [MPa]	Young's Modulus [GPa]	Bonding technique	Reference
Epoxy	Epoxy AxsonSika® ADEKIT A155 / H9955	Bi-component	53	1.9	Secondary bonding	(Sika® adekit-a155-h9955 2020)
SMP	Silane Modified Polymer Sikaflex®-554	Single-component	3.5	-	Secondary bonding	(Sika®Sikaflex-554 2023)
BioPU	Castor-oil-derived Polyurethane Kehl®	Bi-component	42	1.5	Secondary bonding	(de Moura et al. 2021)

C.2.1. Steel surface treatment

The carbon steel plate was sand-blasted and, then degreased using a cloth soaked with acetone to ensure a clean and oil-free surface. One additional cleaning step was done for the steel plates where SMP and BioPU were used, which consisted of cleansing the surface with Sika® Aktivator-205 (Sika® Aktivator-205 2023). This extra-step was realized following the advice of a Sika operator, to achieve better adhesion.

The quality of the treated steel surface was analyzed using the Keyence® VHX-7000 Series numerical microscope. The surface roughness was measured according to the ISO 4287:1997 Standard (ISO 4287:1997 1997). **Table 0-2** displays the specific microscope parameters used for the roughness analysis, and **Figure 0-1** presents the 3D surface profile of the sand-blasted steel plate. The obtained roughness parameters are presented in **Table 0-3** To compare these obtained values, we cite (Akshay Ghumatkar et al. 2017) work where they studied the effect of different steel surface roughnesses on the adhesive bond strength. Different roughnesses were created using mechanical abrasion on a 3mm thick mild steel (AISI 1045 medium carbon steel), and an optimum in average roughness was found at 1.97 μm. (Sarlin et al. 2014) also manufactured well bonded steel/rubber joints by performing sand blasting on a 0.5 mm thick stainless-steel sheet (AISI 304) with 2.46 μm average roughness.

Table 0-2. Parameters for surface roughness analysis based on ISO 4287:1997 Standard

Parameters	Lens magnification	λ_s filter	cut-off λ_c	evaluation length
Values	x500	$8\mu m$	$2.5mm$	$l_n = 5 \times \lambda_c = 12.5mm$

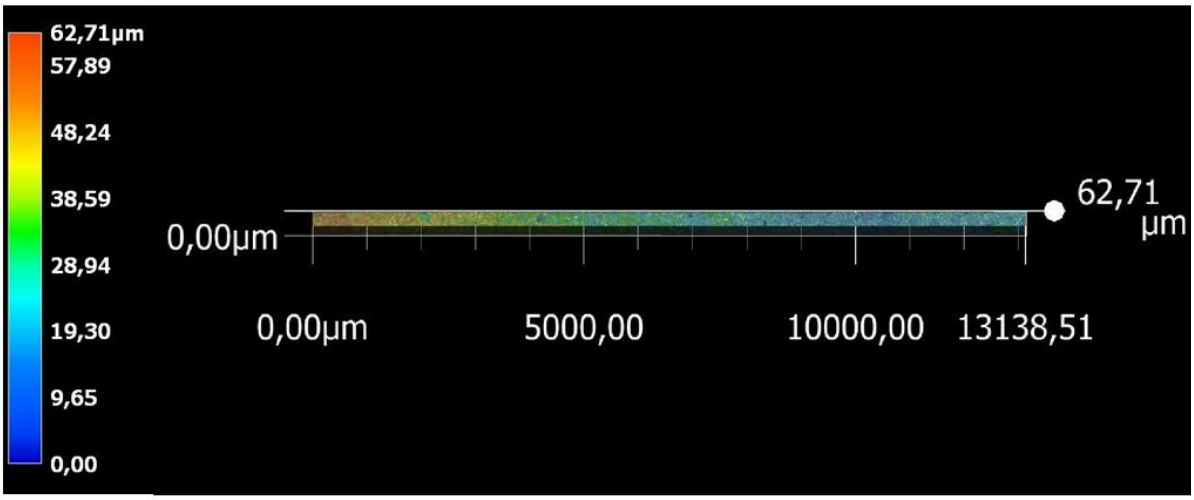

a)

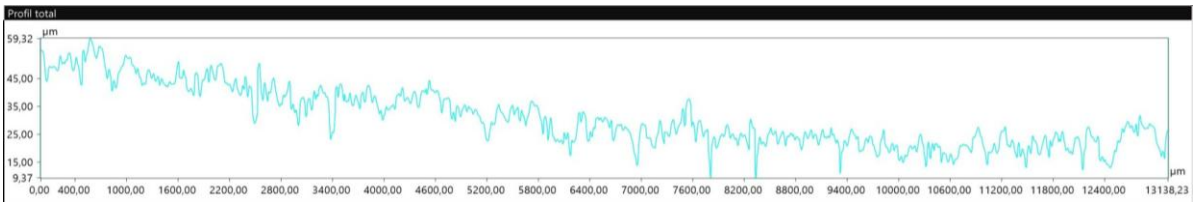

b)

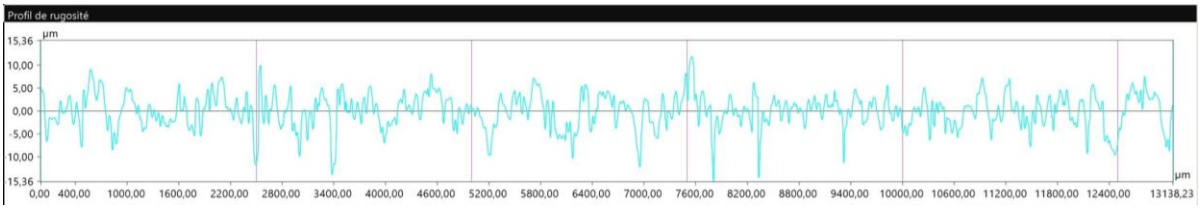

c)

Figure 0-1. Surface roughness analysis results, a) 3D representation, b) Total profile, c) Roughness profile

Table 0-3. Average surface roughness parameters (Ra – Arithmetic Mean Deviation of the roughness profile, Rt – Total Height of roughness profile)

Ra (μm)	Rt (μm)

2.84	21.85

C.2.2. FFRP plate manufacturing

The FFRP plates were manufactured using a vacuum infusion process. The epoxy resin SikaBiresin® CR83 was degassed under vacuum for 15 min prior to use. Twelve plies of Flax fiber, with a total mass of 275 g, were used for the laminate. The final layup configuration consisted of $[\pm 45°]_{12}$ resulting in a plate thickness of 8.21 ± 0.41 mm (average ± standard deviation) and a total mass of 775 g. The curing process took place at room temperature and lasted for 24 hours.

To prepare the surface of adhesion, the composite plate's surface was carefully sanded using sandpaper. Subsequently, any residual dust was removed using a clean cloth and by applying tape bands. These steps aimed to ensure proper adhesion and bonding between the FFRP plates and the steel substrates.

C.2.3. Adhesive application, substrate fixture and curing time

Three different materials were used to bond the dissimilar substrates following **Table 0-1**. Adhesives were applied over the steel surface, the composite plate was placed on top, and pressure was imposed on the assembly using clamps and weights. The thickness of the joint was controlled using metallic wires with a diameter of 1mm in the four extremities of the assembly – see **Figure 0-2**. The curing time for all assemblies was 48h at room temperature, under weight. A Polyethylene non-adherent film was introduced into the assemblies to create a 25mm crack initiation zone as shown in **Figure 0-3**.



Figure 0-2. Assembly set-up and adhesive thickness control

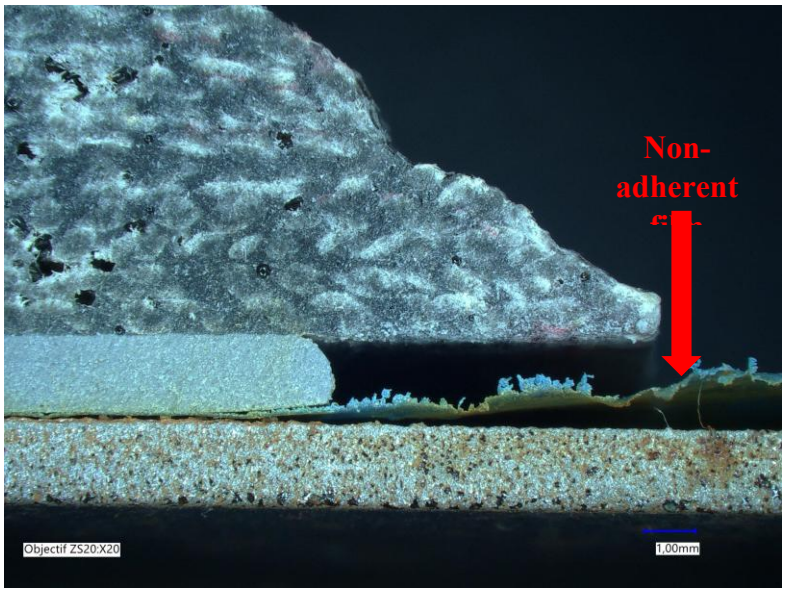

Figure 0-3. Microscope image of the zone of crack initiation

C.2.4. Water jet cutting of the specimens

Once cured, the bonded joints were cut with a water jet cutting machine TCIcutting® BP-C Series 1515. A cannon with a diameter of 0.72 mm was utilized for the cutting process. The cutting process was carried out under a water pressure of 3000 bar, using an Indian garnet 80 mesh abrasive agent with a 225 g/min flow rate. The cutting speed was set at 98 mm/min. The final specimens' dimensions were in accordance with the standard test method ASTM D3167 (ASTM D3167 2017) for floating roller peel tests for metal bonding. Specimens were 23.32 ± 0.54 mm (average ± standard deviation) wide, 300 mm long for the steel arm, 250 mm long for the composite substrate. **Figure 0-4** shows the dimensions of the floating roller peel test specimens. **Table 0-4** lists the total specimens' thickness, width and adhesive thickness (average ± standard deviation) for each specimen type.

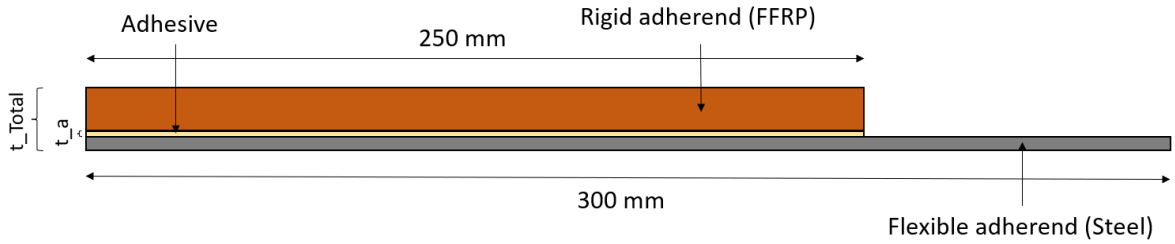

Figure 0-4. Scheme of peel sample dimensions.
t_Total: Total thickness of specimens, and t_a: Adhesive thickness

Table 0-4. Total specimen thickness, width and adhesive thickness

Specimen type	Total thickness [mm]	Adhesive thickness [mm]	Specimen width [mm]
Epoxy	11.05 ± 0.37	1.32 ± 0.18	23.32 ± 0.54
SMP	11.26 ± 0.55	1.42 ± 0.39	
BioPU	11.69 ± 1.34	1.22 ± 1.15	

C.3. Experimental methods

The experimental testing involved conducting Standard Floating Roller Peel Tests (FRPT) on the three batches of specimens, - see **Table 0-1**. Three specimens were tested from each batch. During testing, the flexible adherend (Carbon Steel) is peeled off from the rigid adherend (FFRP).

The testing was carried out using an electro mechanic Zwick machine with a maximum capacity of 20kN. The testing speed was set to 125mm/min in accordance with the (ASTM D3167 2017) standard.

To capture the crack propagation during the tests, a digital camera was used, recording at a frequency of 0.5 frames per second. **Figure 0-5** illustrates the set-up of the peel test.

During testing, load-displacement curves were recorded to assess the bonded joints' mechanical behavior, and peel loads $\frac{F}{b}$ (in Newtons per millimeter width of the specimen) required to separate the adherends were calculated, where F is the recorded load, and b is the width of the specimen.

Moreover, one additional parameter which is the adhesive fracture energy should be possible to calculate using the results of such peel tests. But in what follows we explain why it is very complicated to calculate, and how we bypassed this issue.

FRPT tests are by nature fracture tests, i.e. tests where a cracking process initiates then propagates as the joined materials separate. The analysis of such tests should normally lead to the characterization of adhesive fracture energy G_c. However, it is now well recognized in literature (Kawashita et al. 2006; Kinloch et al. 1994) that the measurement of peel load relates to the calculation of a total input energy G for the peeling process and that an adhesive strength in the form of adhesive energy release rate G_c can only be objectively determined when correction is made for the plastic bending energy G_p associated with the peel arm. A global energy analysis gives:

$$G_c = G - G_p \quad \textbf{(0-1)}$$

Consequently, for most peel tests (where the peel angle is constant) an experimental procedure will measure peel load in order to calculate G and the tensile stress-strain properties of the peel arm material will be used in order to calculate G_p. For instance, **Equation (0-2)** is used for the determination of total input energy G in the specific case of "peel arm test", assuming no tensile deformation of the peel arm, and where θ is the peel angle (Kawashita et al. 2005). Regarding the determination of G_p, analytical methods are generally way more complex (Kawashita et al. 2006).

$$G = \frac{P}{b}(1 - cos\theta) \quad \textbf{(0-2)}$$

In the particular case of FRPT, the calculation of both quantities (G and G_p) requires heavy analytical modeling, because multiple quantities are coupled (adhesive's fracture energy, peel angle, local curvature of the peel arm, etc.), and to the best knowledge of the author, no reference exists on the development of an analytical solution for the calculation of adhesive fracture energy for FRPT. The (ASTM D3167 2017) standard doesn't give any guidance either on calculation of adhesive fracture energy G_c. Consequently, a determination method based on comparison of experimental results with Finite Element Analysis (FEA) results is adopted and is further detailed in **Section C.5**.

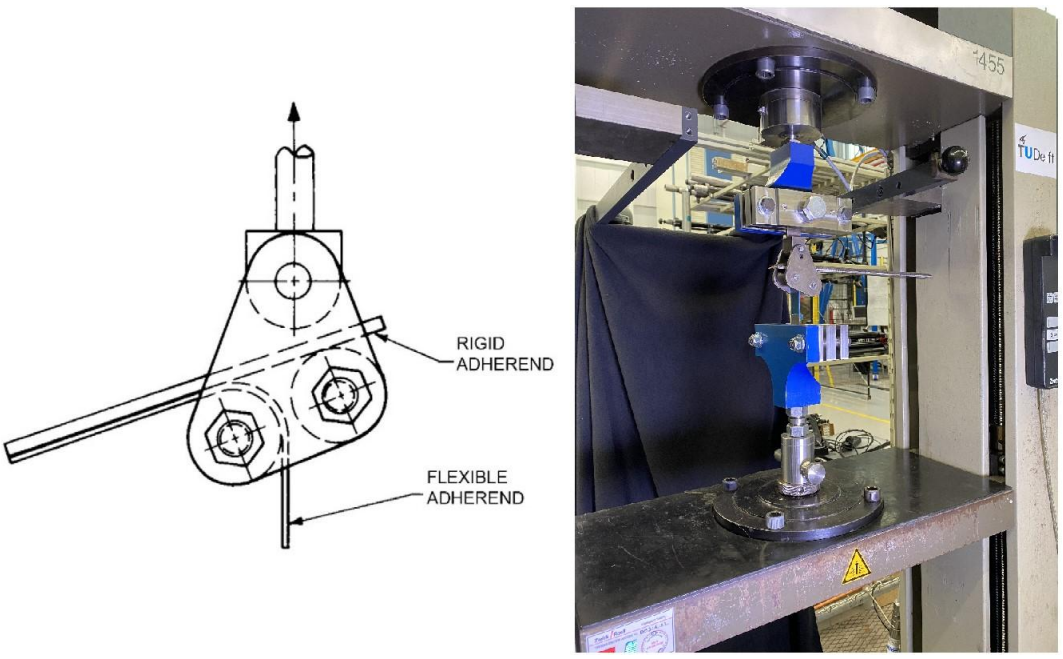

a) b)

Figure 0-5. a) Scheme of Floating roller peel test (Teixeira de Freitas et al. 2017), b) Experimental set-up for floating roller peel tests

C.4. Experimental results and discussion

The results of peel tests, including the average peel load values and failure mechanisms observed on fracture surfaces for each specimen type, are presented in **Table 0-5**. The average peel load values are shown as the average ± standard deviation of the three specimens tested for each adhesive type. These values were determined over a displacement of 100mm, excluding the first 50mm, in accordance with (ASTM D3167 2017) standard for floating roller peel tests.

Two distinct failure mechanism were observed: cohesive failure (CF) occurring within the adhesive layer, and adhesive failure (AF) at the interface between adhesive and adherends. The percentage area of each failure modes was measured based on the visual observations of the specimens' fracture surfaces, using the Fiji image processing package for scientific image analysis. **Figure 0-6** gives a representation of the realized measurements on one of the tested specimens.

The detailed results for each type of specimens are shown in the following subsections.

Table 0-5. Average peel loads and failure mechanisms

Specimen type	Average peel load [N/mm]	CF (%)	AF (%)
Epoxy	11.8 ± 4.5	0	100
SMP	35.1 ± 2.9	100	0
BioPU	3.2 ± 0.8	14	86



Figure 0-6. Example of cohesive failure areas (highlighted) for BioPU Specimen 1. (CF: Cohesive failure, and AF: Adhesive failure)

C.4.1. Epoxy

Figure 0-7 shows the peel strength-displacement curves of the peel tests performed in three samples of the Epoxy specimens, and fracture surface for specimen 1. The results show significant scatter between specimens.

Specimen 1 showed a decrease in peel strength between 17 and 41 mm of displacement. Thereafter, the load has increased until reaching a maximum peel load equal to 17.4 N/mm at 90 mm displacement, where it remained stable for the remaining part of the test.

Specimens 2 and 3 showed different behavior characteristic of stick-slip. In stick-slip behavior, the crack halts at an arrest force and then re-initiates at a higher initiation force in a metastable manner, as (Bartlett et al. 2023) described.

Fracture surface analysis of specimen 1 showed 100% adhesive failure (AF), with all the epoxy remaining on the composite side and no traces of epoxy on the steel surface. The occurrence of adhesive failure is expected as this type of epoxy adhesive is very demanding on substrate surface preparation. However, fracture surface showed a slight color difference between the initial part featuring an area of low adhesion (decrease of peel load – “poor adhesion”), and an area of steady peel force (plateau value of ~17.4 N/mm). The latest indicates an increase in the adhesion strength at the interface adhesive-steel however not sufficient for the crack to propagate inside the adhesive.

We assume that the poor adhesion observed in the three specimens can be explained by the insufficient surface treatment and cleansing prior to the adhesive application. Dust marks can be observed on the surface, as shown in **Figure 0-7 b)**.

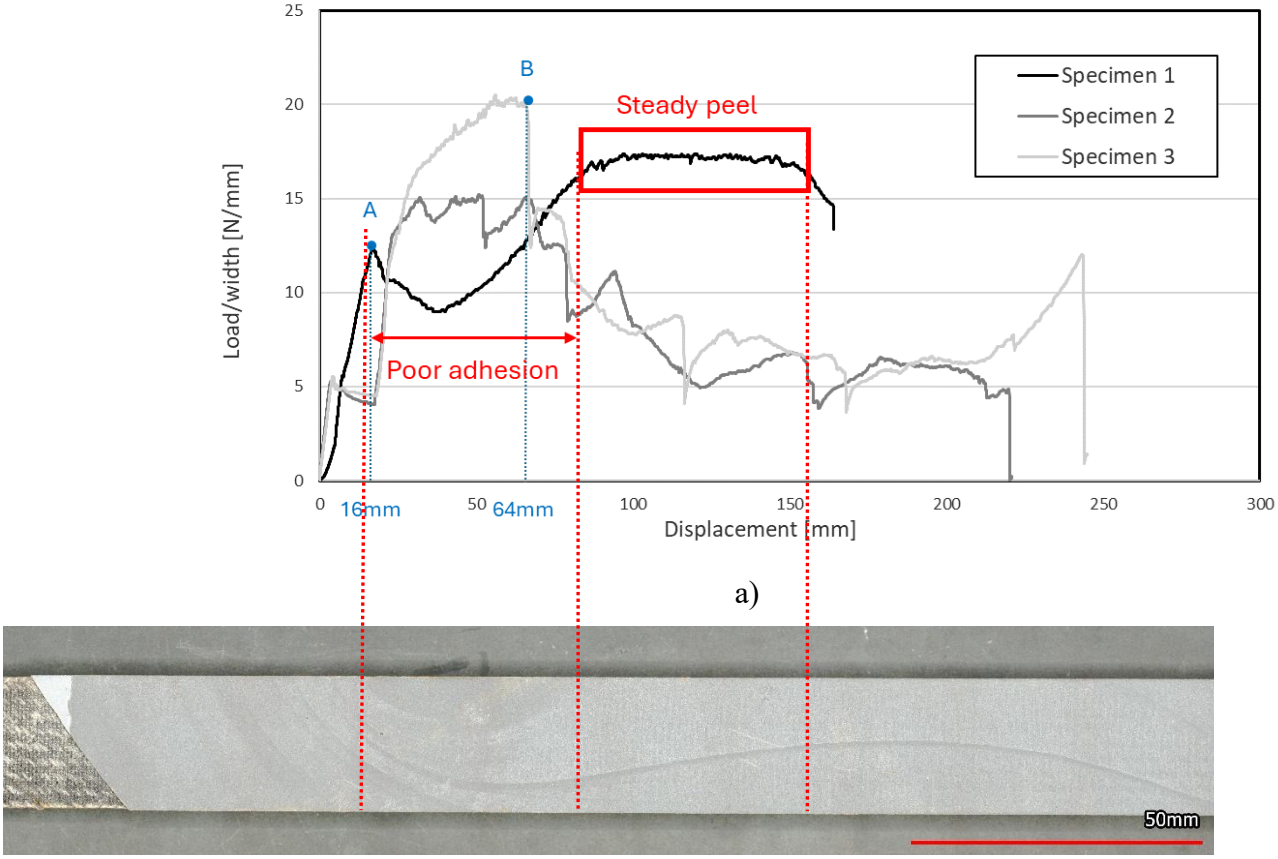

Figure 0-7. Load-displacement curves for Epoxy Specimens (AxsonSika® ADEKIT A155/H9955), and b) corresponding fracture surface of composite rigid adherend for specimen 1

Figure 0-8 represents the peel angle vs displacement curves of the peel tests performed on the specimens. The peel angle is measured between the plane of the FFRP rigid adherend and the vertical plane which passes through the embedding point of the steel adherend as shown in **Figure 0-8 c)**.

We notice that peel angle and peel load are related. A decrease in the peel angle results in a drop in the peel load. Points A and B present on both **Figure 0-7 a)** and **Figure 0-8 a)** show examples of moments of occurrence of drops in both peel angle and peel load for specimens 1 and 3 respectively.

Throughout the tests, the following occurs:

1- Debonding of the flexible adherend from the rigid one prior to the location of the roller (early debonding) – See **Figure 0-8 b)**.

2- Decrease in the peel load and subsequently peel angle – See **Figure 0-8 c)**.

This behavior is mainly due to the weak interfacial adhesion of the epoxy adhesive to the steel surface, but the 1.76 mm thick flexible adherend with high flexural stiffness might have also influence the early debonding seen in **Figure 0-8 a)**.

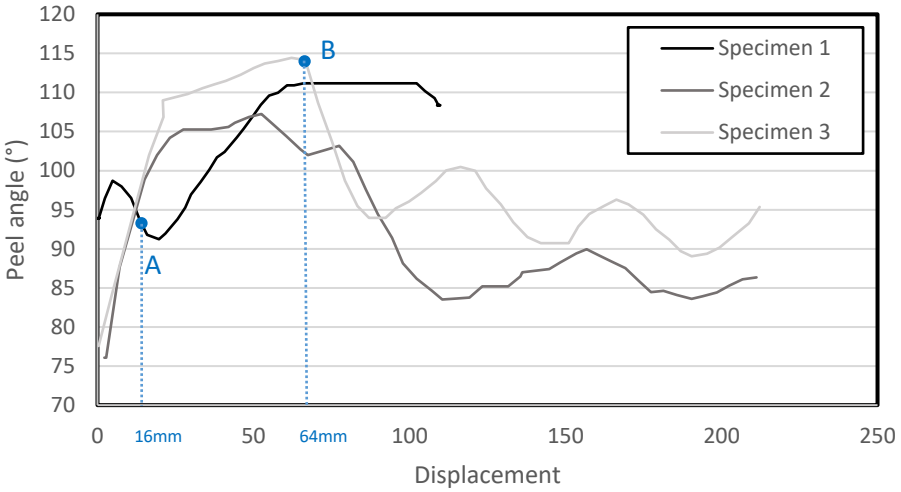

a)

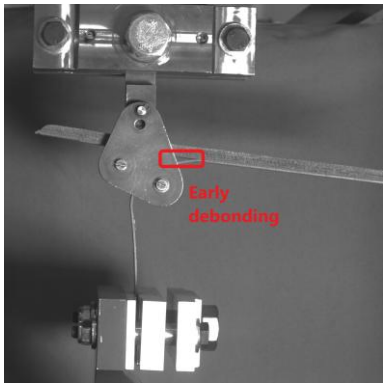

b)

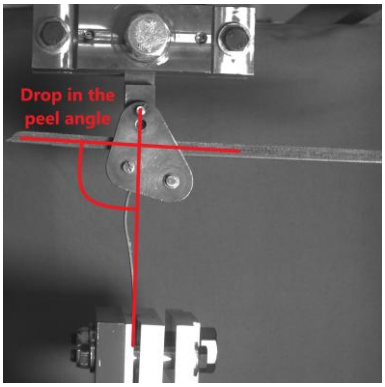

c)

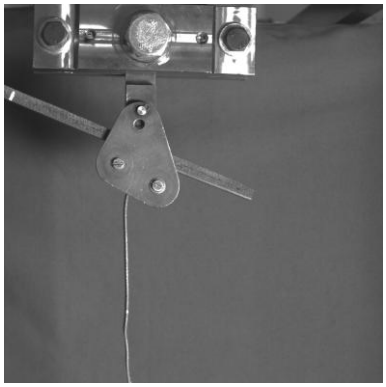

d)

Figure 0-8. a) Peel angle-displacement curves for Epoxy Specimens (AxsonSika® ADEKIT A155/H9955), and specimen 1 pictures, b) Zone of early debonding – Image captured at 16 mm of displacement, c) Drop in peel angle – Image captured at 22 mm of displacement, d) Steady peel force – Image captured at 91 mm of displacement

These observations suggest that proper surface preparation is crucial for achieving optimal adhesion with the AxsonSika® ADEKIT A155/H9955 epoxy adhesive. Additional investigations and improvements in surface treatment protocols may be necessary to enhance the bonding performance of this adhesive in the tested bonded joints.

C.4.2. SMP

Figure 0-9 shows the peel load-displacement curves of the peel tests performed in three specimens of SMP (Sikaflex®-554). All load-displacement curves are consistent and repeatable and the three specimens present similar behaviors with a peel load reaching a plateau value of 35 N/mm approximately.

Figure 0-9 also shows the typical fracture surfaces for specimen 1. Notably, 100% cohesive failure mode was observed, as the SMP adhesive is present on both adherends, which clearly indicates good adhesion. This cohesive failure justifies the steady peel load observed in the load-displacement curves. This favorable outcome might be attributed to the improved surface treatment performed prior to the application of the SMP adhesive by applying an extra cleansing in the steel surface, the Sika® Aktivator-205 as detailed in **Subsection C.2.1**.

Besides, we notice that cohesive failure occurs close to the interface between the FFRP (rigid adherend) and the adhesive. It has been shown in previous studies that due to the asymmetry of the specimens, the failure path is more likely to occur at the interface close to the thin flexible adherend than close to the thick rigid adherend (de Freitas and Sinke 2015; Teixeira de Freitas et al. 2017). We assume that the noticed behavior for steel-to-FFRP specimens bonded with SMP can be due to the better adhesion between the adhesive and treated carbon steel than between the adhesive and the FFRP.

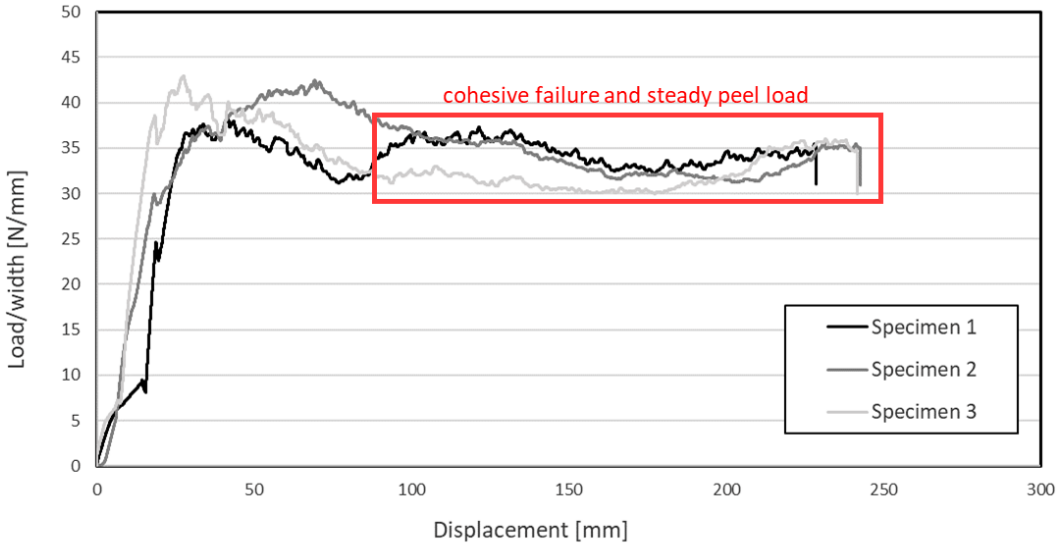

a)



b)



c)

Figure 0-9. a) Load-displacement curves for SMP specimens (Sikaflex®-554), and corresponding fracture surfaces for specimen 1, b) Steel interface and c) FFRP interface

Figure 0-10 represents the peel angle vs displacement curves of the peel tests performed on the three specimens. The peel angle between the flexible and rigid adherend was constant throughout testing and equal to 114.6° ± 0.7° (average ± standard deviation). This average peel angle was determined over 100 mm of displacement disregarding the first 50 mm, using values of all three specimens. For comparison, in (Bartlett et al. 2023) review, they reported that floating roller peel test give peel angles of nominally 135° when using a roller drum peel test fixture.

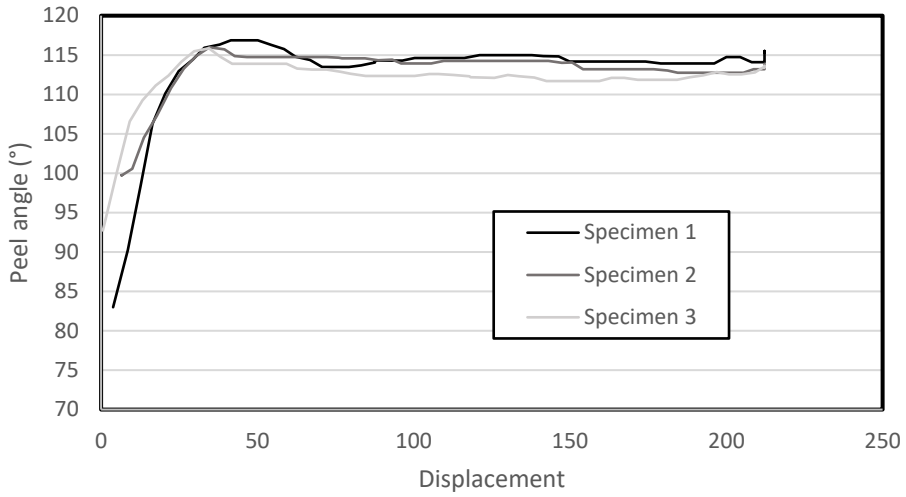

a)

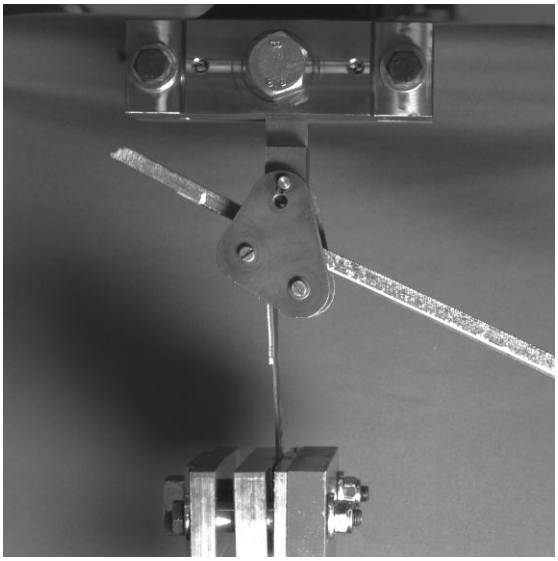

b)

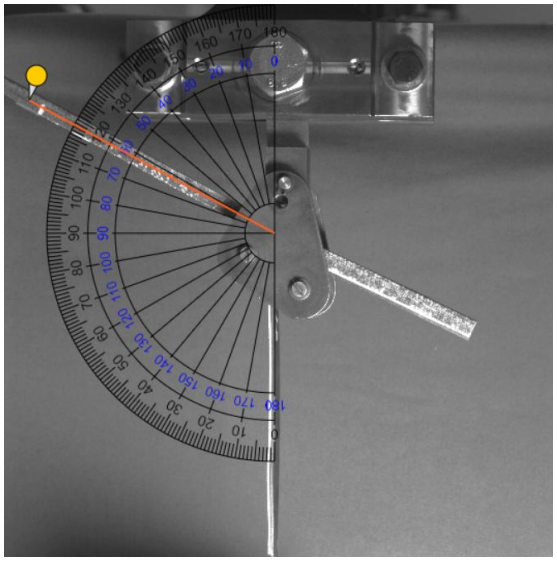

c)

Figure 0-10. Peel angle-displacement curves for SMP specimens (Sikaflex®-554), and specimen 1 pictures, b) Image captured at 76 mm of displacement, c) Image captured at 174 mm of displacement

These results suggest that the SMP adhesive demonstrates promising performance and highlights its potential as a suitable choice for achieving reliable and robust bonding in FFRP-to-steel joints. Furthermore, this finding supports the exploration and development of bio-based PU as an alternative material since its properties are similar to those of SMP adhesives. The use of bio-based polyurethane adhesives can contribute to more sustainable and environmentally friendly bonding solutions in various industries.

C.4.3. BioPU

Figure 0-11 shows the load-displacement curves of the peel tests performed in three samples bonded with the BioPU (Castor-oil derived Polyurethane Kehl®), and fractures surfaces of specimen 1, as well as the corresponding measured adhesive thickness through image processing.

Specimen 1 has a peak load at point F_1 (13.9 N/mm at 18 mm). Thereafter, the peel load decreases significantly to values between 3.3 and 4.3 N/mm for displacement ranging between 33 - 135 mm. Finally, it gradually increased reaching 7.9 N/mm at the end of the test before complete debonding of the flexible adherend. Similar behaviors were observed for Specimen 2 and 3.

The BioPU specimens exhibited challenges related to the control of adhesive thickness. This was shown previously by the adhesive thickness measurement in **Table 0-4** prior to testing and also after testing as it can be observed on fracture surface of the composite rigid adherend in **Figure 0-11 c)**. BioPU is a bi-component adhesive, which involves reacting an isocyanate with the castor-oil derived polyol. Isocyanate is very sensitive to the room conditions while polymerizing with polyol, as the reaction between isocyanate and water from air humidity produces carbon dioxide that may be trapped in the viscous mixture, which harms the integrity of the adhesive and creates stress concentrators inside the adhesive layer as well as non-adhesive areas in the substrate (Wan et al. 2006; E. Silva et al. 2022). Thus, the manufacture process focused on reducing the exposure time of resin to the environmental conditions. However, by doing so, the viscosity of the resin was not sufficient to prevent leakage in the borders of the plate, which ended up causing some areas with no adhesive between the substrates.

These specimens showed that the thickness of the adhesive layer greatly influenced the peel loads and the mode of failure that occurs on the interface.

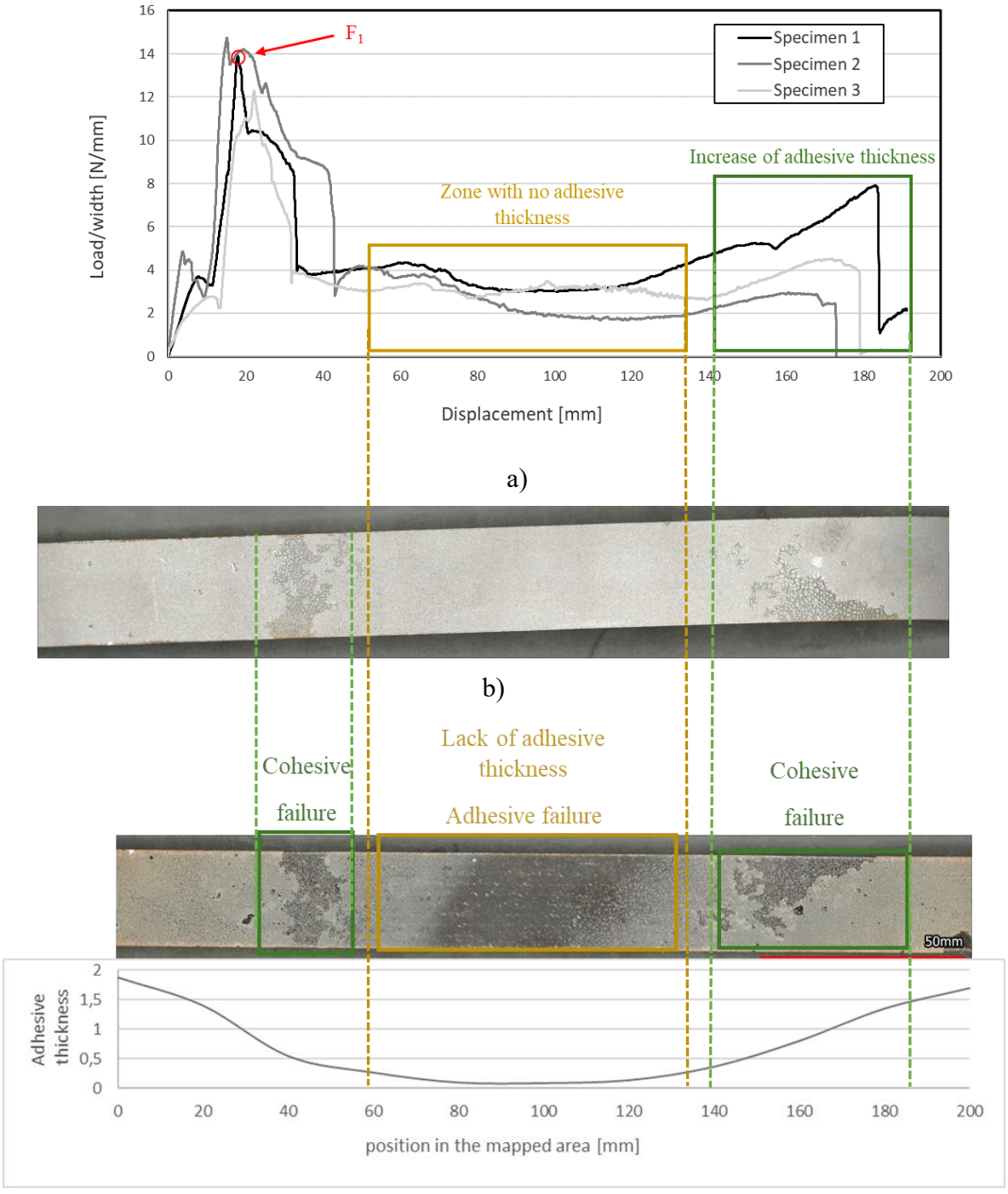

Figure 0-11. Load-displacement curves for BioPU specimens (Castor-oil derived Polyurethane Kehl®), and fracture surfaces for specimen 1, b) Steel interface and c) FFRP interface and corresponding measured adhesive thickness in the mapped area

Figure 0-12 a) represents the peel angle vs displacement curves of the peel tests performed on the specimens, and gives a visual representation of the course of testing for specimen 1. During testing of specimen 1, when the adhesive layer thickness was high (before 18 mm of

displacement) – See **Figure 0-12 b)**, the flexible adherend bent smoothly along the curvature of the roller drum. However, as the adhesive thickness reduced, adhesive failure occurred at 18 mm of displacement (**Figure 0-12 c)**), resulting in a significant reduction of the peel load and peel angle. Towards the end of the test, between 135 and 182 mm of displacement, the adhesive layer thickness increases, leading to occurrence of cohesive failure in the adhesive, bending of the steel arm, and hence an increase in the peel angle before complete debonding – See **Figure 0-12 d)**.

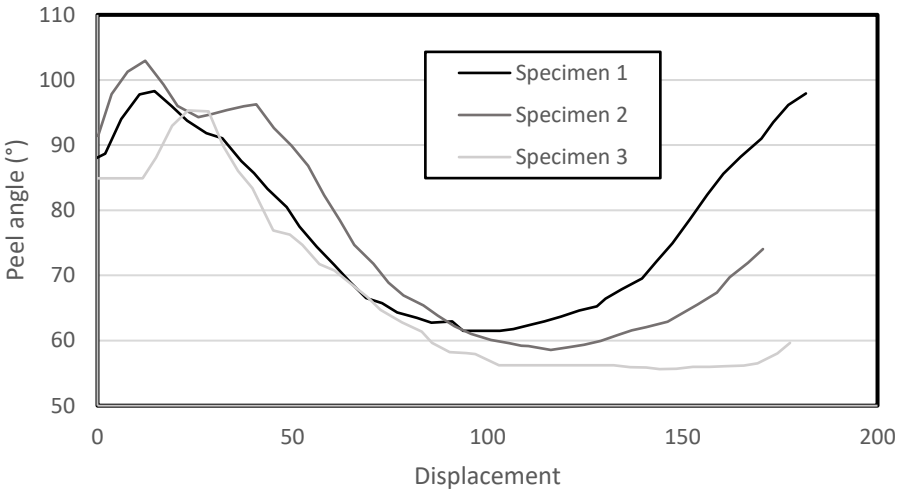

a)

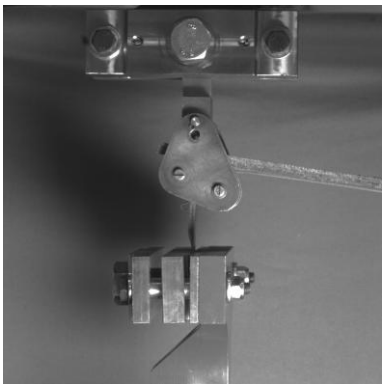

b)

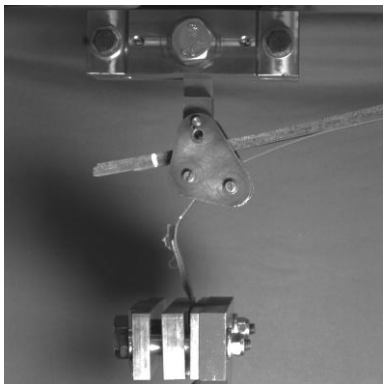

c)

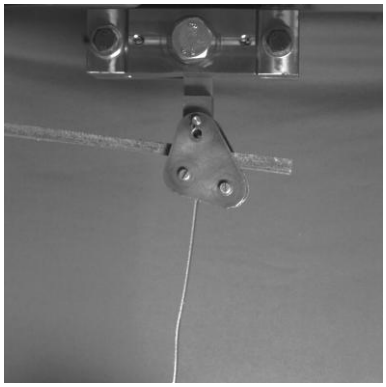

d)

Figure 0-12. a) Peel angle-displacement curves for BioPU specimens (Castor-oil derived Polyurethane Kehl®), and specimen 1 pictures, b) Beginning of loading – Image captured at 11 mm of displacement, c) Zone with no adhesive thickness and brutal debonding occurrence – Image captured at 52 mm of displacement, d) Zone with greater adhesive thickness – Image captured at 178 mm of displacement

These observations highlight the importance of controlling the adhesive layer thickness for achieving consistent and reliable bonding results with the castor-oil derived polyurethane adhesive. Major improvements of the bonding process, and comprehensive understanding of adhesive application, may be necessary to enhance the performance and reliability of this bio-based adhesive, and successfully implement it for structural use.

C.5. Finite element modeling

A 2D plane strain finite element model of the floating roller peel test geometry was developed in Abaqus Explicit solver. The objective of the model is to identify the value of fracture energy G_c of the adhesive by comparison of load-displacement curves recorded experimentally, and parametric load-displacement curves predicted numerically. It should be reminded that characterization of adhesive fracture energy through analytical solutions is very complex, as previously explained in **Section C.3**.

It should be noted that since the only experimental test which was clearly successful (cohesive failure in the adhesive and steady peel angle throughout the test) was the one with SMP adhesive, it will be the only one used as reference for comparison with the finite element model.

Figure 0-13 gives a global representation of the geometry, materials and interactions in the model.

The steel flexible adherend is modeled as a bilinear elasto-plastic material, with a Young's modulus of $200\ GPa$, Poisson's ratio of 0.3, yield stress of $275\ MPa$, ultimate stress of $375\ MPa$ at 20% plastic strain, and a density of $7.85 \times 10^{-9}\ tonne.mm^{-3}$. These input values are in accordance with (ASTM A36 2019).

The rigid FFRP substrate is modeled as a quasi-isotropic elastic material, with an in-plane (laminate reference coordinates) modulus of elasticity $E_1 = 10\ GPa$, and an out-of-plane modulus of elasticity $E_2 = 3.45\ GPa$. These input values are in accordance with provided values from literature (Scida et al. 2017).

The adhesive is modeled using cohesive elements, with $0.1\ mm$ thickness, as shown in the zoom-in of **Figure 0-13**. A traction-separation law is assigned to the cohesive elements.

Stiffness coefficients are chosen equal to $K_{nn} = K_{ss} = 10GPa.mm^{-1}$ A quadratic stress criterion is used for damage initiation, with normal stress $t_n = 1.75\ MPa$ and sear stress $t_s = 5\ MPa$. An energy-based mode-independent damage evolution formulation is chosen for its simplicity, and three values of fracture energy $G_c = 25\ ;30\ and\ 35\ N.mm^{-1}$ are used

The rollers are modeled as rigid elements. MPC constraints are imposed between the reference points of the rollers and the support fixture. Displacement is applied to the extended arm of the steel flexible adherend. An angle of 115° is used between the rigid adherend and the flexible arm, as previously identified in **Figure 0-10**.

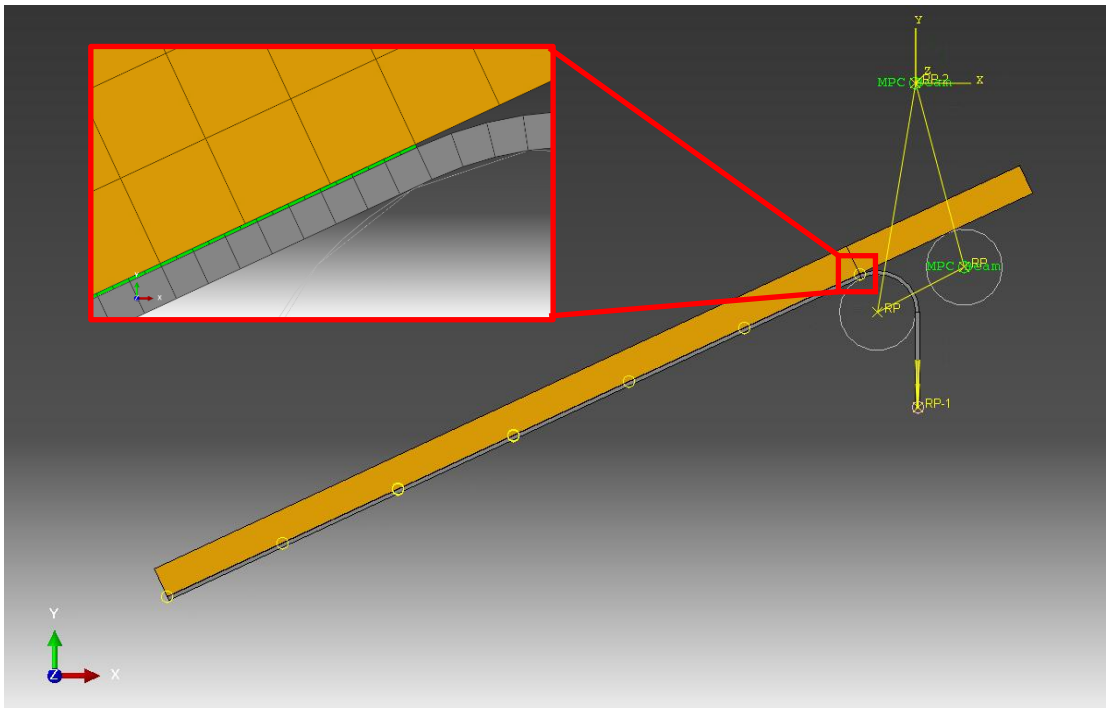

Figure 0-13. Representation of the numerical model of floating roller peel test

Figure 0-14 presents the load-displacement results of specimen 3 bonded with SMP adhesive, in comparison with FEM numerical results of the parametric study on input value of adhesive fracture energy.

Based on the chosen modeling of the cohesive behavior, it can be concluded that the fracture energy of the adhesive is indeed comprised between 25 and 35 $N.mm^{-1}$. At the beginning of the test the fracture energy is closer to 35, than decreases to values close to 25, and finally increases to values close to 30.

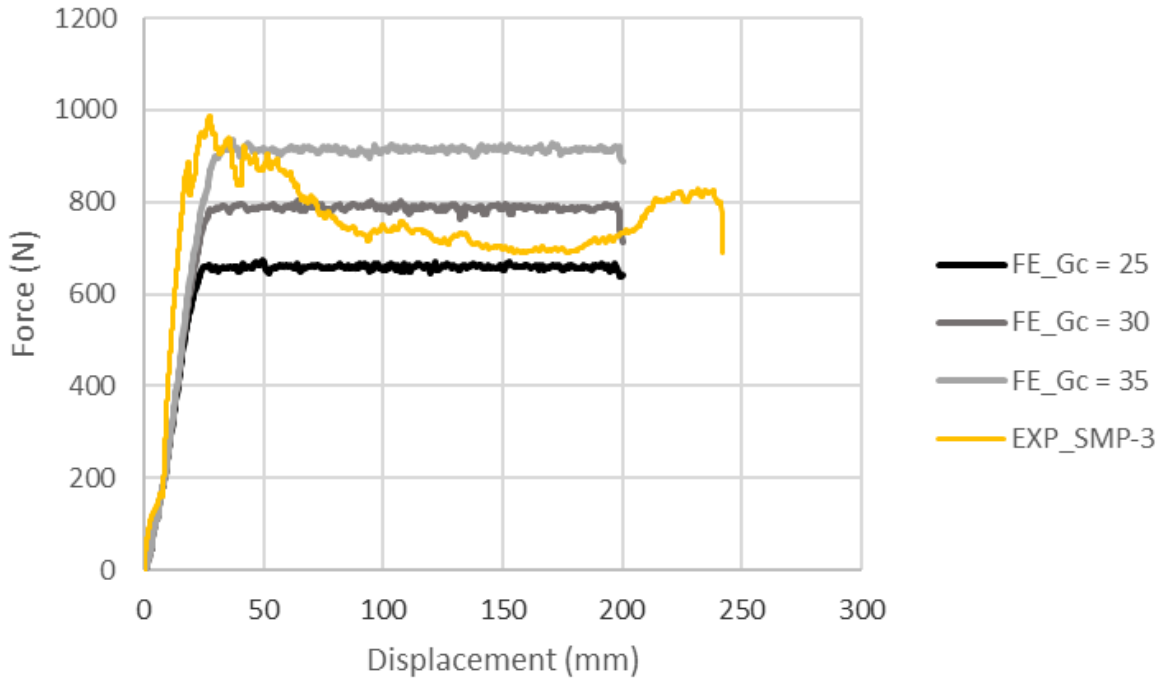

Figure 0-14. Comparison of experimental load-displacement results of specimen 3 bonded with SMP adhesive, with FEM numerical results for $G_c = 25; 30; 35\ N.mm^{-1}$

C.6. Conclusion

This chapter served to evaluate, through standardized floating roller peel testing, the interfacial adhesion quality of a steel–FFRP bonded joint manufactured with three different adhesive types, with the objective of screening adhesive solutions relevant to externally bonded strengthening/repair configurations. The experimental campaign confirmed that FRPT provides a discriminating response for steel–composite dissimilar joints by simultaneously delivering a mechanical indicator (peel load per unit width), a kinematic indicator (peel angle evolution), and direct fracture-path evidence through post-mortem surface observations. Across the three tested specimens per adhesive type, markedly different levels of repeatability and distinctly different failure mechanisms were obtained, enabling a clear adhesion-driven ranking within the scope of the present manufacturing and surface preparation protocols.

Based on the average peel load values and fracture surface observations reported in this chapter, the SMP (Sikaflex®-554) specimens exhibited the most robust and repeatable behavior, with consistent load–displacement curves reaching a stable plateau around the reported peel-load

level, and a fully cohesive failure mode (100% CF). This combination of a steady peel response and cohesive fracture indicates that, under the adopted preparation route, the interface adhesion is not the limiting link; instead, crack propagation is driven through the adhesive layer, which is generally interpreted as a signature of good bonding quality in adhesive joints. In addition, the peel angle remained essentially constant throughout propagation for SMP specimens, reinforcing the interpretation of stable peeling conditions and consistent fracture processes. The observed cohesive fracture path was located close to the FFRP/adhesive interface, indicating a higher steel/adhesive interface fracture energy than FFRP/adhesive one..

In contrast, the Epoxy (AxsonSika® ADEKIT A155/H9955) specimens showed significant scatter between replicate tests and a predominantly interface-controlled failure. The load–displacement curves displayed unstable features, including stick–slip behavior for two specimens and pronounced drops associated with early debonding events, while fracture surface analysis indicated 100% adhesive failure (AF), with epoxy remaining on the composite side and no traces on the steel surface. The coupled decrease of peel load and peel angle observed during early debonding events, together with the interface fracture path, supports the conclusion drawn in the chapter that the steel/epoxy adhesion was insufficient under the adopted surface preparation and cleaning conditions. Within the framework of this work, these results emphasize that this epoxy adhesive is highly demanding in terms of surface condition, and that the observed performance is consistent with an interface-limited regime where modest local improvements in cleanliness/activation can alter the apparent adhesion level, yet remain insufficient to trigger cohesive propagation.

Finally, the BioPU (castor-oil-derived Polyurethane Kehl®) specimens exhibited the lowest average peel load and a mixed failure mode dominated by adhesive failure (high AF fraction with limited CF areas). The experimental curves were strongly affected by manufacturing-induced variability, notably difficulty in controlling the adhesive layer thickness, as evidenced by the thickness measurements and mapped fracture surface observations. The chapter showed that local thickness variations governed both the instantaneous peel load and the peel angle evolution, with abrupt debonding in zones with insufficient or absent adhesive and more cohesive-like behavior in zones where the adhesive layer was thicker. The discussion further linked these observations to processing sensitivity of isocyanate-based systems to ambient humidity, which can promote gas formation and trapped defects during curing and thereby create stress concentrators and non-adhesive areas. In this state, the BioPU results do not yet

provide a reliable basis for structural use, not because the adhesive chemistry is intrinsically unsuitable, but because the present manufacturing protocol did not ensure a consistent and defect-controlled bondline.

The FE modelling effort introduced in this chapter complements the experimental screening by addressing the energetic interpretation of FRPT responses. Because the only configuration that exhibited a clearly stable peeling process with cohesive failure and steady peel angle was SMP, the model comparison was deliberately restricted to that case. Within the adopted 2D plane strain framework and the chosen cohesive modelling assumptions, the parametric study enabled the identification of an adequate range of adhesive fracture energy values that reproduce the experimental load–displacement response, and it highlighted that matching FRPT curves requires accounting for the coupled roles of peel-arm elasto-plasticity, imposed peel angle, and cohesive dissipation. Even though the modelling is not used here to claim an absolute fracture toughness value for all configurations, it provides a justification for why analytical extraction is difficult in FRPT and establishes a practical pathway—calibration by comparison—for exploiting peel tests beyond qualitative adhesion ranking when stable cohesive propagation is achieved.

From the perspective of the remainder of the thesis, the outcomes of Chapter C impose direct constraints on adhesive selection and on interface assumptions for structural-scale tests. First, the SMP adhesive emerges as the most reliable candidate among the tested adhesives for steel–FFRP bonding under the adopted surface preparation, and it therefore provides a justified baseline for the flexural strengthening investigations in Chapter D, where robust load transfer is required to interpret strengthening gains and failure modes without confounding interface deficiencies. Second, the epoxy system, as implemented here, should not be assumed to provide adequate steel adhesion without an improved and better-controlled surface preparation/cleaning protocol. It was consequently decided to substitute it with another epoxy system (SikaPower®-1200), more chemically compatible for steel-FRP bonding for the work performed in Chapter D. Third, the BioPU results motivate targeted process improvements—particularly adhesive thickness control and humidity-controlled curing—before any structural comparison can be considered meaningful. The use of a bio-based adhesive has consequently been abandoned, and substituted with an acrylate adhesive which is chemically compatible with steel-FRP bonded joints, and to serve as an intermediate flexibility and ductility adhesive compared to the epoxy and SMP.

D. Influence of Adhesive Type and Layup of Hybrid Flax/Carbon Composite Patches on the Flexural Performance of Steel Plates

Content

D. Influence of Adhesive Type and Layup of Hybrid Flax/Carbon Composite Patches on the Flexural Performance of Steel Plates 123
Résumé du chapitre en Français 125
D.1. Introduction 127
D.2. Materials 129
D.2.1. Steel substrate 129
D.2.2. Composite substrate 130
D.2.3. Adhesives 131
D.3. Specimen manufacturing 132
D.3.1. Composite patch configurations 132
D.3.2. Surface preparation 133
D.3.2.i Steel adherend 133
D.3.2.ii Composite adherend 134
D.3.3. Bonding process 135
D.4. Experimental methods 137
D.5. Experimental results and discussion 139
D.6. Finite element modeling 144
D.6.1. Model description 144
D.6.2. Material properties and modeling steps 146
D.6.2.i Steel 146
D.6.2.ii Composite patch 146
D.6.2.iii Adhesive 147
D.6.3. Numerical modeling validation 148
D.6.3.i Load-deflection curves 148
D.6.3.ii Displacements and strains 148
D.6.4. Stress analysis 150
D.6.4.i Interfacial stresses (Adhesive **A**) 150
D.6.4.ii Evolution of stresses along thickness of composite patch (Adhesive **B** & **C**) 152

D.7. Conclusion 155

Résumé du chapitre en Français

Ce chapitre évalue le renforcement en flexion de plaques d'acier par patchs composites collés en surface, avec pour objectif de clarifier comment les propriétés mécaniques de l'adhésif et l'empilement de patchs hybrides lin/carbone gouvernent l'efficacité du renforcement, sa répétabilité et les mécanismes de ruine. La configuration étudiée s'inspire de la semelle tendue des poutres en I, dont la capacité en flexion peut être améliorée par collage d'un patch composite, à condition que le transfert de charge soit effectif et le décollement maîtrisé. Le compromis intrinsèque de ces renforts est au cœur du chapitre : un adhésif rigide maximise le transfert de déformation mais élève les contraintes interfaciales de pelage et de cisaillement aux extrémités du patch, favorisant un décollement prématuré, tandis qu'un adhésif souple atténue ces concentrations au prix d'une moindre efficacité de renforcement. À la suite du criblage d'adhérence du chapitre C, un essai à l'échelle de l'éprouvette, représentatif du renforcement de semelles en acier, est proposé pour comparer systématiquement de multiples configurations. Une partie de ces travaux a été soumise à la revue Composite Structures.

Le programme expérimental repose sur des essais de flexion trois points quasi-statiques avec quatre cycles progressifs de charge–décharge (jusqu'à 25 mm de flèche), instrumentés par corrélation d'images numériques (DIC) pour suivre les déplacements et déformations à la surface du patch. Les gains sont quantifiés par rapport à une référence acier non renforcée en termes de charge ultime en flexion et de rigidité flexionnelle. Les matériaux comprennent : un acier ASTM A36 caractérisé en traction (E = 202 GPa, Rp0,2 = 282 MPa) ; des stratifiés carbone/époxy (E ≈ 53,4 GPa) et lin/époxy (E ≈ 9,3 GPa) en sergé [0/90] élaborés par infusion sous vide avec la résine partiellement biosourcée SR GreenPoxy 33 ; et trois adhésifs Sika® aux comportements contrastés — Adhésif A : époxy rigide et fragile SikaPower®-1200 ; Adhésif B : acrylate de flexibilité et ductilité intermédiaires SikaFast®-555 L05 ; Adhésif C : polymère modifié silane souple et ductile SikaFlex®-554 (sélectionné au chapitre C). Quatre configurations de patch à cinq plis sont fabriquées : C5 (tout carbone), F5 (tout lin), et les hybrides F3C2 (asymétrique, plis de lin côté adhésif) et CF3C (symétrique). La préparation de surface (sablage jusqu'au « métal blanc », Ra = 1,52 µm, nettoyage à l'isopropanol) et le contrôle du joint (moules imprimés 3D, épaisseur d'adhésif ≈ 2 mm, parallélisme vérifié au bras de mesure FARO®) garantissent la qualité de fabrication ; trois éprouvettes par configuration assurent une excellente répétabilité.

Les résultats démontrent que le choix de l'adhésif est le paramètre dominant du comportement global et du mode de ruine. Avec l'adhésif A, les gains de charge ultime sont les plus élevés (+58 % à +73 %), avec une réponse quasi linéaire jusqu'à une chute brutale de charge : la ruine survient systématiquement par décollement du patch à l'interface acier/adhésif, l'adhésif rigide constituant le maillon limitant. Avec l'adhésif B, les gains sont intermédiaires (+32 % à +45 %) avec une réponse élastique puis ductile ; le mode de ruine bascule vers la rupture du composite à mi-portée, preuve d'un transfert de charge efficace mobilisant pleinement le patch — la configuration B/F3C2, qui n'a pas rompu à 25 mm de flèche, offre le meilleur renforcement (+45 % en charge, +28 % en rigidité). Avec l'adhésif C, très souple, les gains restent modestes (+5 % à +13 %) : la grande complaisance de l'adhésif limite le transfert de déformation vers le patch, conformément aux analyses classiques des renforts collés.

Une modélisation éléments finis 2D en déformations planes (Abaqus/Implicit) complète l'analyse : acier élasto-plastique trilinéaire, composites élastiques isotropes transverses, adhésif A représenté par des éléments cohésifs (loi bilinéaire, critère quadratique, mixité de mode de type Benzeggagh–Kenane), adhésif B par une loi élasto-plastique bilinéaire et adhésif C par une loi hyperélastique de Yeoh. Le modèle est validé par comparaison aux courbes charge–flèche expérimentales (erreur maximale de 11,3 % sur la charge au pic) et aux champs DIC de déplacement et de déformation. L'analyse des contraintes explique les tendances observées : pour l'adhésif A, les contraintes de pelage (jusqu'à 17,4 MPa) et de cisaillement culminent dans les deux premiers millimètres du bord de patch, avec un critère d'amorçage maximal pour A/C5 et minimal pour A/F5 — montrant que le patch tout carbone n'est pas toujours optimal et que les empilements hybrides réduisent les contraintes interfaciales à capacité portante comparable. Les profils de contrainte dans l'épaisseur du patch révèlent en outre une différence fondamentale de transfert de charge : avec l'adhésif B, tous les plis sont tendus dès les faibles charges (transfert immédiat), alors qu'avec l'adhésif C les plis internes sont comprimés (déformation dominée par la flexion propre du patch, transfert retardé).

En conclusion, le chapitre établit un espace de sélection expérimentalement fondé : maximiser le gain avec un époxy rigide expose au décollement interfacial, tandis qu'un adhésif de ductilité intermédiaire déplace le mécanisme limitant vers le composite et permet une mobilisation structurale plus fiable du patch, y compris pour les empilements hybrides. Ces critères de choix d'adhésif et d'architecture de patch sont portés vers l'étude de durabilité du chapitre E.

D.1. Introduction

The objective of this chapter was to evaluate the mechanical improvement of the flexural response of a steel plate by bonding a composite patch to it. The main type of structure from which we were inspired are I-section beams, which can be flexurally strengthened by adhesive bonding of a composite patch to their tensile flange. In externally bonded reinforcements of metallic structures, this strengthening technique is attractive because it is lightweight, does not require thermal input, and can be deployed as a "cold work" repair on a wide range of geometries; however, its performance is often limited by the bonded interface, as the adhesive layer must simultaneously (i) transfer sufficient load to mobilize the stiffness of the composite patch and (ii) withstand the severe peel/cleavage and shear stress concentrations that develop near patch terminations under bending (Smith and Teng 2001; Deng et al. 2004; Stratford and Cadei 2006). This intrinsic trade-off is central to the work presented in this chapter: an adhesive that is sufficiently stiff to ensure efficient stress transfer can promote high interfacial stresses and premature debonding, whereas a more compliant adhesive can reduce edge stress concentrations but may undermine strengthening efficiency by limiting strain transfer to the patch. Following the adhesion screening performed in Chapter C, the present chapter therefore addresses the structural-scale consequence of adhesive choice under a flexural loading of a steel plate representative of strengthened steel flanges, while keeping a specimen-scale framework that preserves experimental repeatability and allows systematic comparison of multiple material configurations.

We propose a specimen scale test, which is still very representative of strengthening performance and adhesion phenomena, and enables the manufacturing of multiple configurations and use of multiple types of materials. The experimental program is built around quasi-static three-point bending tests carried out with progressive loading–unloading cycles, combined with Digital Image Correlation (DIC) to monitor deformation and strain development on the patch surface. The strengthened assemblies are compared to an unstrengthened steel reference to quantify both the ultimate flexural load gain and the flexural rigidity gain.

Consequently, our contribution through this work was to present ways of reducing the interfacial stresses in the adhesive layer. Two ways were chosen: the first was to see how different adhesives with different mechanical properties would accommodate better for the ductile behavior of the steel substrate. The second technique was by trying different layups of composite patch, and how it would influence the interfacial stresses in the adhesive. Three

commercial adhesive systems are therefore studied and consistently referenced as Adhesive A, Adhesive B and Adhesive C, with contrasted stiffness and ductility: SikaPower®-1200 (Adhesive A), a rigid and brittle epoxy; SikaFast®-555 L05 (Adhesive B), a medium-flexibility ductile acrylate; and SikaFlex®-554 (Adhesive C), a flexible and ductile silane modified polymer. On the patch side, four layup configurations are fabricated with a five-ply manufacturing constraint, using carbon/epoxy and flax/epoxy laminates: a refence pure flax F5 patch, a reference pure carbon C5 patch, and two hybrid configurations F3C2 and CF3C, with all bidirectional plies oriented [0/90]. The specimen manufacturing procedure is designed to control the bonding area and adhesive thickness, and the surface preparation is treated as a critical prerequisite to obtain meaningful comparisons, since inadequate preparation can dominate the response by triggering interface-controlled debonding regardless of the intrinsic merits of the adhesive or laminate (Budhe et al. 2017).

Finally, to complement the experimental assessment and to support local stress interpretation beyond global load–deflection curves, this chapter includes a finite element (FE) modelling section. Two-dimensional plane strain models are developed to replicate the quasi-static three-point bending configuration and to analyze stress and strain development in the steel/adhesive/composite assembly. The modelling effort serves two purposes in the thesis narrative: first, to validate that the observed deformation fields measured by DIC are consistent with the assumed material descriptions and boundary conditions; and second, to interrogate the interfacial stress state (peel and shear) and the stress distribution across patch thickness as a function of adhesive type and layup, thereby clarifying why certain combinations fail by debonding while others fail by composite rupture or do not reach failure within the imposed deflection range.

The remainder of the chapter is structured as follows. Sections D.2 and D.3 presents the materials, patch configurations, surface preparation and specimen manufacturing procedures, then the experimental three-point bending methodology is detailed together with the definitions used to quantify strengthening gains and to classify failure modes in Section D.4. The experimental results are then discussed in Section D.5 by separating the effects of adhesive type and patch layup, with emphasis on repeatability, strengthening efficiency, and the transition between patch debonding and composite failure. The FE modelling Section D.6 subsequently provides an interpretation of the measured responses in terms of interfacial stress development

and load-transfer mechanisms. The chapter concludes by consolidating the implications for adhesive selection and patch design for steel strengthening in Section D.7.

Part of the presented work in this chapter has been submitted and is, to this date, under review for publication in the journal “Composite Structures”.

D.2. Materials

D.2.1. Steel substrate

The metallic substrate used in this study is ASTM A36 steel (ASTM A36 2019). Tensile tests were performed in order to characterize the steel material. **Figure 0-1** presents the tensile engineering stress-strain test curves of four steel specimens, and **Table 0-1** presents the obtained mechanical properties in accordance with ASTM standard E8/E8M (ASTM E8 2024) for tensile testing of metallic materials. Strains were monitored using strain gauges.

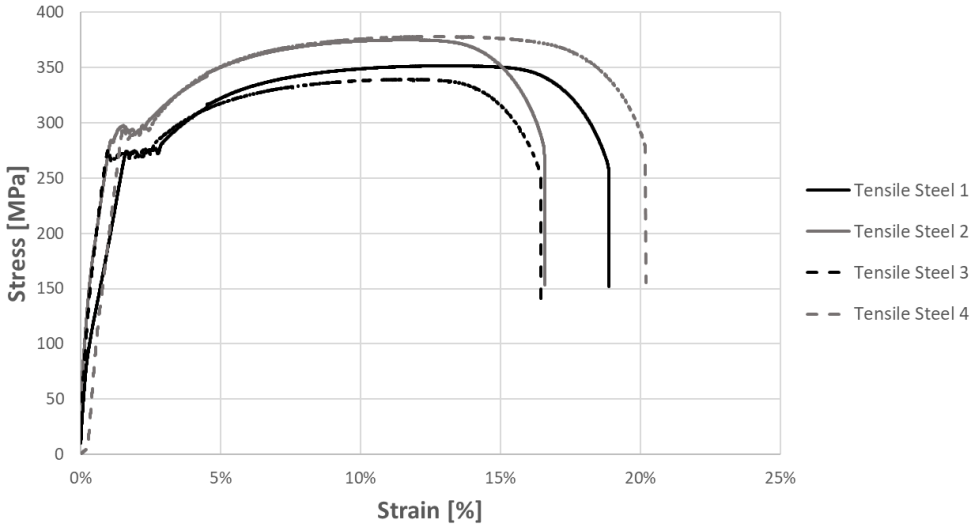

Figure 0-1. Engineering stress-strain curves of tensile tests on steel specimens

Table 0-1. Mechanical properties of ASTM A36 Steel (mean ± standard deviation)

Mechanical properties	ASTM A36 Steel
Young’s modulus E	202 ± 7 GPa
Poisson ratio μ	0.27 ± 0.01
Yield strength $R_{p0,2}$	282 ± 30 MPa
Ultimate tensile strength σ_u	373 ± 7 MPa
Failure strain ϵ_f	18.6 ± 2.4 %

D.2.2. Composite substrate

A 200g/m² 3K carbon fiber twill weave fabric from Composite Distribution® manufacturer, and a 315g/m² flax fiber twill weave fabric from Sicomin® were used as reinforcements for the composite material. The matrix used is the 35% biobased epoxy resin SR GreenPoxy 33 with SD 4773 hardener, also from Sicomin®. All the composite materials were manufactured using a vacuum assisted resin infusion process, in accordance with the supplier's recommendations (Sicomin® GreenPoxy33_sd477x 2023). Specimens of flax/epoxy composite $[0/90]_5$ and carbon/epoxy $[0/90]_5$ were manufactured and tested and their engineering tensile stress-strain curves are presented in **Figure 0-2**. Strains were monitored using strain gauges and a clip-on extensometer for the flax/epoxy composite. **Table 0-2** presents the mechanical properties of the composite materials used in this study, which are obtained in accordance with ASTM D3039 (ASTM D3039 2014) for tensile testing of polymer matrix composites. Given the rectangular geometry of the specimens and the absence of gripping tabs, failure tended to occur near the grips. As a result, the measured ultimate tensile strength and strain likely represent conservative estimates of the material's true performance.

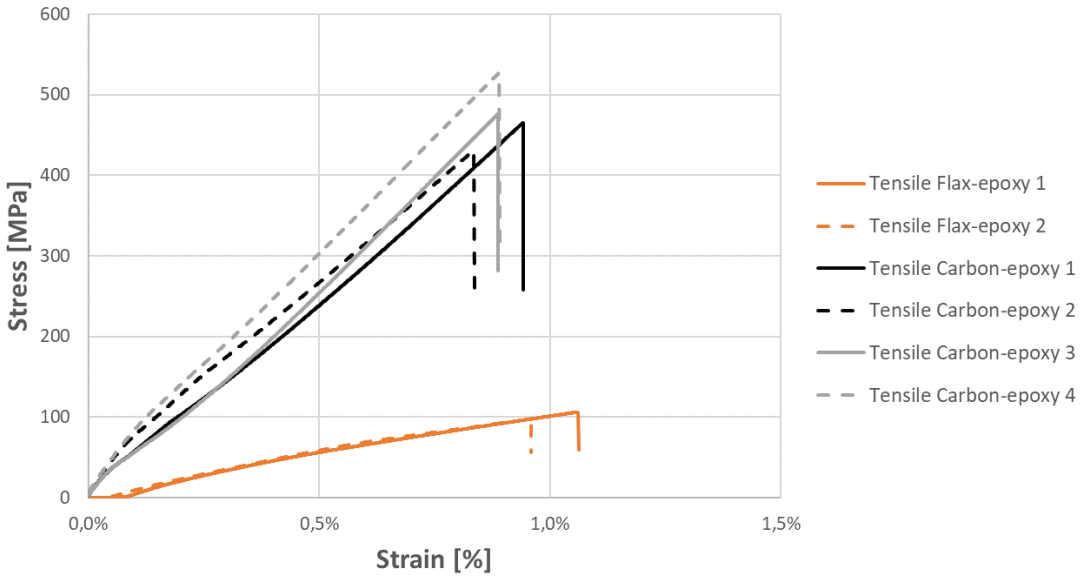

Figure 0-2. Engineering stress-strain curves of tensile tests on FRP specimens

Table 0-2. Mechanical properties of carbon/epoxy and flax/epoxy composites (mean ± standard deviation)

Mechanical properties	**Carbon/epoxy**	**Flax/epoxy**
Young's modulus $E_1 \simeq E_2$	53.4 ± 4.8 GPa	9.3 ± 0.7 GPa
Poisson ratio μ_{12}	0.12 ± 0.02	0.15 ± 0.01

Ultimate tensile strength σ_u	> 475 ± 40 MPa	> 102 ± 6 MPa
Failure strain ϵ_f	> 0.89 ± 0.06 %	> 1.10 ± 0.02 %

D.2.3. Adhesives

Three adhesives supplied by Sika® France, specifically selected owing to their compatibility to steel/composite bonding, were studied in this work:

- SikaPower®-1200: Rigid and brittle Epoxy adhesive (Adhesive **A**).
- SikaFast®-555 L05: Medium flexibility and ductility Acrylate adhesive (Adhesive **B**).
- SikaFlex®-554: Flexible and ductile Silane Modified Polymer (Adhesive **C**).

As shown in **Table 0-3**, these structural adhesives can cover a wide range of mechanical behaviors, from highly flexible and ductile to rigid-brittle. This makes it possible to assess the influence of adhesive type on the induced strengthening behavior. **Table 0-3** summarizes the chosen nomenclatures to designate each adhesive, and presents their relevant mechanical properties based on manufacturer datasheets (Sika®Sikaflex-554 2023; Sika®Sikafast-555-l05 2023; Sika®Sikapower-1200 2023).

Table 0-3. Mechanical properties of Sika® adhesives (based on datasheets (Sika®Sikaflex-554 2023; Sika®Sikafast-555-l05 2023; Sika®Sikapower-1200 2023))

Industrial name	Nomenclature	Young's modulus [MPa]	Tensile strength [MPa]	Tensile lap-shear strength [MPa]	Tensile failure strain [%]	Critical energy release rate G_{Ic} [N/mm]
SikaPower®-1200	A	2600	40	20	3.5	3.5
SikaFast®-555 L05	B	-	11	12	200	-
SikaFlex®-554	C	-	3.5	2.5	500	-

D.3. Specimen manufacturing

The manufacturing process of the steel/composite bonded specimens required three main stages, namely: manufacturing of composite patch configurations, surface preparation of adherends and the final bonding. These operations are detailed in what follows.

Figure 0-3 represents the nominal dimensions and geometry of the specimens.

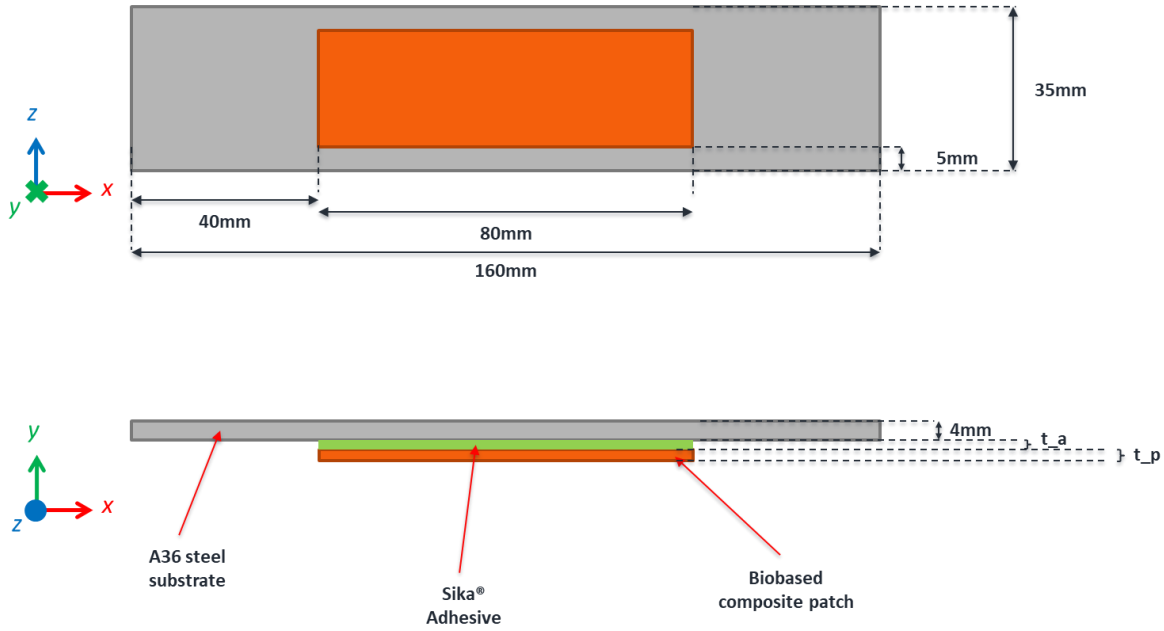

Figure 0-3. Specimen geometry and dimensions.

t_a: thickness of the adhesive, and t_p: thickness of the composite patch

D.3.1. Composite patch configurations

Table 0-4 lists the four patch configurations manufactured. All bidirectional plies are oriented at [0/90] regardless of configuration. Particular attention should be given to configuration F3C2**,** since it is the only asymmetric configuration, the flax fibers are the ones in contact with the adhesive, i.e. closest to the steel adherend.

Table 0-4. Manufactured composite patch layup configurations

Configuration name	Representation	Nominal thickness [mm]	Measured thickness (mean ± standard deviation) [mm]	Number of CFRP plies	Number of FFRP plies
C5		2	1.88 ± 0.21	5	0
F5		3.5	3.46 ± 0.07	0	5
CF3C		2.9	2.72 ± 0.03	2	3
F3C2		2.9	2.78 ± 0.04	2	3

D.3.2. Surface preparation

Surface preparation is the key step before the final structural bonding. It should not be neglected, as poor interfacial adhesion can drastically reduce the mechanical properties of the assembly (Badami et al. 2024). This section describes the thorough surface preparation process of both used adherends.

D.3.2.i Steel adherend

The surface preparation was carried out carefully following three steps:

1. Initial cleaning with isopropyl alcohol, to remove coarse rust stains and contaminants.
2. Sandblasting with SEMANAZ® RUGOS 2000 – 50/80 abrasive.
3. Second cleaning with isopropyl alcohol to remove any traces of grease or residue, to ensure a clean surface ready for adhesive application.

Figure 0-4 shows the visual difference between the steel substrate before and after surface preparation. The surface with higher quality is referred to as “white metal” surface.

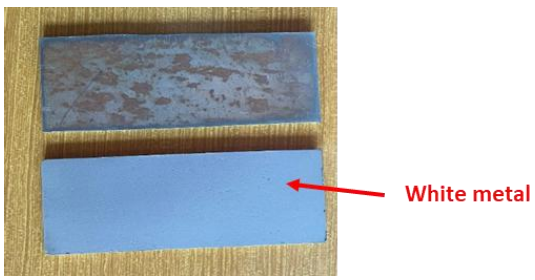

Figure 0-4. Steel substrate before (on top) and after (the white below) surface preparation

The quality of the surface treatment was assessed by roughness analysis using the Keyence® VHX-7000 Series numerical microscope. Roughness measurements were carried out in accordance with the ISO 21920-2:2021 standard on Geometrical Product Specification (GPS) – Surface texture: Profile (ISO 21920-2:2021 2021). **Table 0-5** displays the chosen microscope parameters configured before performing roughness measurements. **Table 0-6** presents the results of roughness analysis on seven steel samples.

Table 0-5. Microscope parameter setting for on-line roughness analysis in accordance with ISO 21920-2:2021

Microscope parameters	**Magnification**	**λ_s Filter**	**λ_c Filter**	**Evaluation length $l_n = 5 \times \lambda_c$**
Values	x500	8µm	2.5mm	12.5mm

Table 0-6. Roughness analysis results

	Arithmetic average roughness R_a [µm]	**Maximum height of the profile R_z [µm]**
Target value (A. Ghumatkar et al. 2016)	1.5 – 2.5	-
Obtained value (mean ± standard deviation)	1.52 ± 0.50	12.35 ± 5.87

D.3.2.ii Composite adherend

Surface preparation of the composite patches involved manual abrasion with Struers® FEPA P#180 sandpaper. The specimens were subsequently cleaned with isopropyl alcohol to remove any surface dust, then left in a fume hood for at least 15 minutes to allow the complete evaporation of isopropyl alcohol prior to bonding.

D.3.3. Bonding process

To develop a high-performance joining structure, controlling the bonding area and the thickness of the adhesive joint is the key procedure when bonding the composite patches to the steel substrates. Control of the bonding area was carried out using two 3D printed molds. Firstly, a 3D printed mold was positioned at the top of the metal to limit the spreading of the adhesive outside the patch ares, as shown in **Figure 0-5**. (a), allowing excess adhesive to be removed. Secondly, the adhesive was applied using a glue gun in the form of a triangular bead, as shown in **Figure 0-5**. (b). The composite patch was then deposited on top of the adhesive (see **Figure 0-5**. (c)), and pressed using 3D-printed U-shaped bracket designed to achieve repeatability over the thickness of the joint, and ensure its parallelism relatively to the steel surface (see **Figure 0-5**. (d)). Adhesive joint thickness control was achieved in accordance with the application methods detailed in the technical data sheets of adhesives (Sika®Sikaflex-554 2023; Sika®Sikafast-555-l05 2023; Sika®Sikapower-1200 2023).

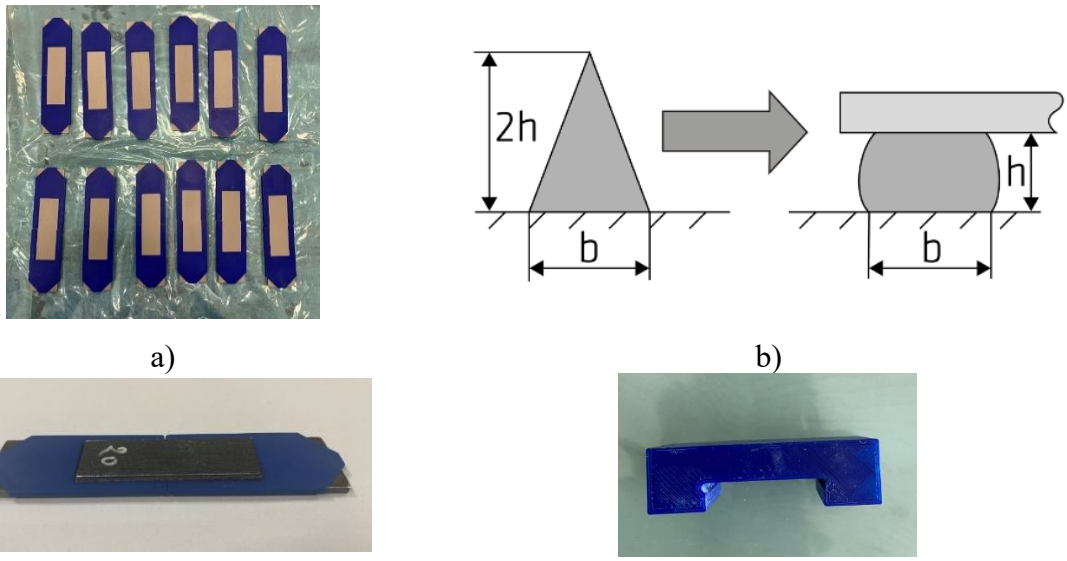

a) b)

c) d)

Figure 0-5. a) Bonding area control using a 3D-printed part, b) Target triangular bead shape of adhesive joint, c) housing of the composite patch in the bonding area and d) 3D-printed U-shaped bracket

A geometric check of the manufactured specimens was carried out using the FARO® G08-02 mechanical arm to measure the thickness of the adhesive joints, and the results are presented in **Table 0-7**. Parallelism measurements between the top planes of composite patches and steel substrates revealed a maximum defect angle equal to 3°19'. This negligible defect in addition to the repeatable joint thickness of around 2mm indicate the high manufacturing quality of all specimens.

Table 0-7. Nomenclature of the test specimens and adhesives thicknesses

Patch layup / Adhesive	F5	C5	F3C2	CF3C	t_adhesive [mm] (Ave +/- STD)
Type A	A/F5	A/C5	A/F3C2	A/CF3C	1.95 ± 0.26
Type B	B/F5	B/C5	B/F3C2	B/CF3C	1.90 ± 0.39
Type C	C/F5	C/C5	C/F3C2	C/CF3C	2.07 ± 0.51

D.4. Experimental methods

The Zwick Z050 universal test machine with a 50kN load cell was used to perform three point bending tests on the specimens. All three point bending tests were carried out in accordance with the ASTM A370 (Standard Test Methods and Definitions for Mechanical Testing of Steel Products), which recommends a constant crosshead speed comprised between 1 and 10 mm/min, and the ASTM D7264 (Standard Test Method for Flexural Properties of Polymer Matrix Composite Materials) (ASTM D7264 2021) recommending a constant crosshead speed comprised between 1 and 5mm/min. Accordingly, four progressive loading-unloading cycles were performed at 5mm/min under loading and 10mm/min under unloading. **Figure 0-6** shows the conceived experimental set-up allowing performance of Digital Image Correlation (DIC) monitoring, together with a graphical representation of loading-unloading cycles imposed.

It can be demonstrated that bonding the composite patch to the steel substrate can enhance its mechanical performance under bending loading by quantifying quantities such as ultimate flexural load and flexural rigidity.

The ultimate flexural load refers to the maximum force recorded during the tests. The ultimate flexural load gain is calculated following **Equation (0-1)**:

$$Ultimate\ load\ gain\ (\%) = \left(\frac{F_u}{F_{u,steel}} - 1\right) \times 100 \qquad \textbf{(0-1)}$$

Where F_u is the ultimate flexural load of a specimen, and $F_{u,steel}$ is the ultimate flexural load of the steel reference specimen.

The flexural rigidity was calculated by linear regression of the force values in the elastic zone during the test. Similarly, the flexural rigidity gain was calculated following **Equation (0-2)**:

$$Rigidity\ gain\ (\%) = \left(\frac{k}{k_{steel}} - 1\right) \times 100 \qquad \textbf{(0-2)}$$

Where k is the flexural rigidity of a specimen, and k_{steel} is the flexural rigidity of the steel reference specimen.

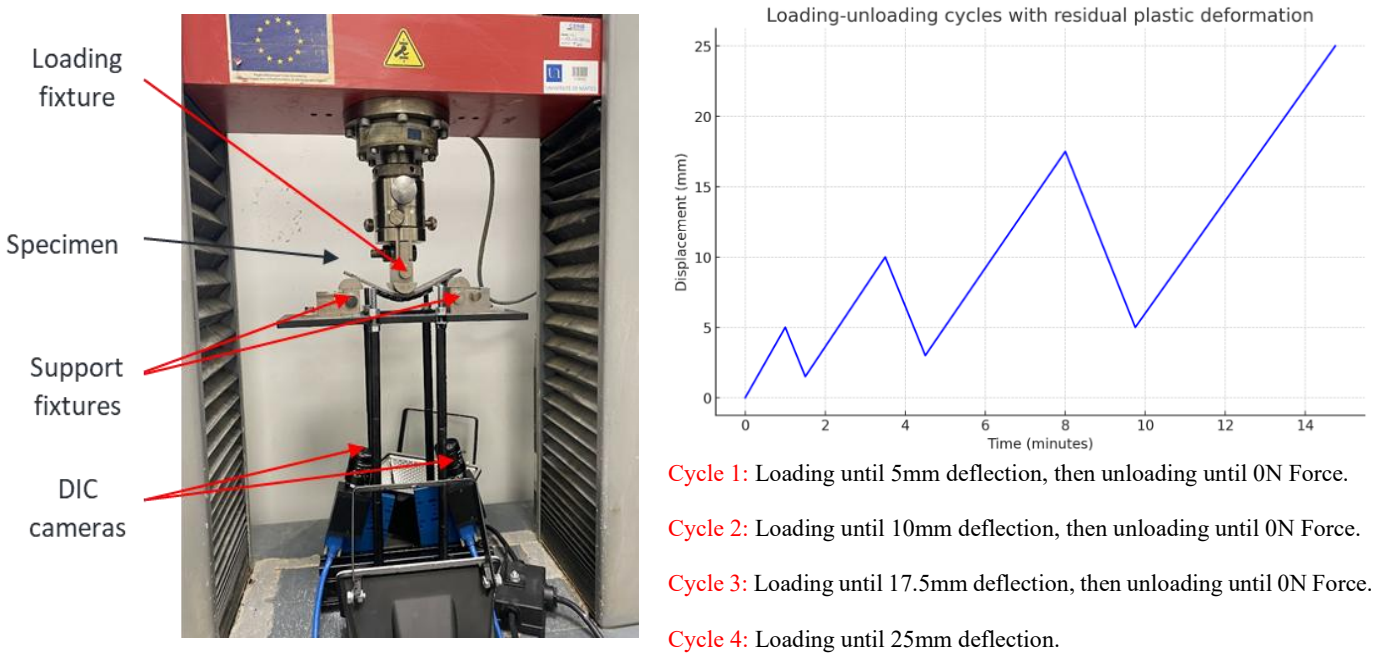

Cycle 1: Loading until 5mm deflection, then unloading until 0N Force.

Cycle 2: Loading until 10mm deflection, then unloading until 0N Force.

Cycle 3: Loading until 17.5mm deflection, then unloading until 0N Force.

Cycle 4: Loading until 25mm deflection.

Figure 0-6. Three point bending test set-up and imposed loading-unloading cycles

Displacements and strains at the outer surface of the composite patch were monitored using two DIC cameras from ISIS correlated solution. The VIC 3D 10 software was used for the post-processing of DIC results. **Figure 0-7** shows a representation of the area of interest (AOI), and data extraction line which is positioned along the 80mm length of the composite patch at mid-width.

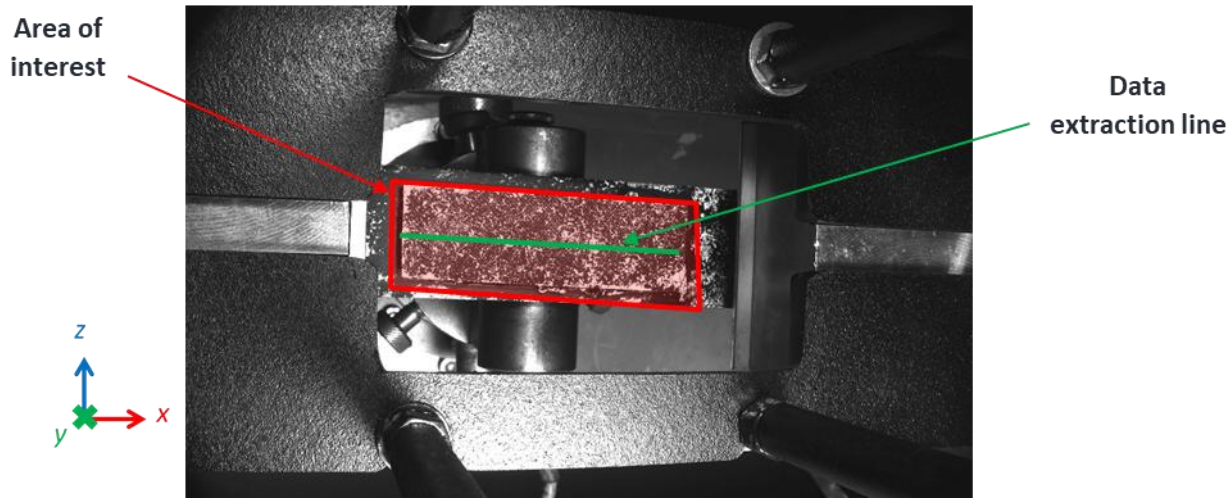

Figure 0-7. Area of interest (AOI) and data extraction line, at the outer surface of the composite patch via DIC monitoring

D.5. Experimental results and discussion

Figure 0-8 shows representative Load-Deflection curves obtained during the three point bending tests, highlighting the influence of each adhesive type, and each of the four composite patch layup configurations. The totality of results of all specimens tested are presented in **Appendix A**. **Table 0-8** summarizes the calculated values of flexural rigidity and ultimate load gains in accordance with **Equations (0-1)** and **(0-2)**, the values of crosshead displacement at failure moment, and failure modes, for each steel-adhesive-patch configuration. A highly satisfying repeatability of results was observed over three tested samples per specimen type. Finally, to better identify the failure modes, **Figure 0-9** and **Figure 0-10** display images of the two primary failure modes observed: patch debonding and composite patch failure. As observed in **Figure 0-9**, composite failure occurs at mid-span, while patch debonding (see **Figure 0-10**) starts at one of the edges of the joint and brutally propagates until arriving at the mid-span location. When patch debonding occurs, a thin cohesive failure can be found on the fracture surface at the steel/adhesive interface, as shown in **Figure 0-10**. (b).

The configurations with adhesive A (rigid and brittle) yields the highest increase in load-bearing capacity (between +58% and +73%) in comparison with the reference steel. All specimen configurations showed a marked linear behavior prior to a sudden load drop (attributed to patch debonding, cf. **Figure 0-10**. (a)), except configuration A/F5 (cf. **Figure 0-8**. (a)), for which a non-linear behavior was observed at the initial stage of loading. This specific mechanical behavior could be the result of the combination of the lower elastic modulus of FFRP in comparison with CFRP, their greater strain to failure, and the intrinsic ductility of steel. The observed differences in behaviors validate the effective load transfer between the steel substrate and the composite patch. However, it should be noted that the rigid adhesive mainly serves the structural role and acts as the limiting factor in the assemblies, as failure occurs at the steel/adhesive interface in all cases.

In the case of joints bonded with adhesive B, a significant increase (between +32% and +45%) in the load-bearing capacity of the strengthened specimens was observed compared to the reference steel specimen. Specimens behave elastically at first, followed by a nonlinear ductile behavior. It should be noted that, with this adhesive, all specimens failed due to composite patch failure at mid-span (cf. **Figure 0-8**. (b)), with the exception of the B/F3C2 configuration which did not fail at the imposed 25mm of deflection. Furthermore, notable difference due to composite configuration is observed in the recorded loads, confirming the effective load transfer between the steel plate and the composite patch layups with this adhesive. B/F5

configuration showed the lowest level of strengthening (+32% in ultimate load and +17% rigidity), followed by B/CF3C (+31% in ultimate load and +20% rigidity) and B/C5 (+32% in ultimate load and +24% rigidity). Finally, B/F3C2 exhibited the highest level of strengthening (+45% in ultimate load and +28% rigidity). Indeed, hybrid configurations have a greater nominal thickness than pure carbon configuration (cf. **Table 0-4**). This geometrical difference explains their comparable or higher flexural loads relative to B/C5 configuration.

Finally, with Adhesive C, a slight increase in load-bearing capacity (between +5% and +13%) was observed compared to the unstrengthened steel reference specimens, while maintaining similar ductile behavior. Only C/C5 and C/CF3C configurations failed at mid span; C/F5 and C/F3C2 configurations did not fail at the imposed 25mm of deflection. This observation can be explained by the lower strain at failure of CFRP plies compared to FFRP ones. Moreover, small difference of strengthening performance was observed between the specimens (cf. **Table 0-8**). Since the adhesive is highly flexible and ductile, it doesn't allow proper load transfer between the steel substrate and the composite patch. This finding is backed-up by multiple interfacial stress studies (Stratford and Cadei 2006; Deng et al. 2004; Smith and Teng 2001), which highlights the capabilities of flexible ductile adhesives to decrease interfacial stress concentrations at the edges of bonded joints, at the expense of stress transfer from the steel substrate to the composite patch.

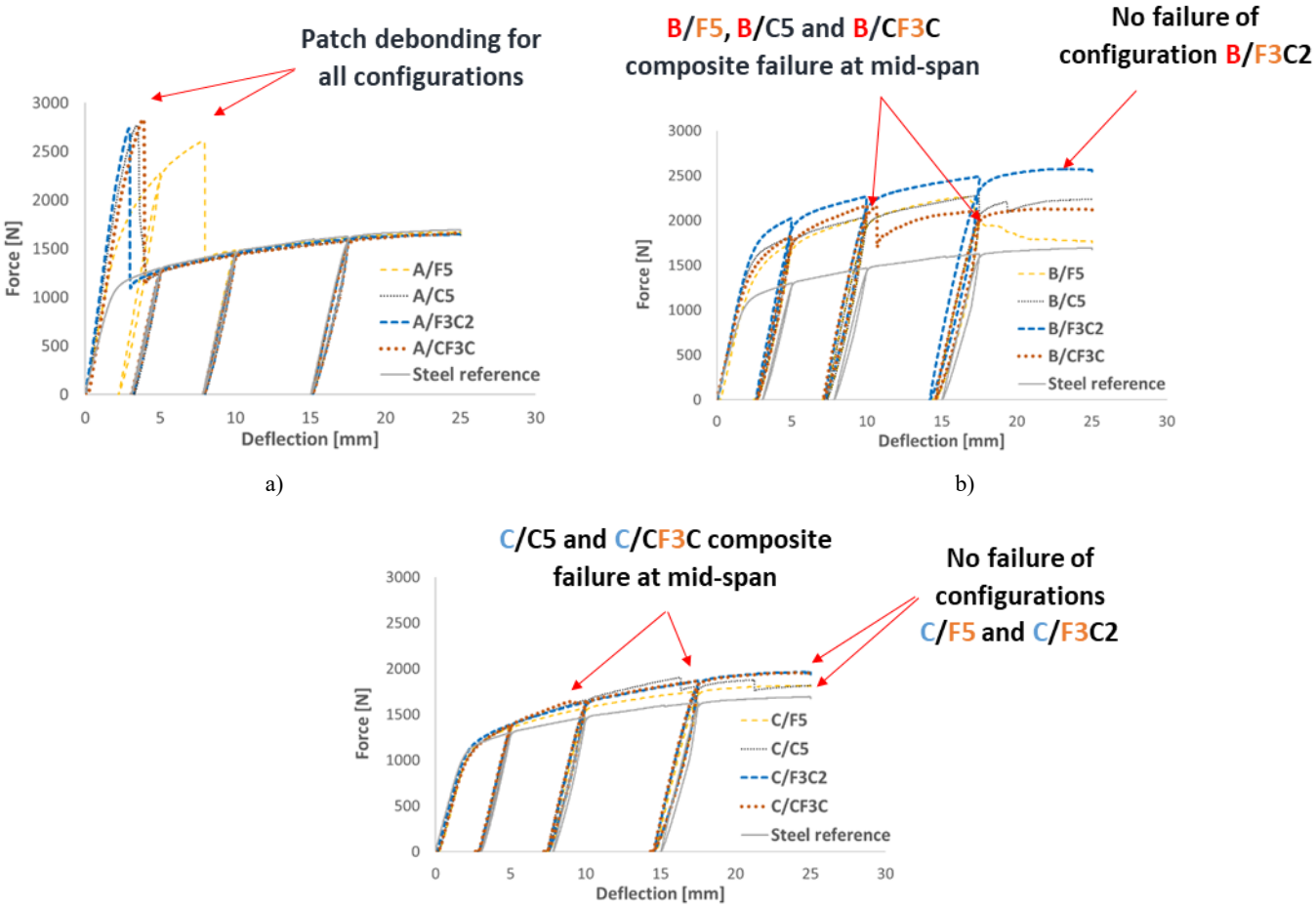

Figure 0-8. Load-deflection curves under three-point bending, regrouped by a) adhesive A, b) adhesive B and c) adhesive C

Table 0-8. Mechanical property gains for bonded assemblies

	Flexural rigidity (mean ±SD) [N/mm]	Flexural rigidity gain [%]	Ultimate flexural load (mean ± SD) [N]	Ultimate flexural load gain [%]	Crosshead displacement at failure [mm]	Mode of failure
Steel (Reference)	609.5 ± 7.1	-	1724.6 ± 29.0	-	-	-
A/F5	798.4 ± 40.2	31.00	2725.2 ± 109.8	58.02	8.2 ± 0.7	Patch debonding
A/C5	1032.0 ± 50.9	69.33	2833.8 ± 55.8	64.32	3.5 ± 0.1	Patch debonding
A/F3C2	1035.6 ± 14.8	69.92	2736.0 ± 18.1	58.65	3.5 + 0.1	Patch debonding
A/CF3C	987.2 ± 35.9	61.97	2978.7 ± 134.0	72.72	3.9 ± 0.1	Patch debonding
B/F5	715.1 ± 19.5	17.33	2279.6 ± 32.1	32.18	20.6 ± 4.0	Patch failure at-midspan
B/C5	757.3 ± 15.2	24.25	2272.9 ± 42.3	31.79	19.2 ± 0.5	Patch failure at-midspan
B/F3C2	779.8 ± 38.4	27.95	2495.9 ± 67.7	44.72	-	No failure
B/CF3C	729.9 ± 19.3	19.76	2256.2 ± 77.9	30.83	11.5 ± 0.8	Patch failure at-midspan
C/F5	620.4 ± 9.3	1.79	1807.5 ± 9.5	4.81	-	No failure
C/C5	613.4 ± 10.5	0.64	1935.9 ± 56.6	12.26	21.2 ± 3.4	Patch failure at mid-span
C/F3C2	628.1 ± 5.9	3.05	1952.9 ± 52.3	13.24	-	No failure
C/CF3C	620.1 ± 7.9	1.73	1953.8 ± 0.7	13.29	9.7 ± 0.7	Patch failure at mid-span



a)

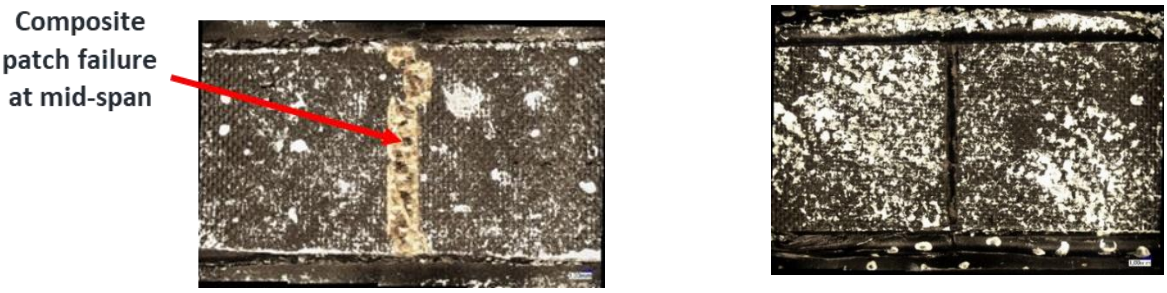

b) c)

Figure 0-9. a) Microscope images of composite failure mode a) side view, b) bottom view with F5 composite configuration and c) with C5 configuration

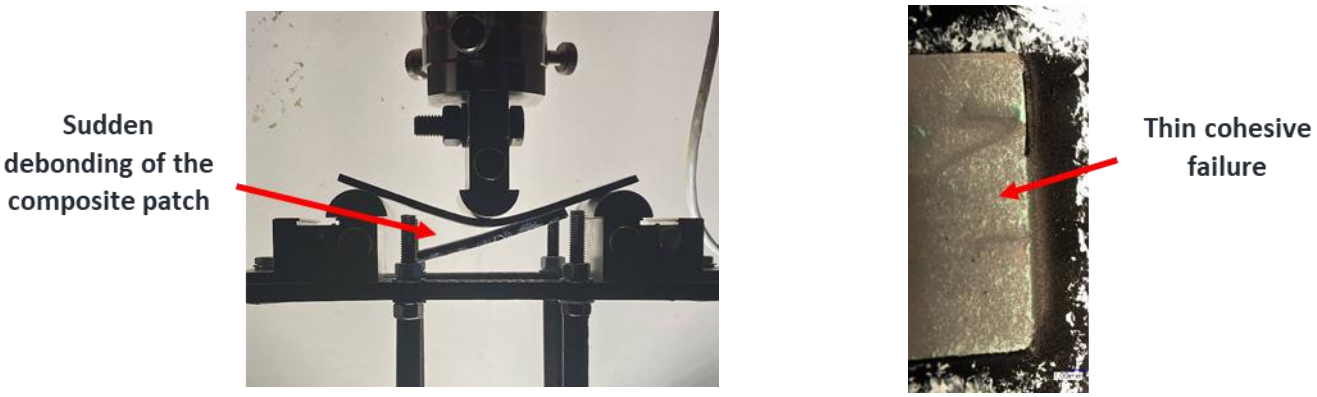

a) b)

Figure 0-10. a) Image of patch debonding failure a) side view and b) thin cohesive failure

Figure 0-11 provides a graphical representation of the mechanical property gains. It can be observed that the influence of adhesive type is usually more significant than that of the composite configuration. Some exceptions can be noted however, in particular A/F5 configuration shows a significantly lower flexural rigidity gain compared to other specimens bonded with adhesive A. Configuration B/F3C2 presents a significantly higher laod and rigidity gain compared to other configurations bonded with adhesive B. Finally, configuration C/F5 shows a significantly lower load gain compared to other configurations bonded with adhesive C.

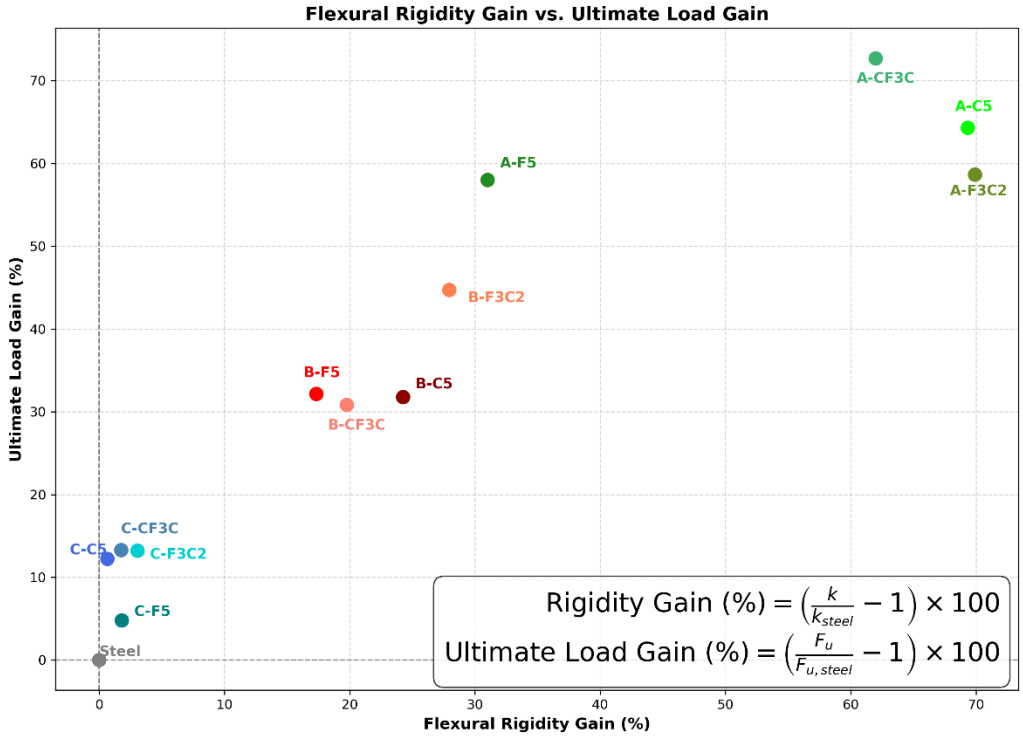

Figure 0-11. Graphical representation of mechanical property gains

D.6. Finite element modeling

D.6.1. Model description

To replicate the performed quasi-static three point bending test, and considering computational efficiency, 2D plane strain finite element analysis models were developed on Abaqus CAE 2024, using Abaqus Standard/Implicit solver. The aim of the models is to help better understand the development of stresses and strains in each part of the steel-adhesive-composite assembly. **Figure 0-12** represents the geometry, boundary conditions and mesh size of the numerical model developed.

Table 0-9 summarizes the different kinds of element types used to model each part of the assembly. Steel part is dominantly meshed with linear quadrilateral elements, and refined linear triangular elements are used in contact region with rigid supports to avoid contact numerical queries. The composite patch is meshed with quadratic quadrilateral elements, since quadratic elements have a better ability to represent curvature with a relatively coarse mesh size. Adhesive A, which fails (cf. **Figure 0-10**) is meshed with cohesive elements. Adhesive B and C, which did not fail, are meshed with quadratic quadrilateral elements. Moreover, since adhesive C is highly flexible and ductile (assumed nearly incompressible), and that it endures large strains, a hybrid formulation has been enabled to ensure convergence and better predict

response of the material (SIMULIA User Assistance 2025). Naturally, a mesh convergence study was performed to guarantee mesh-independent results.

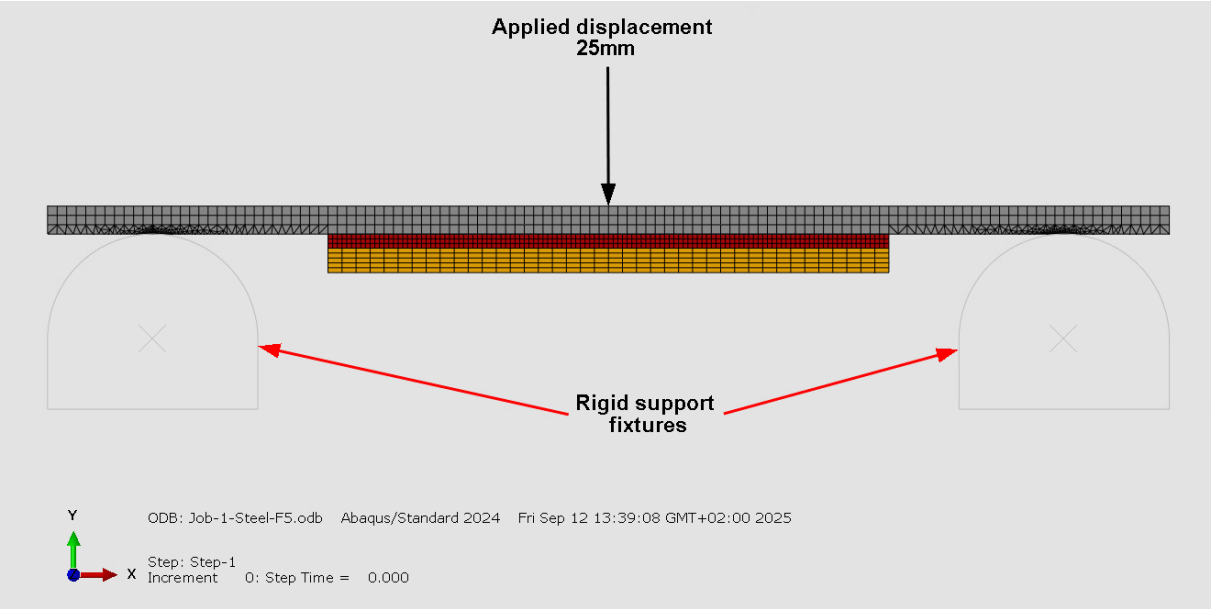

Figure 0-12. Visual representation of the CAE model

Table 0-9. Element types for each part of the assembly

Part	Element type
Steel plate	CPE4R: 4-node bilinear plane strain quadrilateral, reduced integration, hourglass control & CPE3: 3-node linear plane strain triangle
Composite patch	CPE8R: 8-node biquadratic plane strain quadrilateral, reduced integration
Adhesive A	COH2D4: 4-node two-dimensional cohesive element
Adhesive B	CPE8R: 8-node biquadratic plane strain quadrilateral, reduced integration
Adhesive C	CPE8H: 8-node biquadratic plane strain quadrilateral, hybrid, linear pressure
Fixtures	R2D2: 2-node 2D linear rigid link (for use in plane strain)

D.6.2. Material properties and modeling steps

D.6.2.i Steel

The steel substrate is modeled as an isotropic material with a trilinear elastic-plastic stress-strain curve. **Figure 0-13** presents a plot of the von mises stress-strain curve with relevant material properties.

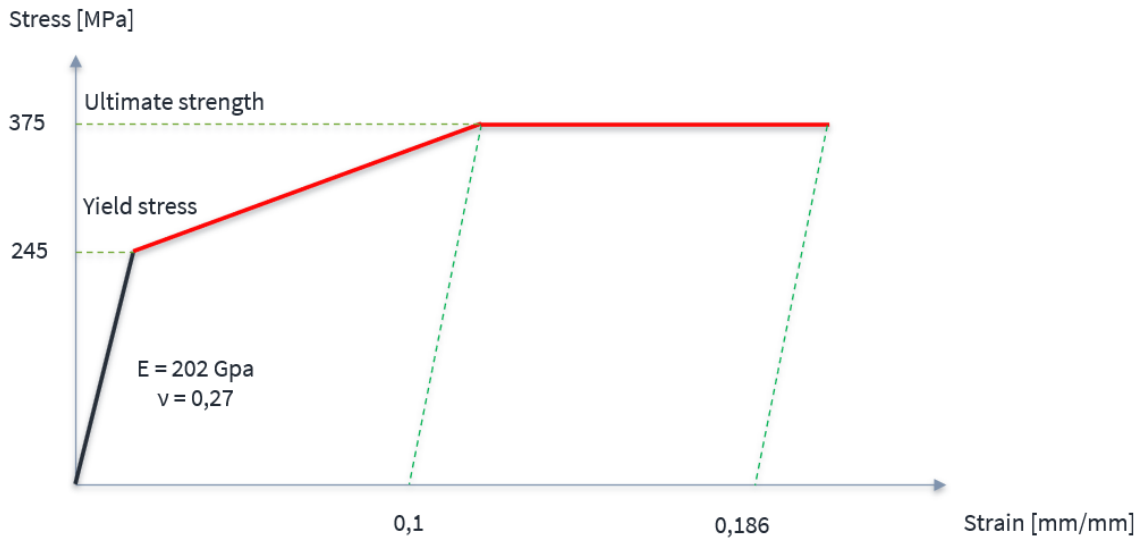

Figure 0-13. Modeling of material behavior of steel

D.6.2.ii Composite patch

The studied composite materials are modeled as elastic transversely isotropic linear materials. **Table 0-10** presents the used engineering constants in the FE model.

Table 0-10. Numerical mechanical properties of carbon/epoxy and flax/epoxy laminates

Mechanical properties	**Carbon/epoxy**	**Flax/epoxy**
[A] Young's modulus $E_1 \simeq E_2$	53.4 GPa	9.3 GPa
[B] Young's modulus E_3	3.45 GPa	3.45 GPa
[A] Poisson ratio μ_{12}	0.12	0.15
[B] Poisson ratio $\mu_{13} \simeq \mu_{23}$	0.378	0.378
[A] Shear modulus G_{12}	23.8 GPa	4.037 GPa
[B] Shear modulus $G_{13} \simeq G_{23}$	1.2 GPa	1.2 GPa

[A] Based on experimental testing results (cf. **Table 0-2**)

[B] Out-of-plane properties were assumed to correspond to the resin mechanical properties reported in the datasheet (Sicomin® GreenPoxy33_sd477x 2023)

D.6.2.iii Adhesive

As mentioned above, three types of adhesives are studied and compared in this work. Considering that these adhesives exhibit different material behaviors – see **Table 0-3**, their modeling protocols differed as well. Adhesive A, which fails by debonding (cf. **Figure 0-10**), is assigned a cohesive bilinear traction-separation law due to its rigid and brittle behavior. The behavior of adhesive B, which did not fail and caused the failure of the composite patch (cf. **Figure 0-9**), has been approached by a bilinear elastic-plastic law due to it medium flexibility and ductility. Finally, the behavior of adhesive C, which did not fail and caused the failure of the patch as well, has been approached by a hyperelastic law to accommodate its high flexibility and ductility. **Table 0-11** presents a summary of the selected modeling strategy for each type of adhesive in Abaqus and their relevant mechanical properties. In addition, the constitutive models of the adhesives are detailed in **Appendix B**. All the material properties of the adhesives are chosen in accordance with values from datasheets (Sika®Sikaflex-554 2023; Sika®Sikafast-555-l05 2023; Sika®Sikapower-1200 2023).

Table 0-11. Numerical mechanical properties of adhesives (based on datasheets)

Adhesive nomenclature	Modeling strategy	Mechanical properties
A	Cohesive elements Quadratic stress damage initiation criterion Energy-based evolution with linear softening, and BK law mix-mode ratio + Tie constraints	K_{nn} = 26 GPa/mm $K_{ss} = K_{tt}$ = 10 GPa/mm t_n^0 = 40 MPa $t_s^0 = t_t^0$ = 20 MPa G_n^c = 0.5 N/mm $G_s^c = G_t^c$ = 1.5 N/mm η = 0.8 – 1.8
B	Bilinear elastic-plastic material + Tie constraints	E = 200 MPa μ = 0.45 σ_y = 6 MPa σ_f = 11 MPa ϵ_f = 200%
C	Hyperelastic bulk material with Yeoh strain energy potential + Tie constraints	C_{10} = 0.755 D_1 = 0.002

D.6.3. Numerical modeling validation

D.6.3.i Load-deflection curves

Load-deflection curves obtained in tests serve as a first basis of comparison and validation of the developed numerical model. **Figure 0-14** shows the comparison between FEM and experimental load-deflection curves for specimens bonded to configuration F3C2. Results for the remaining configurations are presented in **Appendix C**. Except for configuration A/F5 (cf. **Appendix C (b)**), for which the numerical model predicts a failure at 6mm deflection, compared to observed experimental failure around 9mm, a good agreement between the curves can be observed. The maximum relative error on the peak load between the numerical and experimental results was 11.3%, measured for the B/CF3C configuration (cf. **Appendix C (d)**). This comparison serves as a first validation criterion.

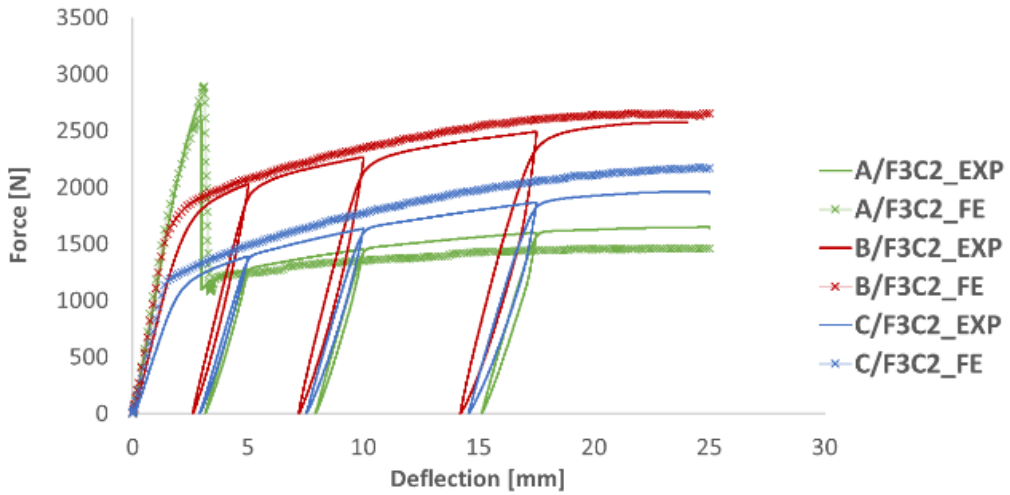

Figure 0-14. Comparison of experimental and FE load-deflection curves for specimens bonded with composite patch configuration F3C2

D.6.3.ii Displacements and strains

Since DIC cameras were used to monitor displacements at the outer surface of the composite patch bonded to the steel plate during three point bending tests, comparison of DIC results with FEM results is discussed here to serve as a second basis of validation of the numerical model prior to stress analysis. **Figure 0-15** represents a comparison of the evolution of out-of-plane displacement W (Y axis, cf. **Figure 0-7**) and first principal in-plane strain ϵ_{11} (X axis, fiber direction) along the 80mm data extraction line shown in **Figure 0-7**, between DIC observations and the FEM modeling results. Results are extracted for different values of crosshead displacement d.

The numerical model accurately captures the composite patch curvature development as observed in **Figure 0-15**. (a), (c) and (e). Naturally, the highest values of tensile strain are in the mid-span of the composite patch as presented in **Figure 0-15**. (b), (d) and (f). It should be noted that when failure occurs (patch debonding or failure at mid-span), DIC strain information is lost, and is subsequently not presented as shown in **Figure 0-15**. (b) and (d). FEM strain results are in good accordance with DIC ones, serving as a second basis of validation.

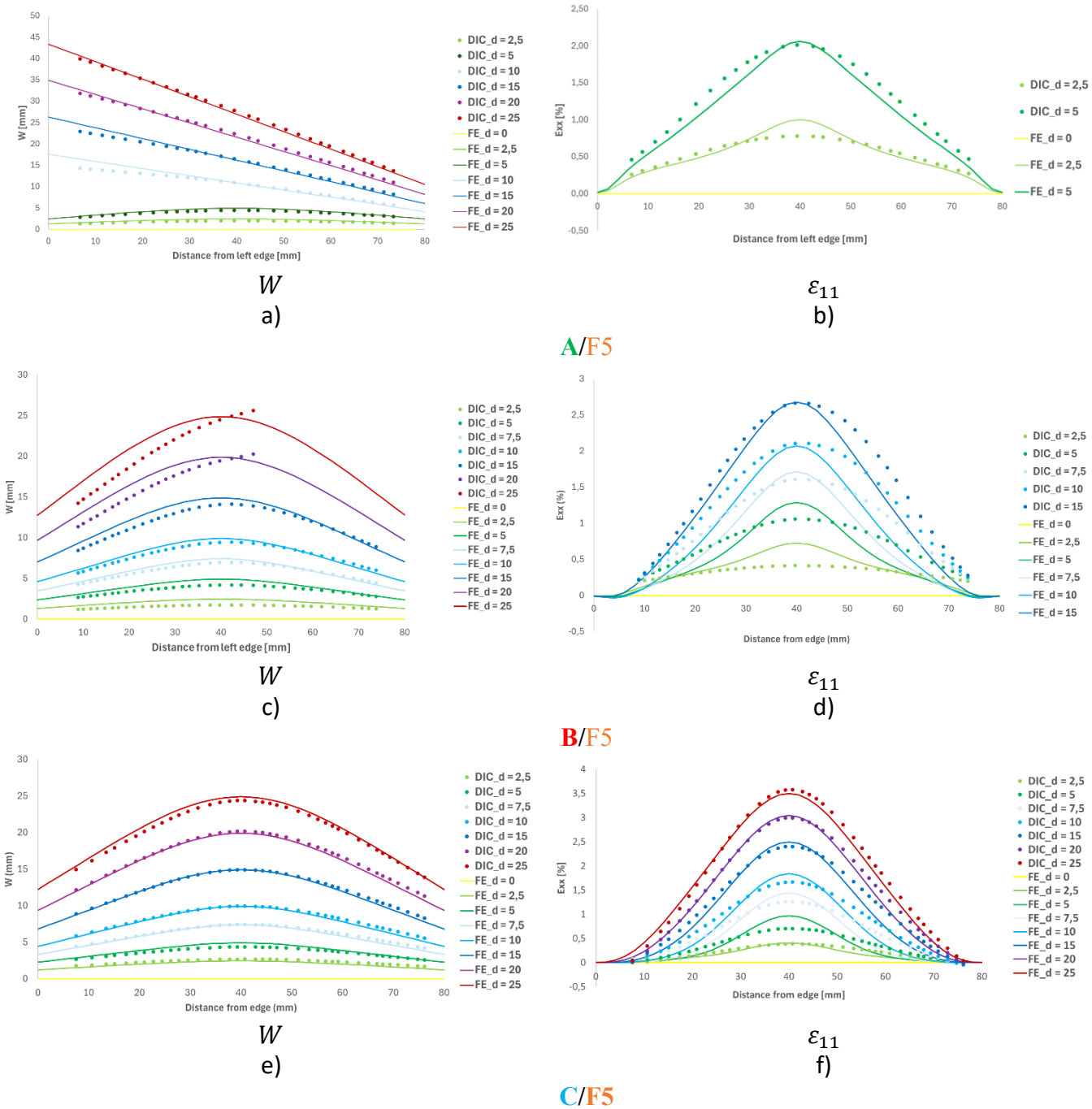

Figure 0-15. Comparison of DIC and FEM out-of-plane displacement W and first principal in-plane strain ϵ_{11} along data extraction line

D.6.4. Stress analysis

To better understand the mechanisms that lead to failure in the composite patches, the stress analysis is focused on the region of the patches that failed during testing. Interfacial stresses at the adhesive bondline is therefore the focus for the configurations bonded with adhesive A, as the failure was at the bondline. For the configurations bonded with adhesives B and C, the failure occurred in the composite substrate, therefore the stress analysis is focused on the composite layers.

D.6.4.i Interfacial stresses (Adhesive A)

Figure 0-16 shows the interfacial peel t_n (Y axis, refer to **Figure 0-12**), shear t_s stresses and damage initiation criterion $QUADS$ values (defined in **Equation (B.2)**) along half of the bond length, starting from the composite patch edge towards mid-span. The results are extracted at 4% of the final imposed displacement, ensuring that no damage has yet initiated in the cohesive elements. Pronounced interfacial stress concentrations are observed at the patch edges, particularly for peel stresses, which exhibit high values (up to 17.4 MPa) within the first 2 mm from the edge, then drop to almost zero stress values in the remaining bondline length (cf. **Figure 0-16**. (a)). This behavior underlines the typical behavior of rigid and brittle adhesives such as adhesive A, and is consistent with analytical models of interfacial stress development in FRP-steel bonded joints (Stratford and Cadei 2006; Deng et al. 2004; Smith and Teng 2001).

In terms of peel stresses in the cohesive layer, illustrated in **Figure 0-16**. (a), results indicate that the highest value is obtained with A/F3C2 configuration (17.4 MPa), followed by A/C5 (15.4 MPa), A/CF3C (14.4 MPa), and finally A/F5 (10.7 MPa). Indeed, it can be discussed that the higher thickness of the flax plies induces a higher bending stiffness of the composite patch, explaining the higher peel stresses of A/F3C2 compared to A/C5.

For shear stresses, presented in **Figure 0-16** b), the ranking differs: cohesive layer reaches the highest peak for A/C5 configuration (15.2 MPa), followed by A/CF3C (11.8 MPa), A/F3C2 (9.3 MPa), and finally A/F5 (6.3 MPa). Indeed, shear stress development in the cohesive layer is governed by the differences of stiffness between the steel adherend and the innermost ply of the composite patch.

Finally, the value of damage initiation criterion, defined in Equation (4) is plotted in **Figure 0-16**. (c). The comparison of value of criterion allows to draw conclusion on the influence of composite patch configuration on the failure initiation. It can be observed from the results that at 4% of final imposed displacement, the highest value of criterion is obtained with A/C5

configuration (0.73), followed by A/CF3C (0.48), A/F3C2 (0.41) and finally A/F5 (0.17). It can be concluded that the application of purely carbon-based patches is not always the optimal solution. As highlighted in previous studies (Wei et al. 2018), the stiff adhesive layer is often the weak link in externally bonded composite reinforcements, and efforts on design of composite bonded patches should be performed to reduce the development of interfacial stresses in the adhesive layer. Consequently, hybrid layups, which produce lower interfacial stresses, with comparable load bearing capacity, may provide a more reliable balance between mechanical strengthening efficiency and environmental impact improvement.

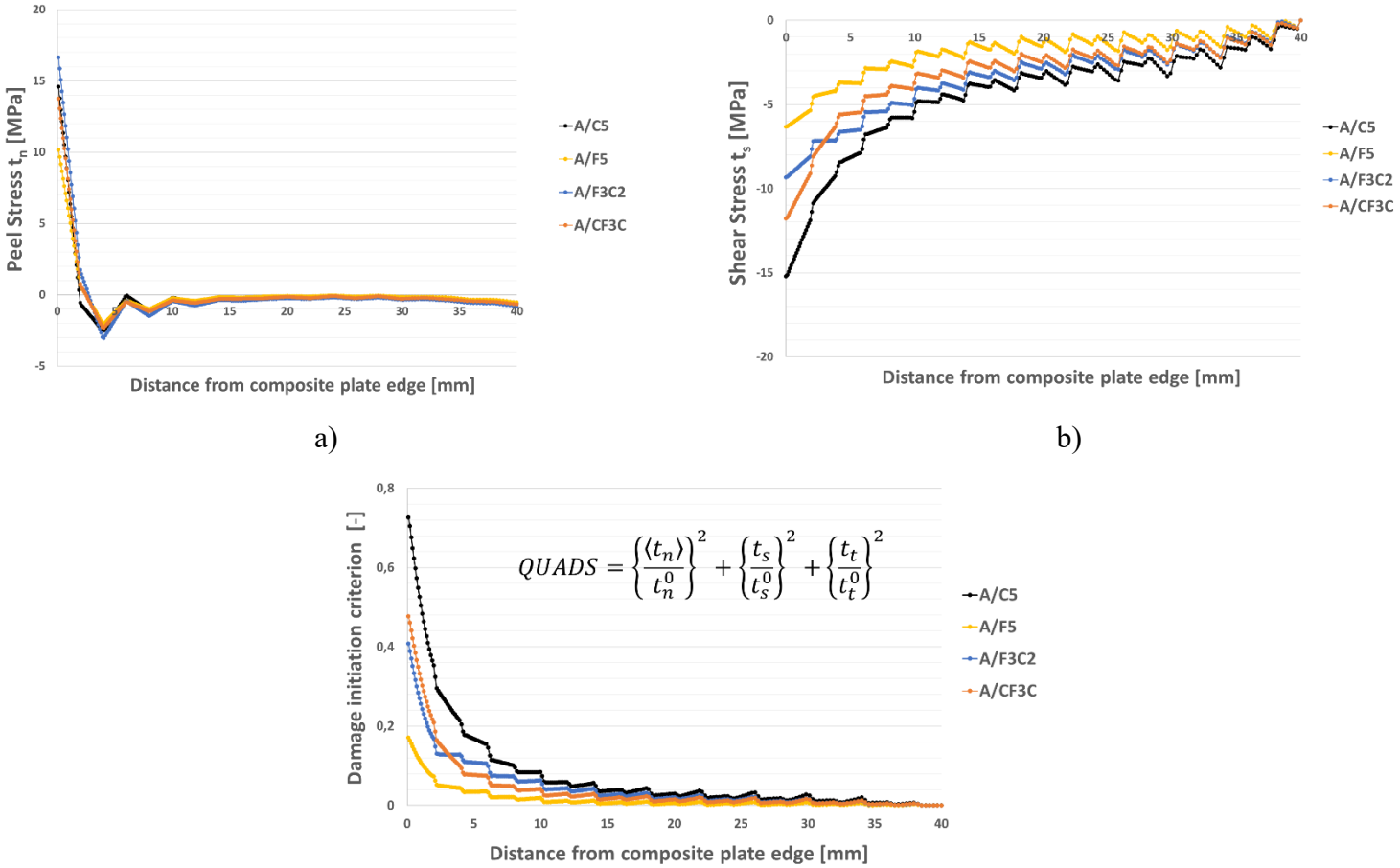

Figure 0-16. a) Peel b) shear stresses, and c) damage initiation criterion along the cohesive elements (Adhesive A) at 4% of final imposed displacement

*D.6.4.ii Evolution of stresses along thickness of composite patch (Adhesive **B** & **C**)*

To further elucidate the role of adhesive properties on strengthening performance, the evolution of longitudinal stresses S_{11} crossing the five plies along the thickness direction of the composite patches, was analyzed at the mid-span location as shown in **Figure 0-17**. Composite plies are numbered from 1 to 5, with Ply 1 being the innermost (adjacent to the adhesive interface) and Ply 5 the outermost. The results, extracted at 5% and 50% of the respective final imposed displacement for each configuration, are presented in **Figure 0-18** and **Figure 0-19**.

a. Stress transfer at early loading stage (5% final imposed displacement)

The stress distributions at lower loading levels shown in **Figure 0-18** reveal fundamental differences in load transfer mechanisms governed by stiffness of the adhesive.

For specimens bonded with the medium-stiffness adhesive B (**Figure 0-18**. (a)), all composite plies are subjected to tensile stresses. This indicates an effective and immediate transfer of tensile strains from the bottom flange of steel substrate, through the adhesive layer, and finally into the composite patch. The sufficient rigidity of adhesive ensures that the patch acts as a true tension flange, contributing to the flexural stiffness of the assembly from the onset of loading.

In contrast, for specimens bonded with the highly flexible adhesive C (**Figure 0-18**. (b)), the stress state is fundamentally different. The innermost plies (1 and 2) experience compressive stresses, while the outermost plies (4 and 5) are under tension. These results are the consequence of the very low shear modulus of adhesive. Instead of being efficiently stretched by the steel substrate, the flexible adhesive layer undergoes significant shear deformation. This allows the composite patch to bend with a local curvature that is decoupled from the global curvature of the steel beam. The patch essentially behaves like a separate, lightly constrained beam resting on a soft foundation, developing its own bending moment and resulting in compression on the inner face and tension on the outer face. This mechanism severely limits the contribution of patch to the overall flexural stiffness at low loads, as validated by the minimal gains in flexural rigidity observed experimentally (**Table 0-8**).

b. Stress state at higher loading stage (50% final imposed displacement)

At 50% of the final imposed displacement (**Figure 0-19**), the results indicate that the composite patches exhibit a relatively similar stress state regardless of the adhesive used. However, the load-bearing capacity of the assemblies differs significantly, as previously shown in **Figure 0-8**. (b) and (c). This confirms that the load-transfer capability of the adhesive is a key parameter

in the design of externally bonded composite patches. This could be influenced by the relatively large thickness of the adhesive layer. Hypothetically, a thinner adhesive bond line would allow for more efficient load transfer to the composite patch. Nevertheless, achieving such thin bond lines is neither straightforward nor generally recommended with this type of adhesive.

c. Performance of hybrid configurations

An insightful observation emerges from analyzing the stresses in the carbon fiber plies of the hybrid configurations. For B/F3C2 and C/F3C2 configurations (carbon plies positioned as Plies 4 and 5), the stress in the carbon layers at 5% load is higher than that in the outer plies of the all-carbon B/C5 and C/C5 configurations (cf. **Figure 0-18**. (a) and (b)). This demonstrates that in the hybrid design, the stiffer carbon fibers effectively carry the load immediately, leveraging their position further from the neutral axis. As loading progresses, the stresses in the B/C5 and C/C5 configurations surpass those in the hybrids (cf. **Figure 0-19**. (a) and (b)), indicating that the higher overall stiffness of the pure carbon patch accelerates stress development. This analysis confirms the structural efficiency of the hybrid design: the carbon fibers play their primary load-bearing role effectively, while the flax plies provide the necessary thickness to position them optimally and contribute to a more gradual stress transfer.

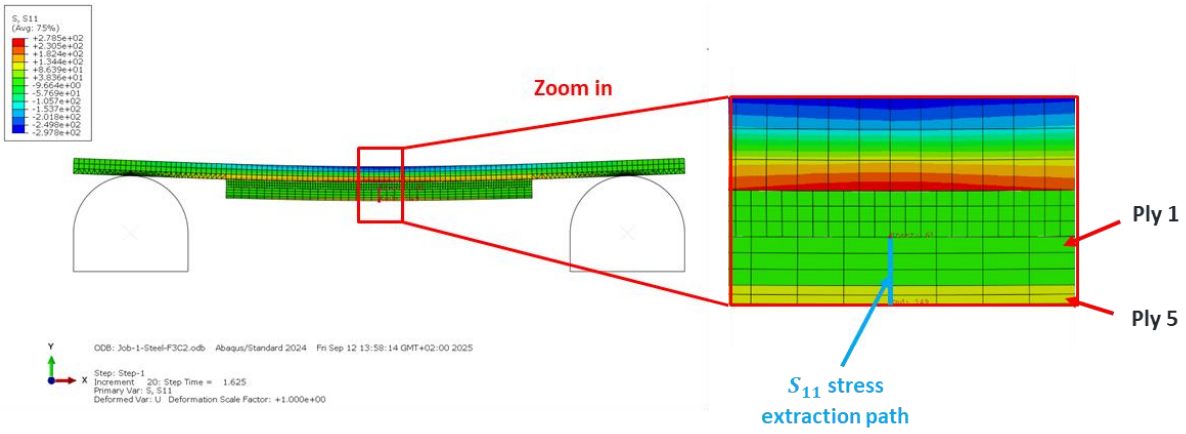

Figure 0-17. Visualization of data extraction path and ply numbering

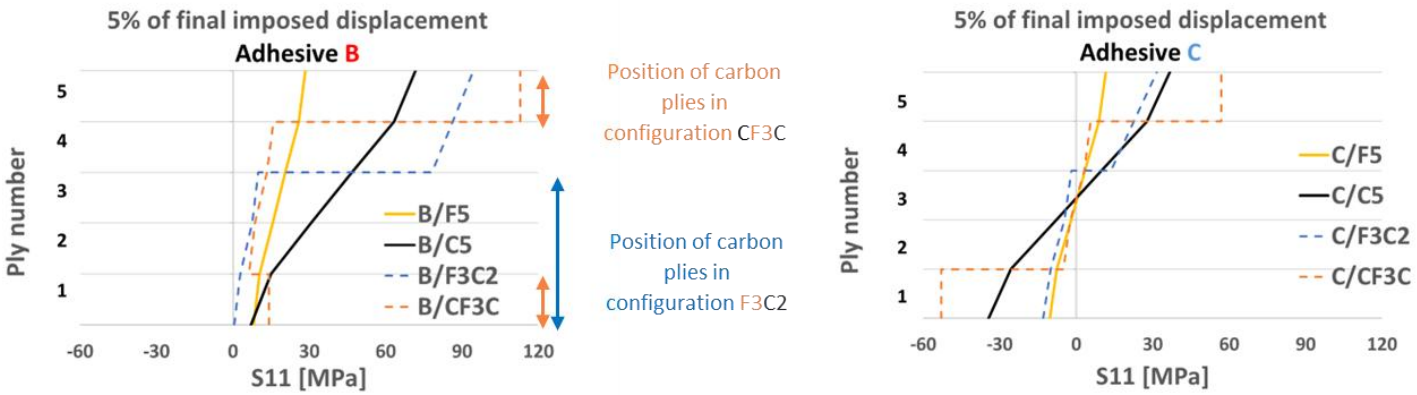

a) b)

Figure 0-18. Longitudinal stresses S11 at 5% of final imposed displacement a) adhesive B b) Adhesive C

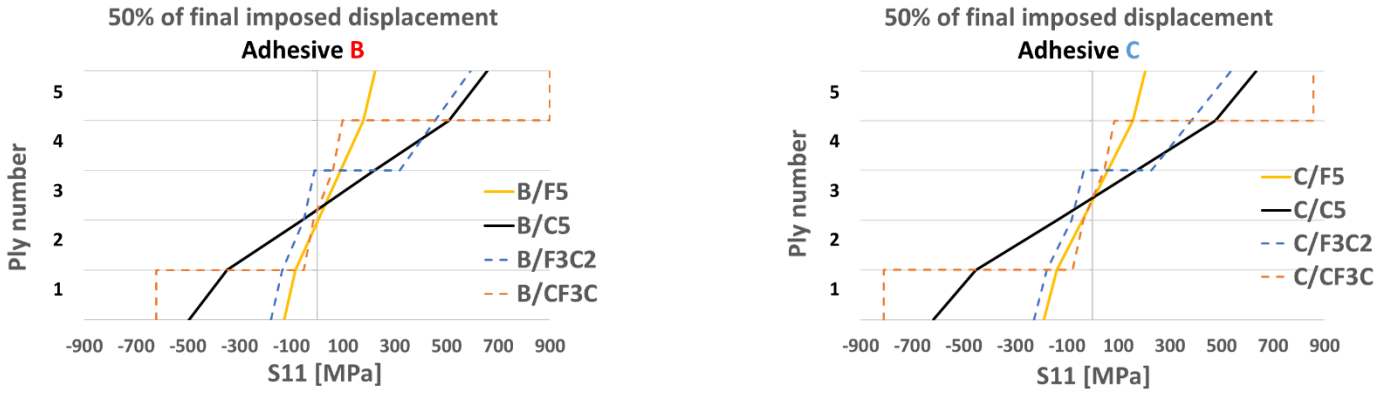

a) b)

Figure 0-19. Longitudinal stresses S11 at 50% of final imposed displacement a) adhesive B b) Adhesive C

D.7. Conclusion

This chapter evaluated the flexural strengthening of steel plates by externally bonded composite patches, with the specific objective of clarifying how adhesive mechanical properties and hybrid flax/carbon patch layups govern strengthening efficiency, repeatability, and failure mechanisms. A specimen-scale three-point bending protocol, combining progressive loading–unloading cycles with DIC monitoring, provided a representative yet controlled framework to compare three adhesive systems (SikaPower®-1200, SikaFast®-555 L05, SikaFlex®-554) and four patch configurations (carbon/epoxy, flax/epoxy, and hybrid flax/carbon laminates). A highly satisfying repeatability of results was observed over three tested samples per specimen type, allowing the observed trends to be attributed to material and design variables rather than experimental scatter.

The experimental results confirmed that adhesive choice is the dominant parameter controlling global strengthening response and the governing failure mode. Assemblies bonded with Adhesive A (rigid and brittle epoxy) achieved the highest ultimate load gains, reported between +58% and +73%, depending on patch configuration, and relative to the unstrengthened steel reference, with an essentially linear response up to a sudden load drop attributed to patch debonding. With this adhesive, failure occurred at the steel/adhesive interface in all cases, indicating that the strengthened response was ultimately limited by interfacial integrity under bending-induced edge stresses rather than by the capacity of the composite patch itself. The A/F5 configuration exhibited a distinct initial nonlinearity compared to the other A-configurations, which the chapter relates to the combined effects of the lower elastic modulus and higher strain-to-failure of FFRP relative to CFRP, together with the intrinsic ductility of the steel substrate; this response nevertheless remained governed by interfacial debonding.

In contrast, assemblies bonded with Adhesive B (medium flexibility and ductility acrylate) exhibited intermediate but substantial strengthening, with ultimate load gains reported between +32% and +45%, and a characteristic transition from an initial elastic stage to a nonlinear ductile response. Importantly, with Adhesive B the dominant failure mode shifted from interfacial debonding to composite patch failure at mid-span for all configurations except B/F3C2, which did not fail within the imposed 25 mm deflection. This change in failure mechanism demonstrates that, within the studied surface preparation and manufacturing conditions, Adhesive B enables effective load transfer such that the patch becomes mechanically mobilized and can reach its own strength limit. The chapter further reports that,

for Adhesive B, composite configuration measurably influenced the recorded loads, consistent with a genuine structural contribution of the patch architecture. Within this set, B/F3C2 provided the highest strengthening (+45% ultimate load and +28% rigidity), whereas B/F5 showed the lowest strengthening level (+32% ultimate load and +17% rigidity), and the hybrid configurations exhibited comparable or higher loads relative to the carbon configuration, partly explained by their greater nominal thickness compared to the pure carbon configuration.

Assemblies bonded with Adhesive C (flexible and ductile SMP) exhibited the lowest strengthening efficiency, with ultimate load gains limited to +5% to +13% and a global response that remained close to the ductile behavior of the unstrengthened steel. Only C/C5 and C/CF3C failed at mid-span, while C/F5 and C/F3C2 did not fail within the imposed 25 mm deflection. In this case, the limited sensitivity to patch configuration and the modest strengthening levels support the conclusion that the high compliance of Adhesive C restricts strain transfer between the steel substrate and the composite patch. This observation is consistent with established analyses of bonded reinforcements showing that more flexible adhesives can reduce stress concentrations at joint edges but do so at the expense of efficient stress transfer to the reinforcement (Smith and Teng, 2001; Deng et al., 2004; Stratford and Cadei, 2006). The global comparison across all configurations further reinforced this conclusion, as the chapter explicitly notes that adhesive type generally has a more significant influence than composite configuration on strengthening gains, with only a few notable exceptions (e.g., A/F5, B/F3C2, C/F5).

The FE modelling developed in this chapter added stress interpretation to these experimental findings by reproducing load–deflection trends and by providing access to interfacial stress fields and through-thickness stress distributions in the patch. The numerical validation against experimental load–deflection curves and DIC-derived curvature/strain development supported the consistency of the adopted modelling assumptions for the strengthened assemblies. Stress analyses then clarified why Adhesive A promoted debonding: interfacial peel and shear stresses peaked near patch ends, and their magnitudes varied with patch configuration, with the chapter reporting specific rankings and peak values for peel and shear stresses at the cohesive layer along the bond length. Complementarily, through-thickness stress profiles at mid-span revealed a fundamental difference in load-transfer mechanisms between Adhesives B and C at low loading levels: with Adhesive B, all plies were in tension, indicating immediate strain transfer from steel to patch, whereas with Adhesive C the innermost plies experienced compressive stresses while outer plies were in tension, reflecting bending-dominated deformation of the

patch with delayed or reduced strain transfer across the compliant adhesive. These results provide a coherent explanation for the experimentally observed trade-off between strengthening efficiency and interfacial stress mitigation across the adhesive set.

From the perspective of the thesis narrative, Chapter D establishes an experimentally grounded selection space for bonded steel–FFRP strengthening. It indicates that maximizing strengthening gains with a rigid epoxy adhesive can drive the assembly toward interface-controlled debonding, whereas a medium-ductility adhesive can shift the limiting mechanism to composite failure and thereby unlock more reliable structural mobilization of the patch, including for hybrid layups. These outcomes directly constrain the adhesive choices and interface assumptions that will be carried forward when interpreting strengthened behavior and failure scenarios in subsequent developments.

E. Hygro-Mechanical Behavior of Hybrid Flax/Carbon Composites and Their Modeling Through the Thermal/Diffusion Analogy in FEM Framework

Content

E. Hygro-Mechanical Behavior of Hybrid Flax/Carbon Composites and Their Modeling Through the Thermal/Diffusion Analogy in FEM Framework 159
Résumé du chapitre en Français 160
E.1. Introduction 163
E.2. Materials and specimen manufacturing 166
E.3. Experimental methods 167
E.3.1. Gravimetric tests 167
E.3.2. Characterization of water diffusion kinetics 167
E.3.2.i Fick's model 167
E.3.2.ii General 3D solution 168
E.3.2.iii Proposed analytical solution for quasi-isotropic materials (bidirectional fabric reinforced polymers) 169
E.3.2.iv Method of identification of diffusion constants 170
E.3.3. Characterization of hygroscopic behavior 170
E.3.4. Flexural tests 171
E.4. Experimental results and discussions 173
E.4.1. Water diffusion kinetics 173
E.4.2. Hygroscopic behavior 176
E.4.3. Three-point bending 178
E.5. Numerical modeling 180
E.5.1. General scheme for Hygro-mechanical FEA of FRP materials 180
E.5.1.i Mono-material case: thermal/stress-diffusion/stress direct analogy 182
E.5.1.ii Multi-material case: thermal/stress-diffusion/stress indirect analogy 183
E.5.2. Hygro-mechanical FEM model 185
E.5.3. Hygro-mechanical FEM results 188
E.5.4. Three point bending FEM results 193
E.6. Conclusion 196

Résumé du chapitre en Français

Ce chapitre évalue le comportement hygro-mécanique des stratifiés lin/époxy, carbone/époxy et hybrides lin/carbone, et en propose une modélisation par éléments finis fondée sur l'analogie thermique–diffusion. Les composites lin/époxy ayant été utilisés comme matériau structural au chapitre D, il était indispensable d'évaluer leur comportement en milieu humide dans le cadre de la thèse : les propriétés des constituants polymères évoluent sous exposition à l'eau, et ces changements à l'échelle du matériau peuvent se traduire, à l'échelle structurale, par une modification du transfert de rigidité, des distributions de contraintes et des scénarios de ruine des assemblages acier–PRF collés — en particulier pour les stratifiés à base de lin, dont la nature hydrophile des fibres végétales favorise une affinité à l'eau bien supérieure à celle des renforts synthétiques. L'objectif est aussi de déterminer si l'hybridation, introduite au chapitre D pour des raisons d'efficacité structurale et de gestion des contraintes interfaciales, modifie également la sensibilité environnementale à l'échelle du matériau. Une partie de ces travaux est destinée à une soumission dans la revue Composites Part B: Engineering.

Quatre configurations de stratifiés à dix plis, exclusivement orientés [0/90], ont été fabriquées par infusion sous vide (résine époxy biosourcée à 38 % SR InfuGreen 810, sergés de carbone 280 g/m² et de lin 315 g/m², cuisson 24 h à température ambiante puis post-cuisson 24 h à 40 °C) : C10 (tout carbone), F10 (tout lin), l'hybride asymétrique F6C4 (6 plis de lin + 4 plis de carbone) et l'hybride symétrique C2F6C2 (2 carbone / 6 lin / 2 carbone). Des éprouvettes rectangulaires de 80 × 25 mm ont été découpées pour l'ensemble des essais.

Le programme expérimental comprend quatre volets. Premièrement, des essais gravimétriques en immersion dans l'eau déminéralisée à 50 °C (température accélératrice mais suffisamment inférieure à la Tg de la résine ≈ 71 °C), après séchage préalable de 14 jours, avec pesées régulières selon la norme ISO 62 jusqu'à saturation. Deuxièmement, l'identification des paramètres de diffusion par un modèle de Fick tridimensionnel (solution analytique de Crank) : le travail portant sur des tissus bidirectionnels, une hypothèse de quasi-isotropie dans le plan ($D_x = D_y$) est adoptée et justifiée par la littérature, et les paramètres sont identifiés par moindres carrés entre courbes expérimentales et solution analytique. Troisièmement, la mesure du gonflement hygroscopique dans les trois directions principales, au moyen d'un capteur laser de déplacement monté sur un bâti imprimé en 3D (directions du plan) et d'un micromètre (épaisseur), la déformation hygroscopique étant reliée linéairement à la teneur en eau par des coefficients d'expansion hygroscopique β, en analogie directe avec la dilatation thermique.

Quatrièmement, des essais de flexion trois points (portée 60 mm, 5 mm/min, d'après ISO 14125) avant et après vieillissement, avec détermination du module de flexion.

Les résultats expérimentaux révèlent un contraste marqué entre les deux stratifiés de référence. Le C10 absorbe très peu d'eau (Csat = 1,51 %, Dz = $2{,}05 \cdot 10^{-7}$ mm²/s) tandis que le F10 présente une absorption rapide et massive (Csat = 12,03 %, Dz = $2{,}62 \cdot 10^{-6}$ mm²/s), la forte anisotropie de diffusion ($D_x \gg D_z$) reflétant dans les deux cas l'architecture stratifiée, les plis constituant des chemins préférentiels de diffusion dans le plan. Les hybrides saturent autour de 8–9 % ; une loi des mélanges basée sur les fractions volumiques de plis estime leurs paramètres effectifs, avec une légère surestimation attribuée aux zones riches en résine aux interfaces, non prises en compte par ce modèle simplifié. Le gonflement hygroscopique du F10 est fortement anisotrope : contraction dans le plan ($\beta_{xx} \approx \beta_{yy} \approx -0{,}09$, effet de type Poisson lié au gonflement radial des fibres) et gonflement d'épaisseur prononcé ($\beta_{zz} = 0{,}895$), alors que le C10 reste quasi stable dimensionnellement, avec des déformations d'un ordre de grandeur inférieur, gouvernées par la seule matrice. En flexion, le C10 conserve après vieillissement une réponse fragile quasi inchangée (module : −6,3 %), tandis que le F10 subit une dégradation sévère : baisse de la contrainte maximale, forte augmentation de la déformation à rupture — transition d'un comportement fragile vers un endommagement ductile et progressif — et chute du module de flexion de plus de la moitié (−53,6 %), imputable à la plastification de la matrice, au gonflement des fibres et à l'affaiblissement de l'interface fibre/matrice.

Le volet numérique développe un cadre éléments finis de couplage séquentiel diffusion–mécanique dans Abaqus/Standard, exploitant l'analogie thermique–diffusion (loi de Fourier ↔ seconde loi de Fick, dilatation thermique ↔ gonflement hygroscopique). Si cette analogie est directe pour les mono-matériaux, la teneur en eau est en revanche discontinue aux interfaces entre matériaux de saturations différentes : le chapitre adopte donc le concept de « wetness fraction » (fraction d'humidité $w = c/C_{sat}$), issu de la microélectronique, qui rétablit la continuité du champ moteur aux interfaces moyennant une adaptation des paramètres d'entrée (conductivité analogue à $D \cdot C_{sat} \cdot \rho$, capacité analogue à Csat) et un post-traitement de reconversion en teneur en eau — la contribution originale étant l'implémentation et la validation de cette formulation dans un logiciel éléments finis, avec le code Python fourni en annexe. Un modèle 3D au quart d'éprouvette (éléments DC3D8 puis C3D8, maille de 0,35 mm, immersion simulée d'environ trois mois) est calibré uniquement sur les propriétés identifiées des stratifiés de référence, les hybrides étant simulés sans recalage afin d'éprouver la capacité prédictive ; les constantes élastiques dépendent du champ d'humidité par interpolation linéaire entre états sec

et saturé. Les résultats numériques reproduisent les cinétiques gravimétriques des quatre configurations — dont l'absorption plus lente du C2F6C2, ses peaux carbone faisant écran à la diffusion vers le cœur de lin — et prédisent de forts gradients d'humidité et effets de bord dans le F10, la non-saturation du C10 à trois mois, ainsi que la courbure induite par l'humidité de l'hybride asymétrique F6C4 (le sous-stratifié carbone bridant le gonflement du sous-stratifié lin, générant un moment de flexion interne), observée expérimentalement, tandis que la symétrie du C2F6C2 convertit ce même mécanisme de bridage en un champ de contraintes auto-équilibré sans courbure prononcée.

En conclusion, le chapitre montre que la sélection de matériaux pour le renforcement de l'acier ne peut reposer sur les seules adhérence initiale et performances mécaniques à l'état sec : les propriétés du patch riche en lin ne peuvent être supposées invariantes dans le temps en service humide, l'hybridation gouverne la conversion des déformations hygroscopiques en courbure ou en contraintes internes, et le cadre de modélisation validé fournit une base pour intégrer champs d'humidité et propriétés dépendantes de l'humidité dans les futures simulations de durabilité des assemblages multi-matériaux collés.

E.1. Introduction

Since flax/epoxy composites have been used as a structural material in Chapter D, it seemed unreasonable to not assess their behavior in moist environment, within the framework of the thesis.

Indeed, the main driver of the work performed in Chapter E was to evaluate the hygro-mechanical behavior of flax/epoxy and carbon/epoxy composites, and to understand whether the hybrid configurations used in Chapter D could provide any positive effects on hygro-mechanical response. Polymer-based constituents (composite patch and adhesive) properties can evolve under moisture exposure. From a structural perspective, moisture-driven changes at the material scale can translate into modified stiffness transfer, altered stress distributions, and potentially different failure scenarios in bonded steel–FRP assemblies, especially for flax-based laminates where the hydrophilic nature of plant fibers is known to promote higher moisture affinity than synthetic reinforcements (Saidane et al. 2016; Djellouli et al. 2021). As a result, beyond the initial adhesion screening of Chapter C and the mechanical strengthening assessment of Chapter D, a dedicated chapter at the composite-material scale is needed to quantify how fast and how much moisture is absorbed, the hygroscopic strains induced by this absorption, and the extent to which flexural mechanical behavior is altered by hygrothermal ageing.

To address these points, a thorough experimental program was performed, starting with gravimetric tests, identification of diffusion constants, monitoring of swelling behavior, and finally characterizing flexural behavior before and after ageing through three-point bending tests. Gravimetric monitoring follows the general framework of moisture uptake quantification in polymers and FRPs, where transport is often reasonably approximated by Fick's diffusion model for many epoxy-based systems over relevant ranges of exposure conditions (Fick 1855). In this chapter, the diffusion problem is formulated through Fick's laws and associated analytical solutions, and since the present work focuses on bidirectional twill fabrics, and because multiple studies have reported close diffusivity values along the two principal fiber directions for such architectures, a quasi-isotropic in-plane assumption is adopted to simplify identification and support an efficient analytical treatment.

Hygroscopic swelling is then quantified experimentally by tracking dimensional changes along the three principal directions as immersion progresses, using a laser displacement measurement

protocol. Consistent with common constitutive descriptions for hygroscopic deformation in FRPs, hygroscopic strain is treated as linearly related to moisture content through hygroscopic swelling coefficients, in direct analogy with thermal expansion coefficients in thermoelasticity. This experimental characterization is particularly important for hybrid laminates, where mismatched swelling tendencies between flax/epoxy and carbon/epoxy sublaminates can generate internal constraint stresses and moisture-induced curvature, even in the absence of external loading.

Finally, mechanical consequences of moisture diffusion are evaluated using three-point bending tests. The choice of bending is motivated by its direct relevance to the strengthening configuration studied in Chapter D, where bonded patches primarily aim to increase flexural stiffness and strength of steel substrates, and where service moisture may modify the patch response and, indirectly, the interface loading environment. In that sense, Chapter E provides the material-level basis required to anticipate how environmental exposure can alter the "effective" patch properties used in structural interpretation and design.

Numerical modelling of hygro-mechanical behavior is also a subject of clear interest, particularly for multi-material laminates. Most commercial FEM software environments do not natively support fully coupled hygro-mechanical analysis, and a common engineering practice is to exploit the thermal–diffusion analogy (Fourier-type transport with expansion strains) to simulate moisture diffusion and swelling using heat transfer and thermal expansion capabilities (Yoon et al. 2007). While this approach is relatively straightforward for mono-materials, additional care is required for multi-material systems because water content fields are generally discontinuous across interfaces between materials with different saturation contents. To address this, the present chapter builds on the "wetness fraction" concept introduced for electronic packaging and later adopted in polymer composite contexts, where normalization by saturation content restores continuity of the driving field across interfaces and enables robust numerical implementation (Ee Hua Wong et al. 1998; Xie et al. 2009; Cocaud 2019). In this work, the novel contribution is that the modelling framework is implemented in an FE solver (Abaqus Standard) using sequentially coupled diffusion–stress analyses, and it is validated against the experimental gravimetric and deformation experimental results for the studied laminates.

The remainder of the chapter is structured as follows. Section E.2 presents the material systems and the four manufactured layup configurations (C10, F10, F6C4 and C2F6C2) produced by vacuum-assisted resin infusion. Section E.3 details the gravimetric protocol, the diffusion-parameter identification methodology, the hygroscopic swelling measurements, and the three-

point bending procedure used to quantify flexural response before and after ageing. Section E.4 then discusses the experimental results, distinguishing water uptake kinetics, hygroscopic behavior, and flexural performance evolution. Section E.5 introduces the FEM framework based on the thermal–diffusion analogy for mono- and multi-material laminates and compares numerical predictions to experimental observations. Overall, Chapter E establishes the modelling ingredients needed to incorporate moisture-driven fields and property changes when assessing bonded composite/steel systems in humid service conditions.

Part of the works presented in this chapter are currently under review by the co-authors, and are to be submitted to the journal “Composites Part B: Engineering”

E.2. Materials and specimen manufacturing

A 280g/m² 3K carbon fiber twill weave fabric, and a 315g/m² flax fiber twill weave fabric from Sicomin® are used as reinforcements for the composite material. The matrix used is the 38% biobased epoxy resin SR InfuGreen 810 with SD 8824 hardener, also from Sicomin®. Four 10-ply rectangular composite layup configurations were manufactured, combining carbon and flax fabrics, exclusively oriented at [0°/90°]: C10 (10 carbon plies), F10 (10 flax plies), F6C4 (4 carbon + 6 flax plies) and C2F6C2 (2 carbon + 6 flax + 2 carbon plies). All composite plates were manufactured using a vacuum assisted resin infusion process, in accordance with the supplier's recommendations (Sicomin® GreenPoxy33_sd477x 2023). They were first left to cure at room temperature for 24h, then underwent a post-curing in an oven at 40°C for another 24h. **Table 0-1** summarizes the relevant information about the manufactured composite layups. Rectangular specimens with dimensions of 80 mm x 25mm, were subsequently cut from the composite plates using a water rotary cutter. These specimens were used to perform gravimetric and flexural tests described in **Section E.3**.

Table 0-1. Manufactured composite layup configurations.

Configuration name	Representation	Nominal thickness [mm]	Measured thickness (mean ± standard deviation) [mm]	Number of CFRP plies	Number of FFRP plies
C10	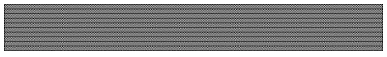	3	3.11 ± 0.08	10	0
F10		7	6.60 ± 0.04	0	10
C2F6C2		5.4	5.79 ± 0.14	4	6
F6C4		5.4	5.30 ± 0.06	4	6

E.3. Experimental methods

E.3.1. Gravimetric tests

Gravimetric tests were carried out to evaluate the water uptake behavior of the composites immersed in demineralized water at 50°C. The temperature was selected to be sufficiently below the glass transition temperature of the resin (≈ 71°C) to avoid any change in the polymer's physical state during immersion, while being high enough to accelerate the water absorption process. Prior to immersion, specimens were conditioned in an oven at 50°C for 14 days to remove residual moisture, homogenize the internal moisture distribution, and complete the potential post-curing of the resin. The initial dry mass of each specimen, m_0, was measured using an analytical balance with an accuracy of 1mg. Specimens were then immersed in thermostatically controlled water at 50°C to ensure isotherm condition. According to ISO 62 standard for determination of water absorption (International Organization for Standardization 2008), following a regular immersion time scale (24h, 48h, 96h, 192h, etc.), the specimens were removed, gently wiped to eliminate surface water, and immediately weighted to record their mass evolution $m(t)$. This procedure was repeated until equilibrium was reached, enabling the determination of the water uptake kinetics. The global water content $C(t)$ of a specimen was calculated according to **Eq.(0-1)**.

$$C(t) = \frac{m(t) - m_0}{m_0} \quad \textbf{(0-1)}$$

E.3.2. Characterization of water diffusion kinetics

E.3.2.i Fick's model

Fick's diffusion model is the most commonly used model to predict water diffusion with a polymer matrix (Fick 1855). It is based on the analogy with the heat conduction equation introduced by Fourier (Fourier 1822). Fick's first law states that the mass flux is proportional to the gradient of the local water concentration field c:

$$\vec{J} = -[D]\vec{\nabla}c \quad \textbf{(0-2)}$$

Where the mass flux $\vec{J}$ (in $kg.m^{-2}.s^{-1}$) and the local water concentration c (in $kg.m^{-3}$) are functions of space and time, and where $[D]$ is the diffusion coefficient tensor of the studied material (expressed in $m^2.s^{-1}$).

The conservation of mass of the diffusing substance within an infinitesimal volume over a time interval implies that:

$$\frac{\partial c}{\partial t} = -\vec{\nabla}.\vec{J} \quad \textbf{(0-3)}$$

By considering Fick's first law and assuming that the tensor $[D]$ is constant, one obtains Fick's second law:

$$\frac{\partial c}{\partial t} = [D]\nabla^2 \mathrm{c} \quad \textbf{(0-4)}$$

E.3.2.ii General 3D solution

We consider a parallelepiped with dimensions (L, b, h), where L, b and h are respectively its length, width and thickness. The x, y and z directions respectively correspond to the specimen's length, width and thickness directions. The diffusivity tensor $[D]$ is represented by a diagonal matrix, with each component depending on a spatial variable:

$$[D] = \begin{bmatrix} D_x & 0 & 0 \\ 0 & D_y & 0 \\ 0 & 0 & D_z \end{bmatrix} \quad \textbf{(0-5)}$$

The local water concentration c is consequently function of the spatial variables (x, y, z) and of time t.By integrating to Fick's second law (**Eq. (0-4))**, we obtain:

$$\frac{\partial c}{\partial t} = D_x \frac{\partial^2 c}{\partial x^2} + D_y \frac{\partial^2 c}{\partial y^2} + D_z \frac{\partial^2 c}{\partial z^2} \quad \textbf{(0-6)}$$

Moreover, the initial (I.C) and boundary conditions (B.C) to which the studied specimen is subjected are expressed as follow:

I.C $$c(x, y, z, t) = c_0, \quad \text{pour} \quad \begin{cases} 0 < x < L \\ 0 < y < b, \\ 0 < z < h \end{cases} \quad t = 0 \quad \textbf{(0-7)}$$

B.C $$c(x, y, z, t) = c_L, \quad \text{pour} \quad \begin{cases} x = \{0, L\} \\ y = \{0, b\}, \\ z = \{0, h\} \end{cases} \quad t = 0 \quad \textbf{(0-8)}$$

Where c_0 is the homogenous water content at initial state, and c_L is the constant water content at the boundaries of the specimen.

An analytical solution to this problem was proposed by Crank (Crank 1976), and is presented in the following equation:

$$\frac{c-c_0}{c_L-c_0}=1-\left(\frac{4}{\pi}\right)^3\sum_{n=0}^{\infty}\sum_{m=0}^{\infty}\sum_{p=0}^{\infty}\frac{(-1)^n(-1)^m(-1)^p}{(2n+1)(2m+1)(2p+1)}\times\exp\left(-\pi^2 t\left(\boldsymbol{D_x}\left(\frac{2n+1}{L}\right)^2+\boldsymbol{D_y}\left(\frac{2m+1}{b}\right)^2+\boldsymbol{D_z}\left(\frac{2p+1}{h}\right)^2\right)\right)\times\cos\left(\frac{(2n+1)\pi x}{L}\right)\cos\left(\frac{(2m+1)\pi y}{b}\right)\cos\left(\frac{(2p+1)\pi z}{h}\right) \quad \textbf{(0-9)}$$

Where, we remind, that the local water concentration c is function of the spatial coordinates (x, y, z) and of time t.

Assuming that the specimen is initially dry, and that the surfaces directly exposed to water are initially at their saturation state, we have then, $c_0 = 0$ and $c_L = c_{sat}$, and by integrating on the specimen's volume and dividing by its initial mass, we obtain:

$$C(t)=\left[1-\left(\frac{8}{\pi^2}\right)^3\sum_{n=0}^{\infty}\sum_{m=0}^{\infty}\sum_{p=0}^{\infty}\frac{1}{(2n+1)^2(2m+1)^2(2p+1)^2}\times\exp\left(-\pi^2 t\left(\boldsymbol{D_x}\left(\frac{2n+1}{L}\right)^2+\boldsymbol{D_y}\left(\frac{2m+1}{b}\right)^2+\boldsymbol{D_z}\left(\frac{2p+1}{h}\right)^2\right)\right)\right]\times\boldsymbol{C_{sat}} \quad \textbf{(0-10)}$$

Where $C(t)$ (unitless) is the global water content in the specimen at time t, and C_{sat} (also unitless) is its global water content at saturation, i.e. after an infinite time.

E.3.2.iii Proposed analytical solution for quasi-isotropic materials (bidirectional fabric reinforced polymers)

To identify the diffusion parameters, the 3D Fick solution can involve a long time of computation. To simplify it, and since this work is focused on bidirectional fabric reinforced polymers, we assume that the diffusion coefficients in the principal fiber directions of the composite are equal, i.e. $D_x = D_y = \boldsymbol{D_f}$. Indeed, multiple authors have shown by identification of the diffusion parameters on twill fabric reinforced polymers using **Eq. (0-10)**, that these coefficient are closely equal (Chilali et al. 2018; Saidane et al. 2016; Chilali et al. 2017; Zouari et al. 2019).

$$C(t) = \left[1 - \left(\frac{8}{\pi^2}\right)^3 \sum_{n=0}^{\infty}\sum_{m=0}^{\infty}\sum_{p=0}^{\infty} \frac{1}{(2n+1)^2(2m+1)^2(2p+1)^2} \times \exp\left(-\pi^2 t\left(\boldsymbol{D_f}\left(\frac{2n+1}{L}\right)^2 + \boldsymbol{D_f}\left(\frac{2m+1}{b}\right)^2 + \boldsymbol{D_z}\left(\frac{2p+1}{h}\right)^2\right)\right)\right] \times \boldsymbol{C_{sat}} \quad \textbf{(0-11)}$$

E.3.2.iv Method of identification of diffusion constants

Let $C_{exp}(t)$ be a diffusion kinetic curve obtained from regular gravimetric measurements of a specimen made of a given material, obtained according to **Eq. (0-1)**. In the case where this kinetic corresponds to a diffusion problem for which an analytical solution $C_{ana}(t)$ exists, the most commonly used method to identify the diffusion parameters is the least squares method. It was first used by (Pierron et al. 2002), and has been largely used ever since (Chilali et al. 2018; Saidane et al. 2016, 2014).

The identification of diffusion parameters is thus carried out by comparing the experimental values with those of the analytical solution. Using an optimization algorithm, the diffusion parameters are determined so as to minimize the following error quantity q:

$$q = \sum_{i,j}\left[C_{ana}(t_j) - C_{exp,i}(t_j)\right]^2 \quad \textbf{(0-12)}$$

Where $C_{ana}(t_j)$ is the analytical global water content calculated at time t_j, and $C_{exp,i}(t_j)$ is the experimental global water content measured for specimen i at time t_j.

E.3.3. Characterization of hygroscopic behavior

Hygroscopic swelling was characterized by measuring the dimensional changes of the specimens along the three principal directions (length, width and thickness) during immersion. The experimental setup, shown in **Figure 0-1**, consist of a Keyence LK-G82 laser displacement sensor mounted on a 3D-printed frame allowing precise positioning and linear scanning of the laser beam along the specimen surface. Before each measurement, the laser sensor was calibrated using a stainless-steel reference specimen, considered dimensionally stable over time to ensure accuracy and repeatability. For the in-plane directions (length and width), the laser was positioned at mid-thickness and scanned the surface along a line to record the displacement profile. The average value along this line was then used to determine the dimensional variations during immersion. To minimize thermal effects, specimens were kept in water at room

temperature for 15 minutes after being removed from the 50°C bath to reach thermal equilibrium, as all measurements were performed at ambient temperature. The trough-thickness dimensional changes were measured using a micrometer with a precision of 1 µm.

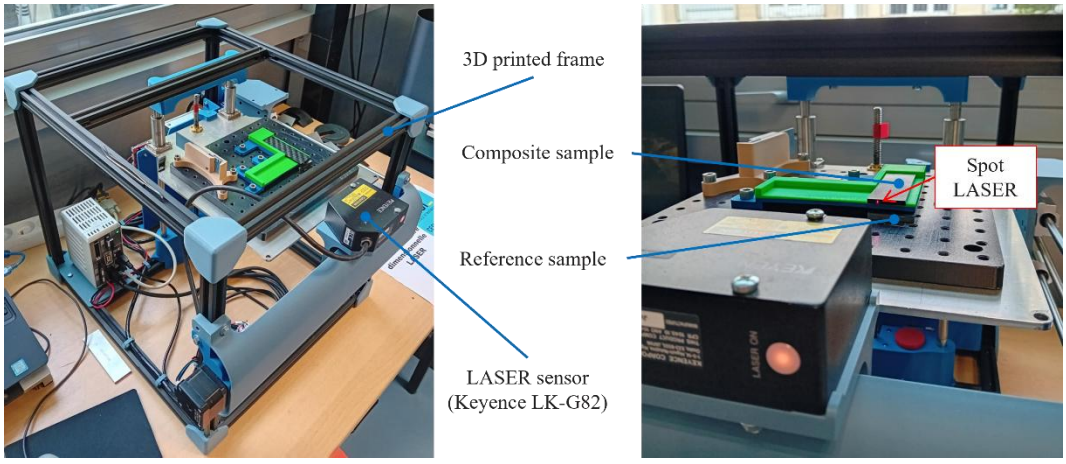

Figure 0-1. Experimental setup used for hygroscopic swelling measurements: the laser displacement sensor scans the specimen surface along a line while a stainless steel reference ensures calibration stability.

At each immersion time, the specimen was gently wiped to remove surface water and immediately measured. The hygroscopic strain ϵ_i in each principal direction i (x for length, y for width and z for thickness) was calculated (**Eq. (0-13)**) as the relative change between the current dimension $U_i(t)$ and the initial dry dimension $U_{i,0}$.

$$\varepsilon_i(t) = \frac{U_i(t) - U_{i,0}}{U_{i,0}} \quad \textbf{(0-13)}$$

From the analytical point of view, hygroscopic swelling is analogue to the thermal expansion. For FRPs, it has been shown that hygroscopic swelling (strains caused by water diffusion) is usually a linear function of moisture content and is expressed following equation:

$$\varepsilon_{ij}^{hyg}(t) = \beta_{ij} \times C(t) \quad \textbf{(0-14)}$$

Where β_{ij} is the hygroscopic swelling coefficient and $C(t)$ is the global water content at time t.

E.3.4. Flexural tests

Flexural tests were conducted using a 3R Labo universal testing machine equipped with a 10kN load cell, following the general principles of the ISO 14125 standard for fiber-reinforced composites. The tests were performed in a three-point bending configuration, with a support

span of 60 mm. The lower supports and the central loading nose had a radius of 5mm to ensure uniform load distribution and to minimize local stress concentrations. Although the span-to-thickness ratio (≈ 10) is slightly below the value recommended by ISO 14125, this configuration was chosen to ensure consistent comparison between aged and unaged specimens. Each specimen was loaded at a crosshead displacement rate of 5 mm.min^{-1} until rupture. A digital camera was positioned laterally to record the entire test, providing a visual comparison of the deformation and fracture mechanisms between unaged and water-aged specimens (cf. **Figure 0-2**). The force-displacement data were continuously recorded to determine the flexural stress-strain response.



Figure 0-2 Experimental setup used for three-point bending tests showing the 3R Labo testing machine, specimen, digital camera and 60 mm support span with 5 mm radius supports and loading nose.

The flexural stress σ_f and strain ϵ_f were calculated according to ISO 14125 where P is recorded machine load, s mid-span deflection, L support span, b specimen width, and d its thickness (**Eq. (0-15)**).

$$\sigma_f = \frac{3PL}{2bd^2} \quad , \quad \varepsilon_f = \frac{6sd}{L^2} \tag{0-15}$$

The flexural modulus, E_f was determined from the slope $m = \frac{dP}{ds}$ in the initial linear region of the curve.

$$E_f = \frac{L^3 m}{4bd^3} \tag{0-16}$$

Eq. (0-16) is valid for rectangular sections and small deflections, and is sufficiently accurate for comparing the mechanical behavior before and after ageing despite the relatively low span-to-thickness ratio.

E.4. Experimental results and discussions

E.4.1. Water diffusion kinetics

Figure 0-3 shows the evolution of the water content $C(t)$ as a function of square of time for the ten-ply carbon (C10) and flax (F10) composites. The experimental data points correspond to the five specimens tested for each configuration, while the solid lines represent the fitting of the analytical three-dimensional Fickian diffusion model. The mean and standard deviation of each diffusion parameter are reported in **Figure 0-3** in accordance with method of identification presented in **Subsection E.3.2.iv**.

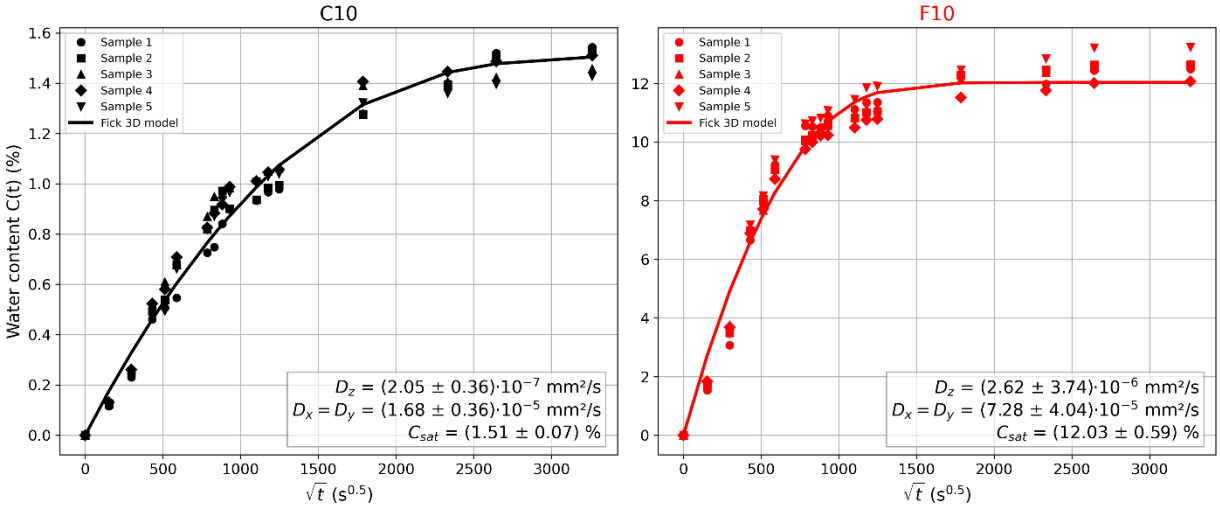

Figure 0-3. Evolution of water content as a function of the square root of immersion time for two composite configurations. The flax composite (F_{10}) exhibits the highest water uptake, while the carbon composite (C_{10}) shows minimal absorption.

The C10 composite exhibits a slow diffusion rate and a very limited water uptake, characterized by a through-thickness diffusion coefficient $D_z = (2.05 \pm 0.36).10^{-7} mm^2.s^{-1}$, an in-plane diffusion coefficients $D_x = D_y = (1.68 \pm 0.36).10^{-5} mm^2.s^{-1}$, and a global water content at saturation $C_{sat} = 1.51 \pm 0.07\ \%$. The much higher in-plane diffusion compared to the through-thickness direction ($D_x \gg D_z$) indicated that moisture transport is mainly governed by the fiber and matrix arrangement within the laminate. The plies act as preferential diffusion paths along the fiber direction, while the interfaces between layers and the dense epoxy-rich interlaminar regions hinder diffusion across the thickness. This anisotropic diffusion behavior, combined with the hydrophobic nature of both the carbon fibers and the epoxy matrix, results

in very limited overall water uptake. In contrast, the F10 composite shows a much faster and higher moisture absorption, with $D_z = (2.62 \pm 3.74).10^{-6} mm^2.s^{-1}$, $D_x = D_y = (7.28 \pm 4.04).10^{-5} mm^2.s^{-1}$, and $C_{sat} = 12.03 \pm 0.59\,\%$. The significantly larger diffusion coefficients and global water content at saturation reflect the strong hydrophilicity of flax fibers and the presence of microvoids within the lignocellulosic network, which facilitate capillary transport and water retention. The anisotropy observed between in-plane and through-thickness diffusion ($D_x \gg D_z$) is again consisten with the layered architecture of the laminate, where fibers create continuous channels promoting in-plane moisture migration. The good agreement between experimental data and the 3D Fickian model confirms that both composites follow a predominantly Fickian diffusion regime, although with markedly different magnitudes and anisotropies of diffusivity, arising from their contrasting microstructures and fiber-matrix interactions.

Figure 0-4 shows the evolution of water content $C(t)$ as a function of the square root of immersion time for the hybrid composites F6C4 and C2F6C2. The experimental data points correspond to the five specimens tested for each configuration, with each specimen represented by a distinct marker. The F6C4 composites consist of four plies of carbon and six plies of flax, while the C2F6C2 composites are composed of two plies of carbon, six plies of flax and two plies of carbon. The results show a similar evolution of water content, with a progressive absorption followed by saturation, reaching around 8% of water content at saturation for both configurations. It is important to note that no fitting with the Fick 3D diffusion model was performed for the hybrid composites. This decision is based on the complex and heterogeneous nature of these materials, where the interaction between different fibers and fiber-matrix interfaces makes the application of a classical Fickian model irrelevant. Diffusion behavior in hybrid composites is influenced by the differences in physical properties between flax and carbon fibers, as well as by the ply arrangement within the laminate architecture. Applying a uniform diffusion model such as Fick 3D may not properly reflect these interactions and the anisotropic behaviors of the materials. To better interpret the diffusion behavior of the hybrid composites, a mixing law approach was implemented to estimate the effective diffusion parameters from the properties of the reference laminates F10 and C10. The volumetric fractions of flax and carbon plies were first determined for each hybrid configuration based on their measured average thicknesses prior to immersion: 6.50 mm for F10, 3.13 mm for C10, 5.39 mm for F6C4, and 5.70 mm for C2F6C2. Assuming that the total laminate thickness is the

sum of the individual ply thicknesses, the thickness of one ply of flax e_f and one ply of carbon e_c were calculated as **equation 0-17**.

$$e_f = 0.65\ mm \quad ; \quad e_c = 0.31\ mm \tag{0-17}$$

From these values, the theoretical volumetric fractions of flax V_f and carbon V_c within the hybrid laminates with thickness e_h were obtained using **equation 0-18** where n_f and n_c are the numbers of flax and carbon plies, respectively.

$$V_f = \frac{n_f e_f}{e_h} \quad ; \quad V_c = 1 - V_f \tag{0-18}$$

The effective diffusion parameters of the hybrids were then estimated using a linear mixing law applied to each relevant property P (diffusion coefficients D_z, D_x, and C_{sat} (**equation 0-19**).

$$P_{hydrid} = V_f . P_{F10} + V_c . P_{C10} \tag{0-19}$$

The diffusion parameters obtained for the reference and hybrid composites are summarized in **Table 0-2**. The table presents the identified diffusion coefficients in the through-thickness D_z and in-plane D_x directions, the equilibrium water content C_{sat}, the flax volumetric fraction V_f, and the measured average thickness e for each configuration. These values were used as inputs for the mixing-law model applied to the hybrid laminates.

Table 0-2. Identified diffusion parameters and geometric characteristics of the reference (C10, F10) with 3D Fick model and hybrid (F6C4, C2F6C2) composites with mixing-law model.

	D_z (mm².s^{-1})	D_x (mm².s^{-1})	C_{sat} (%)	V_f (-)	e (mm)
C10	$(2.05 \pm 0.36).10^{-7}$	$(1.68 \pm 0.36).10^{-5}$	1.51 ± 0.07	-	3.13
F10	$(2.62 \pm 3.74).10^{-6}$	$(7.28 \pm 4.04).10^{-5}$	12.03 ± 0.59	-	6.50
F6C4	$1.95.10^{-6}$	$5.74.10^{-5}$	9.12	72.4 %	5.39
C2F6C2	$1.86.10^{-6}$	$5.51.10^{-5}$	8.71	68.4 %	5.70

Figure 0-4 compares the experimental water uptake curves of the hybrid composites F6C4 and C2F6C2 with the predictions obtained from the mixing law model. A good qualitative agreement is observed regarding the general shape of the diffusion behavior; however, the model tends to slightly overestimate the water content, particularly in the saturation region. This discrepancy can be attributed to the presence of resin-rich zones within the laminate, which are not accounted for in the simplified mixing approach. These zones, located at the interfaces

between plies or near the outer surfaces, act as diffusion barriers and reduce the overall moisture uptake of the composite. Consequently, the effective diffusion coefficient and the equilibrium water content are lower than those predicted by the idealized volumetric mixture of flax and carbon plies. This effect is especially significant in the through-thickness direction, where the resin layers form a serial resistance to diffusion, slowing down water transport across the laminate.

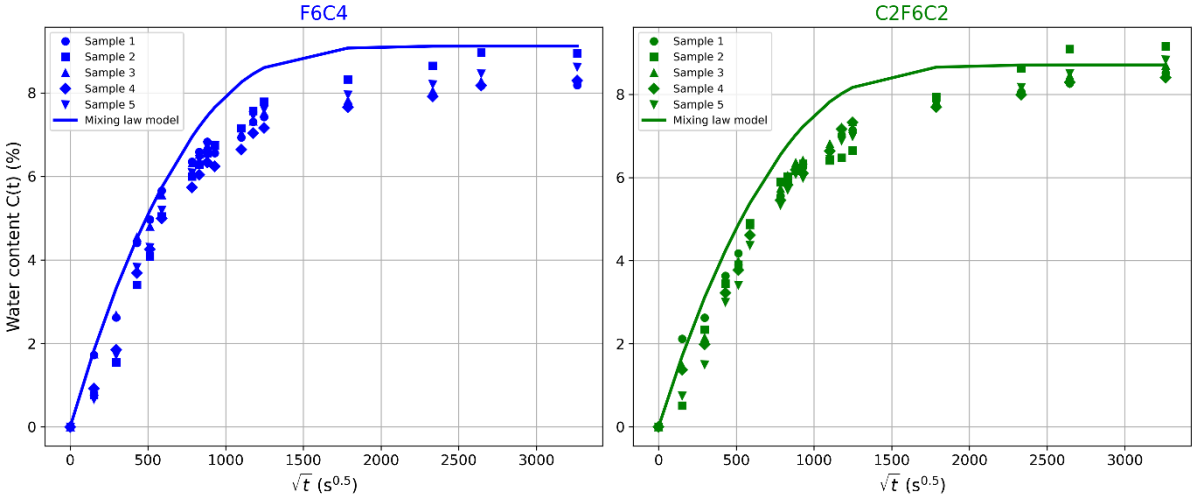

Figure 0-4. Evolution of water content as a function of the square root of immersion time for two composite configurations. The hybrid composite with two configurations: F6C4 and C2F6C2.

E.4.2. Hygroscopic behavior

Figure 0-5 shows the evolution of the hygroscopic strain components (ϵ_{xx}, ϵ_{yy} and ϵ_{zz}) as a function of the water content for the flax (F10) and carbon (C10) composites. Each marker symbol corresponds to an individual specimen, and the solid lines represent the linear fits obtained for the five samples of each material. The slopes of these regressions define the coefficients of hygroscopic expansion (β_{xx}, β_{yy} and β_{zz}), which quantify the strain induced per unit change in water content, and these values are summarized in.**Table 0-3**

For the flax composites (F10), the material exhibits a strong and anisotropic swelling response, with $\beta_{xx} = -0.089 \pm 0.010$, $\beta_{yy} = -0.093 \pm 0.009$, and $\beta_{zz} = 0.895 \pm 0.061$. The negative in-plane coefficients indicate a contraction along the fiber directions upon moisture absorption, which is consistent with the swelling of individual flax fibers radially and the resulting Poisson-like effect at the composite scale. The similarity between β_{xx} and β_{yy} confirms that the swelling behavior is nearly identical in both in-plane directions, as expected from the quasi-symmetric stacking sequence of the laminate. The large positive out-of-plane

coefficient reveals a pronounced thickness increase, governed by matrix expansion and the opening of interfacial gaps between fibers and matrix during water uptake. In contrast, the carbon composite (C10) shows a much weaker hygroscopic strain response, with $\beta_{xx} = 0.090 \pm 0.006$, $\beta_{yy} = 0.053 \pm 0.006$, and $\beta_{zz} = 0.079 \pm 0.003$. The small and positive coefficients in all directions indicate a nearly isotropic but limited swelling behavior, mainly governed by the epoxy matrix since the carbon fibers are dimensionally stable and non-hygroscopic. Because the overall strain levels are very low, the relative measurement uncertainties become significant, which can explain part of the dispersion observed between directions. In theory, as fibers do not contribute to moisture-induced deformation, the swelling should be essentially isotropic and controlled by the matrix. The experimental results are consistent with this expectation, confirming the negligible influence of the fibers on the hygroscopic response. Overall, these results highlight the strong contrast between the flax-fiber and carbon-fiber composites: the flax laminates exhibits a highly anisotropic and moisture-sensitive swelling behavior, while the carbon composite remains dimensionally stable, with deformations almost one order of magnitude lower.

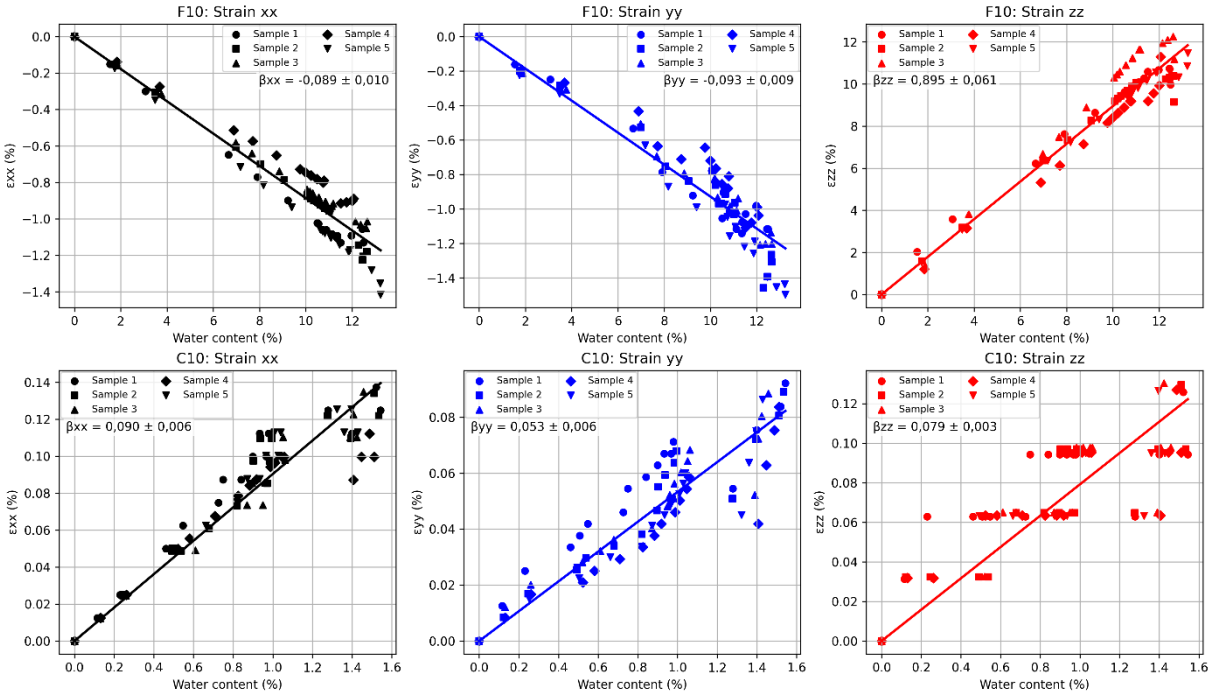

Figure 0-5. Evolution of hygroscopic strain components (ε_{xx}, ε_{yy} and ε_{zz}) as a function of water content for flax (F10) and carbon (C10) composites. Experimental data are shown for fiver specimens per material, and solid lines represent the linear regression.

Table 0-3. Hygroscopic expansion coefficients identified for the reference C10 and F10 configurations.

	β_{xx} (-)	β_{yy} (-)	β_{zz} (-)
C10	0.090 ± 0.006	0.053 ± 0.006	0.079 ± 0.003
F10	-0.089 ± 0.010	-0.093 ± 0.009	0.895 ± 0.061

E.4.3. Three-point bending

Figure 0-6 presents the stress–strain curves obtained from three-point bending tests for the C10 and F10 composites, using three unaged specimens and five aged specimens for each material. Stresses and strains were calculated directly from the experimental measurements in accordance with the standard procedure, allowing a direct comparison of the influence of hygrothermal ageing on the flexural response of these two reference architectures. The carbon composite C10 exhibits a highly stable behavior, with ageing producing only a marginal effect on both the initial stiffness and the maximum stress. The overall shape of the curves remains unchanged, and the material retains a predominantly brittle failure mode, confirming the very low sensitivity of the carbon laminate to moisture uptake under bending. In contrast, the flax composite F10 shows a pronounced modification of its flexural response after ageing. While the unaged specimens display a relatively stiff behavior followed by abrupt failure, the aged specimens exhibit a clear reduction in maximum stress together with a substantial increase in strain at failure. This evolution reflects a transition from a brittle response to a more ductile and progressive damage behavior under bending, highlighting the strong sensitivity of the flax-based composite to hygrothermal ageing.

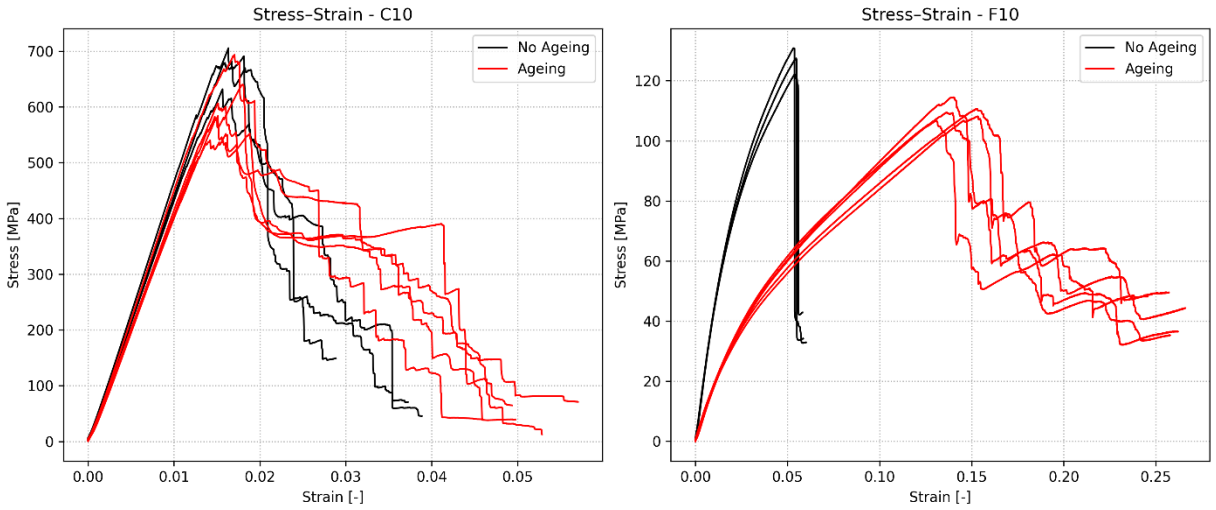

Figure 0-6. Stress–strain curves obtained from three-point bending tests for the C10 and F10 composites, comparing unaged (3 specimens) and aged (5 specimens) conditions.

Figure 0-7 shows the evolution of the flexural modulus measured according to ISO 178 for the C10 and F10 composites, comparing unaged and aged conditions. The percentages displayed

above the bars and summarized in **Table 0-4** quantify the reduction in modulus induced by hygrothermal ageing and are referred to as α, with:

$$\alpha = \frac{E_{f,Ageing} - E_{f,No\ ageing}}{E_{f,No\ ageing}} \tag{20}$$

The carbon composite C10 exhibits only a slight decrease in flexural modulus after ageing (–6.3%), confirming its very low sensitivity to moisture and the stability of its elastic response under bending. In contrast, the flax composite F10 shows a pronounced degradation, with a reduction of more than half of its initial flexural modulus (–53.6%). This strong loss of stiffness highlights the significant influence of water uptake on flax fibers and the associated weakening of the fiber–matrix load transfer, leading to a severe deterioration of the flexural elastic properties.

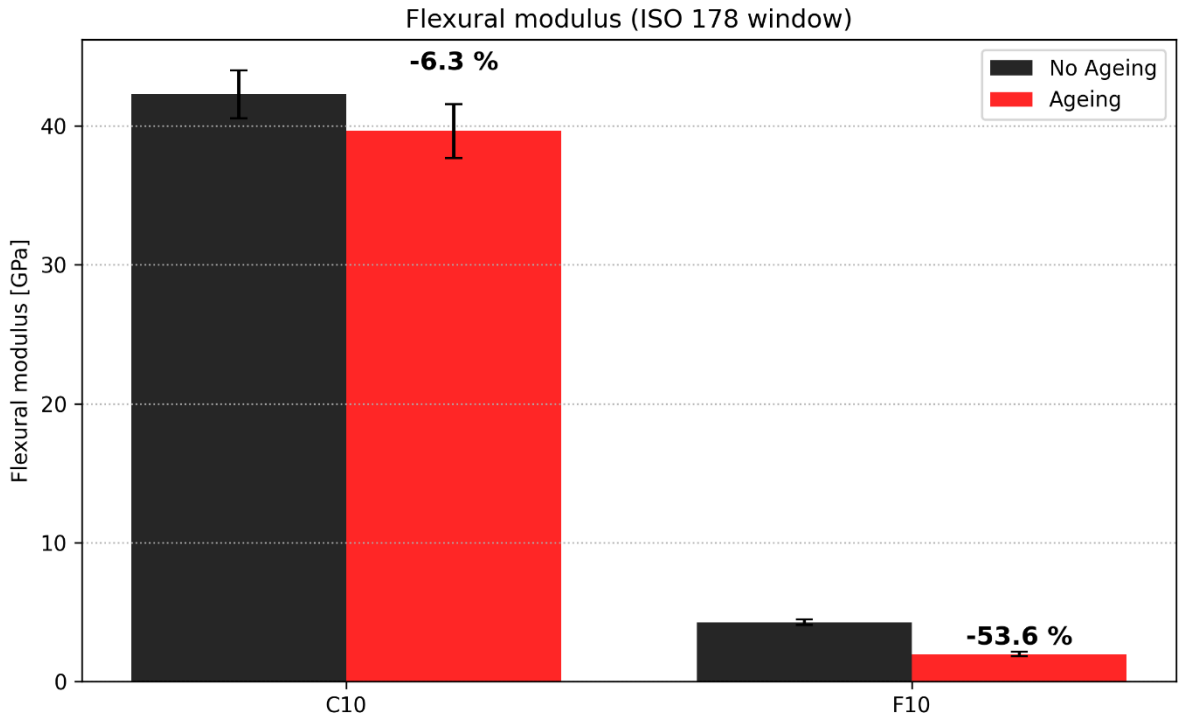

Figure 0-7. Flexural modulus (ISO 178) of the C10 and F10 composites before and after ageing, with percentage values indicating the relative decrease in modulus due to hygrothermal exposure.

Table 0-4. Coefficient of reduction in modulus induced by hygrothermal ageing identified for the reference C10 and F10 composites.

	E_f No Ageing (GPa)	E_f Ageing (GPa)	α (%)
C10	42.28 ± 1.74	39.63 ± 1.96	-6.3
F10	4.25 ± 0.20	1.97 ± 0.18	-53.6

E.5. Numerical modeling

E.5.1. General scheme for Hygro-mechanical FEA of FRP materials

A hygro-mechanical problem in fiber-reinforced composites arises from the interaction between moisture transport within the material and the mechanically induced response associated with hygroscopic deformation and stiffness evolution. From a modelling standpoint, this requires solving the transient diffusion equation to determine the spatial and temporal distribution of moisture concentration, followed by the evaluation of the corresponding stress–strain fields generated by moisture-dependent expansion and elastic properties. These two physical phenomena may be treated either in a fully coupled formulation or through a sequential approach when the influence of stress on diffusion remains negligible.

As in other multi-physics problems, hygro-mechanical behavior can be simulated using the finite element method. However, rather than relying on dedicated mass-diffusion–mechanical coupling modules, the common practice consists of using the available heat transfer, thermal expansion and mechanical functions in FEM commercial softwares, to model water diffusion and hygroscopic behavior, by making the analogy between thermal problems (Fourier's law + thermal expansion) and diffusion problems (second Fick's law + hygroscopic swelling) (Yoon et al. 2007).

This modeling scheme is well established and commonly used for mono-materials. However, its direct extension to heterogeneous laminates requires particular attention. Indeed, in a multi-material system, contrary to the behavior of a temperature field, the water content field is discontinuous at the interface between two different materials, because each constituent exhibits its own saturation concentration and diffusion characteristics, as shown in **Figure 0-8.a)**. This discontinuity leads to numerical inconsistencies when the classical thermal–diffusion analogy is applied without modification, since temperature is inherently continuous across interfaces in standard heat-transfer formulation.

To bypass this issue, Wong et al. (Ee Hua Wong et al. 1998) proposed the notion of "wetness fraction", defined as the local moisture concentration normalized by the material-specific saturation concentration. This normalized variable ensures field continuity across interfaces while preserving the physical contrast in moisture content between adjacent materials (**Figure 0-8.b)**).

The use of this proposed normalization method with FEM has been examined, and validated by multiple authors (D. Liu et al. 2016; Xie et al. 2009) and more recently in Cocaud's thesis (Cocaud 2019), through comparison with independent numerical schemes such as the Finite Differences Method (FDM), thereby confirming the robustness of the formulation for heterogeneous assemblies. However, to the authors knowledge, it has not been implemented and validated yet in a FEM software.

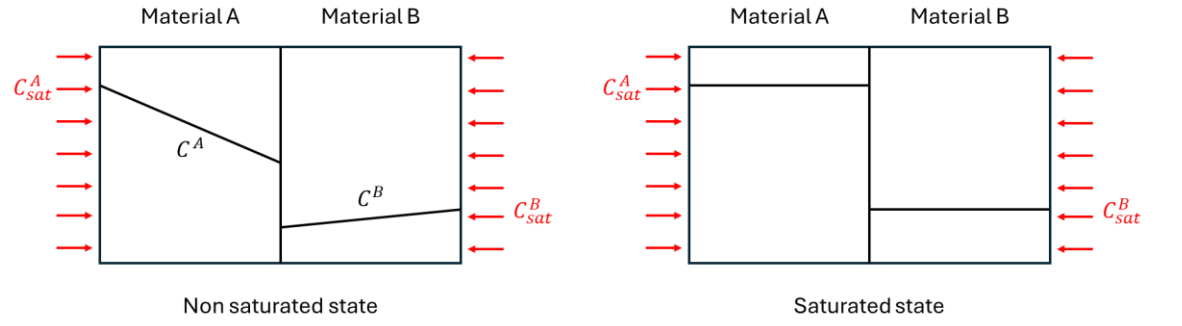

a)

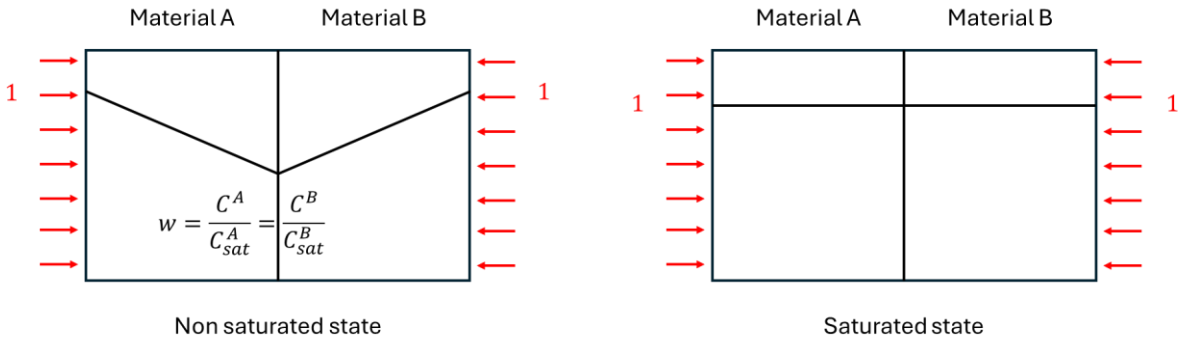

b)

Figure 0-8. Representation of a) discontinuity of water content ($C^A$and C^B) at the interface between two materials (A and B) having two respective water content saturations C^A_{sat} and C^B_{sat}. b) continuity of wetness fraction (w) at the interface of two materials (A and B) with respective water contents at saturation C^A_{sat} and C^B_{sat} (adapted from (Ee Hua Wong et al. 1998)).

In the following two subsections, methodologies of input of material parameters will be presented for mono-materials and multi-materials in order to respect the scheme of thermal-diffusion analogy to perform diffusion-stress analysis.

E.5.1.i Mono-material case: thermal/stress-diffusion/stress direct analogy

As previously explained, the use of a heat transfer analysis to model Fickian water diffusion in mono-materials is straightforward, provided that a consistent equivalence between thermal and diffusion parameters is defined. This analogy and input adjustment are presented in Table 0-5. The temperature variable T becomes the local water content c. Regarding material properties to input in the FEA software, thermal conductivity λ is analogue to the diffusion coefficient D, thermal expansion coefficient α is analogue to hygroscopic coefficient β, and the density ρ and thermal capacity c_{th} are taken equal to 1. It is important to note that the initial condition of temperature equal to 0 is analogue to an initial homogenous dry state of the material. The boundary condition which would be the imposed temperature, becomes the value of water content at saturation of the modeled material.

Table 0-5. Methodology of FEA parameters input for thermal-diffusion analogy in mono-material case.

	Variable	Parameters				I.C	B.C
Thermal	T	λ	ρ	c_{th}	α	$T=0$	T_{imp}
Fickian Diffusion	c	D	1	1	β	$c=0$	C_{sat}

Once the diffusion step is finished, we can sequentially launch a stress analysis, based on the obtained water content field. The temperature dependent elasticity matrice $[S](T)$ and the orthotropic hygroscopic coefficients β should be input for stress analysis. The general procedure for performing a sequentially coupled hygro-mechanical analysis is presented in **Figure 0-9**.

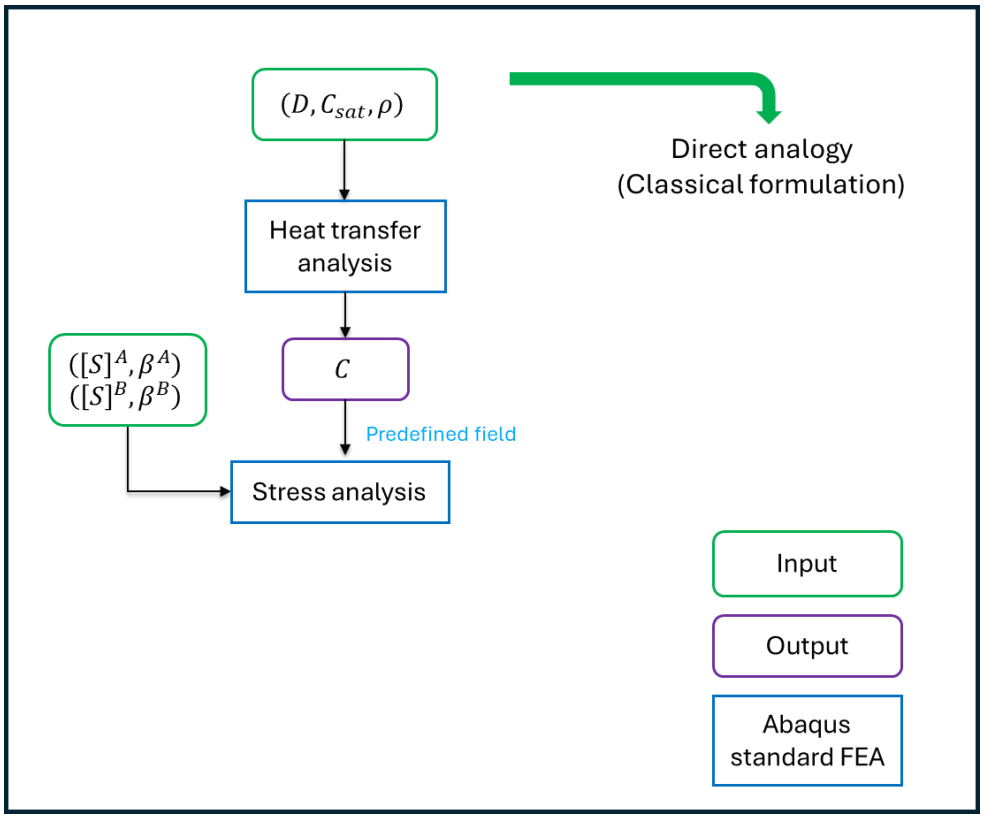

Figure 0-9. Procedure for hygro-mechanical analysis using thermal-diffusion analogy for mono-materials.

E.5.1.ii Multi-material case: thermal/stress-diffusion/stress indirect analogy

As previously explained, for multi-materials, the direct thermal–diffusion equivalence cannot be applied without modification due to the discontinuity of moisture concentration at material interfaces. A specific normalization procedure must therefore be introduced to ensure both numerical consistency and physical accuracy in heterogeneous laminates.

The analogy and input adjustment for multi-materials are presented in **Table 0-6**. The temperature variable T becomes the wetness fraction $w = \frac{c}{c_{sat}}$. Regarding material properties to input in the FEA software, thermal conductivity λ becomes analogue to the product of diffusion coefficient, density and water content at saturation. The density should now be specified as the real value of density of the material. The thermal capacity c_{th} becomes analogue to the water content at saturation. Finally, the boundary condition takes the value of 1 and the initial condition is unchanged and is equal to 0.

Table 0-6. Methodology of FEA parameters input for thermal-diffusion analogy in multi-material case.

		Variable	Parameters			I.C	B.C
Thermal		T	λ	ρ	c_{th}	$T=0$	T_{imp}
Fickian Diffusion	Material A	$w=\frac{c^A}{C^A_{sat}}$	$D^A \times C^A_{sat} \times \rho^A$	ρ^A	C^A_{sat}	$w=0$	1
	Material B	$w=\frac{c^B}{C^B_{sat}}$	$D^B \times C^B_{sat} \times \rho^B$	ρ^B	C^B_{sat}	$w=0$	1

It should now be clear that in order to obtain the water content fields in each material, a post-processing step is necessary. This post-processing step consists of multiplying the wetness fraction in each material by its corresponding water content at saturation. The obtained post-processed water content field can then be input as pre-field for the stress analysis. The explained procedure is summarized in **Figure 0-10**. The corresponding python code is provided in **Appendix D**.

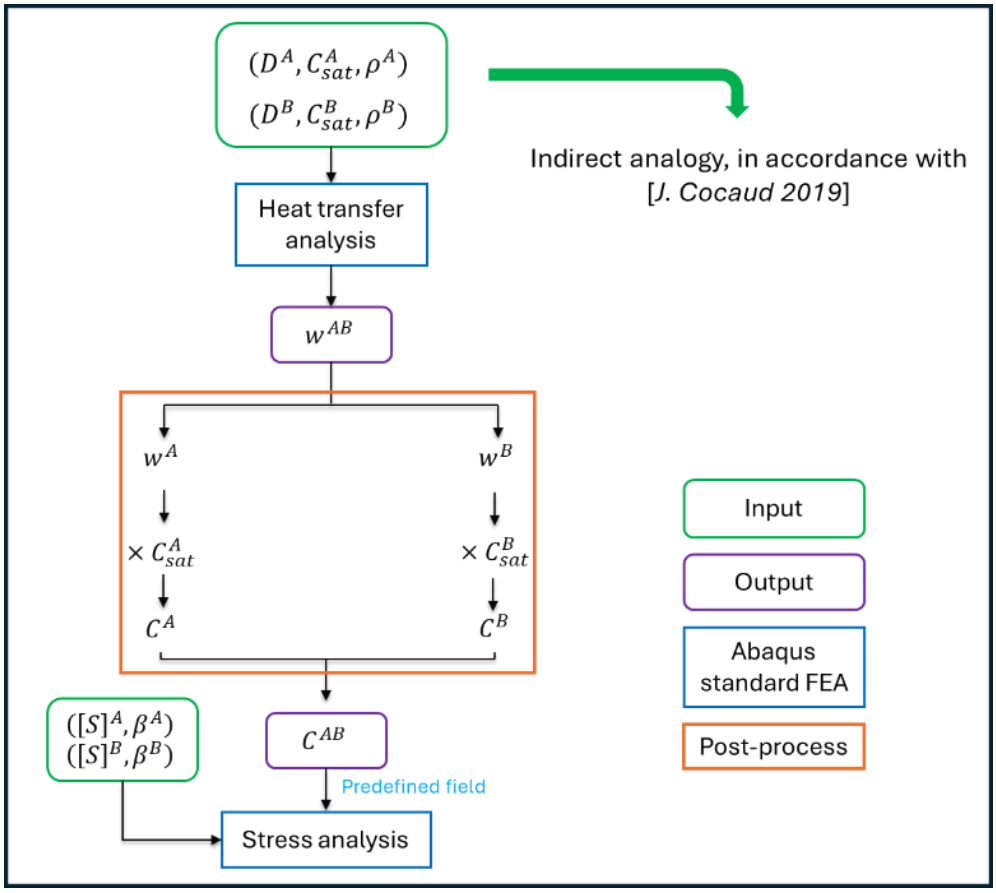

Figure 0-10. Procedure for hygro-mechanical analysis using thermal-diffusion analogy for multi-materials.

E.5.2. Hygro-mechanical FEM model

To numerically reproduce the hygromechanical response of the flax/epoxy, carbon/epoxy, and hybrid laminates under immersion, a 3D finite element model was developed in Abaqus/CAE 2024 using the Standard/Implicit solver. The model aims at predicting (i) the moisture uptake kinetics (gravimetric curves), (ii) the associated hygroscopic swelling, and (iii) the resulting change in elastic response of the specimens, thereby enabling a direct quantitative comparison with the experimental measurements. The modelling strategy is calibrated exclusively using the experimentally identified moisture transport, swelling and elastic properties of the reference laminates (C10 and F10), while the hybrid configurations are analyzed without additional parameter fitting in order to assess the predictive capability of the framework.

The simulated geometry corresponds to the rectangular specimens used experimentally (80 mm × 25 mm, nominal thickness depending on the layup, cf. **Table 0-1**). Since the diffusion boundary conditions and mechanical loading are symmetric with respect to the longitudinal and transverse mid-planes, a quarter-model representation is adopted to reduce computational cost while preserving the three-dimensional nature of the moisture and stress fields (**Figure 0-11**). Symmetry boundary conditions are applied on the two cut planes for both analyses. For the diffusion analysis, symmetry is enforced by imposing zero normal moisture flux across the symmetry planes, which is satisfied by leaving these surfaces without prescribed boundary conditions. For the mechanical analysis, symmetry constraints are introduced by enforcing zero normal displacement and the appropriate rotational constraints on the corresponding planes, ensuring kinematic equivalence with the full specimen.

A structured hexahedral mesh is employed. The diffusion analysis is performed using DC3D8 elements (8-node linear heat transfer bricks), and the subsequent mechanical (swelling + elasticity) analysis uses C3D8 elements (8-node linear bricks), ensuring consistency of spatial interpolation between the diffusion and mechanical fields. A mesh convergence study was conducted and led to a final global element size of $0.35\,mm$, selected to ensure stable predictions of both the gravimetric response and the swelling (notably near edges and outer surfaces). The same mesh density is retained for both analyses to ensure mesh and field compatibility between analyses.

Moisture transport is simulated through a “Heat transfer step “by applying the thermal–diffusion analogy described in **Subsection E.5.1**. The diffusion simulation time is chosen to match the immersion duration, and is taken equal to $t = 8.64 \times 10^6\ s \sim 3\ months$. After

completion of the diffusion analysis, the computed scalar field (moisture content C, or post-processed $C = w \times C_{sat}$ for hybrids) is transferred as a predefined field into a subsequent "Static general step" to compute hygroscopic strains and the associated stress/strain state. This static general analysis is performed over a time period $t = 8.64\,s$, with a $0.0864\,s$ incrementation. From a numerical standpoint, mechanical equilibrium is assumed to be reached incrementally in accordance with the characteristic diffusion time scale (each mechanical increment corresponds to a diffusion one). The duration assigned to the mechanical step therefore does not represent a physical loading time but is introduced solely for numerical implementation purposes within the sequential framework. Using identical increment definitions in the diffusion and mechanical steps simplifies sequential coupling by enabling direct field mapping without temporal interpolation.

For the reference laminates (C10 and F10), the specimen is modeled as a homogeneous orthotropic solid with properties corresponding to the tested experimental values. This homogenized representation is justified by the quasi-symmetric architecture of the laminates and the objective of capturing their macroscopic diffusion and elastic response. For the hybrid laminates (F6C4 and C2F6C2), the specimen volume is partitioned through the thickness to represent the ply-block arrangement, and each sub-volume is assigned the corresponding constituent properties (flax/epoxy or carbon/epoxy). Perfect bonding is assumed between adjacent layers (no interfacial slip), which is consistent with the objective of reproducing global diffusion kinetics and elastic bending response in the absence of explicit interfacial decohesion modeling.

To represent the stiffness change between unaged and saturated conditions, the elastic constants are defined as field-dependent properties using two reference states (dry and saturated) and linear interpolation by Abaqus between these bounds. This linear dependence is adopted as a first-order approximation of the experimentally observed stiffness degradation between the two limiting conditions. This approach allows the elastic response to evolve consistently with the local moisture field, while maintaining numerical robustness and avoiding the introduction of additional phenomenological parameters. The objective here is to capture the elastic response prior to failure, rather than to model progressive damage or irreversible interfacial degradation mechanisms.

Finally, **Table 0-7** summarizes the complete set of numerical inputs used in the diffusion and mechanical steps (diffusivities, saturation contents, hygroscopic coefficients, density, and

elastic constants for dry and saturated states), and Figure 0-11 specifies the immersed boundary surfaces.

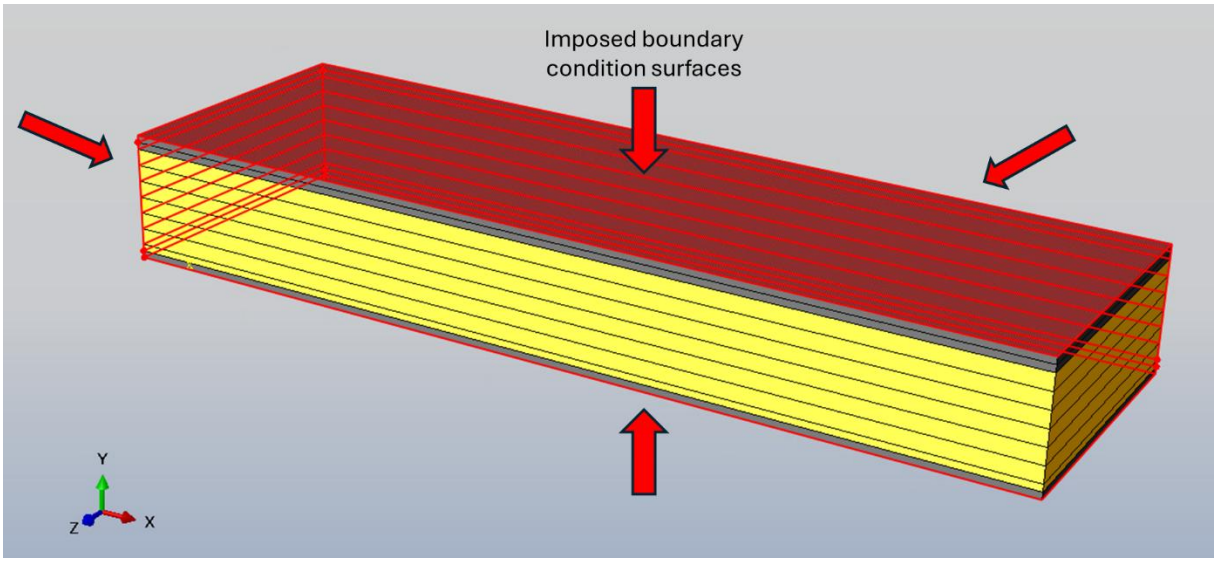

Figure 0-11. Surfaces where water diffusion boundary condition is imposed (highlighted in red) for configuration C2F6C2.

Table 0-7. Input numerical material parameters.

Quantity	**Carbon/epoxy No ageing**	**Carbon/epoxy Ageing**	**Flax/epoxy No ageing**	**Flax/epoxy Ageing**
Diffusivity $[mm^2.s^{-1}]$	$D_x = D_y = 1.68 \times 10^{-5}$ $D_z = 2.05 \times 10^{-7}$		$D_x = D_y = 7.28 \times 10^{-5}$ $D_z = 2.62 \times 10^{-6}$	
Water content at saturation [%]	$C_{sat} = 1.51$		$C_{sat} = 12.03$	
Hygroscopic swelling $[-]$	$\beta_{xx} = 0.090$ $\beta_{yy} = 0.053$ $\beta_{zz} = 0.079$		$\beta_{xx} = -0.089$ $\beta_{yy} = -0.093$ $\beta_{zz} = 0.895$	
Density $[tonne.mm^{-3}]$	$\rho = 1.61 \times 10^{-9}$		$\rho = 1.27 \times 10^{-9}$	
Young's modulus $[GPa]$	$E_{xx} = E_{yy} = 42.28$ $E_{zz} = 3.45$	$E'_{xx} = E'_{yy} = E_{xx} \times (1 + \alpha) = 39.63$ $E'_{zz} = E_{zz} \times (1 + \alpha) = 3.23$	$E_{xx} = E_{yy} = 4.25$ $E_{zz} = 3.45$	$E'_{xx} = E'_{yy} = 1.97$ $E_{zz} = 1.6$

Poisson ratio $[-]$	$\nu_{xy} = 0.12$ $\nu_{xz} = \nu_{yz} = 0.378$		$\nu_{xy} = 0.15$ $\nu_{xz} = \nu_{yz} = 0.378$	
Shear modulus $[GPa]$	$G_{xy} = 18.88$ $G_{xz} = G_{yz} = 1.2$	$G_{xy} = 17.69$ $G_{xz} = G_{yz} = 1.12$	$G_{xy} = 1.85$ $G_{xz} = G_{yz} = 1.2$	$G_{xy} = 0.86$ $G_{xz} = G_{yz} = 0.56$

E.5.3. Hygro-mechanical FEM results

Table 0-8 presents the nodal temperature NT11 (analog to local water content C) results of hygro-mechanical analysis at the first, fifth and last increments of the analysis. These snapshots provide a direct visualization of the moisture content evolution driving hygroscopic strains.

For laminate F10, the model predicts strong moisture gradients during the early stages, with pronounced edge effects. This translates into localized swelling near the specimen boundaries, which progressively propagates toward the core as diffusion proceeds. Such behavior is consistent with the high affinity of flax constituents for water and the resulting rapid uptake and swelling.

Conversely, laminate C10 exhibits a much slower diffusion process. The computed moisture content field does not reach steady state at the end of the simulated immersion duration (~ 3 months), indicating that full saturation is not reached within the considered analysis time period. This result supports the experimentally observed low sensitivity of carbon/epoxy to hygrothermal ageing in terms of moisture uptake.

For the hybrid laminate F6C4, the model predicts an asymmetric moisture-driven deformation. Because the flax-rich sublaminate absorbs water and swells much more than the carbon-rich sublaminate, the latter mechanically restrains the former. This mismatch in free swelling generates an internal bending moment and results in an overall curvature of the specimen (as observed experimentally in **Figure 0-12.a)**.

For the symmetric hybrid laminate C2F6C2, the same restraint mechanism exists (carbon layers limiting the free swelling of the flax core), but the layup symmetry largely balances the swelling mismatch across the thickness. As a result, the dominant effect is a global constraint of deformation (especially in-plane) rather than a pronounced curvature, since the carbon skins impose a stiffer, less hygroscopic outer “shell”.

Figure 0-13 compares the experimental gravimetric curves with the FEM predictions. The numerical gravimetric response is obtained by integrating the water content field over the

specimen volume using the Abaqus “Volume Weighted Average Temperature” plug-in. With the adopted analogy, this operation yields a volume-average measure directly comparable to the experimentally measured global water content.

Overall, the numerical model provides a satisfying prediction of the hybrid laminates (F6C4 and C2F6C2) and reproduces the specific influence of stacking sequence on water uptake kinetics. Indeed, the model predicts a smaller water diffusion slope, and value of saturation for configuration C2F6C2 compared with configuration F6C4. This difference can be explained by the fact that for F6C4 configuration, moisture rapidly penetrates through the flax/epoxy sublaminate, and the resulting water content gradient accelerates transport toward the carbon/epoxy region. In contrast, for C2F6C2, the external carbon/epoxy plies introduce an additional diffusion resistance in the through-thickness direction, slowing down moisture ingress toward the flax-rich core and resulting in reduced absorption kinetics.

The slight overestimation of moisture uptake predicted by the numerical models compared with the experimental measurements for the hybrid laminates, may be attributed to modelling assumptions inherent to the layered representation. In the present formulation, each sublaminate is considered as a homogeneous flax/epoxy or carbon/epoxy region, and potential resin-rich interlaminar zones are not explicitly represented. Hybrid laminates manufactured by resin infusion are particularly prone to the formation of such resin-dominated regions at the interfaces between dissimilar ply blocks due to differences in reinforcement architecture and local permeability. Since the epoxy matrix exhibits a significantly lower moisture uptake compared to flax fibers, the presence of these resin-rich regions effectively reduces the global absorption capacity measured experimentally. Neglecting this local heterogeneity in the numerical model may therefore explain the moderate discrepancy observed between predicted and measured global uptake values. These results show that the proposed sequential hygro-mechanical FEM framework is able to reproduce the main trends of moisture uptake for the different laminate configurations and provide physically meaningful water content field distributions that explain the contrasted swelling behavior of flax and carbon-based laminates, and the intermediate response of hybrid configurations.

Table 0-8. Visual representation of nodal temperature field output at the first, fifth and last increment of the hygro-mechanical analysis for the four composite configurations.

Configuration	Def. scale	1st increment (1 day)	5th increment (5 days)	Last increment (~ 3 months)
F10	5	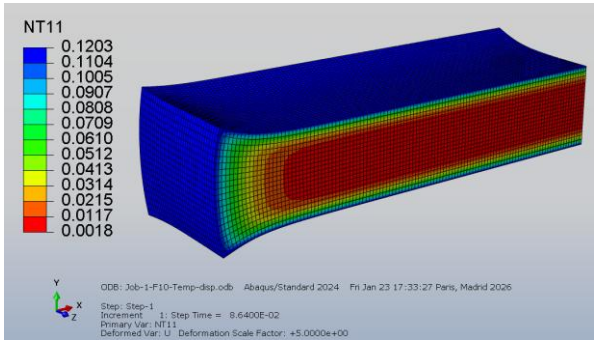	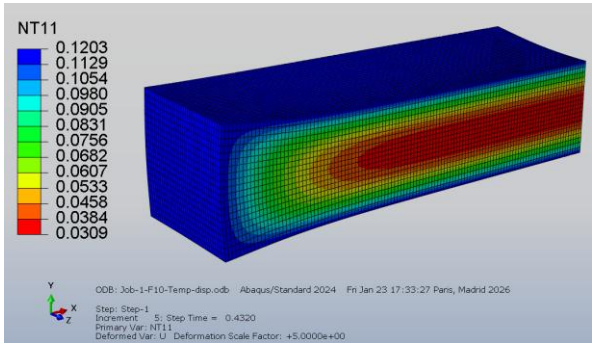	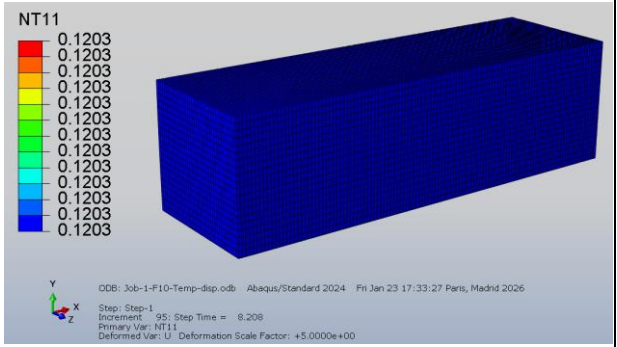
C10	100	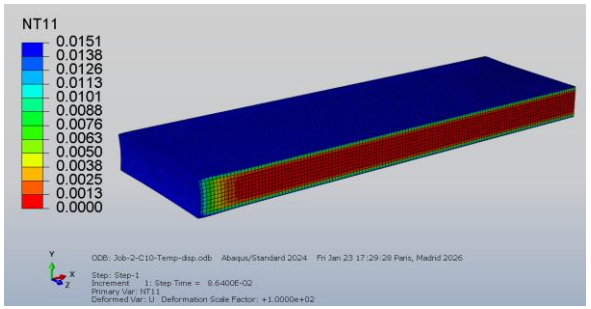	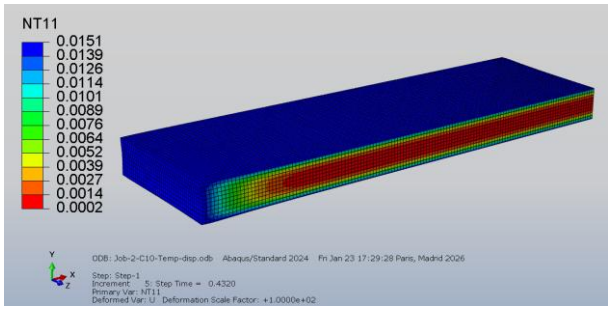	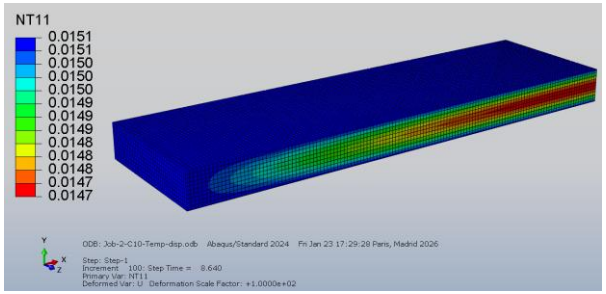

F6C4	1	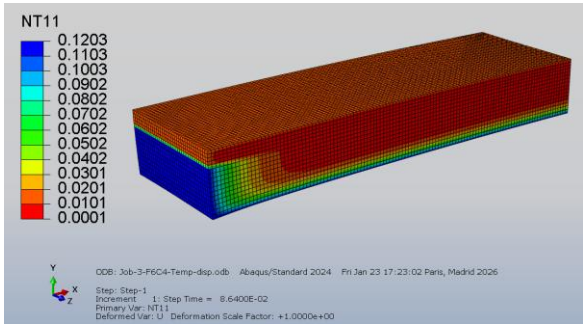	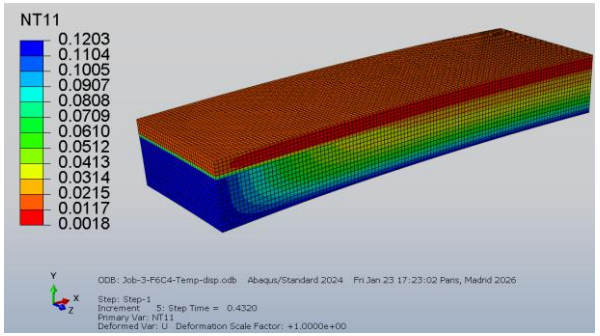	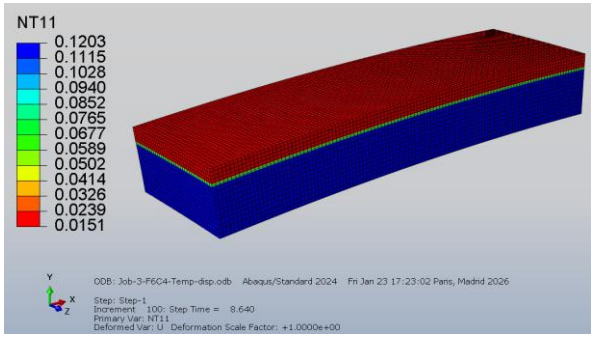
C2F6C2	5	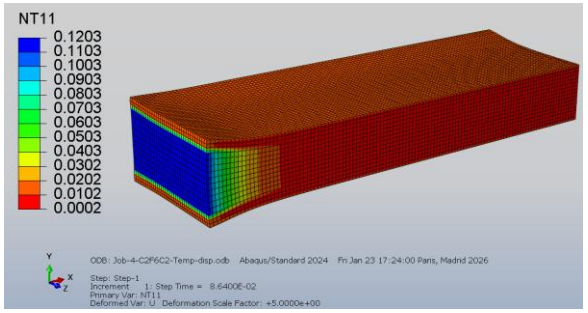	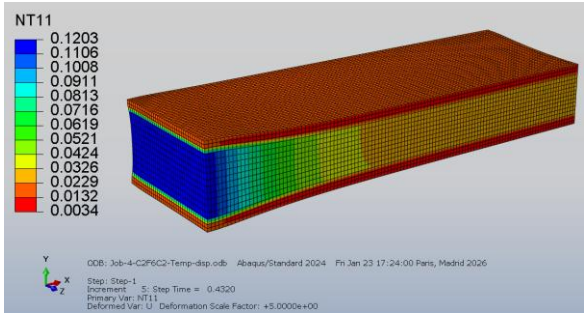	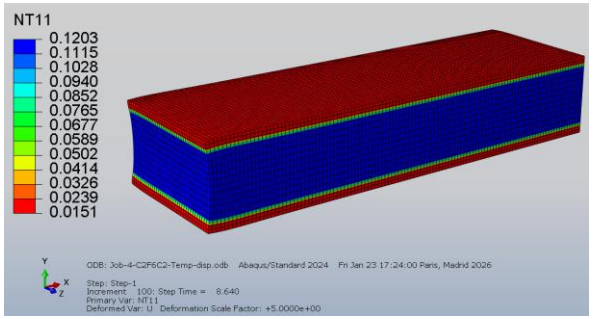

F6C4



→ Curvature (maximal deflection ≃ 1,25 mm)

a)

C2F6C2



→ No curvature

b)

Figure 0-12. Visual observation of geometric change for hybrid laminates a) F6C4 and b) C2F6C2.

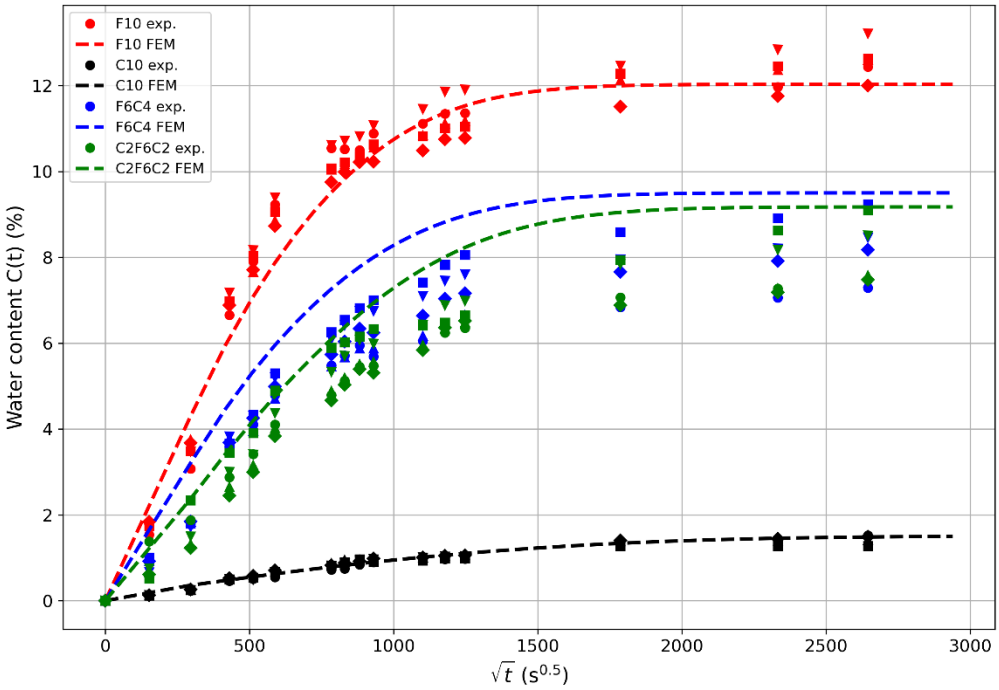

Figure 0-13. Comparison of FEM vs Experimental gravimetric results.

Figure 0-14 compares the experimental hygroscopic strain components (ε_{xx}, ε_{yy} and ε_{zz}) measured for the symmetric hybrid laminate C2F6C2 with the corresponding finite element predictions as a function of the global water content. Each marker symbol corresponds to an individual specimen, and the dashed lines represent the linear fits obtained for the five samples of each material. It should be reminded that the experimental procedure for measurement of hygroscopic strain components is presented in **Subsection E.3.3**, and the numerical data extraction is based on the same concept.

The hybrid configuration naturally exhibits a strongly anisotropic swelling response, as a combination of two materials with anisotropic hygroscopic coefficients. The through-thickness component ε_{zz} increases with water content, reaching $\sim 8-10\%$ compared to $\sim 12\%$ for the reference F10 configuration, and the numerical model accurately predicts these results and confirm a linear evolution of the hygroscopic strain as a function of water content.

For the in-plane components ε_{xx} and ε_{yy}, they remain negative similarly to the reference F10 configuration (indicating an apparent in-plane contraction). The numerical model suggests a non-linear dependence on water content. Indeed, because of the presence of the external carbon fibers, the out-of-plane swelling of flax/epoxy laminate compensates for the in-plane retraction,

at the expense of generation of internal stresses, which will not be addressed in the present paper.

Moreover, maximum values of in-plane strain components are $\sim -0.2\%$ and $\sim -0.4\%$ respectively for fiber and transverse directions, compared to $\sim -1.2\%$ for both direction in the reference F10 configuration. These results indicate that the presence of the carbon skins mechanically restrains the flax fibers through-thickness and in-plane deformations.

Overall, the numerical predictions capture the correct signs, anisotropy and order of magnitude of the three strain components, and underline the non-linear trend observed for the in-plane response.

As for the hybrid asymmetric F6C4 configuration, the experimental measurement of hygroscopic strains was more complicated due to the curvature of the specimens generated by moisture diffusion as shown in **Figure 0-12.a)**. Consequently, the comparison of experimental and numerical hygroscopic behavior for configuration F6C4 will not be presented.

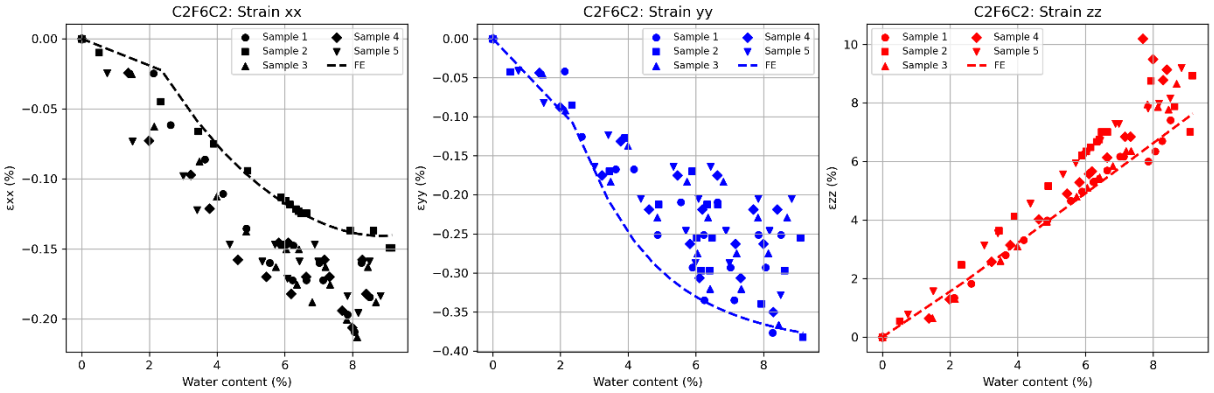

Figure 0-14. Evolution of hygroscopic strain components (ε_{xx}, ε_{yy} and ε_{zz}) as a function of water content for hybrid composite C2F6C2. Experimental data are shown as markers for five specimens per material, and dashed lines represent the numerical predictions.

E.5.4. Three point bending FEM results

A second mechanical step was carried out to reproduce the elastic response in three-point bending for the four laminate configurations, before (dry state) and after ageing (subsequent to hygromechanical step). The objective of this step is not to predict failure, but to verify whether the moisture dependent elastic properties introduced in **Subsection E.5.2** can correctly reproduce the initial force-deflection slope measured experimentally.

Figure 0-15 illustrates the 3D bending model implemented in Abaqus/Standard. The specimen is placed on one rigid support and loaded by a rigid nose, consistent with the experimental fixture geometry (radius 5 mm). The rigid tooling is modeled with R3D4 elements, and the specimens are modeled as solid laminate with the same stacking-sequence partitioning adopted in the previous hygro-mechanical simulations.

Boundary conditions are applied at the rigid bodies' reference points to reproduce the test conditions. The support prevents vertical displacement along the Y-axis (cf. **Figure 0-15**), and the loading nose is driven by an imposed displacement also along the same axis, ensuring displacement-controlled quasi-static bending conditions.

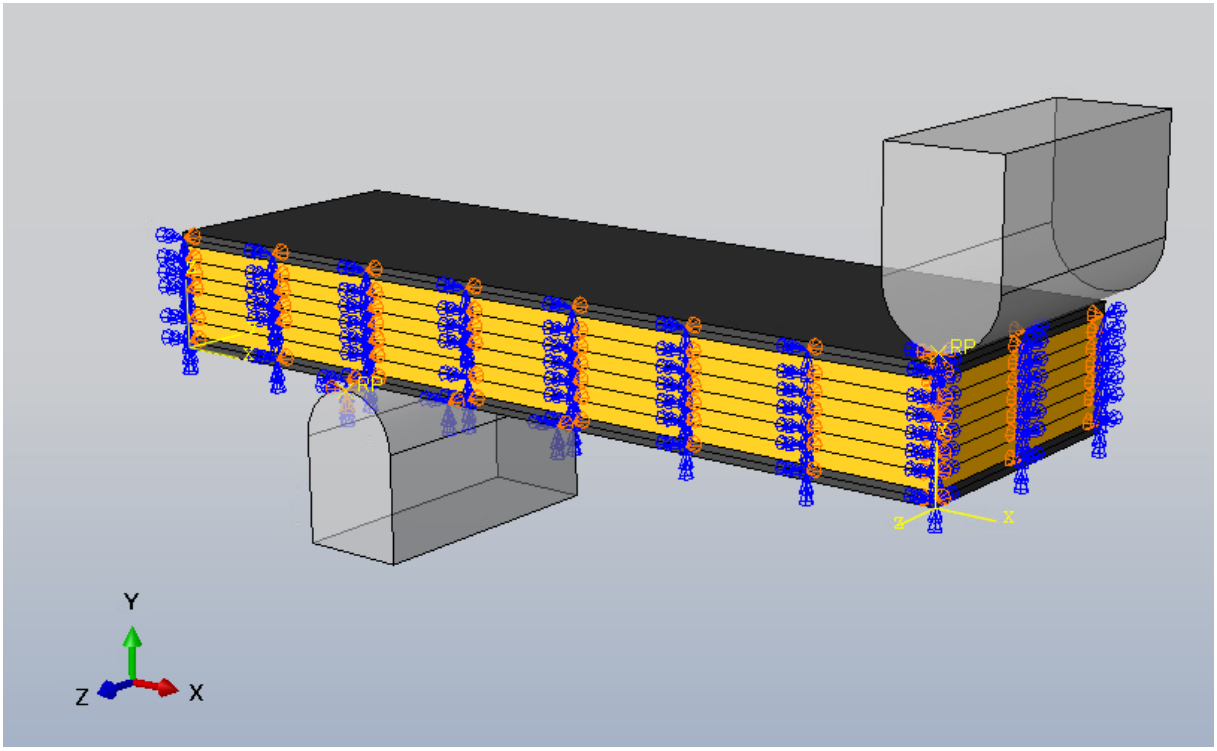

Figure 0-15. Numerical model representation of three point bending test for configuration C2F6C2.

The comparison between experimental force–deflection curves and FEM predictions is presented in **Figure 0-16**. In each panel of the figure, the FEM curves correspond to the linear elastic portion of the response (dashed lines), whereas the experimental curves include progressive nonlinearity, peak load (failure), and post-failure behavior.

For F10, the experimental response shows pronounced non-linearity (especially after ageing), with a large increase in deflection capacity and progressive degradation mechanisms. This behavior is associated with matrix plasticization, fiber–matrix interface degradation, and progressive cracking induced by moisture exposure. In contrast, the FEM prediction, as it is

built, remains purely elastic and therefore cannot reproduce this progressive behavior, since no damage or nonlinear constitutive law is introduced in the present formulation. For C10, the experimental curves remain close to linear up to the peak load, both before and after ageing, which is consistent with the material's low moisture uptake and relatively brittle behavior. In this case, the FEM prediction matches the initial slope reasonably well and also reproduces the slight rigidity decrease after ageing. The agreement in bending stiffness confirms that the moisture-dependent elastic properties identified for the carbon/epoxy laminate provide a consistent description of its macroscopic response within the elastic regime.

For the hybrid laminates, the FEM predictions fall closer to the experimental curves in the early stage than for F10, indicating that the global bending rigidity of the hybrid architectures is predominantly governed by elastic interactions between the carbon and flax sublaminates. The improved agreement observed for the hybrids suggests that the proposed framework is particularly suitable for configurations where elastic coupling effects dominate over progressive damage mechanisms.

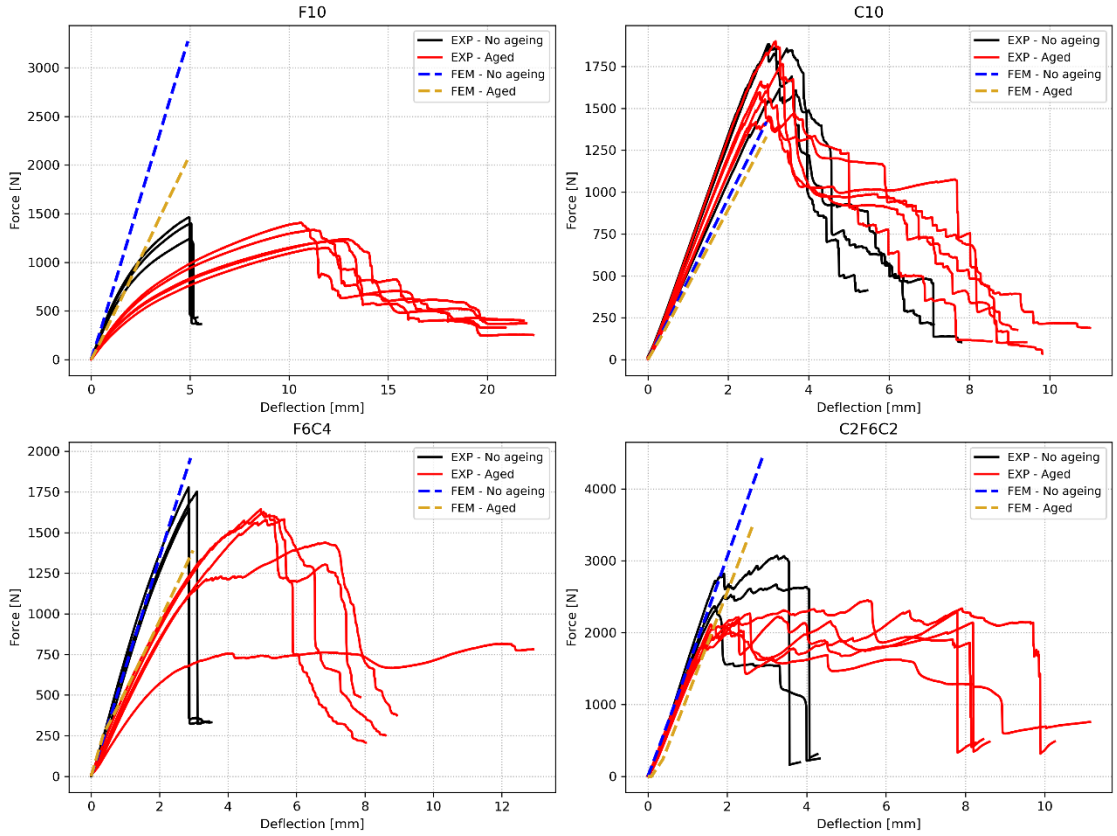

Figure 0-16. Comparison of experimental three point bending test results with FEM predictions of elastic behavior before and after ageing for the four composite specimen configurations.

E.6. Conclusion

This chapter evaluated the hygro-mechanical behavior of flax/epoxy, carbon/epoxy, and hybrid flax/carbon laminates manufactured with the same bidirectional twill architecture used earlier in the thesis, with the objective of determining whether hybridization—introduced in Chapter D primarily for structural efficiency (Banea 2023) and interfacial stress management—also modifies environmental sensitivity at the material scale. The work combined gravimetric immersion at 50 °C, identification of diffusion parameters through Fickian modelling, experimental monitoring of hygroscopic swelling in three directions, and flexural characterization by three-point bending before and after hygrothermal ageing. In parallel, a numerical framework based on the thermal–diffusion analogy was implemented in Abaqus to simulate moisture transport and the associated strain/stress fields in both mono-material and multi-material laminates, using the wetness-fraction approach to ensure consistency at material interfaces.

The experimental results first confirmed a strong contrast in moisture uptake propensity between the two reference laminates. The flax composite F10 exhibited the highest absorption, whereas the carbon composite C10 showed minimal uptake, consistent with the fundamentally different fiber chemistries and interphase sensitivities to water. This contrast was reflected not only in the gravimetric kinetics but also in the subsequent mechanical response: under bending, the carbon laminate retained a predominantly brittle response and an essentially unchanged curve shape after ageing, indicating very low sensitivity of its flexural behavior to the considered moisture exposure.

In contrast, the flax laminate displayed a pronounced evolution after ageing, with reduced maximum stress and increased strain at failure, evidencing a transition from abrupt brittle failure to a more ductile and progressive damage behavior under bending. The flexural modulus measurements further quantified this divergence: the chapter reports only a slight decrease for C10 (–6.3%), while F10 exhibited a reduction exceeding half of its initial modulus (–53.6%). Within the scope of the present study, these observations support the interpretation that moisture uptake in flax-based laminates substantially degrades effective stiffness and modifies damage development, plausibly through combined effects of matrix plasticization, fibre swelling, and fibre/matrix interphase weakening, whereas carbon/epoxy laminates remain comparatively stable under the same exposure conditions (Dhakal et al., 2007; Saidane et al., 2016).

A second key outcome concerns the role of hybrid architecture on hygroscopic deformation. The numerical hygro-mechanical results predict strong moisture gradients and edge effects in F10 during early immersion stages, with swelling progressively propagating from the boundaries toward the core as diffusion proceeds. For the asymmetric hybrid laminate F6C4, the modelling predicts an asymmetric moisture-driven deformation: the flax-rich region absorbs and swells significantly more than the carbon-rich region, while the latter mechanically restrains the former, generating an internal bending moment and an overall curvature, consistent with the experimental observation of curvature reported in the chapter. For the symmetric hybrid laminate C2F6C2, the same restraint mechanism exists, but the layup symmetry largely balances the through-thickness mismatch, leading primarily to a global constraint of deformation rather than pronounced curvature. These results highlight that hybridization does not only change stiffness and stress-transfer (as shown in Chapter D), but also governs how hygroscopic eigenstrains are internally constrained and converted into bending-type distortions or self-equilibrated stress fields.

From a modelling standpoint, the chapter demonstrates that the thermal–diffusion analogy provides a practical and effective route to simulate sequentially coupled diffusion and swelling in Abaqus for both mono-material and multi-material laminates. The wetness-fraction formulation is shown to be particularly valuable for hybrid composites, because it bypasses the discontinuity of local water content at material interfaces and enables stable computation of spatial moisture fields that can be compared to gravimetric measurements through volume averaging. Beyond matching global uptake trends, the modelling adds mechanistic insight by revealing where moisture gradients are highest, how constraint between sublaminates drives curvature, and why symmetric versus asymmetric hybridization leads to qualitatively different deformation modes under hygrothermal exposure.

In terms of perspectives for the rest of the thesis, these findings constrain how flax, carbon, and hybrid patches should be interpreted in bonded strengthening applications when moisture exposure is expected. First, the pronounced stiffness loss and altered damage behavior of F10 after ageing indicate that patch mechanical properties used to rationalize strengthening efficiency in Chapter D cannot be assumed time-invariant for flax-rich configurations in humid service. Second, the predicted hybrid-specific swelling constraints and curvature tendencies suggest that environmental exposure can introduce additional eigenstrains and secondary stresses that may interact with interface loading states, especially near stress concentrators

typical of bonded patches under bending. Finally, the validated FEM framework provides a basis to incorporate moisture fields and moisture-dependent properties in future simulations of multi-material bonded systems, which is a necessary step toward bridging material ageing to joint-scale durability considerations.

Overall, Chapter E completes the thesis narrative established by Chapters C and D by showing that material selection for steel strengthening cannot be based solely on initial adhesion and dry mechanical performance: the intrinsic hygro-mechanical sensitivity of flax-based laminates and the architecture-dependent response of hybrids must also be accounted for when anticipating long-term behavior. In the broader thesis conclusions, these results provide the environmental "material baseline" needed to interpret how strengthening efficiency and failure mechanisms may evolve when moisture alters composite response, and they motivate the inclusion of moisture-dependent constitutive and diffusion–swelling descriptions when extending modelling toward service-like conditions.

Appendix A

This appendix presents the totality of three point bending tests performed in chapter D.

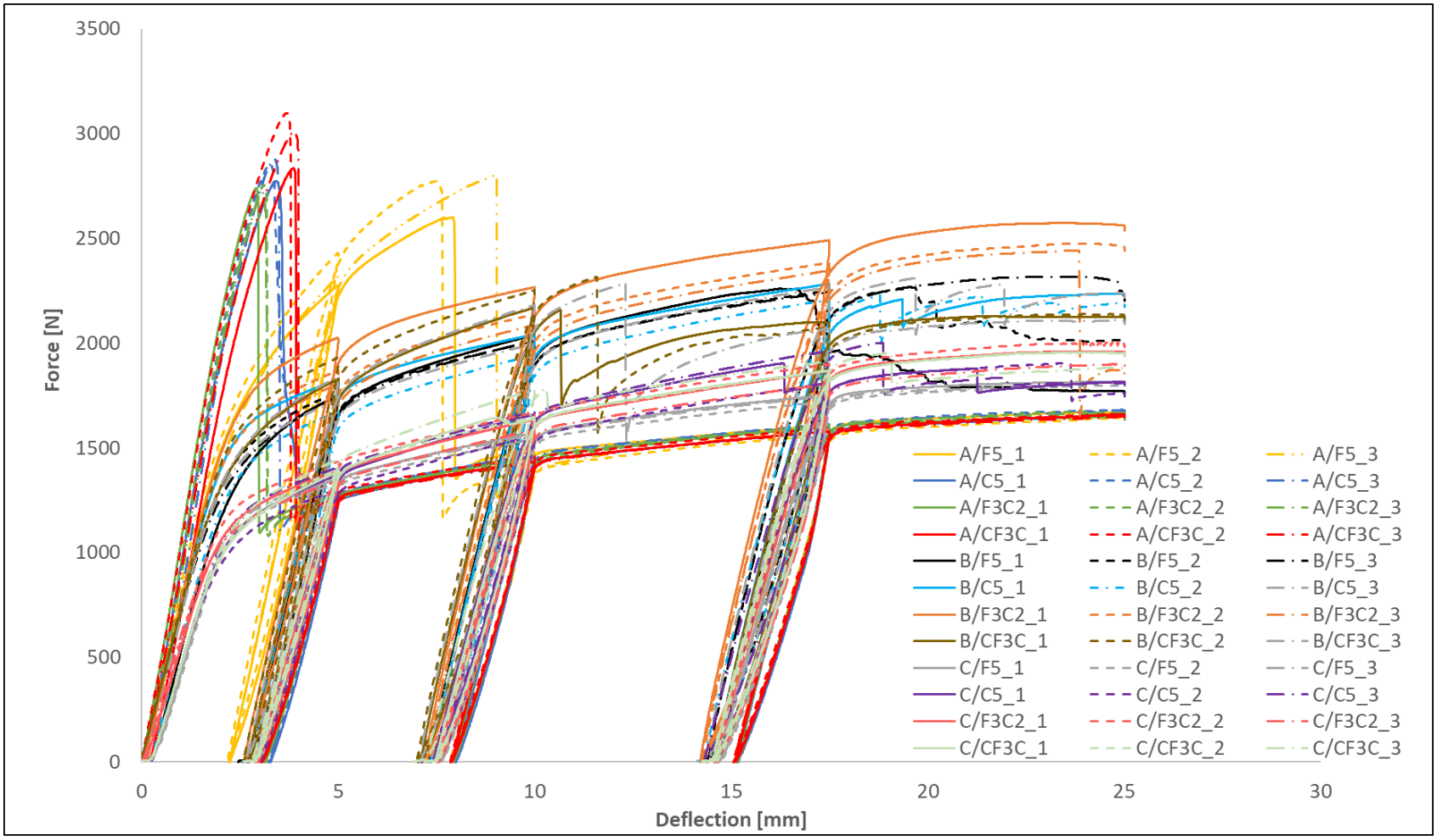

Appendix B

Constitutive models of adhesives

a) Adhesive A

Adhesive A is modeled with cohesive elements following a triangular linear traction-separation law. The elastic behavior can be written as

$$\boldsymbol{t} = \begin{Bmatrix} t_n \\ t_s \\ t_t \end{Bmatrix} = \begin{bmatrix} K_{nn} & 0 & 0 \\ 0 & K_{ss} & 0 \\ 0 & 0 & K_{tt} \end{bmatrix} \begin{Bmatrix} \delta_n \\ \delta_s \\ \delta_t \end{Bmatrix} \quad \textbf{(B.1)}$$

Where t_n, t_s and t_t represent the normal (mode I) and the two shear (mode II and III) tractions, respectively. The corresponding separations are denoted by δ_n, δ_s and δ_t. Similarly, K_{nn}, K_{ss} and K_{tt} are the corresponding elastic stiffnesses.

The damage initiation of the cohesive layer under mixed-mode loading was predicted by the quadratic stress failure criterion

$$QUADS = \left\{\frac{\langle t_n \rangle}{t_n^0}\right\}^2 + \left\{\frac{t_s}{t_s^0}\right\}^2 + \left\{\frac{t_t}{t_t^0}\right\}^2 = 1 \quad \textbf{(B.2)}$$

Where t_n^0, t_s^0 and t_t^0 represent the peak values of the nominal stress when the deformation is either purely normal to the interface or purely in the first or the second shear direction, respectively.

Damage evolution is based on the Benzeggagh-Kenane (BK) fracture criterion (Benzeggagh and Kenane 1996), which is particularly useful when the critical fracture energies during deformation purely along the first and the second shear directions are the same; that is, $G_s^C = G_t^C$. It is given by:

$$G_n^C + (G_s^C - G_n^C)\left\{\frac{G_S}{G_T}\right\}^\eta = G^C \quad \textbf{(B.3)}$$

Where G_n^C, G_s^C and G_t^C refer to the critical fracture energies required to cause failure in the normal, first and second shear directions, respectively.

$G_S = G_s + G_t$, $G_T = G_n + G_S$, and η is a material parameter fit by performing sensitivity analysis.

Denoted by G_n, G_s and G_t are the work done by the tractions and their conjugate relative displacements in the normal, first, and second shear directions, respectively.

b) Adhesive B

Adhesive B is modeled following a bilinear elastic-plastic law. The elastic response is given by:

$$\sigma = E\epsilon \text{ , for } \epsilon < \epsilon_y \quad \textbf{(B.4)}$$

With E The young's modulus and $\epsilon_y = \frac{\sigma_y}{E}$; where σ_y and ϵ_y are the yield stress and strain, respectively.

After yield (σ_y), the stress follows:

$$\sigma = \sigma_y + H(\epsilon_p) \quad \textbf{(B.5)}$$

Where H is the hardening modulus calibrated from the failure stress and strain σ_f and ϵ_f:

$$H = \frac{\sigma_f - \sigma_y}{\epsilon_f - \epsilon_y} \quad \textbf{(B.6)}$$

c) Adhesive C

This very flexible adhesive is modeled as a bulk hyperelastic material with a Neo-Hooke strain energy potential:

$$U = C_{10}(I_1 - 3) + \frac{1}{D_1}(J^{el} - 1)^2 \quad \textbf{(B.7)}$$

Where I_1 is the first deviatoric strain invariant, C_{10} and D_1 are temperature-dependent material pameters. The latter parameters are required by the abaqus Standard/implicit solver, and are given by the initial shear modulus μ_0 and bulk modulus K_0 of the adhesive as follow:

$$\mu_0 = 2C_{10}, \qquad K_0 = \frac{2}{D_1} \quad \textbf{(B.8)}$$

Appendix C

This appendix shows the comparison of load-deflection curves of all numerical models with corresponding representative experimental result.

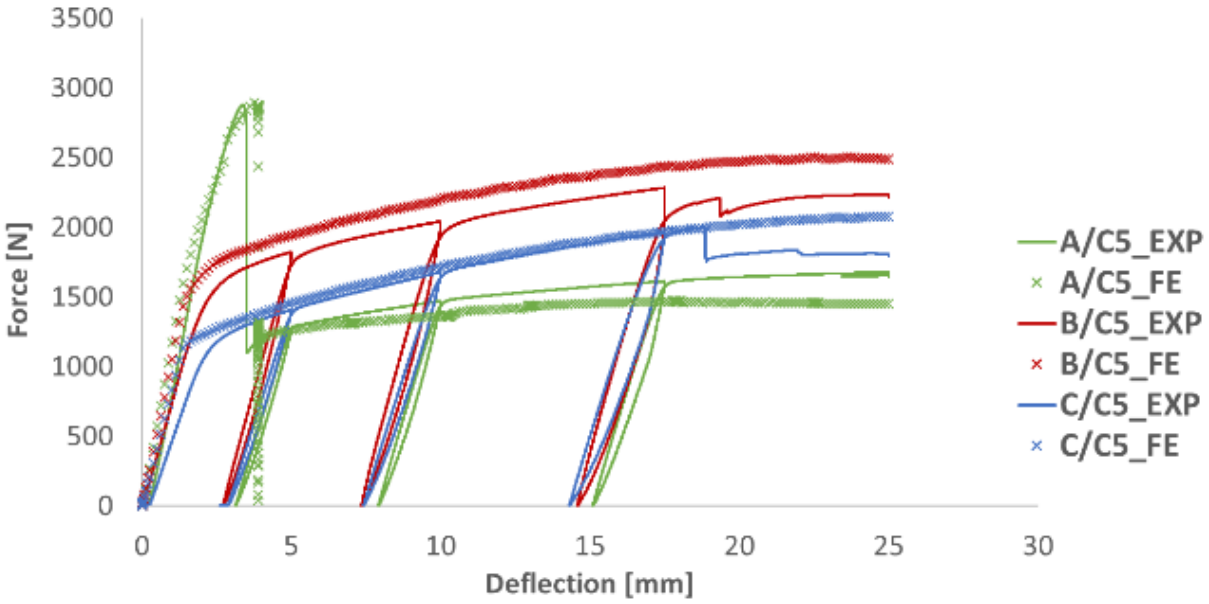

C5

a)

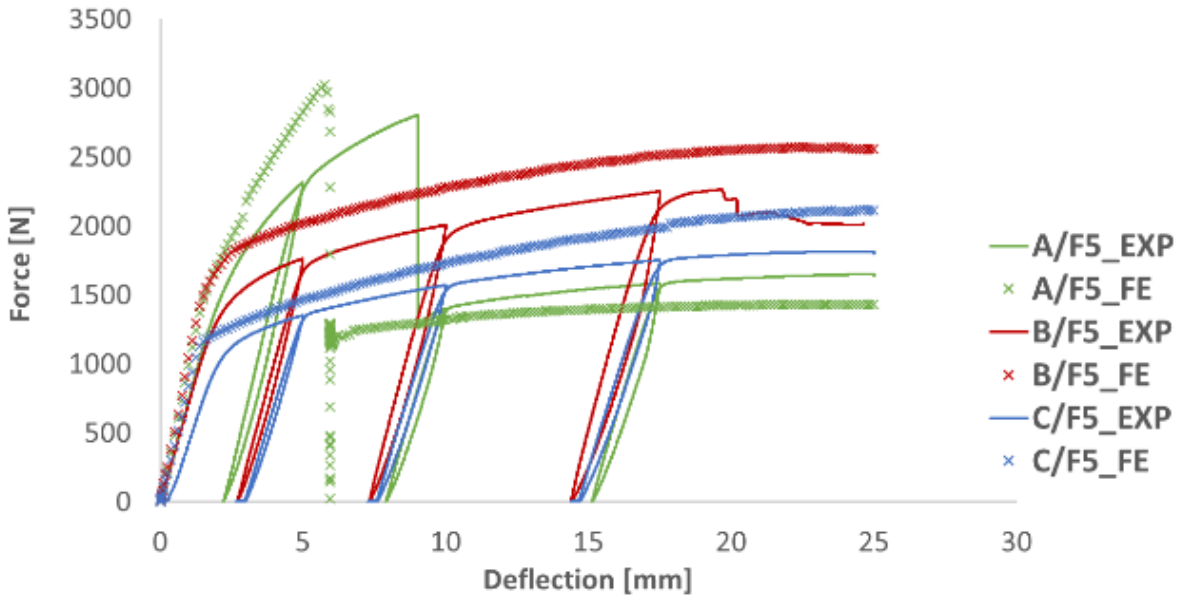

F5

b)

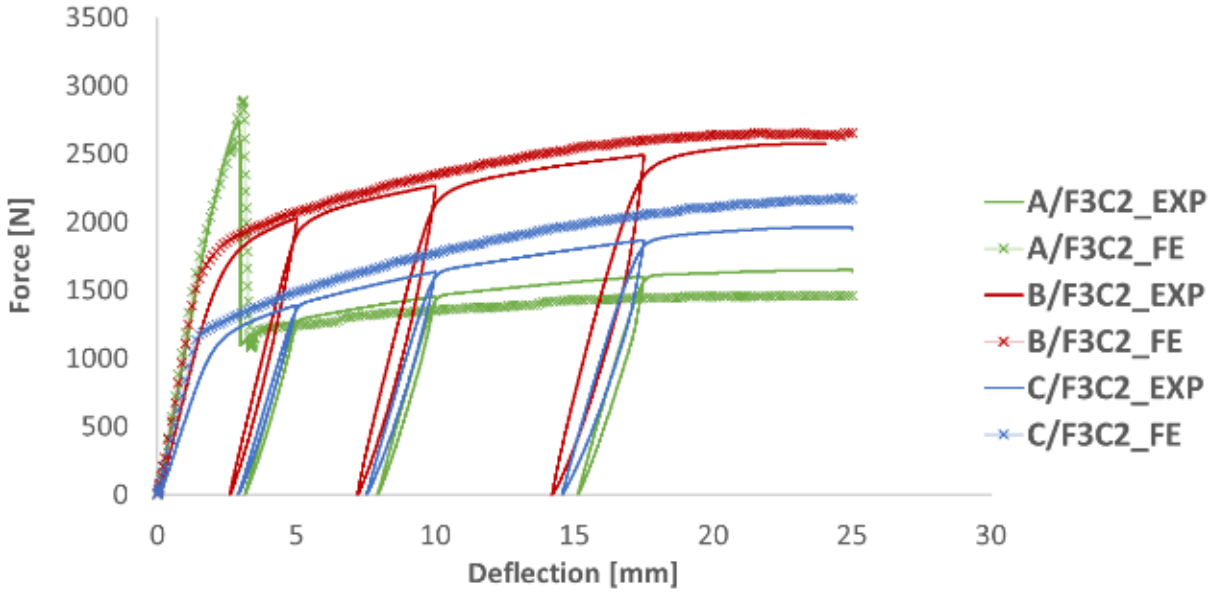

F3C2

c)

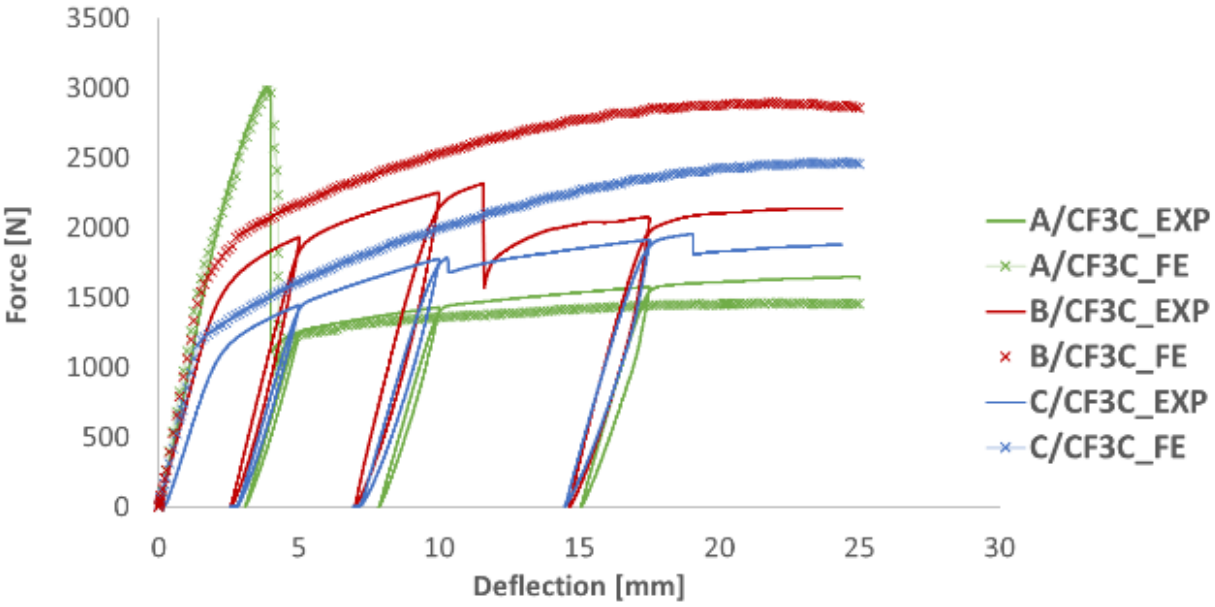

CF3C

d)

Caption. Comparison of experimental and FE load-deflection curves for specimens bonded to a) C5, b) F5, c) F3C2 and d) CF3C composite patch configuration

Appendix D

This appendix presents the developed python code for post-processing of wetness fraction, to calculate the true water content fields in hygro-mechanical simulation of multi-materials.

```
import shutil
import os
from odbAccess import openOdb
from abaqusConstants import *

# === USER INPUT ===
# User defined paths (example for F6C4 configuration)
odb_path = "Job-3-F6C4.odb"
new_odb_path = "Job-3-F6C4_withTemps.odb"

# Definition of value of water content at saturation for each material
node_sets = {
    "SET-C": 0.0151,
    "SET-F": 0.1203
}

# Make a copy of .odb file at file system level
shutil.copyfile(odb_path, new_odb_path)

# Open the copy in write mode
odb = openOdb(new_odb_path, readOnly=False)

# Work on the last step of the original analysis
last_step_name = list(odb.steps.keys())[-1]
last_step = odb.steps[last_step_name]

# Precompute node labels in each set
set_labels = {}
```

```
for set_name in node_sets:
    labels = set(n.label for n in odb.rootAssembly.nodeSets[set_name].nodes[0])
    set_labels[set_name] = labels

# Instance (assumes only one)
first_instance = list(odb.rootAssembly.instances.values())[0]
#print(first_instance.name)
#odb.close()

# === Create a new step in the ODB ===
new_step = odb.Step(name='Step-2',
                    description='Step with modified NT11 for sequential analysis',
                    domain=TIME,
                    timePeriod=1.0)

# === Loop through all frames of last step ===
for i, frame in enumerate(last_step.frames):
    if 'NT11' not in frame.fieldOutputs:
        continue
    src_field = frame.fieldOutputs['NT11']
    field_values = list(src_field.values)

    labels = []
    data = []
    for val in field_values:
        coeff = None
        for set_name, factor in node_sets.items():
            if val.nodeLabel in set_labels[set_name]:
                coeff = factor
                break
        if coeff is not None:
            new_val = val.data * coeff
```

```
        else:
            new_val = val.data
        labels.append(val.nodeLabel)
        data.append(new_val)

    # Create corresponding frame in new step
    new_frame = new_step.Frame(incrementNumber=i,
                               frameValue=frame.frameValue,
                               description="Modified temps frame {}".format(i))

    # Write modified NT11
    new_field = new_frame.FieldOutput(name="NT11",
                                      description="Modified nodal temperature",
                                      type=SCALAR)
    #print(new_field)
    #odb.close()
    #os.remove("Job-3-F6C4_withTemps.odb")

    new_field.addData(position=NODAL,
                      instance=first_instance,
                      labels=tuple(labels),
                      data=tuple((val,) for val in data))



# Save and close
odb.save()
odb.close()
print("New step 'MODIFIED_TEMPS' added to:", new_odb_path)
```

References

A

AASHTO/NSBA. 2024. “Guidelines for Field Repairs and Retrofits of Steel Bridges.” American Association of State Highway and Transportation Officials / National Steel Bridge Alliance.

ABS. 2022. *Requirements for Bonded and Composite Repairs of Steel Structures and Piping 2022*.

Akpinar, Salih, Muhammet Onur Doru, Adnan Özel, Murat Demir Aydin, and Hamed Ghaffarzadeh Jahanpasand. 2013. “The Effect of the Spew Fillet on an Adhesively Bonded Single-Lap Joint Subjected to Bending Moment.” *Composites Part B: Engineering* 55 (December): 55–64. https://doi.org/10.1016/j.compositesb.2013.05.056.

Al-Azzawi, Ahmad S. M., C. A. Featherston, Colin Lupton, et al. 2024. “Impact Characteristics of S2-Glass Fibre/FM94-Epoxy Composites under High and Cryogenic Temperatures: Experimental and Numerical Investigation.” *Composites Part B: Engineering* 287 (December): 111786. https://doi.org/10.1016/j.compositesb.2024.111786.

Al-Saidy, Abdullah Hilal. 2001. “Structural Behavior of Composite Steel Beams Strengthened/Repaired with Carbon Fiber Reinforced Polymer Plates.” Graduate College Iowa State University.

Al-Shawaf, A., R. Al-Mahaidi, and X. L. Zhao. 2009. “Effect of Elevated Temperature on Bond Behaviour of High Modulus CFRP/Steel Double-Strap Joints.” *Australian Journal of Structural Engineering* 10 (1): 63–74. https://doi.org/10.1080/13287982.2009.11465033.

Anderson, Ted L. 2005. *Fracture Mechanics: Fundamentals and Applications, Third Edition*. 0 ed. CRC Press. https://doi.org/10.1201/9781420058215.

Arouche, M. M., S. Budhe, L. A. Alves, S. Teixeira de Freitas, M. D. Banea, and S. de Barros. 2018. “Effect of Moisture on the Adhesion of CFRP-to-Steel Bonded Joints Using Peel Tests.” *Journal of the Brazilian Society of Mechanical Sciences and Engineering* 40 (1): 10. https://doi.org/10.1007/s40430-017-0959-6.

Arouche, Marcio M, Sandip Budhe, Mariana D. Banea, Sofia Teixeira de Freitas, and Silvio de Barros. 2019. “Interlaminar Adhesion Assessment of Carbon-Epoxy Laminates under Salt Water Ageing Using Peel Tests.” *Proceedings of the Institution of Mechanical Engineers, Part L: Journal of Materials: Design and Applications* 233 (8): 1555–63. https://doi.org/10.1177/1464420718766626.

ASTM A36. 2019. “ASTM A36 Steel, Plate.” https://www.matweb.com/search/DataSheet.aspx?MatGUID=afc003f4fb40465fa3df05129f0e88e6&ckck=1.

ASTM D3039. 2014. “ASTM D3039: Tensile Test on Composites.” ASTM D3039: Tensile Test on Composites. https://www.zwickroell.com/industries/composites/astm-d3039-tensile-test-on-composites/.

ASTM D3167. 2017. “ASTM D3167 Adhesive Floating Roller Peel Testing.” https://www.admet.com/testing-applications/testing-standards/astm-d3167-adhesive-floating-roller-peel-testing/.

ASTM D3528. 2002. *Standard Test Method for Strength Properties of Double Lap Shear Adhesive Joints by Tension Loading*.

ASTM D7264. 2021. “Standard Test Method for Flexural Properties of Polymer Matrix Composite Materials.” Standard Test Method for Flexural Properties of Polymer Matrix Composite Materials. https://www.astm.org/d7264_d7264m-21.html.

ASTM E8. 2024. “ASTM E8: Standard & Specimens for Metals Tensile Test.” ASTM E8: Standard & Specimens for Metals Tensile Test. https://www.zwickroell.com/industries/metals/metals-standards/metals-tensile-test-astm-e8/.

Azwa, Z. N., B. F. Yousif, A. C. Manalo, and W. Karunasena. 2013. “A Review on the Degradability of Polymeric Composites Based on Natural Fibres.” *Materials & Design* 47 (May): 424–42. https://doi.org/10.1016/j.matdes.2012.11.025.

Badami, Andrea, Maria Letizia Raffa, Olga Klinkova, Raffaella Rizzoni, Tony Da Silva Botelho, and Georges Zambelis. 2024. “Surface Roughness Influence on the Behaviour of Biocomposite Adhesive Joints.” *International Journal of Mechanical Sciences* 283 (December): 109624. https://doi.org/10.1016/j.ijmecsci.2024.109624.

B

Baley, Christophe. 2020. “Fibres naturelles de renfort pour matériaux composites.” *Matériaux fonctionnels - Matériaux biosourcés*, ahead of print. https://doi.org/10.51257/a-v1-n2220.

Banea, Mariana Doina. 2023. “Natural Fibre Composites and Their Mechanical Behaviour.” *Polymers* 15 (5): 5. https://doi.org/10.3390/polym15051185.

Bartlett, Michael D., Scott W. Case, Anthony J. Kinloch, and David A. Dillard. 2023. “Peel Tests for Quantifying Adhesion and Toughness: A Review.” *Progress in Materials Science* 137 (August): 101086. https://doi.org/10.1016/j.pmatsci.2023.101086.

Benzeggagh, M. L., and M. Kenane. 1996. “Measurement of Mixed-Mode Delamination Fracture Toughness of Unidirectional Glass/Epoxy Composites with Mixed-Mode Bending Apparatus.” *Composites Science and Technology* 56 (4): 439–49. https://doi.org/10.1016/0266-3538(96)00005-X.

Blackman, B., and A. Kinloch. 2001. “Fracture Tests on Structural Adhesive Joints.” In *European Structural Integrity Society*, vol. 28. Elsevier. https://doi.org/10.1016/S1566-1369(01)80036-4.

Blackman, B. R. K., A. J. Brunner, and P. Davies. 2001. “Delamination Fracture of Continuous Fibre Composites: Mixed-Mode Fracture.” In *European Structural Integrity Society*, edited by D. R. Moore, A. Pavan, and J. G. Williams, vol. 28. Fracture Mechanics Testing Methods for Polymers, Adhesives and Composites. Elsevier. https://doi.org/10.1016/S1566-1369(01)80040-6.

Blackman, B. R. K., A. J. Kinloch, and M. Paraschi. 2005. “The Determination of the Mode II Adhesive Fracture Resistance, GIIC, of Structural Adhesive Joints: An Effective Crack Length Approach.” *Engineering Fracture Mechanics* 72 (6): 877–97. https://doi.org/10.1016/j.engfracmech.2004.08.007.

Bonilla Mora, Veronica, Magdalena Mieloszyk, and Wieslaw Ostachowicz. 2018. “Model of Moisture Absorption by Adhesive Joint.” *Mechanical Systems and Signal Processing* 99 (January): 534–49. https://doi.org/10.1016/j.ymssp.2017.06.042.

Bordes, M., P. Davies, J. Y. Cognard, L. Sohier, V. Sauvant-Moynot, and J. Galy. 2009. “Prediction of Long Term Strength of Adhesively Bonded Steel/Epoxy Joints in Sea Water.” *International Journal of Adhesion and Adhesives* 29 (6): 595–608. https://doi.org/10.1016/j.ijadhadh.2009.02.013.

Borrie, Daniel, Saad Al-Saadi, Xiao-Ling Zhao, R. K. Singh Raman, and Yu Bai. 2021. “Bonded CFRP/Steel Systems, Remedies of Bond Degradation and Behaviour of CFRP Repaired Steel: An Overview.” *Polymers* 13 (9): 1533. https://doi.org/10.3390/polym13091533.

Bouchikhi, A. S., A. Megueni, S. Gouasmi, and F. B. Boukoulda. 2013. “Effect of Mixed Adhesive Joints and Tapered Plate on Stresses in Retrofitted Beams Bonded with a Fiber-Reinforced Polymer Plate.” *Materials & Design* 50 (September): 893–904. https://doi.org/10.1016/j.matdes.2013.03.052.

Bourmaud, Alain, Johnny Beaugrand, Darshil U. Shah, Vincent Placet, and Christophe Baley. 2018. “Towards the Design of High-Performance Plant Fibre Composites.” *Progress in Materials Science* 97 (August): 347–408. https://doi.org/10.1016/j.pmatsci.2018.05.005.

Brunner, A. J., B. R. K. Blackman, and P. Davies. 2001. “Mode I Delamination.” In *European Structural Integrity Society*, edited by D. R. Moore, A. Pavan, and J. G. Williams, vol. 28. Fracture Mechanics Testing Methods for Polymers, Adhesives and Composites. Elsevier. https://doi.org/10.1016/S1566-1369(01)80038-8.

Budhe, S., M. D. Banea, S. de Barros, and L. F. M. da Silva. 2017. “An Updated Review of Adhesively Bonded Joints in Composite Materials.” *International Journal of Adhesion and Adhesives* 72 (January): 30–42. https://doi.org/10.1016/j.ijadhadh.2016.10.010.

Budzik, Michal K., Markus Wolfahrt, Paulo Reis, et al. 2022. “Testing Mechanical Performance of Adhesively Bonded Composite Joints in Engineering Applications: An Overview.” *The Journal of Adhesion* 98 (14): 2133–209. https://doi.org/10.1080/00218464.2021.1953479.

C

Calabrese, Angelo Savio, Tommaso D'Antino, and Pierluigi Colombi. 2024. "Effect of Adhesive Ductility on the Bond Behavior of CFRP-Steel Cohesive Interfaces Made with Toughened Epoxy Resin." *Composites Science and Technology* 257 (October): 110824. https://doi.org/10.1016/j.compscitech.2024.110824.

Célino, Amandine, Sylvain Fréour, Frédéric Jacquemin, and Pascal Casari. 2013. "Characterization and Modeling of the Moisture Diffusion Behavior of Natural Fibers." *Journal of Applied Polymer Science* 130 (1): 297–306. https://doi.org/10.1002/app.39148.

Célino, Amandine, Sylvain Fréour, Frédéric Jacquemin, and Pascal Casari. 2014. "The Hygroscopic Behavior of Plant Fibers: A Review." *Frontiers in Chemistry* 1. https://doi.org/10.3389/fchem.2013.00043.

Cerema. 2017. "Instruction Technique Pour La Surveillance et l'entretien Des Ouvrages d'art."

Chang, Peng-Hsiang, and Tso-Liang Teng. 2004. "Numerical and Experimental Investigations on the Residual Stresses of the Butt-Welded Joints." *Computational Materials Science* 29 (4): 511–22. https://doi.org/10.1016/j.commatsci.2003.12.005.

Chataigner, Sylvain, Karim Benzarti, Gianluca Gemignani, et al. 2017. *Experimental Evaluation of the Developed Reinforcement System in FASSTBridge Project*.

Chataigner, Sylvain, and Emilie Lepretre. 2025. "Illustration of the Use of Adhesively Bonded Carbon Fiber Reinforced Polymer Reinforcement to Increase Fatigue Life of Steel Bridges." In *Rehabilitation of Metallic Structural Systems Using Fiber Reinforced Polymer (FRP) Composites*. Elsevier. https://doi.org/10.1016/B978-0-443-22084-5.00003-8.

Chilali, Abderrazak, Mustapha Assarar, Wajdi Zouari, Hocine Kebir, and Rezak Ayad. 2017. "Effect of Geometric Dimensions and Fibre Orientation on 3D Moisture Diffusion in Flax Fibre Reinforced Thermoplastic and Thermosetting Composites." *Composites Part A: Applied Science and Manufacturing* 95 (April): 75–86. https://doi.org/10.1016/j.compositesa.2016.12.020.

Chilali, Abderrazak, Mustapha Assarar, Wajdi Zouari, Hocine Kebir, and Rezak Ayad. 2018. "Analysis of the Hydro-Mechanical Behaviour of Flax Fibre-Reinforced Composites: Assessment of Hygroscopic Expansion and Its Impact on Internal Stress." *Composite Structures* 206 (December): 177–84. https://doi.org/10.1016/j.compstruct.2018.08.037.

Cocaud, Julie. 2019. "Viellissement Humide de Matériaux Composites de Pales d'hélicoptères : Caractérisations et Modélisations, de l'échelle de La Résine à Celle d'assemblages Multi-Matériaux." Université de Nantes.

Čolić, A., F. Wiesner, D. Hopkin, M. Spearpoint, W. Wu, and L. Bisby. 2024. "Application of Microscale Methods to Study the Heat-Induced Delamination in Engineered Wood

Products Bonded with One-Component Polyurethane Adhesives." *International Journal of Adhesion and Adhesives* 135 (December): 103834. https://doi.org/10.1016/j.ijadhadh.2024.103834.

Colombi, Pierluigi, and Carlo Poggi. 2006. "An Experimental, Analytical and Numerical Study of the Static Behavior of Steel Beams Reinforced by Pultruded CFRP Strips." *Composites Part B: Engineering* 37 (1): 64–73. https://doi.org/10.1016/j.compositesb.2005.03.002.

Crank, John. 1976. *The Mathematics of Diffusion*. 2. ed., Reprint. Clarendon Press.

D

Datla, N. V., J. Ulicny, B. Carlson, M. Papini, and J. K. Spelt. 2011. "Mixed-Mode Fatigue Behavior of Degraded Toughened Epoxy Adhesive Joints." *International Journal of Adhesion and Adhesives* 31 (2): 88–96. https://doi.org/10.1016/j.ijadhadh.2010.11.007.

Davies, P., B. R. K. Blackman, and A. J. Brunner. 2001. "Mode II Delamination." In *European Structural Integrity Society*, edited by D. R. Moore, A. Pavan, and J. G. Williams, vol. 28. Fracture Mechanics Testing Methods for Polymers, Adhesives and Composites. Elsevier. https://doi.org/10.1016/S1566-1369(01)80039-X.

Delzendeh Moghadam, Mohamadreza, Abbas Fathi, and Omar Chaallal. 2024. "Retrofitting of Steel Structures with CFRP: Literature Review and Research Needs." *Applied Sciences* 14 (13): 5958. https://doi.org/10.3390/app14135958.

Deng, Jun, and Marcus M. K. Lee. 2007. "Behaviour under Static Loading of Metallic Beams Reinforced with a Bonded CFRP Plate." *Composite Structures* 78 (2): 232–42. https://doi.org/10.1016/j.compstruct.2005.09.004.

Deng, Jun, and Marcus M. K. Lee. 2008. "Effect of Plate End and Adhesive Spew Geometries on Stresses in Retrofitted Beams Bonded with a CFRP Plate." *Composites Part B: Engineering* 39 (4): 731–39. https://doi.org/10.1016/j.compositesb.2007.05.004.

Deng, Jun, Marcus M. K. Lee, and Stuart S. J. Moy. 2004. "Stress Analysis of Steel Beams Reinforced with a Bonded CFRP Plate." *Composite Structures* 65 (2): 205–15. https://doi.org/10.1016/j.compstruct.2003.10.017.

Djellouli, Belahcen, Wajdi Zouari, Mustapha Assarar, and Rezak Ayad. 2021. "Analysis of the Hygroscopic and Hygroelastic Behaviours of Water Aged Flax-Epoxy Composite." *Composite Structures* 265 (June): 113692. https://doi.org/10.1016/j.compstruct.2021.113692.

DNV. 2011. *DNV-RP-C203: Fatigue Design of Offshore Steel Structures*.

DNV. 2015. *DNV-RP-C301: Design, Fabrication, Operation and Qualification of Bonded Repair of Steel Structures*.

Donaldson, Steven L. 1988. “Mode III Interlaminar Fracture Characterization of Composite Materials.” *Composites Science and Technology* 32 (3): 225–49. https://doi.org/10.1016/0266-3538(88)90022-X.

Dong, Kai, Xiao Peng, Jiajin Zhang, Bohong Gu, and Baozhong Sun. 2017. “Temperature-Dependent Thermal Expansion Behaviors of Carbon Fiber/Epoxy Plain Woven Composites: Experimental and Numerical Studies.” *Composite Structures* 176 (September): 329–41. https://doi.org/10.1016/j.compstruct.2017.05.036.

E

Ee Hua Wong, Yong Chua Teo, and Thiam Beng Lim. 1998. “Moisture Diffusion and Vapour Pressure Modeling of IC Packaging.” *1998 Proceedings. 48th Electronic Components and Technology Conference (Cat. No.98CH36206)*, 1372–78. https://doi.org/10.1109/ECTC.1998.678922.

EN 1993-1-9 (Eurocode 3). 2005. *EN 1993-1-9: Eurocode 3: Design of Steel Structures - Part 1-9: Fatigue*.

Esfandiari, Kourosh, Morteza Banihashemi, and Parinaz Soleimani. 2020. “Influence of Impressed Current Cathodic Protection Systems on Chemical Characteristics of Underground Water.” *Water Environment Research* 92 (12): 2105–11. https://doi.org/10.1002/wer.1371.

Esposito, Marco, Salvatore Buontempo, Angelo Petriccione, et al. 2013. “Fiber Bragg Grating Sensors to Measure the Coefficient of Thermal Expansion of Polymers at Cryogenic Temperatures.” *Sensors and Actuators A: Physical* 189 (January): 195–203. https://doi.org/10.1016/j.sna.2012.09.016.

European Commission. Directorate General for Research and Innovation. 2014. *Fatigue Damage Control and Assessment for Railways Bridges (FADLESS): Final Report.* Publications Office. https://data.europa.eu/doi/10.2777/59688.

F

Fick, Adolph. 1855. “V. *On Liquid Diffusion*.” *The London, Edinburgh, and Dublin Philosophical Magazine and Journal of Science* 10 (63): 30–39. https://doi.org/10.1080/14786445508641925.

Fourier, Jean-Baptiste Joseph. 1822. *Théorie analytique de la chaleur*. Firmin Didot, Père et Fils. https://gallica.bnf.fr/ark:/12148/bpt6k9611041v.

Frangopol, Dan, Richard Sause, and Chad Kusko, eds. 2010. *Bridge Maintenance, Safety, Management and Life-Cycle Optimization*. Vol. 20100869. Bridge Maintenance, Safety and Management. CRC Press. https://doi.org/10.1201/b10430.

Freitas, Sofia Teixeira de, and Jos Sinke. 2014. “Adhesion Properties of Bonded Composite-to-Aluminium Joints Using Peel Tests.” *The Journal of Adhesion* 90 (5–6): 511–25. https://doi.org/10.1080/00218464.2013.850424.

Freitas, Sofia Teixeira de, and Jos Sinke. 2015. “Test Method to Assess Interface Adhesion in Composite Bonding.” *Applied Adhesion Science* 3 (1): 9. https://doi.org/10.1186/s40563-015-0033-5.

G

Gholami, Mehran, Abdul Rahman Mohd Sam, Jamaludin Mohamad Yatim, and Mahmood Md Tahir. 2013. “A Review on Steel/CFRP Strengthening Systems Focusing Environmental Performance.” *Construction and Building Materials* 47 (October): 301–10. https://doi.org/10.1016/j.conbuildmat.2013.04.049.

Ghumatkar, A., S. Budhe, R. Sekhar, M. D. Banea, and S. De Barros. 2016. “Influence of Adherend Surface Roughness on the Adhesive Bond Strength.” *Latin American Journal of Solids and Structures* 13 (13): 2356–70. https://doi.org/10.1590/1679-78253066.

Ghumatkar, Akshay, Ravi Sekhar, and Sandip Budhe. 2017. “Experimental Study on Different Adherend Surface Roughness on the Adhesive Bond Strength.” *Materials Today: Proceedings*, International Conference on Advancements in Aeromechanical Materials for Manufacturing (ICAAMM-2016): Organized by MLR Institute of Technology, Hyderabad, Telangana, India, vol. 4 (8): 7801–9. https://doi.org/10.1016/j.matpr.2017.07.115.

Gomez-Campos, Alejandra, Claire Vialle, Antoine Rouilly, Caroline Sablayrolles, and Lorie Hamelin. 2021. “Flax Fiber for Technical Textile: A Life Cycle Inventory.” *Journal of Cleaner Production* 281 (January): 125177. https://doi.org/10.1016/j.jclepro.2020.125177.

Goodenough, Jacob, Annabel Fitzgerald, Keith Bean, et al. 2023. “Reversible Adhesives and Debondable Joints for Fibre-Reinforced Plastics: Characteristics, Capabilities, and Opportunities.” *Materials Chemistry and Physics* 299 (April): 127464. https://doi.org/10.1016/j.matchemphys.2023.127464.

Graciani, Enrique, Jesús Justo, and Patricia Lucía Zumaquero. 2020. “Determination of In-Plane and through-the-Thickness Coefficients of Thermal Expansion in Composite Angle Brackets Using Digital Image Correlation.” *Composite Structures* 238 (April): 111939. https://doi.org/10.1016/j.compstruct.2020.111939.

Grangeat, Romain. 2019. “Durabilité Des Assemblages Collés En Environnement Humide - Instrumentation Par Capteurs à Fibre Optique.” Université Bretagne Loire.

Guo, Dong, Yun-Lin Liu, Wan-Yang Gao, and Jian-Guo Dai. 2023. “Bond Behavior of CFRP-to-Steel Bonded Joints at Different Service Temperatures: Experimental Study and FE Modeling.” *Construction and Building Materials* 362 (January): 129836. https://doi.org/10.1016/j.conbuildmat.2022.129836.

H

Hansen, Ole, Leon Freitag, Stefan Friebel, and Jens Lüttke. 2024. “Influence of the Thermal Expansion on the Surface Quality of Coated and Non-Coated Natural-Fiber-Reinforced Composites.” *Composites Part C: Open Access* 13 (March): 100428. https://doi.org/10.1016/j.jcomc.2023.100428.

Heshmati, Mohsen, Reza Haghani, and Mohammad Al-Emrani. 2015. “Environmental Durability of Adhesively Bonded FRP/Steel Joints in Civil Engineering Applications: State of the Art.” *Composites Part B: Engineering* 81 (November): 259–75. https://doi.org/10.1016/j.compositesb.2015.07.014.

Heshmati, Mohsen, Reza Haghani, and Mohammad Al-Emrani. 2017. “Durability of Bonded FRP-to-Steel Joints: Effects of Moisture, de-Icing Salt Solution, Temperature and FRP Type.” *Composites Part B: Engineering* 119 (June): 153–67. https://doi.org/10.1016/j.compositesb.2017.03.049.

Hollaway, L. C., and J. Cadei. 2002. “Progress in the Technique of Upgrading Metallic Structures with Advanced Polymer Composites.” *Progress in Structural Engineering and Materials* 4 (2): 131–48. https://doi.org/10.1002/pse.112.

I

IDRRRIM. 2024. “11468-IDRRIM_Rapport_ONR_2024.”

Imam, B., and M. K. Chryssanthopoulos. 2010. “A Review of Metallic Bridge Failure Statistics.” *Bridge Maintenance, Safety and Management: Proceedings of the Fifth International IABMAS Conference*, July 7, 3275–82. https://openresearch.surrey.ac.uk/esploro/outputs/conferencePresentation/A-review-of-metallic-bridge-failure/99513427802346.

International Organization for Standardization. 2008. *Plastics — Determination of Water Absorption*. ISO 62:2008. International Organization for Standardization (ISO). https://www.iso.org/standard/41672.html.

ISO 4287:1997. 1997. “ISO 4287:1997.” https://www.iso.org/standard/10132.html.

ISO 21920-2:2021. 2021. “ISO 21920-2:2021.” https://www.iso.org/fr/standard/72226.html.

K

Karam, Ehab Clovis. 2015. “RETROFITTING OF COMPOSITE STEEL BEAMS PRE-DAMAGED IN FLEXURE USING FIBER REINFORCED POLYMERS.” American University of Sharjah.

Katsivalis, Ioannis, and Stefanie Feih. 2022. “Prediction of Moisture Diffusion and Failure in Glass/Steel Adhesive Joints.” *Glass Structures & Engineering* 7 (3): 381–97. https://doi.org/10.1007/s40940-022-00194-w.

Katsivalis, Ioannis, Ole Thybo Thomsen, Stefanie Feih, and Mithila Achintha. 2020. “Effect of Elevated Temperatures and Humidity on Glass/Steel Adhesive Joints.”

International Journal of Adhesion and Adhesives 102 (October): 102691. https://doi.org/10.1016/j.ijadhadh.2020.102691.

Kawashita, L. F., D. R. Moore, and J. G. Williams. 2005. "Comparison of Peel Tests for Metal–Polymer Laminates for Aerospace Applications." *The Journal of Adhesion* 81 (6): 561–86. https://doi.org/10.1080/00218460590954557.

Kawashita, L. F., D. R. Moore, and J. G. Williams. 2006. "Protocols for the Measurement of Adhesive Fracture Toughness by Peel Tests." *The Journal of Adhesion* 82 (10): 973–95. https://doi.org/10.1080/00218460600876142.

Ke, Lu, Chuanxi Li, Jun He, Shuai Dong, Can Chen, and Yang Jiao. 2020. "Effects of Elevated Temperatures on Mechanical Behavior of Epoxy Adhesives and CFRP-Steel Hybrid Joints." *Composite Structures* 235 (March): 111789. https://doi.org/10.1016/j.compstruct.2019.111789.

Kinloch, A. J., C. C. Lau, and J. G. Williams. 1994. "The Peeling of Flexible Laminates." *International Journal of Fracture* 66 (1): 45–70. https://doi.org/10.1007/BF00012635.

Kumar, Bikash, Tushar R. Dandekar, and Soran Birosca. 2024. "Probing the Temperature Field and Residual Stress Transformation in Multi-Track, Multi-Layered System." *Materials Today Communications* 38 (March): 108056. https://doi.org/10.1016/j.mtcomm.2024.108056.

L

Lau, Kin-tak, Pui-yan Hung, Min-Hao Zhu, and David Hui. 2018. "Properties of Natural Fibre Composites for Structural Engineering Applications." *Composites Part B: Engineering* 136 (March): 222–33. https://doi.org/10.1016/j.compositesb.2017.10.038.

Lee, G. C., S. B. Mohan, C. Huang, and B. N. Fard. 2013. *A Study of U.S. Bridge Failures (1980-2012)*.

Leguillon, Dominique. 2002. "Strength or Toughness? A Criterion for Crack Onset at a Notch." *European Journal of Mechanics - A/Solids* 21 (1): 61–72. https://doi.org/10.1016/S0997-7538(01)01184-6.

Lepretre, E., S. Chataigner, L. Dieng, and L. Gaillet. 2018. "Fatigue Strengthening of Cracked Steel Plates with CFRP Laminates in the Case of Old Steel Material." *Construction and Building Materials* 174 (June): 421–32. https://doi.org/10.1016/j.conbuildmat.2018.04.063.

Lepretre, Emilie. 2017. "Efficacité du renforcement par composites collés vis-à-vis de la propagation de fissures de fatigue pour une application aux structures rivetées."

Li, Anbang, Shanhua Xu, Youde Wang, Cheng Wu, and Biao Nie. 2022. "Fatigue Behavior of Corroded Steel Plates Strengthened with CFRP Plates." *Construction and Building Materials* 314 (January): 125707. https://doi.org/10.1016/j.conbuildmat.2021.125707.

Linghoff, D., M. Al-Emrani, and R. Kliger. 2010. “Performance of Steel Beams Strengthened with CFRP Laminate – Part 1: Laboratory Tests.” *Composites Part B: Engineering* 41 (7): 509–15. https://doi.org/10.1016/j.compositesb.2009.05.008.

Liu, Dapeng, Jing Wang, Ruiyang Liu, and S. B. Park. 2016. “An Examination on the Direct Concentration Approach to Simulating Moisture Diffusion in a Multi-Material System.” *Microelectronics Reliability* 60 (May): 109–15. https://doi.org/10.1016/j.microrel.2016.03.012.

Liu, Xiangdong. 2003. “Rehabilitation of Steel Bridge Members with FRP Composite Materials.” https://scholarsmine.mst.edu/doctoral_dissertations/1508.

Lye, Hui Li, Bashar S. Mohammed, Mohamed Mubarak Abdul Wahab, and Mohd Shahir Liew. 2021. “Bond Relationship of Carbon Fiber-Reinforced Polymer (CFRP) Strengthened Steel Plates Exposed to Service Temperature.” *Materials* 14 (13): 3761. https://doi.org/10.3390/ma14133761.

M

Mesquita, Francisco, Yentl Swolfs, Stepan V. Lomov, and Larissa Gorbatikh. 2022. “In-Situ Synchrotron Computed Tomography Tensile Testing Observations of the Hybrid Effect: A Comparison with Theory.” *Composites Part B: Engineering* 235 (April): 109765. https://doi.org/10.1016/j.compositesb.2022.109765.

Miller, Trent C., Michael J. Chajes, Dennis R. Mertz, and Jason N. Hastings. 2001. “Strengthening of a Steel Bridge Girder Using CFRP Plates.” *Journal of Bridge Engineering* 6 (6): 514–22. https://doi.org/10.1061/(ASCE)1084-0702(2001)6:6(514).

Mohabeddine, Anis, Ghassan Malik, José Correia, Abílio De Jesus, Nicholas Fantuzzi, and José Miguel Castro. 2023. “High Performance and Cost-Effective Hybrid Steel/CFRP Joints Using Bi-Adhesive Technique for the Repair of Metallic Infrastructures.” *Composite Structures* 321 (October): 117284. https://doi.org/10.1016/j.compstruct.2023.117284.

Moura, Ana P. de, Enio HP da Silva, Vanessa S. dos Santos, et al. 2021. “Structural and Mechanical Characterization of Polyurethane-CaCO3 Composites Synthesized at High Calcium Carbonate Loading: An Experimental and Theoretical Study.” *Journal of Composite Materials* 55 (21): 2857–66. https://doi.org/10.1177/0021998321996414.

Mubashar, A., I. A. Ashcroft, G. W. Critchlow, and A. D. Crocombe. 2009. “Moisture Absorption–Desorption Effects in Adhesive Joints.” *International Journal of Adhesion and Adhesives* 29 (8): 751–60. https://doi.org/10.1016/j.ijadhadh.2009.05.001.

Mulle, M., R. Zitoune, F. Collombet, P. Olivier, and Y. H. Grunevald. 2007. “Thermal Expansion of Carbon–Epoxy Laminates Measured with Embedded FBGS – Comparison with Other Experimental Techniques and Numerical Simulation.” *Composites Part A: Applied Science and Manufacturing* 38 (5): 1414–24. https://doi.org/10.1016/j.compositesa.2006.08.008.

N

Neto, Jorge, Henrique Queiroz, Ricardo Aguiar, Rosemere Lima, Daniel Cavalcanti, and Mariana Doina Banea. 2022. “A Review of Recent Advances in Hybrid Natural Fiber Reinforced Polymer Composites.” *Journal of Renewable Materials* 10 (3): 561–89. https://doi.org/10.32604/jrm.2022.017434.

P

Paboeuf, S., M. Deydier, E. Leprêtre, S. Chataigner, and Q. Sourisseau. 2025. “Composite Patch Repairs – A New Qualification Methodology.” *Offshore Technology Conference*, April 28, D031S039R007. https://doi.org/10.4043/35895-MS.

Peiris, A., and I. Harik. 2021. “Steel Beam Strengthening with UHM CFRP Strip Panels.” *Engineering Structures* 226 (January): 111395. https://doi.org/10.1016/j.engstruct.2020.111395.

Peiris, Nisal Abheetha. 2011. “STEEL BEAMS STRENGTHENED WITH ULTRA HIGH MODULUS CFRP LAMINATES.” University of Kentucky.

Pierron, F., Y. Poirette, and A. Vautrin. 2002. “Identification d’une Loi de Fick 3D Anisotrope : Théorie et Validation.” *Journal de Physique IV (Proceedings)* 12 (11): 251–58. https://doi.org/10.1051/jp4:20020500.

R

Ramalho, L. D. C., R. D. S. G. Campilho, J. Belinha, and L. F. M. Da Silva. 2020. “Static Strength Prediction of Adhesive Joints: A Review.” *International Journal of Adhesion and Adhesives* 96 (January): 102451. https://doi.org/10.1016/j.ijadhadh.2019.102451.

Ran, Zhiguo, Ying Yan, Jianfeng Li, Zhongxing Qi, and Lei Yang. 2014. “Determination of Thermal Expansion Coefficients for Unidirectional Fiber-Reinforced Composites.” *Chinese Journal of Aeronautics* 27 (5): 1180–87. https://doi.org/10.1016/j.cja.2014.03.010.

Ruoranen, Johanna. 2018. “Effects of Static Loading and Environmental Conditions on the Aging Behavior of Aluminum Adhesive Joints.” Tampere University of Technology.

S

Saidane, El Hadi, Daniel Scida, Mustapha Assarar, and Rezak Ayad. 2014. *Identification of 3D Moisture Diffusion Coefficients on Flax Fibre- Epoxy Composite*.

Saidane, El Hadi, Daniel Scida, Mustapha Assarar, and Rezak Ayad. 2016. “Assessment of 3D Moisture Diffusion Parameters on Flax/Epoxy Composites.” *Composites Part A: Applied Science and Manufacturing* 80 (January): 53–60. https://doi.org/10.1016/j.compositesa.2015.10.008.

Saidane, El Hadi, Daniel Scida, and Rezak Ayad. 2021. “Thermo-Mechanical Behaviour of Flax/Green Epoxy Composites: Evaluation of Thermal Expansion Coefficients and Application to Internal Stress Calculation.” *Industrial Crops and Products* 170 (October): 113786. https://doi.org/10.1016/j.indcrop.2021.113786.

Samali, Bijan, Parisa Shadan, and Nariman Saeed. 2023. “Bond Degradation at Environmentally Exposed FRP-Strengthened Steel Elements: State of the Art.” *Composites Part C: Open Access* 12 (October): 100374. https://doi.org/10.1016/j.jcomc.2023.100374.

Sarfaraz, Roohollah, Luis P. Canal, Georgios Violakis, John Botsis, Véronique Michaud, and Hans G. Limberger. 2015. “An Experimental–Numerical Investigation of Hydrothermal Response in Adhesively Bonded Composite Structures.” *Composites Part A: Applied Science and Manufacturing* 73 (June): 176–85. https://doi.org/10.1016/j.compositesa.2015.03.005.

Sarlin, E., E. Heinonen, J. Vuorinen, M. Vippola, and T. Lepistö. 2014. “Adhesion Properties of Novel Corrosion Resistant Hybrid Structures.” *International Journal of Adhesion and Adhesives* 49 (March): 51–57. https://doi.org/10.1016/j.ijadhadh.2013.12.009.

Schijve, Jaap. 2009. *Fatigue of Structures and Materials*. Springer Netherlands Springer e-books.

Schnerch, D., M. Dawood, S. Rizkalla, and E. Sumner. 2007. “Proposed Design Guidelines for Strengthening of Steel Bridges with FRP Materials.” *Construction and Building Materials* 21 (5): 1001–10. https://doi.org/10.1016/j.conbuildmat.2006.03.003.

Schnerch, David, and Sami Rizkalla. 2008. “Flexural Strengthening of Steel Bridges with High Modulus CFRP Strips.” *Journal of Bridge Engineering* 13 (2): 192–201. https://doi.org/10.1061/(ASCE)1084-0702(2008)13:2(192).

Scida, Daniel, Alain Bourmaud, and Christophe Baley. 2017. “Influence of the Scattering of Flax Fibres Properties on Flax/Epoxy Woven Ply Stiffness.” *Materials & Design* 122 (May): 136–45. https://doi.org/10.1016/j.matdes.2017.02.094.

Selvan, Ananth, Indran Suyambulingam, Arun Srinivasan, Sunesh Narayanaperumal, and P. Senthamaraikannan. 2026. “A Comprehensive Review on the Mitigation of Residual Strain in the Composite–Adhesive–Flange Interface of Liquid Hydrogen Storage Tanks.” *Cryogenics* 156 (April): 104298. https://doi.org/10.1016/j.cryogenics.2026.104298.

Shakir Abbood, Imad, Sief Aldeen Odaa, Kamalaldin F. Hasan, and Mohammed A. Jasim. 2021. “Properties Evaluation of Fiber Reinforced Polymers and Their Constituent Materials Used in Structures – A Review.” *Materials Today: Proceedings* 43: 1003–8. https://doi.org/10.1016/j.matpr.2020.07.636.

Shelly, Daksh, Varun Singhal, Sachin Jaidka, Mariana Doina Banea, Seul-Yi Lee, and Soo-Jin Park. 2025. “Mechanical Performance of Bio-based Fiber Reinforced Polymer Composites: A Review.” *Polymer Composites*, May 5, pc.30000. https://doi.org/10.1002/pc.30000.

Shiu, Sung-Chiun, and Jia-Lin Tsai. 2014. “Characterizing Thermal and Mechanical Properties of Graphene/Epoxy Nanocomposites.” *Composites Part B: Engineering* 56 (January): 691–97. https://doi.org/10.1016/j.compositesb.2013.09.007.

Sicomin® GreenPoxy33_sd477x. 2023. “srGreenPoxy33_sd477x.”

Sideridou, Irini, Dimitris S. Achilias, and Eleni Kyrikou. 2004. “Thermal Expansion Characteristics of Light-Cured Dental Resins and Resin Composites.” *Biomaterials* 25 (15): 3087–97. https://doi.org/10.1016/j.biomaterials.2003.09.078.

Sika® adekit-a155-h9955. 2020. “ADEKIT A155 / H9955.”

Sika® Aktivator-205. 2023. “Sika Aktivator-205.”

Sika®Sikafast-555-l05. 2023. “Sikafast-555-L05.”

Sika®Sikaflex-554. 2023. “Sikaflex-554.”

Sika®Sikapower-1200. 2023. “Sikapower-1200.”

Silva, EHP, JCF Aguiar, G. Waldow, RRC Costa, V. Tita, and ML Ribeiro. 2022. “Compression and Morphological Properties of a Bio-Based Polyurethane Foam with Aluminum Hydroxide.” *Proceedings of the Institution of Mechanical Engineers, Part L: Journal of Materials: Design and Applications* 236 (7): 1408–18. https://doi.org/10.1177/14644207211059077.

Silva, Lucas Filipe Martins da, Andreas Öchsner, and Robert D. Adams. 2018. *Handbook of Adhesion Technology*. 2nd edition. Springer.

SIMULIA User Assistance. 2025. “Hybrid Incompressible Solid Element Formulation - Assistance Utilisateur SIMULIA 2025.” https://help.3ds.com/2025/english/dssimulia_established/simacaetherefmap/simathe-c-hybridincompress.htm?contextscope=all.

Siwowski, Tomasz W., and Paulina Siwowska. 2018. “Experimental Study on CFRP-Strengthened Steel Beams.” *Composites Part B: Engineering* 149 (September): 12–21. https://doi.org/10.1016/j.compositesb.2018.04.060.

Smith, S. T., and J. G. Teng. 2001. “Interfacial Stresses in Plated Beams.” *Engineering Structures* 23 (7): 857–71. https://doi.org/10.1016/S0141-0296(00)00090-0.

Sourisseau, Quentin, Emilie Leprêtre, Sylvain Chataigner, Xavier Chapeleau, Luc Mouton, and Stéphane Paboeuf. 2022. “Adhesively Bonded FRP Reinforcement of Steel Structures: Surface Preparation Analysis and Influence of the Primer.” *Volume 1: Offshore Technology*, June 5, V001T01A022. https://doi.org/10.1115/OMAE2022-79079.

Stephens, Ralph I., and Henry Otten Fuchs, eds. 2001. *Metal Fatigue in Engineering*. 2. ed. A Wiley-Interscience Publication. Wiley.

Stratford, Tim, and John Cadei. 2006. “Elastic Analysis of Adhesion Stresses for the Design of a Strengthening Plate Bonded to a Beam.” *Construction and Building Materials* 20 (1–2): 34–45. https://doi.org/10.1016/j.conbuildmat.2005.06.041.

Stratford, Tim, John Cadei, and Len Hollaway. 2004. “CIRIA C595 – STRENGTHENING METALLIC STRUCTURES USING EXTERNALLY-BONDED FRP.” In *Advanced Polymer Composites for Structural Applications in Construction*. Elsevier. https://doi.org/10.1533/9781845690649.7.693.

T

Tabrizi, Salar, Hamid Kazem, Sami Rizkalla, and Akira Kobayashi. 2015. “New Small-Diameter CFRP Material for Flexural Strengthening of Steel Bridge Girders.” *Construction and Building Materials* 95 (October): 748–56. https://doi.org/10.1016/j.conbuildmat.2015.07.109.

Tafsirojjaman, T., Attiq Ur Rahman Dogar, Yue Liu, Allan Manalo, and David P. Thambiratnam. 2022. “Performance and Design of Steel Structures Reinforced with FRP Composites: A State-of-the-Art Review.” *Engineering Failure Analysis* 138 (August): 106371. https://doi.org/10.1016/j.engfailanal.2022.106371.

Takeda, Tomo, Fumio Narita, Yasuhide Shindo, and Kazuaki Sanada. 2015. “Cryogenic Through-Thickness Tensile Characterization of Plain Woven Glass/Epoxy Composite Laminates Using Cross Specimens: Experimental Test and Finite Element Analysis.” *Composites Part B: Engineering* 78 (September): 42–49. https://doi.org/10.1016/j.compositesb.2015.03.076.

Takeda, Tomo, Yasuhide Shindo, and Fumio Narita. 2004. “Three-Dimensional Thermoelastic Analysis of Cracked Plain Weave Glass/Epoxy Composites at Cryogenic Temperatures.” *Composites Science and Technology* 64 (15): 2353–62. https://doi.org/10.1016/j.compscitech.2004.04.003.

Tazi, Mohamed Amine, Rosemere de Araujo Alves Lima, Enio Henrique Pires da Silva, et al. 2024. “Experimental Evaluation of Interface Adhesion of a Flax Fiber Composite Patch with Epoxy and Polyurethane Adhesives for the Reinforcement of Steel Structures.” *International Journal of Adhesion and Adhesives* 129 (February): 103559. https://doi.org/10.1016/j.ijadhadh.2023.103559.

Teixeira de Freitas, S., M. D. Banea, S. Budhe, and S. de Barros. 2017. “Interface Adhesion Assessment of Composite-to-Metal Bonded Joints under Salt Spray Conditions Using Peel Tests.” *Composite Structures* 164 (March): 68–75. https://doi.org/10.1016/j.compstruct.2016.12.058.

Teixeira De Freitas, S., M. D. Banea, S. Budhe, and S. De Barros. 2017. “Interface Adhesion Assessment of Composite-to-Metal Bonded Joints under Salt Spray Conditions Using Peel Tests.” *Composite Structures* 164 (March): 68–75. https://doi.org/10.1016/j.compstruct.2016.12.058.

Teng, J. G., T. Yu, and D. Fernando. 2012. “Strengthening of Steel Structures with Fiber-Reinforced Polymer Composites.” *Journal of Constructional Steel Research* 78 (November): 131–43. https://doi.org/10.1016/j.jcsr.2012.06.011.

Tsai, C. L., Y. L. Guan, D. C. Ohanehi, J. G. Dillard, D. A. Dillard, and R. C. Batra. 2014. “Analysis of Cohesive Failure in Adhesively Bonded Joints with the SSPH Meshless Method.” *International Journal of Adhesion and Adhesives* 51 (June): 67–80. https://doi.org/10.1016/j.ijadhadh.2014.02.009.

Tsai, M. Y., and J. Morton. 1995. “The Effect of a Spew Fillet on Adhesive Stress Distributions in Laminated Composite Single-Lap Joints.” *Composite Structures* 32 (1–4): 123–31. https://doi.org/10.1016/0263-8223(95)00059-3.

W

Wan, Y. Z., L. Hong, S. R. Jia, et al. 2006. “Synthesis and Characterization of Hydroxyapatite–Bacterial Cellulose Nanocomposites.” *Composites Science and Technology* 66 (11): 1825–32. https://doi.org/10.1016/j.compscitech.2005.11.027.

Wang, Zhen, and Guijun Xian. 2021. “Effects of Thermal Expansion Coefficients Discrepancy on the CFRP and Steel Bonding.” *Construction and Building Materials* 269 (February): 121356. https://doi.org/10.1016/j.conbuildmat.2020.121356.

Wei, Kai, Yiwei Chen, Maojun Li, and Xujing Yang. 2018. “Strength and Failure Mechanism of Composite-Steel Adhesive Bond Single Lap Joints.” *Advances in Materials Science and Engineering* 2018 (1): 5810180. https://doi.org/10.1155/2018/5810180.

X

Xie, B., X. J. Fan, X. Q. Shi, and H. Ding. 2009. “Direct Concentration Approach of Moisture Diffusion and Whole-Field Vapor Pressure Modeling for Reflow Process—Part I: Theory and Numerical Implementation.” *Journal of Electronic Packaging* 131 (3): 031010. https://doi.org/10.1115/1.3144147.

Y

Yan, Libo, Nawawi Chouw, and Krishnan Jayaraman. 2014. “Flax Fibre and Its Composites – A Review.” *Composites Part B: Engineering* 56 (January): 296–317. https://doi.org/10.1016/j.compositesb.2013.08.014.

Yang, Muye, Jian Tang, and Shigenobu Kainuma. 2025. “Inhibition and Facilitation Mechanisms of Galvanic Corrosion between Carbon Fiber and Steel in Atmospheric Environments.” *Composites Part B: Engineering* 297 (May): 112332. https://doi.org/10.1016/j.compositesb.2025.112332.

Yang, Yongming, Hugo Biscaia, Carlos Chastre, and Manuel A. G. Silva. 2017. “Bond Characteristics of CFRP-to-Steel Joints.” *Journal of Constructional Steel Research* 138 (November): 401–19. https://doi.org/10.1016/j.jcsr.2017.08.001.

Yoon, Samson, Bongtae Han, and Zhaoyang Wang. 2007. “On Moisture Diffusion Modeling Using Thermal-Moisture Analogy.” *Journal of Electronic Packaging* 129 (4): 421–26. https://doi.org/10.1115/1.2804090.

Z

Zain, Norazwani Muhammad, Eida Nadirah Roslin, and Sahrim Ahmad. 2016. “Preliminary Study on Bio-Based Polyurethane Adhesive/Aluminum Laminated Composites for Automotive Applications.” *International Journal of Adhesion and Adhesives* 71 (December): 1–9. https://doi.org/10.1016/j.ijadhadh.2016.08.001.

Zeng, Jun-Jie, Wan-Yang Gao, and Feng Liu. 2018. “Interfacial Behavior and Debonding Failures of Full-Scale CFRP-Strengthened H-Section Steel Beams.” *Composite Structures* 201 (October): 540–52. https://doi.org/10.1016/j.compstruct.2018.06.045.

Zhao, Xiao-Ling, and Lei Zhang. 2007. “State-of-the-Art Review on FRP Strengthened Steel Structures.” *Engineering Structures* 29 (8): 1808–23. https://doi.org/10.1016/j.engstruct.2006.10.006.

Zouari, Wajdi, Mustapha Assarar, Abderrazak Chilali, Rezak Ayad, and Hocine Kebir. 2019. “Numerical Modelling of the Transient Hygroscopic Behavior of Flax-Epoxy Composite.” *Journal of Renewable Materials* 7 (9): 839–53. https://doi.org/10.32604/jrm.2019.06773.

Mohamed Amine TAZI

Renforcement en flexion de structures en acier par collage de patchs composites carbone et lin : performances mécaniques et effets du vieillissement en milieu aqueux

Résumé : Cette thèse porte sur le renforcement en flexion de structures en acier par collage externe de patchs en polymère renforcé de fibres (PRF). Elle compare l'influence de différents adhésifs structuraux ainsi que celle de renforts PRF carbone/époxy, lin/époxy et hybrides carbone-lin/époxy, puis analyse l'effet d'un vieillissement par immersion sur la performance de ces renforcements. Le renforcement par patch composite collé constitue une alternative attractive « à froid » au soudage ou au boulonnage, permettant de limiter les contraintes résiduelles, de réduire la masse ajoutée et de s'adapter à des géométries variées. Le travail se situe dans le cadre du renforcement de pièces acier saines, c'est-à dire l'amélioration de leur rigidité et de leur capacité par rapport à l'état initial, où la compréhension du transfert de charge acier–adhésif–composite est déterminante, l'adhésif concentrant fréquemment les contraintes interfaciales critiques. La première phase de la thèse a consisté à évaluer l'adhérence interfaciale d'assemblages collés acier/PRF lin au moyen du test de pelage standard dit « floating roller peel test ». Ce test a permis de comparer les efforts de pelage, d'identifier les modes de rupture et de sélectionner des adhésifs adaptés au collage de substrats acier et PRF. Bien que ce test soit principalement employé pour la résistance au pelage et l'analyse des surfaces de rupture, il peut aussi être exploité dans une approche de mécanique de la rupture ; une contribution de modélisation par éléments finis a ainsi été développée afin d'identifier des grandeurs énergétiques pertinentes, tel que l'énergie de libération, associées à la propagation de la rupture dans l'adhésif, à partir des résultats expérimentaux. La deuxième phase a porté sur des essais de flexion quasi-statique de plaques d'acier renforcées par patchs PRF collés, en mobilisant des adhésifs de comportement contrasté, allant d'un époxy rigide à des solutions plus ductiles (acrylate et polymère modifié silane). Cette partie met en évidence l'intérêt de stratégies de conception visant à réduire les concentrations de contraintes interfaciales, par le choix de l'adhésif et par l'optimisation de l'architecture des patchs hybrides, afin de retarder l'amorçage et le développement du décollement. La troisième phase a été consacrée à la caractérisation du comportement hygro-mécanique des patchs PRF, par essais gravimétriques en immersion, mesure du gonflement hygroscopique et essais de flexion avant/après vieillissement. Les résultats confirment une sensibilité très faible du composite carbone aux effets de l'eau en flexion, alors que le composite lin présente une dégradation marquée de la rigidité et une évolution vers une réponse plus ductile après vieillissement, avec une baisse du module en flexion de l'ordre de 6,3 % pour le carbone contre 53,6 % pour le lin, dans les conditions étudiées. Enfin, une stratégie de modélisation éléments finis des comportements hygro-mécaniques est proposée, en s'appuyant sur l'analogie entre conduction thermique et diffusion de l'eau, ainsi que sur une formulation de type « wetness fraction » permettant de traiter la discontinuité de teneur en eau aux interfaces. L'ensemble apporte des éléments de compréhension et des leviers de conception pour des renforcements acier composite collés plus performants et plus robustes vis-à-vis de l'eau.

Mots clés : Patches composites, Renforcement, Adhésion, Acier, Fibres de lin, Vieillissement.